ISBN 978-82-326-0852-2 (printed version)
ISBN 978-82-326-0853-9 (electronic version)
ISSN 1503-8181

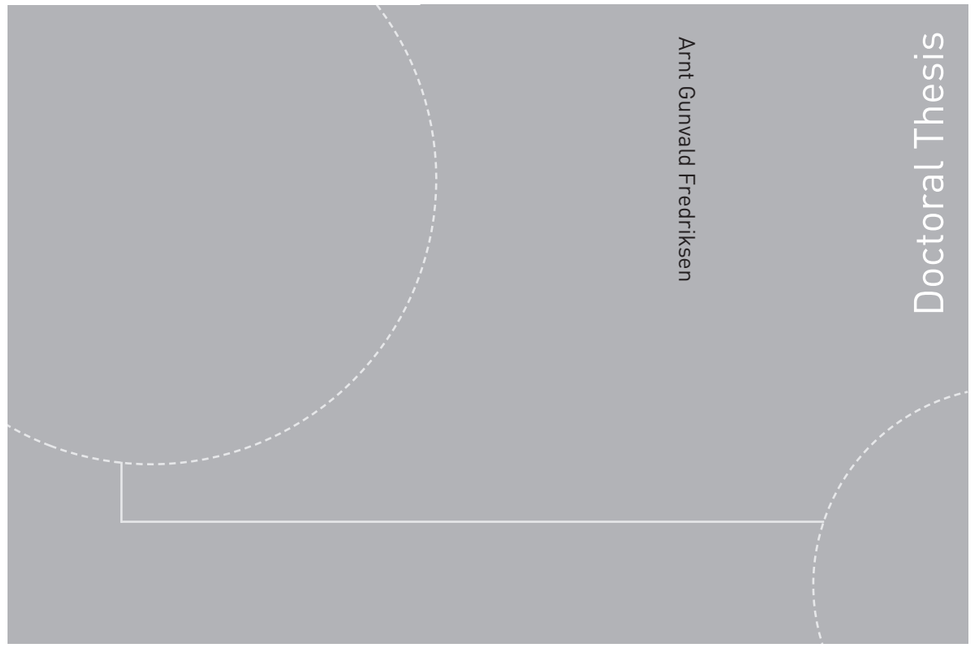

Doctoral theses at NTNU, 2015:98

Arnt Gunvald Fredriksen

A numerical and experimental study of a two-dimensional body with moonpool in waves and current

NTNU – Trondheim
Norwegian University of
Science and Technology

Doctoral theses at NTNU, 2015:98

NTNU

NTNU
Norwegian University of
Science and Technology
Faculty of Engineering
Science and Technology
Department of Marine
Technology

NTNU – Trondheim
Norwegian University of
Science and Technology

Arnt Gunvald Fredriksen

A numerical and experimental study of a two-dimensional body with moonpool in waves and current

Thesis for the degree of Philosophiae Doctor

Trondheim, May 2015

Norwegian University of Science and Technology
Faculty of Engineering Science and Technology
Department of Marine Technology

NTNU – Trondheim
Norwegian University of
Science and Technology

NTNU
Norwegian University of Science and Technology

Thesis for the degree of Philosophiae Doctor

Faculty of Engineering Science and Technology
Department of Marine Technology

ISBN 978-82-326-0852-2 (printed version)
ISBN 978-82-326-0853-9 (electronic version)
ISSN 1503-8181

Doctoral theses at NTNU, 2015:98

Printed by Skipnes Kommunikasjon as

Abstract

The present work has relevance for the behaviour of a vessel equipped with a moonpool in ocean waves. A moonpool is an opening in the middle of the vessel used for various marine operations. Resonant wave oscillations in the moonpool with the water moving as a vertical piston occur and cause operational limits. It is again confirmed by both numerical calculations and experiments in idealized two-dimensional flow conditions that flow separation from the lower entrance to the moonpool has a clear limiting effect on the resonant moonpool oscillations. Furthermore, the influence of low forward velocity on the piston-mode amplitude has been investigated and found insignificant. By considering incoming waves on a freely-floating vessel, it is found that the water behavior in the moonpool has a significant effect on the body motions in 2D-flow.

The present work is divided in two parts, first forced heave motion with and without low forward velocity of a two-dimensional body with moonpool has been considered. The second part is regular wave-induced behaviour of a floating stationary two-dimensional body with a moonpool, with focus on resonant piston-mode motion in the moonpool and rigid-body motions. Two separate dedicated two-dimensional experimental programmes have been performed. The outcome has been used to validate the two developed numerical hybrid methods that are used in the present work. The two hybrid methods are here named the "semi-nonlinear hybrid method" and the "nonlinear hybrid method", and both couple potential and viscous flow. The semi-nonlinear hybrid method uses linear free-surface and body-boundary conditions. The nonlinear hybrid method uses fully nonlinear free-surface and exact body-boundary conditions. The harmonic polynomial cell (HPC) method is used to solve the Laplace equation in the potential flow domain, while the finite volume method (FVM) is used to solve the Navier–Stokes equations in the viscous flow domain near the corners of the body. Results from the two hybrid methods are compared with the experimental data. The nonlinear hybrid method compares well with the data, while certain discrepancies are observed for the semi-nonlinear method. In particular, the roll motion is over-predicted by the semi-nonlinear hybrid method. Error sources in the semi-nonlinear hybrid method are discussed and investigated in detail in a separate section.

The first part of the work involved both experimental and numerical study of selected parameters and their effect on the piston-mode amplitude during forced heave oscillations. More precisely we investigated the effect of different drafts, moonpool edge profiles, heave oscillation amplitudes and low forward velocities.

In the second part regular wave-induced behaviour of a floating two-dimensional body with a moonpool was also studied by experimental and numerical methods. Here we have investigated the effect of different wave steepnesses, vessel drafts and moonpool edge profiles on a stationary floating body. The rigid-body and moonpool wave amplitude

response in head and following seas are also studied numerically. We see from the results that the moonpool strongly affects heave motions in a frequency range around the piston-mode resonance frequency of the moonpool. No resonant water motions occur in the moonpool at the piston-mode resonance frequency. Instead large moonpool motions occur at a heave natural frequency associated with small damping near the piston-mode resonance frequency.

Acknowledgements

This work has been carried out under the supervision of Professor Odd M. Faltinsen and dr. Trygve Kristiansen at the Centre for Ships and Ocean Structures (CeSOS)/ Department of Marine Technology, Norwegian University of Science and Technology. Their continuously support, deep understanding of hydrodynamics and excellent guidance during these five years are most appreciated and this work would not have been possible without their contribution.

The major part of this work has been financed by the Norwegian Research Council, through CeSOS. I am thankful for their support.

I would also like to thank all my fellow friends within hydrodynamics for many interesting and helpful discussions throughout my time in Trondheim: Babak, Bjørn, David, Jikun, Maxime, Mohsen, Reza, Yanlin and Zhao.

It has been challenging to finish this work after I moved from Trondheim to Tromsø, therefore I am grateful to my employer Multiconsult for giving me time and support during the last phases of this work.

Special attention and all my gratitude goes to my family for always supporting me.

Nomenclature

α	Phase angle between heave acceleration and moonpool motion
β	Phase angle between heave and roll acceleration
δy	Cell length.
δz	Cell height.
δ_{bl}	Oscillating boundary layer thickness
η_4^{Max}	Largest roll angle expected during a numerical nonlinear hybrid method simulation
Γ	Circulation around a closed curve in the liquid domain
$\mathbf{u}$	Absolute liquid particle velocity
$\mathbf{u}^*$	Temporary artificial liquid velocity after the advection step
$\mathbf{u}^{**}$	Temporary artificial liquid velocity after the advection and diffusion steps
$\mathbf{u}_r$	Relative liquid particle velocity in the body-fixed coordinate system
μ	Dynamic viscosity of the liquid
∇	Nabla operator
ν	Kinematic viscosity of the liquid
ν_w	Damping coefficient of numerical beach
ω	Angular frequency
ω_e	Angular frequency of encounter
Ω_{pot}	Potential flow domain part of the liquid domain
Ω_{CFD}	Viscous domain part of the liquid domain
ψ	Linear acceleration potential
ρ	Liquid density
τ	Viscous frictional stress, note there are many stress components

τ_w	Dimensionless parameter for wave characteristics, $\tau_w = \omega_e U/g$
$\tilde{p}$	$\frac{p}{\rho} + gz$
φ	Velocity potential
ξ	Damping ratio
B	Breadth of one side hull
B'	Total breadth of moonpool hull including screws in longitudinal direction
B_s	Length of the screw connecting the hull to the mooring line
B_{T}	Total breadth of the body, $2B + b$.
d	Hull draft
F_{pre}	Pre-tension in mooring lines
g	Acceleration of gravity
h	Water depth
I	Roll moment of inertia about the center of gravity
k	Wave number
k_s	Total spring stiffness constant
m	Body mass
r_{xx}	Radius of gyration in roll
Re	Reynolds number
S_{BP}	Potential flow part of hull surface
S_{BV}	Viscous flow part of hull surface
U	Forward velocity
z_b	Vertical position of center of buoyancy from the calm free surface, positive upwards
z_s	Vertical distance from the screw to the center of gravity
z_{G}	Vertical position of center of gravity from the calm free surface, positive upwards
(y, z)	The body-fixed coordinate system, the origio is attached to the center of gravity and it followes and rotates with the motion of the body
(y_e, z_e)	The Earth-fixed coordinate system, remains fixed in time and space to the free surface at the centerline of the initial position of the body

App.	Appendage at moonpool inlet
b	Moonpool gap width
BBC	Body-boundary conditions
BEM	Boundary Element Method
BICGSTAB	Biconjugate Gradient Stabilized method
CA	Control area
CFD	Computational Fluid Dynamics
CFL	Courant-Friedrichs-Lewy number
COG	Center of gravity
FDM	Finite Difference Method
FEM	Finite Element Method
FFT	Fast Fourier Transform
Fn	Froude number
FVM	Finite Volume Method
GM	Metacentric height
GMRES	Generalized Minimal Residual method
HPC	Harmonic Polynomial Cell
ILU	Incomplete Lower Upper
NL	Nonlinear
NS	Navier-Stokes
S-NL	Semi-nonlinear
TVD	Total Variation Diminishing scheme
VOF	Volume Of Fluid
WAMIT	Potential flow calculation software in the frequency domain

Contents

Chapter 1

Introduction

A moonpool is defined as an opening in the bottom of a ship hull. The opening allows for better access to the water below, and provides shelter and protection for most of the environmental conditions. Marine operations from ships often involve moonpools to lower or lift devices such as subsea modules and ROVs. A moonpool allows, for instance, divers a more protected environment to enter or leave the water. Resonant piston-mode resonance can be excited by the relative vertical ship motions in the neighborhood of the moonpool and cause strong amplification of the dynamic wave elevation in the moonpool. Here the piston-mode resonance is defined as the resonant liquid motion in the moonpool causing a net liquid flux through the lower entrance of the moonpool. The resonant flow is nearly vertical and one-dimensional in most of the moonpool. The word piston is associated with that the liquid motion appears like the motion of a piston. The stronger the shed vorticity due to flow separation at the moonpool entrance and inside the moonpool is, the larger the damping is, and the smaller the maximum resonant piston-mode wave amplitude is for a given ship in a given sea condition. It is of practical interest to know the free-surface elevation in the moonpool and the ambient flow velocities and accelerations in the vicinity of the moonpool in order to assess the loads on devices being lifted or lowered through the moonpool.

The use of moonpools to perform marine operations is expected to increase significantly. One reason is the rapid increase in development of subsea factories. Operators have defined goals such as near all-year availability for maintenance and repair, requiring operability in e.g. significant wave height $H_S = 4.5$m in the Aasgaard field in the North Sea. Specialized offshore vessels with moonpool are regarded as one of the key elements of achieving this. However, this requires careful design of the moonpool in order to avoid excessive resonant piston-mode motion

Moonpools are frequently designed to be used on fishing vessels. The purpose is then that the moonpool will work as a hauling well located in the centre of the hull where the longline will be hauled in. This feature, which helps reduce fish losses and improves crew safety, will also allow continuation of fishing even in bad weather. An example of this is the longliner fishing vessel M/S "Geir".

Another area of application for moonpools is for underwater diving bells or underwater habitats. Here, the moonpool is the only entry or exit point. It is the pressure inside the diving bell that balances the hydrostatic pressure at the surface of the moonpool. The pressure will therefor increase with increasing depth. In the current work, this application is out of scope.

1.1 Moonpool piston-mode resonance

One of the first articles discussing moonpool behaviour is Aalbers (1984). He related the moonpool motion to a mass spring system, and found empirical values through an experimental campaign. There has been studies like in Faltinsen (1990) based on neglecting the effect from outside the moonpool and assuming one-dimensional vertical potential flow in the moonpool.

Molin (2001) predicted the natural periods in moonpools by a quasi-analytical potential-flow approach. The work was for both the two- and three-dimensional case on infinite water depth by approximating the flow outside the moonpool. The outcome was a practical engineering friendly formula for the piston-mode natural period of the moonpool.

By using 2D potential and viscous flow methods, Lu et al. (2010) studied the wave amplitude inside narrow gaps between three adjacent boxes subjected to incoming waves. Model tests and numerical calculations in 3D of the gap resonance between two rigidly linked side by side barges were performed by Molin et al. (2009). The rigid-body motions of two freely floating adjacent barges in 3D were considered in Sun, Taylor, and Taylor (2010) by using a first- and second-order potential flow analysis.

Faltinsen et al. (2007) investigated forced heave oscillations of a two-dimensional moonpool section using a domain-decomposition (DD) scheme within the framework of linear potential flow theory. The hull parts were rectangular shaped and finite water effects were considered. Their DD scheme led to a system of integral equations on the transmission interfaces that solved for the piston-mode natural frequency and the steady-state piston-mode amplitude. To improve the potential flow models some authors have tried to fit an artificial, empirically based damping to the free-surface condition inside the moonpool. This is known as a numerical damping lid. Two ships side-by-side was investigated by Huijsmans et al. (2001), who used a lid approach to damp the moonpool motion to get realistic ship motions of a FPSO moored together with LNG carrier. Several other authors have also chosen the same strategy, i.e. to damp the potential flow solution by an artificial, empirically based numerical lid on the free-surface inside the moonpool gap (see for instance Buchner et al. (2001)). Lee et al. (2002) studied the "Navis Explorer I", which is a drillship equipped with 3 large moonpools. By using a numerical lid on the free-surface inside the moonpools, good agreement with experimental results was achieved. Pauw et al. (2007) analysed the effect the numerical lid had on the linear versus second order wave drift quantities. Lu et al. (2011) investigated the possibility of finding the lid damping coefficient based on experimental and CFD results. The damping coefficient was in their work observed not to be sensitive to the variation of moonpool gap width, body draft, breadth-to-draft ratio and number of bodies. Their focus was on wave forces, where Lu et al. (2011) used the same setup with focus on the wave elevation in the moonpool. It is not known when using a numerical damping lid how well the flow in the vicinity of the moonpool is predicted. Lu and Chen (2012) investigated what contributed to the dissipation of the piston-mode amplitude generated from incoming waves. Both the dissipation from the boundary layers inside the moonpool gap, and in which fluid areas around the moonpool gap the vorticity dissipation was largest were studied.

Wang and Wu (2008) studied both vertical and horizontal forcing motions of two box shaped structures with a distance of 7b between the two boxes, where b is the breadth of one box. They used a Finite Volume Method (FVM) based on potential flow with a second order perturbation scheme to solve the free-surface condition. Their focus was

on sloshing modes inside the moonpool. Later Wang et al. (2011) studied the problem further using nonlinear free-surface conditions, and found that the second order solution in Wang and Wu (2008) was bounded by nonlinear effects. Meaning that there will be an energy transfer to higher modes as in the normal sloshing problem, see Faltinsen and Timokha (2009).

Recently Kristiansen et al. (2013) validated a hybrid method based on coupling potential and viscous flow against a 3D moonpool set-up with sharp corners at the lower moonpool entrance. Their results showed that the resonant free-surface amplitude in the moonpool decreases from around 70 times the forced heave motion, to between 10-20 times the forced heave motion when flow separation is included.

Sphaier et al. (2007) have studied a monocolumn platform equipped with a moonpool named the MONOBR, where the objective was to use the moonpool as a heave minimization device for the response in the wave period domain. Torres et al. (2008) continued this analysis, and created a simplified mass-spring-damped model to analyse the system, where the moonpool is represented as a separate body with mass, damping, stiffness and coupling terms with the monocolumn. Unfortunately some coefficients still need to be experimentally found.

A preliminary CFD study including turbulence modelling of the vorticity generated in a moonpool between two infinite barges subjected to an incoming steady current were performed by Heiden et al. (2013). Results for the water motion in the moonpool due to the steady current are also given.

A closely related problem featuring piston-mode resonance is the mooring of a tanker to a terminal, this was studied by Kristiansen (2009) using a BEM with a vortex tracking method. His thesis includes the works Kristiansen and Faltinsen (2008), Kristiansen and Faltinsen (2009) and Kristiansen and Faltinsen (2010).

Molin et al. (2002) designed an experimental programme to quantify the energy dissipation due to flow separation at the lower edges of rectangular moonpools. By considering the dissipation of a propagating wave between two ice sheets the drag coefficient suggested to be used for design was found to be 0.5. In addition it was estimated that the frictional contribution to the energy dissipation was about 15% in model scale conditions.

In addition to the challenges with piston-mode resonance in a moonpool, the presence of a moonpool in a ship hull has also been found to increase the resistance in transit, van 't Veer and Tholen (2008) has experimentally studied various solutions on how to for instance minimize the added resistance due to a moonpool. Gaillarde and Cotteleer (2005) present a summary of various moonpool motions studies and give many practically useful solutions on how to damp out moonpool motions. Among the results presented are studies on how to reduce the added resistance due to an open moonpool at transit.

Yeung and Seah (2007) studied the piston-mode and higher-order resonance modes for a moonpool between two heaving rectangular floating cylinders using an eigenfunction matching method.

Two-dimensional moonpool resonance in a two-layer liquid is studied in Zhang and Bandyk (2013) and Zhang and Bandyk (2014) by potential flow theory. In the first study the interface between the two liquids with different density is located below the structure, here the resonances are found to be similar to the one-liquid case. It is also found that the resonances are closely associated with the free-surface elevation inside the moonpool gap, not the wave elevation at the interfacial surface. In the follow up study Zhang and Bandyk (2014), the moonpool structure is both free surface and interface piercing. The

piston-mode resonance is slightly changed and more resonance frequencies are found due to sloshing modes at the interface.

The rigid-body wave induced motions of a full scale drillship with and without a moonpool located midships by linear potential flow theory using a BEM have been conducted by Yang et al. (2013). The influence of the moonpool on the response amplitude operators for all 6 degree of freedoms is compared. Their results show some change in the heave motion for wave periods below the natural heave period.

An extensive experimental programme of a the rigid-body and moonpool motions of barge equiped with a large moonpool covering approximately 45% of the overall length and one third of the width is described in Maisondieu and Boulluec (2001) and Maisondieu and Ferrant (2003).

A related problem is the linear potential-flow study of trapped modes in the frequency domain. The trapped mode was first "discovered" by McIver (1996) in two-dimensions. A trapped mode is defined as a free-surface oscillation between bodies at a certain frequency that does not radiate waves to the far-field. An inverse procedure can be used to calculate the form of bodies with trapped modes. The inverse procedure works like the following, first two sources are placed at the free surface with a distance of half a wave length between them. Then the frequency where the far-field waves from one of the sources cancel with waves from the other source is found, such that there are not generated any waves in the far-field. The last step is to create the stream-function and look at the streamlines around the sources, as the streamlines guarantees that there is no flow perpendicular to the streamline. The streamlines can be taken to be shape of the body. Further studies have revealed many interesting properties of these trapped modes. One of these is that the trapped mode cannot be excited by incoming waves. At the trapped mode frequency the added mass goes to infinity, while it changes between large positive and large negative values in the vicinity of the trapped mode frequency.

Later McIver and McIver (1997) used a ring source to create similar results in 3 dimensions. Newman (1999) studied the added mass, damping and exciting forces of the shape found in McIver and McIver (1997) using WAMIT. More three-dimensional shapes where found in McIver and Newman (2003), including shapes that are non-axisymmetric.

McIver and McIver (2006) created a trapping structure that exists also for a freely floating problem. This means that the motion of a decay test will not decay in time. However, in the case from McIver (1996) a decay tests will not excite the trapped mode, and therefore decay in time. The floating trapped mode is a consequence of that the heave natural period coincides with the piston-mode natural period. Again it is important to stress that this is done using linear potential flow theory.

1.2 Applicable numerical methods

In order to develop a suitable and applicable numerical method to study the moonpool problem, we must carefully consider which physical effects that are important to model. There are three obvious conclusions for our problem; first we assume that a large part of the water domain away from the the corners of the body can be described using potential flow, secondly that flow separation from the hull must be accounted for and last that the air flow around the structure can be neglected. The last assumption is based on that the moonpool is open to the to the atmospheric pressure. Based on these assumptions we have

here chosen to couple a potential flow solver with a viscous flow solver. In addition, it is a question if turbulence matters in our problem. However, it is believed to be secondary in our application when flow separation from sharp corners occurs. Hence we do not consider it.

Another good reason for not applying the assumptions of viscous flow in the entire fluid domain, which may imply solving the Navier-Stokes equation with a free-surface tracking method, is the major disadvantages in CPU time. Although the proposed hybrid methods in this work are expected to speed up performance, we have not done any comparison study towards a commercially available CFD solver with regards to accuracy or efficiency. Meaning that we will not report the achieved CPU time in our simulations.

There exist several strategies for coupling viscous flow and potential flow models. It can simply be done by using a potential-flow model to generate initial conditions to a viscous flow model. An example of this is by using a potential-flow model to simulate a wave breaking up to when the free surface intersects itself, then use the potential flow results to generate initial conditions to a viscous flow simulation, see Grilli et al. (2004). A stronger coupling strategy which is similar to ours is summarized in Grilli (2008). Basically a potential-flow problem is solved on a large domain using the boundary element method (BEM). On a smaller viscous domain, the Navier-Stokes (NS) equations are split in an inviscid (with superscript I) and a viscous part (with superscript V), $\mathbf{u} = \mathbf{u}^I + \mathbf{u}^V$ and $p = p^I + p^V$. Since the inviscid part is known from the potential flow BEM calculation, the NS-equations can be used to solve for $\mathbf{u}^V$ and p^V. They use this strategy to solve a sediment transport model, where the viscous domain is located close to the sea bottom.

Kim et al. (2010) proposed to use a transmission zone between a BEM solving for the potential flow and the (NS)-equations with a volume of fluid (VOF) technique for free-surface capturing to generate a two-way coupling between the potential and viscous flow domains.

The green water on deck problem has been investigated in a series of publications by Colicchio et al. (2006), Greco et al. (2007), Greco et al. (2013) and other related articles by the same authors using a one-way domain decomposition technique where a BEM is used to solve for incoming waves, and a Navier-Stokes solver with a level-set technique to capture the evolution of the air-water interface is used to generate the breaking wave on the structure. When one uses a BEM combined with a one-fluid (air-water) solver, then one must also solve partly the air problem by the BEM. Furthermore, one has to consider the inconsistency that a BEM provides a sharp air-water interface while a surface capturing method like level-set and VOF does not. A fully nonlinear domain decomposition solver for efficient computations of wave loads on surface piercing structures is proposed by Paulsen et al. (2014). They combine a Navier-Stokes/VOF solver in the inner domain around a cylindrical surface piercing structure, with a fully potential flow solver in the outer domain. Their approach is a one-way coupling, meaning that they have to damp out the diffraction waves due to the structure before it reaches the potential flow domain.

Campana et al. (1995) applied a domain decomposition method to analyse the flow past a ship hull. Here an overlapping region was used, and the solution between the two domains was matched through iteration between the potential flow and viscous flow solver.

Recently Zhang et al. (2014) and Zhang (2013) coupled a potential-flow BEM with a viscous-flow Finite Element Method (FEM) with no overlapping domain, and performed various validation studies including dam break, solitary wave over an obstacle and solitary

wave breaking on an irregular 3D bathymetry.

In this work the hybrid method from Kristiansen and Faltinsen (2012) is used as basis and developed further. Kristiansen and Faltinsen (2012) solved for linear potential flow theory using the linear acceleration potential and coupled it to the pressure in the Navier-Stokes equation. The governing equations were solved by the FVM in both domains.

Another option for modelling flow separation in potential flow methods such as BEM is to apply an inviscid vortex tracking method. This approach was applied by among others Kristiansen (2009), Braathen (1987) and Faltinsen and Pettersen (1987).

Also when it comes to numerical methods for potential flow there exist a vast selection of available methods. The most popular one is perhaps the BEM originally from Hess and Smith (1962), which only involves discretizing of the boundaries of the water domain. The number of unknowns can further be reduced by applying suitable Green functions that satisfy some of the boundary conditions.

Among the many methods available we will in this work mostly employ the Harmonic Polynomial Cell (HPC) method for discretizing and solution of the potential flow domain. The HPC method is a field method where the entire water domain has to be discretized by cells. The HPC method was first introduced by Shao and Faltinsen (2012a) to solve the Laplace equation for potential flow. The inspiration was taken from the conventional FDM, however, in the HPC method harmonic polynomials that satisfy the Laplace equation are used as basis. Later publications Shao and Faltinsen (2012b) and Shao and Faltinsen (2013) have shown improvements of the method into 3D and various validation studies have been performed. The most recent article about the HPC method can be found in Shao and Faltinsen (2014), where a detailed comparison of the efficiency and accuracy against various other methods are presented. The comparison shows improvements over both other field methods (FVM, FEM and FDM), boundary element methods (BEM) and Fast Multipole Accelerated BEM.

More review and details about the HPC method in 2D will be given later in the thesis, since they are important for the understanding of the coupling between the potential and viscous flow.

Chapter 2

Mathematical formulations

In the present chapter the mathematical background of a two-dimensional numerical wave tank (NWT) will be presented and described. One part of the NWT will be described by potential flow theory, which assumes that the flow is irrotational and the liquid inviscid and incompressible. The other part of the NWT will be described by the Navier-Stokes equations for a viscous and incompressible liquid assuming laminar flow. The main contribution from this numerical work is the coupling between the two liquid domains based on different numerical methods.

The main reason for not choosing only a potential flow method to solve our problem is that vorticity separated from the sharp corners at the inlet of the moonpool is previously found to contribute significantly to the damping of the moonpool piston-mode motion. Furthermore, it is experienced by others that the propagation of waves can be most accurately done by using a potential flow method. In addition, it is computationally expensive to solve the entire liquid domain using only a viscous solver.

Meaning that for all parts of the liquid domain that potential flow theory can be used instead of viscous flow theory, more simplifications in the theory behind the physical problem can be done, and the corresponding numerical solution will become faster. This will become clearer to the reader after the next two chapters.

2.1 Governing equations for the liquid

The liquid domain is decomposed into two separate, but strongly connected and coupled domains. In a domain near the body we seek the solution of the pressure and velocities in the liquid from the Navier-Stokes equations. The derivation and detailed explanation of the Navier-Stokes equations can be found in many textbooks, i.e. White (2006) and Faltinsen and Timokha (2009). The Navier-Stokes equations in an Earth-fixed coordinate system for an incompressible liquid is

$$\frac{\partial \mathbf{u}}{\partial t} + \mathbf{u} \cdot \nabla \mathbf{u} = -\frac{1}{\rho}\nabla p - g\mathbf{k} + \nu \nabla^2 \mathbf{u} \qquad \text{in } \Omega_{\text{CFD}}, \tag{2.1}$$

where Ω_{CFD} is the viscous domain part of the total liquid domain. To be precise: We have assumed that the Earth-fixed coordinate system is an inertial coordinate system. The latter assumption is appropriate for our applications. Here $\mathbf{u} = (v, w)$ is the absolute liquid particle velocity, ρ is the density of the liquid, g is the acceleration of gravity, $\mathbf{k}$ is

the unit vector in vertical z_e-direction in the Earth-fixed coordinate system with positive direction upwards, ν is the kinematic viscosity of the liquid, ∇ is the nabla operator and p is the total pressure in the liquid. Note that equation (2.1) does not include any turbulence model and is based on a laminar flow assumption. It can be used for turbulent flow of a Newtonian fluid. However, it is computational time that prohibits it. So instead some empirical turbulence models are commonly used. Further, the continuity equation for liquid mass reads,

$$\nabla \cdot \mathbf{u} = 0 \qquad \text{in } \Omega_{\text{CFD}}. \tag{2.2}$$

The transformation of equations (2.1) and (2.2) into a body-fixed noninertial coordinate system will be given later, where the noninertial coordinate system will be fixed to an object that is accelerating in translation and rotation in time.

For the problems considered in this work the Navier-Stokes equations will be solved in a domain near the body, that includes the edges, where vorticity is expected to be shed. Further away from the hull, the Laplace equation for the velocity potential φ or linear acceleration potential ψ will be solved. In addition, the entire free surface is within the potential-flow domain.

The basic assumptions behind the Laplace equation for φ or ψ are the following: The liquid flow is irrotational, the liquid is inviscid and incompressible in the potential flow domain. This implies that there exists a velocity potential φ that satisfy,

$$\nabla^2 \varphi = 0 \qquad \text{in } \Omega_{\text{pot}}. \tag{2.3}$$

Here Ω_{pot} is the potential flow part of the liquid domain, and the absolute liquid velocity is defined as $\mathbf{u} = \nabla\varphi$.

It will later be used that also the linear acceleration potential ψ satisfies the Laplace equation. Within linear potential flow theory the acceleration potential is defined as $\psi = \partial\varphi/\partial t$. Here the acceleration of the liquid at a fixed point can be found from the linear acceleration potential as $\mathbf{a} = \nabla\psi$, which further needs to be time integrated to find the velocity, based on the chosen time-integration method.

It should be noted that the Laplace equation is invariant, meaning that it does not change from an inertial coordinate system to a noninertial coordinate system. In our case, the Earth-fixed coordinate system is an inertial coordinate system, and the considered body-fixed coordinate system is a noninertial coordinate system.

2.1.1 Body-fixed coordinate system

To begin explaining the governing equations for the liquid flow in a body-fixed coordinate system the difference between two coordinate systems, an Earth-fixed coordinate system and a body-fixed coordinate system will be explained. (See Figure 2.1.) The Earth-fixed (y_e, z_e)-coordinate system will remain fixed in time and space to the free surface at the initial position of the ship, while the body-fixed (y, z)-coordinate system will follow the center of gravity of the body and rotate with the roll motion of the body.

In order to rotate a vector $\mathbf{b}_{0e}$ in the Earth-fixed coordinate system to the body-fixed coordinate system at rest, the standard two-dimensional rotation matrix is applied

$$\begin{bmatrix} b_{y0} \\ b_{z0} \end{bmatrix} = \begin{bmatrix} \cos\eta_4 & -\sin\eta_4 \\ \sin\eta_4 & \cos\eta_4 \end{bmatrix} \begin{bmatrix} b_{y0e} \\ b_{z0e} \end{bmatrix}, \tag{2.4}$$

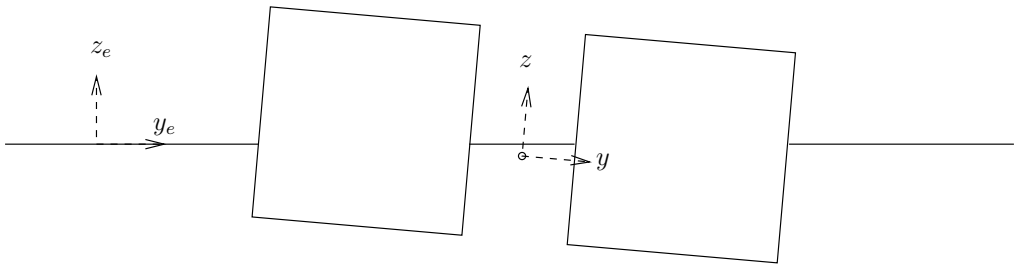

Figure 2.1: Definition of the two coordinate systems. The body-fixed (y, z)-coordinate system is fixed to the center of gravity of the body, and it will follow and rotate with the motions of the body. The Earth-fixed (y_e, z_e)-coordinate system is fixed to the initial position of the body at the calm free surface.

where η_4 is the angle between the two coordinate systems, here exemplified with the roll angle, as will be the case for all rotations in this work.

The relation between the *relative* liquid velocity as seen in the body-fixed coordinate system and the *absolute* liquid velocity as seen in the Earth-fixed coordinate system is given as,

$$\mathbf{u}_r = \mathbf{u} - \mathbf{u}_0 - \boldsymbol{\omega}_0 \times \mathbf{r} \tag{2.5}$$

Here $\mathbf{u}_r$ is the relative liquid particle velocity seen from the body-fixed coordinate system. $\mathbf{u}$ is the absolute liquid particle velocity seen in the Earth-fixed coordinate system, but rotated with the same angle as the body-fixed coordinate system. $\boldsymbol{\omega}_0$ is the angular velocity of the body (which contains only the roll-angular velocity $\dot{\eta}_4$ in this two-dimensional case), $\mathbf{u}_0$ is the translatory velocity of the origin of the body-fixed coordinate system and $\mathbf{r}$ is the radius vector from the origin of the coordinate system to the liquid particle. Here the origin of the body-fixed coordinate system is assumed to coincide with the center of gravity of the body.

The Navier-Stokes equations (2.1) and (2.2) are changed to reflect that the governing equations are solved in a body-fixed rotating coordinate system. The detailed derivation on how to transform the Navier-Stokes equations from an inertial to a noninertial coordinate system can be found in Faltinsen and Timokha (2009) and parts of it is given in Appendix A. A similar derivation is also applied when the equations of motion are transformed from the Earth-fixed coordinate system to the body-fixed coordinate system.

The Navier-Stokes equations in a body-fixed coordinate system are given as,

$$\begin{aligned} \frac{\partial^b \mathbf{u}_r}{\partial t} + \mathbf{u}_r \cdot \nabla \mathbf{u}_r &= -\frac{1}{\rho}\nabla p + \mathbf{g} + \nu \nabla^2 \mathbf{u}_r - \mathbf{a}_0 \\ &- (\boldsymbol{\omega}_0 \times \mathbf{u}_0) - \dot{\boldsymbol{\omega}}_0 \times \mathbf{r} \qquad \text{in } \Omega_{\text{CFD}}, \\ &- 2\,(\boldsymbol{\omega}_0 \times \mathbf{u}_r) - \boldsymbol{\omega}_0 \times (\boldsymbol{\omega}_0 \times \mathbf{r}) \end{aligned} \tag{2.6}$$

$$\nabla \cdot \mathbf{u}_r = 0 \qquad \text{in } \Omega_{\text{CFD}}. \tag{2.7}$$

where the term $2\,(\boldsymbol{\omega}_0 \times \mathbf{u}_r)$ is the Coriolis acceleration and the term $\boldsymbol{\omega}_0 \times (\boldsymbol{\omega}_0 \times \mathbf{r})$ is the centripetal acceleration. Furthermore, ∇ is now the differential operator in body-fixed

(y, z)-coordinates. $\frac{\partial^b \mathbf{u}_r}{\partial t}$ is defined as the time-derivative of $\mathbf{u}_r$ for a fixed point in the body-fixed coordinate system, and that the unit vectors are not time-differentiated.

In two dimensions with a yz-coordinate system, we have only two nonzero components in $\mathbf{u}_r = [0, v_r, w_r]$ and a single component in $\boldsymbol{\omega}_0 = [\dot{\eta}_4, 0, 0]$. Note that the gravitational constant $\mathbf{g} = -g\,[0, \sin(\eta_4), \cos(\eta_4)]$ changes with time and depends on the roll-angular position.

The Laplace equation is invariant, meaning that

$$\nabla^2\varphi = \frac{\partial^2\varphi}{\partial y^2} + \frac{\partial^2\varphi}{\partial z^2} = \frac{\partial^2\varphi}{\partial y_e^2} + \frac{\partial^2\varphi}{\partial z_e^2} = 0 \tag{2.8}$$

In addition to the governing equations, the boundary conditions must be changed to reflect that the problem is solved in a body-fixed coordinate system. The initial conditions remain the same, as everything is assumed to start at rest within both the body-fixed coordinate system and Earth-fixed coordinate system, the only difference is an offset by the distance from the center of gravity to the free surface.

2.2 Coupling between potential and viscous flow

On the intersection between the potential and viscous flow, the solutions for both pressure and liquid velocity must be continuous. To achieve continuous pressure across the intersection the Bernoulli equation is applied. The equation is true for unsteady, irrotational and inviscid liquid motion, here given in an Earth-fixed coordinate system as,

$$\frac{p}{\rho} + \frac{\partial\varphi}{\partial t} + \frac{1}{2}\left|\nabla\varphi\right|^2 + gz_e = C(t) \tag{2.9}$$

where $C(t)$ is an arbitrary function. If now the time dependency is included in the velocity potential, $C(t)$ becomes a constant. Next we evaluate the equation at $z = 0$ without water motion where $p = p_a$, then $C(t) = p_a$ can be determined. On the viscous flow side the pressure p is solved for and on the potential flow side the absolute velocity potential φ or its time-derivative, i.e. the linear acceleration potential $\psi = \frac{\partial\varphi}{\partial t}$ is solved for.

In addition to the requirement of a continuous pressure field across the intersection, the velocities should be continuous in both tangential and normal direction to the intersection. One requirement here is that the vorticity generated in the viscous flow domain cannot reach the intersection. Meaning that either the intersection should be as far away as possible, or a numerical scheme to damp out vorticity close to the intersection should be implemented. It is here focused on the first option. These requirements and limitations are discussed further in the section on numerical methods. Sensitivity studies have been performed to check the importance of the location of the intersection on the numerical solution.

2.3 Free-surface boundary conditions in potential flow

In this section free-surface conditions to be applied in the potential flow domain using a body-fixed coordinate system are sought. The starting point is the well-established non-linear kinematic and dynamic free-surface boundary conditions in an (non-accelerating)

inertial Earth-fixed coordinate system. Our objective is to find the corresponding semi-Lagrangian nonlinear free-surface conditions in a noninertial rotating body-fixed coordinate system. By semi-Lagrangian it is here meant that the free-surface profile is followed in z-direction. Furthermore, surface tension is neglected.

The kinematic free-surface condition is found by assuming that a liquid particle on the free surface remains on the free surface. Then the kinematic free-surface condition is mathematically given in an Earth-fixed coordinate system as the material derivative of a function $Z = z - \zeta(y,t) = 0$, see Faltinsen and Timokha (2009)

$$\frac{D\left(\zeta - z\right)}{Dt} = \frac{\partial \zeta}{\partial t} + \frac{\partial \varphi}{\partial y}\frac{\partial \zeta}{\partial y} - \frac{\partial \varphi}{\partial z} = 0 \tag{2.10}$$

where $\zeta(y,t)$ is the free-surface elevation. Note that ζ is assumed to be a single-valued function for each y-node, i.e. the simulation will break down for overturning waves.

Change of time-derivative from an inertial coordinate system to a body-fixed (noninertial) coordinate system is represented by (here exemplified with use of φ)

$$\frac{\partial^b \varphi}{\partial t} = \frac{\partial \varphi}{\partial t} + \left(\mathbf{u}_0 + \boldsymbol{\omega}_0 \times \mathbf{r}\right) \cdot \nabla \varphi \tag{2.11}$$

Here the time-derivative $\frac{\partial^b}{dt}$ represents change of a value in time seen from a point fixed in the body-fixed rotating coordinate system, as earlier defined and used in equation (2.6). The kinematic free-surface condition in a body-fixed coordinate system when combining equations (2.10) and (2.11), and noting that we should exchange φ with the function Z in equation (2.11) then becomes

$$\frac{\partial^b \zeta}{\partial t} = \frac{\partial \varphi}{\partial z} - \frac{\partial \varphi}{\partial y}\frac{\partial \zeta}{\partial y} + \left(\dot{\eta}_2 - \dot{\eta}_4 z\right)\frac{\partial \zeta}{\partial y} - \dot{\eta}_3 - \dot{\eta}_4 y \qquad \text{on } z = \zeta \tag{2.12}$$

On the free surface continuity in pressure across the interface is required, such that the pressure in the liquid at the free surface is equal to the pressure p_a in the air. This is a consequence of neglecting surface tension. The continuity in pressure is described by using the Bernoulli equation (2.9) and combining it with equation (2.11) to transform Bernoulli's equation to the dynamic free-surface condition in a body-fixed coordinate system,

$$\frac{\partial^b \varphi}{\partial t} = -g\zeta_{ef} - \frac{1}{2}\left|\nabla\varphi\right|^2 + \left(\dot{\eta}_2 - \dot{\eta}_4 z\right)\frac{\partial \varphi}{\partial y} + \left(\dot{\eta}_3 + \dot{\eta}_4 y\right)\frac{\partial \varphi}{\partial z} \qquad \text{on } z = \zeta. \tag{2.13}$$

where ζ_{ef} is the vertical z_e-position of the free-surface node in the Earth-fixed coordinate system. We reach the final expression for the dynamic free-surface boundary condition by rewriting Bernoulli's equation to express the time rate of change of φ on the free surface, as one travels with the free surface in z-direction of the body-fixed rotating coordinate system. Similarly as equation (2.11) we can set up a relationship between the time derivative when following a liquid particle in z-direction in a semi-Lagrangian manner and the time derivative of a point fixed in a body-fixed coordinate system.

$$\frac{d^* \varphi}{dt} = \frac{\partial^b \varphi}{\partial t} + \frac{\partial z}{\partial t}\frac{\partial \varphi}{\partial z} = \frac{\partial^b \varphi}{\partial t} + \frac{d^b \zeta}{dt}\frac{\partial \varphi}{\partial z} \tag{2.14}$$

Inserting for equation (2.13) and (2.12) into equation (2.14) gives

$$\frac{d^*\varphi}{dt} = -g\zeta_{ef} - \frac{1}{2}\left(\frac{\partial\varphi}{\partial y}\right)^2 + \frac{1}{2}\left(\frac{\partial\varphi}{\partial z}\right)^2 - \frac{\partial\varphi}{\partial z}\frac{\partial\varphi}{\partial y}\frac{\partial\zeta}{\partial y} + (\dot{\eta}_2 - \dot{\eta}_4 z)\left(\frac{\partial\varphi}{\partial y} + \frac{\partial\varphi}{\partial z}\frac{\partial\zeta}{\partial y}\right) \qquad \text{on } z = \zeta. \tag{2.15}$$

Here the derivative $\frac{d^*}{dt}$ express the time-derivative when following a particle in a semi-Lagrangian manner in z-direction of the body-fixed coordinate system. Here we have used that $\frac{\partial^b z}{\partial t} = \frac{d^b\zeta}{dt}$, meaning that the node attached to the free surface will follow the wave elevation ζ in z-direction of the body-fixed coordinate system.

Chapter 3

Numerical methods

The following sections will present the numerical methods and our approaches used in the present work. Two new numerical hybrid methods combining the Finite Volume Method (FVM) for the numerical solution of the viscous flow domain and the Harmonic Polynomial Cell (HPC) method for the numerical solution of the potential flow domain are used throughout the present study.

The FVM implemented in the present work is second-order accurate for the solution of the pressure. The basis can be found in many textbooks (i.e. Ferziger and Perić (2002)). However, it is felt necessary to present most of the details such that the coupling part can be understood.

3.1 Finite Volume Method

The Finite Volume Method is a common and well established numerical method that uses the volume integral of the governing equations as its starting point, or in two dimensions the area integral. The numerical formulation here will be for two dimensions, but similar derivation can be performed in three-dimensional space. The first formulation here is inspired by Faltinsen and Timokha (2009). It is here presented in detail to further understand the coupling approach between the FVM and the HPC method.

Assume that the liquid domain is divided into a finite number of contiguous control areas (CAs). Then the area integral of the Laplace equation over each CA for the velocity potential will look like,

$$\int_{\mathrm{CA}} \nabla^2 \varphi \, \mathrm{d}\Omega = 0 \tag{3.1}$$

The divergence theorem can now be applied to equation (3.1), and the equation can be rewritten from an area integral into a line integral. First the divergence theorem is given as:

$$\int_{\mathrm{CA}} (\nabla \cdot \mathbf{F}) \, \mathrm{d}\Omega = \int_{\mathrm{S}} (\mathbf{F} \cdot \mathbf{n}) \, \mathrm{d}S, \tag{3.2}$$

where $\mathbf{F}$ is a continuously differentiable vector field and $\mathbf{n}$ is the normal vector to the line S pointing outwards. Furthermore, S is the closed line around the CA, i.e. the line that consist of the four edges of the CA.

The area-integrated Laplace equation (3.1) can then be reduced to a line integral, by noting that $\nabla^2\varphi = \nabla \cdot \nabla\varphi$, i.e.

$$\int_S \frac{\partial \varphi}{\partial n}\,\mathrm{d}S = 0. \tag{3.3}$$

Now assume that φ varies linearly over each cell. Then the normal derivatives across the edges are also constant along each edge. The integral is then a sum of four constant line integrals

$$\sum_{i=1}^{4} \left(\frac{\partial \varphi}{\partial n}\right)_i \mathrm{d}S_i = 0, \tag{3.4}$$

where the values of φ are expressed at the geometrical center of each cell. Further,

$$\delta z \left(\frac{\partial \varphi}{\partial y}\right)_e - \delta z \left(\frac{\partial \varphi}{\partial y}\right)_w + \delta y \left(\frac{\partial \varphi}{\partial z}\right)_n - \delta y \left(\frac{\partial \varphi}{\partial z}\right)_s = 0, \tag{3.5}$$

where the subscripts e, w, n and s indicates whether it is the east, west, north and south edge of the CA that are evaluated. Assume that the CA is a rectangle, such that the north and south edge has the same length, and that the east and west edge has the same length. Further, δy is the width of the cell and δz is the height of the cell. To keep the notation here as simple as possible both δy and δz are assumed constant for all cells. However, note that the code implementation allows for different cell sizes, as long as the cell remains rectangular. The gradients can be found as first order finite difference approximations between the φ values at the considered cell and its cell neighbours. The horizontal first-order finite difference gradient approximations are then,

$$\left.\frac{\partial \varphi}{\partial y}\right|_e = \frac{\varphi_\mathrm{E} - \varphi_\mathrm{P}}{\delta y}, \quad \left.\frac{\partial \varphi}{\partial y}\right|_w = \frac{\varphi_\mathrm{P} - \varphi_\mathrm{W}}{\delta y}, \tag{3.6}$$

where φ_E and φ_W are the corresponding velocity potential values at the geometrical center of the east and west neighbouring cells. Similar first-order finite difference approximations for the derivatives in z-direction.

$$\left.\frac{\partial \varphi}{\partial z}\right|_n = \frac{\varphi_\mathrm{N} - \varphi_\mathrm{P}}{\delta z}, \quad \left.\frac{\partial \varphi}{\partial z}\right|_s = \frac{\varphi_\mathrm{P} - \varphi_\mathrm{S}}{\delta z}, \tag{3.7}$$

where φ_N and φ_S are the corresponding velocity potential values of the geometrical center of the north and south cells. The equation (3.5) can then finally be rewritten to look like,

$$\frac{\delta z}{\delta y}\varphi_\mathrm{E} + \frac{\delta z}{\delta y}\varphi_\mathrm{W} + \frac{\delta y}{\delta z}\varphi_\mathrm{N} + \frac{\delta y}{\delta z}\varphi_\mathrm{S} - 2\left(\frac{\delta z}{\delta y} + \frac{\delta y}{\delta z}\right)\varphi_\mathrm{P} = 0. \tag{3.8}$$

For an implementation with different cell sizes, the distance between the two cell nodes are different from the width or height of the cells, and equation 3.8 will change.

Equation (3.8) is only valid for cells that are not adjacent to any boundaries of the liquid domain, these cells are categorized into cell-type 1 (see Figure 3.1). Boundary conditions are easily implemented by changing the gradient terms in equation (3.5), and then updating equation (3.8). A typical example of this can be for cell-type 15, where the north edge of the cell is on the body boundary. The resulting equation for cell-type 15 is then

$$\frac{\delta z}{\delta y}\varphi_\mathrm{E} + \frac{\delta z}{\delta y}\varphi_\mathrm{W} + \frac{\delta y}{\delta z}\varphi_\mathrm{S} - \left(2\frac{\delta z}{\delta y} + \frac{\delta y}{\delta z}\right)\varphi_\mathrm{P} = -\delta y \left.\frac{\partial \varphi}{\partial z}\right|_n, \tag{3.9}$$

6	5	5	5	17	0	0	16	5	5	5	7
2	1	1	1	13	0	0	12	1	1	1	3
2	1	1	1	13	0	0	12	1	1	1	3
2	1	1	1	1	15	15	1	1	1	1	3
2	1	1	1	1	1	1	1	1	1	1	3
2	1	1	1	1	1	1	1	1	1	1	3
8	4	4	4	4	4	4	4	4	4	4	9

Figure 3.1: Overview of the mesh categorization into different cell-types. In addition there are other cell-type connected to the appendages and the intersection between potential and viscous flow domains. Cell-type 0 represents the position of the hull. The FVM node values are located in the middle of each cell.

where $\frac{\partial \varphi}{\partial z}\big|_n$ will be known from the body boundary condition.

We now explain what is done when the velocity potential is known at an edge. The cell-type 5 next to the free surface is used as an example. The north node is moved to the north edge of the cell, and the north gradient is between the known velocity potential value of the north edge and the velocity potential value at the center of the cell.

The categorization of the different cell-types in the FVM scheme are given in Figure 3.1. Other cell-types will be introduced when the coupling between the HPC and FVM is presented. Also other cell-types will be introduced when the coupling between potential and viscous flow is presented. Cell-types 12, 13, 15, 16 and 17 are on the body boundary. Further, 5, 6, 7, 16, and 17 are on the free surface, and last, 2, 3, 4, 6, 7, 8 and 9 are on the outer walls of the wave tank. The resulting matrix system is sparse, with values on the diagonal and on four off-diagonal lines.

A staggered mesh arrangement is applied in the present work. This means that the liquid velocities will be evaluated on the edges of the cells and the pressure in the middle of the cells. Here the horizontal v-velocities are valid on the east and west edges of the cells (see Figure 3.2), and the vertical w-velocities are evaluated on the north and south edges of the cells (see Figure 3.3). The velocities are clearly defined between two cells. On the boundary of the liquid, the velocities are either specified or calculated by extrapolation. This applies to v-cell-types 2, 3, 12 and 13, and to w-cell-types 4, 5 and 15.

3.1.1 Time integration method

It was early in the development phase decided to use the explicit fourth-order Runge-Kutta method for time integration. The main motivation behind this was the experience of others and its known capability to evolve the free-surface conditions in time.

For solution of the Navier-Stokes equations Chorin's fractional step method is used to solve each sub-step in the explicit fourth-order Runge-Kutta method. There are other and well established time integration methods for solving the Navier-Stokes equations than the combination of the Chorin's fractional step method and the explicit fourth-

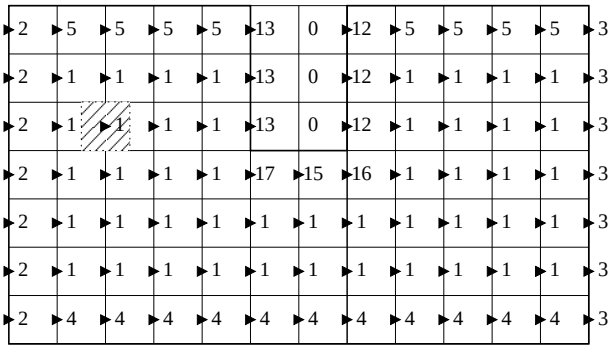

Figure 3.2: v-cell-types for horizontal v-velocity nodes in a staggered mesh arrangement. The striped area illustrates how the control area for each v-velocity cell is defined.

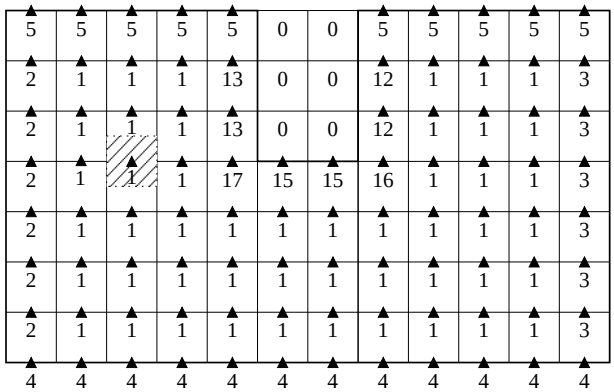

Figure 3.3: w-cell-types for vertical w-velocity nodes in a staggered mesh arrangement. The striped area illustrates how the control area for each w-velocity cell is defined.

order Runge-Kutta method. However, the combination has been proven to be stable and capable of evolving all the different steps in the present hybrid method forward in time. For more details about the numerical implementation of the combination of the explicit fourth-order Runge-Kutta method and the Chorin's fractional step method the reader is referred to the pseudocode in Appendix C.1. In addition Ferziger and Perić (2002) or other text books on numerical methods for fluid dynamics can be used as a source for finding suitable time integration methods.

The following sub-sections will illustrate how the FVM and the Chorin's fractional step method Chorin (1968) are implemented for solving the Navier-Stokes equations in an Earth-fixed coordinate system (2.1). To simplify the notation Chorin's fractional step method will be given for the explicit forward Euler method, and not for the implemented explicit fourth-order Runge-Kutta. Extensions of the method by including the additional terms in the body-fixed Navier-Stokes equation (2.7) are straightforward. However, they lead to some problems when solving the equations of rigid-body motion.

3.1.2 Advection sub-step

The first step in the Chorin's fractional step method Chorin (1968) is the advection term, i.e. a sub-step in the time integration method is performed with only the advection step from the equation (2.1). The result is a temporary artificial velocity field $\mathbf{u}^*$ that is not divergence free ($\nabla \cdot \mathbf{u}^* \neq 0$),

$$\mathbf{u}^* = \mathbf{u}^m - \Delta t \, (\, \mathbf{u}^m \cdot \nabla \mathbf{u}^m) \tag{3.10}$$

where m refers to values at the present time-step. Further, equation (3.10) is integrated over the CA and simplified using the divergence theorem (from equation (3.2)).

$$\int_{\mathrm{CA}} \frac{\partial \mathbf{u}}{\partial t} \, \mathrm{d}\Omega = - \int_{\mathrm{S}} (\mathbf{u} \cdot \mathbf{n}) \, \mathbf{u} \, \mathrm{d}S \tag{3.11}$$

This can first be split into one equation for each of the two velocity components,

$$v^* = v^m - \frac{\Delta t}{\delta y \delta z} \left(v_e^2 \, \delta z - v_w^2 \, \delta z + v_n \, w_n \, \delta y - v_s \, w_s \, \delta y \right) \tag{3.12}$$

$$w^* = w^m - \frac{\Delta t}{\delta y \delta z} \left(v_e \, w_e \, \delta z - v_w \, w_w \, \delta z + w_n^2 \, \delta y - w_s^2 \, \delta y \right) \tag{3.13}$$

note that the CAs are different for the two velocity components than for the pressure nodes, see Figures (3.2) and (3.3). Furthermore, they are evaluated on different locations. These equations are valid for velocity cell-types 1, which is in the middle of the liquid domain and away from all boundaries.

There exists a great deal of literature on how to discretize the advection step and various total variation diminishing (TVD) schemes have been proposed. To ensure a quick implementation and stable solution the first-order upwind method is chosen here. This basically means that for each cell the direction of the flow is check, and values from the nearest cell in the upstream direction are used in equations (3.12) and (3.13). To what degree our results are sensitive to the choice of numerical solution to the advection step is unknown for the case studied here. However, by choosing the first-order upwind method for the advection step, a large numerical diffusion should be expected Ferziger and Perić (2002).

3.1.3 Diffusion sub-step

The second step in Chorin's fractional step method is to do a sub-step from $\mathbf{u}^*$ by including the diffusion term in the Navier-Stokes equation (2.1), the results is then a second temporary artificial velocity field $\mathbf{u}^{**}$ that is not divergence free,

$$\mathbf{u}^{**} = \mathbf{u}^* + \Delta t\, \nu\, \nabla^2 \mathbf{u}^m. \tag{3.14}$$

Again integrating over the control areas centered around the velocity nodes and using the divergence theorem, the equation becomes,

$$\int_{\mathrm{CA}} \frac{\partial \mathbf{u}}{\partial t}\, \mathrm{d}\Omega = \nu \int_{\mathrm{S}} \frac{\partial \mathbf{u}}{\partial n}\, \mathrm{d}S \tag{3.15}$$

Splitting into the horizontal and vertical velocity components,

$$v^{**} = v^* + \frac{\Delta t}{\delta y \delta z}\, \nu \sum_{i=1}^{4} \left(\frac{\partial v}{\partial n}\, \mathrm{dS} \right)_i \tag{3.16}$$

$$w^{**} = w^* + \frac{\Delta t}{\delta y \delta z}\, \nu \sum_{i=1}^{4} \left(\frac{\partial w}{\partial n}\, \mathrm{dS} \right)_i \tag{3.17}$$

Further, the resulting explicit equation for the diffusion step of the Chorins method for velocity nodes with cell-type 1

$$v^{**} = v^* + \frac{\Delta t}{\delta y \delta z}\, \nu \left[\left(\frac{\partial v}{\partial y} \right)_e \delta z - \left(\frac{\partial v}{\partial y} \right)_w \delta z + \left(\frac{\partial v}{\partial z} \right)_n \delta y - \left(\frac{\partial v}{\partial z} \right)_s \delta y \right] \tag{3.18}$$

$$w^{**} = w^* + \frac{\Delta t}{\delta y \delta z}\, \nu \left[\left(\frac{\partial w}{\partial y} \right)_e \delta z - \left(\frac{\partial w}{\partial y} \right)_w \delta z + \left(\frac{\partial w}{\partial z} \right)_n \delta y - \left(\frac{\partial w}{\partial z} \right)_s \delta y \right]. \tag{3.19}$$

Again a first order finite difference in space is used to approximate the derivatives. The no-slip boundary condition can be satisfied through the equations above.

3.1.4 Pressure sub-step

After the temporary artificial non-divergence free velocity field $\mathbf{u}^{**}$ is found, the last step in the Chorin's fractional step method is to update the velocity field with the pressure gradient which is still an unknown.

$$\frac{\mathbf{u}^{m+1} - \mathbf{u}^{**}}{\Delta t} = -\frac{1}{\rho} \nabla \left(p^{m+1} + \rho g z \right) \tag{3.20}$$

Due to the continuity equation (2.2), the velocity field at the next time-step must be divergence free, i.e. $\nabla \cdot \mathbf{u}^{m+1} = 0$. The resulting equation for the pressure in the liquid then becomes the Poisson equation,

$$\nabla^2 \tilde{p}^{m+1} = -\frac{1}{\Delta t} \nabla \cdot \mathbf{u}^{**} \tag{3.21}$$

where we define $\tilde{p} = \frac{p}{\rho} + gz$. Again integrating over the control areas with the pressure node in the center and rewriting using the divergence theorem, the Poisson equation can be rewritten to look like,

$$\int_{\mathrm{S}} \frac{\partial \tilde{p}}{\partial n} \mathrm{dS} = -\frac{1}{\Delta t} \int_{\mathrm{S}} \mathbf{u}^{**} \cdot \mathbf{n} \, \mathrm{dS} \tag{3.22}$$

The left hand side is discretized in a similar way as the Laplace equation (3.3), and the right hand side is equal to

$$\int_{\mathrm{S}} \mathbf{u}^{**} \cdot \mathbf{n} \, \mathrm{d}S = \sum_{i=1}^{4} \left(\mathbf{u}^{**} \cdot \mathbf{n} \right)_i = \left(v_e^{**} \delta z - v_w^{**} \delta z + w_n^{**} \delta y - w_s^{**} \delta y \right) \tag{3.23}$$

The total discretized Poisson equation for the pressure then becomes,

$$\begin{aligned} & \frac{\tilde{p}_{\mathrm{E}} - \tilde{p}_{\mathrm{P}}}{\delta y} \delta z - \frac{\tilde{p}_{\mathrm{P}} - \tilde{p}_{\mathrm{W}}}{\delta y} \delta z + \frac{\tilde{p}_{\mathrm{N}} - \tilde{p}_{\mathrm{P}}}{\delta z} \delta y - \frac{\tilde{p}_{\mathrm{P}} - \tilde{p}_{\mathrm{S}}}{\delta z} \delta y \\ = \; & \frac{1}{\Delta t} \left(v_e^{**} \delta z - v_w^{**} \delta z + w_n^{**} \delta y - w_s^{**} \delta y \right) \end{aligned} \tag{3.24}$$

which is valid for all cells inside the liquid, cell-type 1 from Figure 3.1. The present implementation of the Navier-Stokes solver is based on the Chorin's fractional step method presented in this and the previous sub-chapters. The following limitation applies: The mesh must remain constant in time, i.e. it does not allow re-meshing close to the body boundary. The consequence is that body motions cannot be simulated without linearizing the body-boundary conditions around its mean position. This limitation is one of the reasons for choosing to solve the governing equations in a body-fixed coordinate system. To do this, the governing equations are changed, and additional steps need to be included in the sub-steps of the Chorins method.

3.1.5 Time-step size

The Courant-Friedrichs-Lewy number (CFL) (see among others Ferziger and Perić (2002)) sets an upper bound on the time-step size in order to achieve a stable numerical solution. For a one-dimensional case with constant mesh size Δx the CFL number is defined as,

$$CFL = \frac{u \, \Delta t}{\Delta x} \tag{3.25}$$

where u is the liquid velocity.

This corresponds to the ratio of the time-step Δt to the characteristic advection time, $u/\Delta x$, the time required for a disturbance to be advected a distance Δx. In practice we use CFL$= 0.5$. There is also an upper limitation on the time-step due to the discretization of the diffusion term. This is, however, due to the low kinematic viscosity of the liquid a less strict requirement on the time-step size than the CFL criterion.

To solve the free-surface boundary condition another stability criteria can be used. Dommermuth and Yue (1987) performed a von Neumann stability analysis for the fourth-order Runge Kutta scheme with linearized free-surface conditions and obtained the Courant condition

$$\Delta t^2 \leq \frac{8}{\pi} \frac{\Delta x}{g}. \tag{3.26}$$

It is not known by the author of any similar stability analysis for the nonlinear free-surface condition as used here in the nonlinear hybrid method.

The choice of the time-step and mesh size also affect numerically the dispersion and damping properties of free-surface waves. A detailed stability analysis was performed by Ommani (2013). The latter is based on potential flow, and numerical dispersion and damping errors were discussed.

How these were implemented and time-step limits will be given when each of the two hybrid methods are presented.

3.2 Harmonic Polynomial Cell method

Details in this section are mostly from Shao and Faltinsen (2012b), but given here to make the details in the coupling at the intersection between potential and viscous flow domains clearer. The focus here is on a two-dimensional implementation. Recently Shao and Faltinsen (2014) extended the HPC method into three dimensions.

It is complicated and demands a lot of programming work with the FVM to implement a scheme with higher than second-order spatial accuracy. The main motivation for introducing the HPC method is the higher order spatial accuracy gained with similar implementation effort compared to using the second order FVM. By using a higher-order spatial accurate method, it also implies that larger cells can be used to gain the same accuracy as with a lower order method.

It was found that the wave dispersion properties with a low-order FVM was sensitive to the discretization of the $\partial\varphi/\partial z$-term in the kinematic free-surface condition. The numerical damping of the waves was also too large to be able to use the FVM with incoming waves on a floating structure. By using the HPC method the free-surface waves will be propagated with higher accuracy, and the waves can be propagated from the wavemaker to the structure without losing to much energy due to numerical damping. In particular, the wave celerity is captured more accurately than with a conventional FVM. The second order accurate FVM is similar to a second order accurate FDM. Bingham and Zhang (2007) investigated the accuracy of nonlinear water waves by using the FDM with different orders of accuracies. They showed how many cells were needed for a given accuracy with different order of the FDM. For instance, the second-order accurate method requires around 25 times more cells than the fourth-order accurate method to gain the same accuracy.

Another feature that makes the HPC method attractive is that the harmonic polynomials automatically satisfy the Laplace equation everywhere. Then we only have to make sure that the multiplying factors of each polynomial are consistent with the boundary conditions both globally and locally. Since the harmonic polynomials satisfy the Laplace equation, the numerical scheme will conserve liquid mass.

When describing the two-dimensional HPC method, we will operate with a local Cartesian coordinate system for each cell. The harmonic polynomials are in two dimensions given by the real and imaginary parts of the complex polynomial

$$z^n = (x + \mathrm{i}y)^n \,, \tag{3.27}$$

where n is the order of the polynomial and $\mathrm{i} = \sqrt{-1}$ is the imaginary unit. If the considered domain is star-shaped relative to the origin, the representation of equation (3.27) in terms

of a sum of all harmonic polynomials is a complete set of polynomials which satisfy Laplace equation, see e.g. Vekua (1953). In this method we include all harmonic polynomials up to third-order, and the fourth-order harmonic polynomial corresponding to real part of equation (3.27). Then we can write φ as a linear combination of 8 different harmonic polynomials $f_j(y,z)$, where each individual polynomial satisfy the Laplace equation, i.e.

$$\begin{aligned}\varphi(y,z) &= \sum_{j=1}^{8} b_j f_j(y,z) \\ &= b_1 + b_2 y + b_3 z + b_4\left(y^2 - z^2\right) + b_5 yz \\ &+ b_6\left(y^3 - 3yz^2\right) + b_7\left(3y^2 z - z^3\right) + b_8\left(y^4 - 6y^2 z^2 + z^4\right). \end{aligned} \tag{3.28}$$

Note that z is no longer a complex number, but a coordinate in the z-direction. The y-axis is the horizontal axis and the z-axis is the vertical axis, positive upwards. It is strictly speaking not necessary to choose 8 different polynomials. It is mostly due to convenience, as the achieved accuracy is high enough and the required influence area includes the 8 neighbouring nodes. I.e. for higher accuracy, more polynomials and a larger influence area is needed (more neighbouring nodes).

Equation (3.28) leads to a linear system of equations, where we find φ at 8 different locations $\varphi = \varphi_i$, on a rectangular mesh at $y = y_i$ and $z = z_i$ where $i = 1..8$. (See Figure 3.4 for a definition on the local HPC numbering.) This gives a linear relationship between the coefficients b_j and the values φ_i,

$$\varphi_i = \sum_{j=1}^{8} d_{i,j} b_j \tag{3.29}$$

where the element in $d_{i,j} = f_j(y_i, z_i)$ from (3.28) defines the matrix $[\mathbf{D}]$. Assuming 8 points where the value of φ are known, the coefficients b_i are found as,

$$b_i = \sum_{j=1}^{8} c_{i,j} \varphi_j. \tag{3.30}$$

Here the matrix $[\mathbf{C}]$ is defined by the elements $c_{i,j}$ and is the inverse of the matrix $[\mathbf{D}]$. Further, given a ninth point in the middle of the 8 points (see Figure 3.4), we have a basis for constructing a polynomial valid at the middle point. This means

$$\varphi(y,z) = \sum_{i=1}^{8} \left[\sum_{j=1}^{8} c_{j,i} f_j(y,z) \right] \varphi_i. \tag{3.31}$$

Choosing the middle ninth point to be $y_9 = 0$ and $z_9 = 0$ the above equation simplifies to only consist of the first constant polynomial. The reason is that $f_1 = 1$ and $f_j = 0$ where $j = 2..8$, such that

$$\varphi_9(y_9, z_9) = \sum_{i=1}^{8} c_{1,i} \varphi_i. \tag{3.32}$$

This implies that φ_9 can be written as a linear combination of the 8 neighbouring node-values of φ.

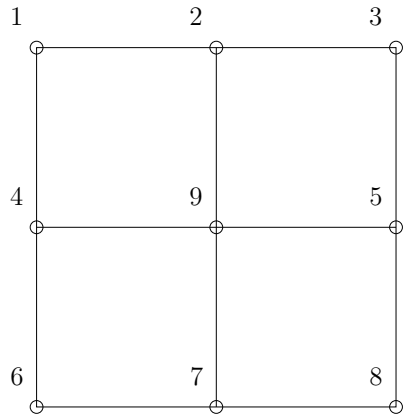

Figure 3.4: An overview of the local HPC numbering. Note that this local mesh will overlap with neighbouring meshes. I.e. node 9 in the above mesh can be any of the other 8 nodes in the neighbouring cells. This is the standard HPC configuration used for all HPC cell-types 1, see Figure 3.5.

Since analytical expressions for the derivatives $\frac{\partial}{\partial y}$ and $\frac{\partial}{\partial z}$ of polynomials easily can be found, then also expressions for $\frac{\partial \varphi}{\partial y}$ and $\frac{\partial \varphi}{\partial z}$ can be found,

$$\frac{\partial \varphi_9}{\partial y}\left(y_9 = 0, z_9 = 0\right) = \sum_{i=1}^{8} c_{2,i}\varphi_i \tag{3.33}$$

$$\frac{\partial \varphi_9}{\partial z}\left(y_9 = 0, z_9 = 0\right) = \sum_{i=1}^{8} c_{3,i}\varphi_i \,. \tag{3.34}$$

Determining the coefficients in the matrix [**C**] can be solved as a sub Dirichlet problem for each node. The 8 neighbouring points will span the boundary edge on the local polynomial for the ninth point, and these points will define the elements $d_{i,j}$ of matrix [**D**]. The wanted row in the matrix [**C**] can now be found by inverting the matrix [**D**]. Doing this for all nodes throughout the liquid will lead to a sparse matrix system with at most 9 non-zeros on each row. For global boundary nodes (all HPC cell-types above 1, see Figure 3.5) we can choose a different local numbering than in Figure 3.4 and use any of the boundary nodes to be point 9 with local coordinates $y = 0$ and $z = 0$.

3.2.1 Limitations and benefits

The present implementation of the HPC method has some limitations in how the boundary conditions are satisfied. We can only satisfy the boundary conditions point-wise on HPC nodes, and not in an integral way as in FVM. The integrated alternative of equations (3.33) and (3.34) across the cell edge was tried and found unstable. The reason is associated with the fact that we have overlapping cells in the HPC method, which means that the velocity potential is not uniquely defined outside of the HPC nodes.

There is a second problem connected to the way boundary conditions are satisfied in the current implementation of the HPC method. On sharp corner nodes where the

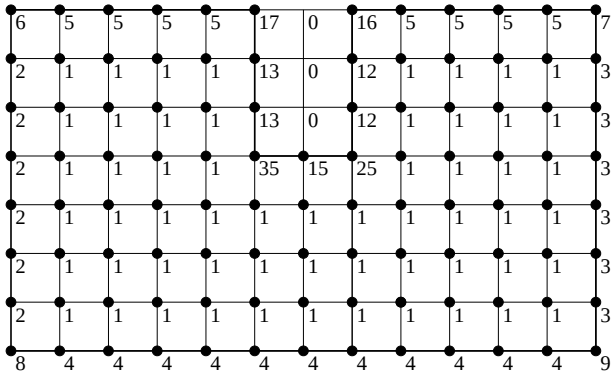

Figure 3.5: Definition of the different HPC cell-types, note that all HPC values are at the corners of FVM cells (see Figure 3.1). Here cell-type node 35 and cell-type node are at the corners of the body.

normal direction is not uniquely defined, two separate boundary conditions should be satisfied. For instance, corner nodes in the liquid where both zero relative velocity in y- and z-direction should be satisfied. On the intersection between the free surface and the vertical hull side this is solved by forcing φ to be the value time-stepped by the free-surface condition. Further, the body-boundary condition is used when the free-surface values at the body intersection are time-stepped forward in time. This does not guarantee that the body-boundary condition is satisfied on the next time-step, but only forcing the previous time-step to be correct. This correction can only be performed for the nonlinear free-surface conditions, and not the linear free-surface conditions.

On an inner sharp corner node, we need to take precautions, see HPC cell-types 25 and 35 in Figure 3.5. It is not clear how to best pick the 8 other points to construct a harmonic polynomial valid at the corner node. In addition, we need to pick one of the boundary conditions to be satisfied. The other boundary condition could be satisfied by adding an extra equation to the equation system, and solving the matrix system through a least square technique. However, this was not found satisfactory, and did not guarantee a good solution. In addition, it increased the computational time significantly. The reason for an increase in computational time is that a matrix system based on the least square method will have a much higher condition number, and then a lower convergence rate when using an iterative matrix solver. A similar corner problem exists in the Boundary Element method (BEM), but there it is in practice solvable by using more elements close to the corner. Similarly can the problem be solved in a HPC method, then on an unstructured mesh or with a meshing method with local refinement. Note that it does not have to do with a BEM in general, but with how the methods are discretized and which basis functions that are applied.

With the present hybrid methods for solving potential flow the problem is avoided by not using HPC cells around the sharp corners, i.e. the bilges of the ship. Here FVM cells are used instead, which has the node values in the center of the cell. Note that in addition to the above problems with inner sharp corner nodes we should remember that velocities are in fact singular in a potential flow solution, such that a singularity should

be added locally to handle the solution around the corner. This does not apply to the present hybrid methods when viscous flow is considered, then all our sharp corners are covered by the viscous domain, where all values remain finite. However, when for instance added mass and potential damping coefficients are calculated, the liquid domain must be covered with FVM cells around the sharp corners.

Recently, to overcome the problems mentioned above Liang et al. (2015) matched a local singular solution in an inner domain around the sharp corners with an outer solution using the HPC method. The improved HPC method was applied to a double-wedge oscillating in infinite liquid and free-surface problems with non-vertical walls.

The HPC method does not set any limitations on how the mesh should be created or how it should be changed between time-steps. Therefore, re-meshing the top layer in the wave zone does not reduce the accuracy of the solution. No interpolations schemes between time-steps are used, but we still need to update the matrix system and possibly change the preconditioner matrix. This simplifies the re-meshing process compared to using FVM, where the flux normal to the edge is needed.

3.3 Coupling between FVM and HPC

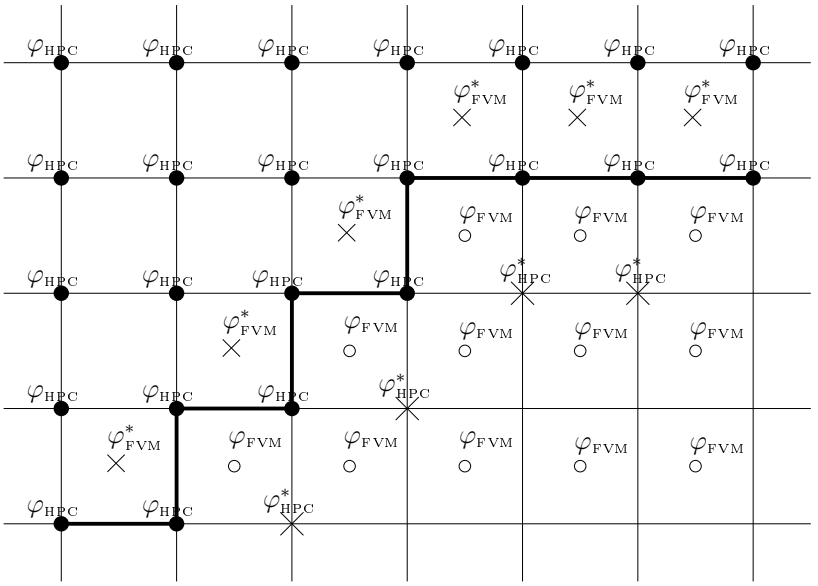

Figure 3.6: Overview of where the different nodes are located. The thick line represents the intersection which divides the liquid domain into a HPC domain and a FVM domain. Here the superscript * symbolize that interpolation is needed to obtain the value. φ could here be any function, not only the velocity potential.

In the previous sections both the FVM and the HPC method were presented in detail. Here it will be shown how to couple these two methods when solving a potential flow problem.

As seen from Figures 3.1 and 3.5 the FVM center nodes and HPC corner nodes are not evaluated at the same location. This is solved by interpolating to a value of φ on the FVM center node in the HPC domain. The problem is that φ is not uniquely defined for any given point outside the HPC nodes, i.e. φ can be evaluted from four different harmonic polynomials. The reason is that four HPC cells (see Figure 3.6) overlap each FVM node. Instead of evaluating the average of four different harmonic polynomials, which would involve in total 16 values of φ, a linear weight function is applied, such that the HPC node closest to the FVM node gets the most influence.

$$\varphi^*_{\text{FVM}} = W_{nw}\varphi^{nw}_{\text{HPC}} + W_{ne}\varphi^{ne}_{\text{HPC}} + W_{se}\varphi^{se}_{\text{HPC}} + W_{sw}\varphi^{sw}_{\text{HPC}} \tag{3.35}$$

where W_{nw} and $\varphi^{nw}_{\text{HPC}}$ refer to the weight applied to the closest φ_{HPC} node to the north west, and similar for the north east (ne) node, the south east (se) node and the south west (sw) node. The weight functions are found as the following here exemplified with W_{nw}:

$$W_{nw} = \frac{A - A^{nw}}{A} \tag{3.36}$$

where A is the area of the FVM cell, and A_{nw} is the area of the rectangular sub-cell with two of its corners at the φ^*_{FVM} node and the $\varphi^{nw}_{\text{HPC}}$ node. By applying the same scheme to the other weight functions it follows that $W_{nw} + W_{ne} + W_{se} + W_{sw} = 1$. Note that locally the higher order accuracy of the HPC method is lost, and the accuracy is in the same order as in the FVM. We have not performed studies using other weight functions. It is believed that the linear weight function is sufficient.

It is unknown if increasing the local accuracy here gives any improvements on the overall accuracy of the method. An increased HPC area would be needed to evaluate the average of four different harmonic polynomials. When predicting the piston-mode damping due to vorticity separation from the edge, it is important to get as large viscous flow area as possible, and therefore the low-order approach in equation 3.35 is chosen.

When interpolating the φ^*_{HPC} value at a HPC corner node inside the FVM domain a similar approach as in equation 3.35 is used.

Additional HPC cell-types are created compared to Figure 3.5 to deal with the HPC-FVM coupling.

3.4 Coupling between potential and viscous flow

The numerical implementation of the requirements from section 2.2 will be discussed here. The explicit time-discretized equivalent of the Bernoulli equation (2.9) in an Earth-fixed coordinate system becomes,

$$\frac{\varphi^{m+1} - \varphi^m}{\Delta t} + \frac{1}{2}|\nabla\varphi^m|^2 + gz = -\frac{p^{m+1}}{\rho}. \tag{3.37}$$

Notice that the first term in the equation is a first order finite difference approximation in time of $\partial\varphi/\partial t$, and is best approximated between two time-steps $(m+1/2)$. Therefore, there will be a short time-lag of half a time-step between the first term and the pressure term on the right hand side. A requirement for matching the pressure using equation (3.37) is that the vorticity generated in the viscous domain does not reach the intersection between the viscous and potential flow domains.

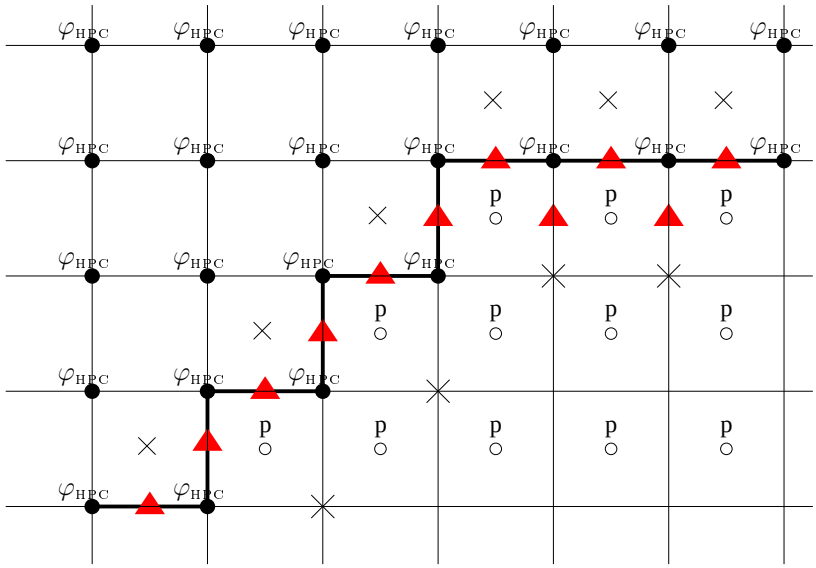

Figure 3.7: Overview of where the velocity potential nodes in the potential-flow domain and the pressure nodes in the viscous-flow domain are located. The thick line represents the intersection which divides the liquid domain. The red ▲ triangles represents the liquid velocity nodes where the artificial velocity $\mathbf{u}^{**}$ are replaced with equation (3.41).

To achieve that both the normal and tangential velocities at the intersection are continuous, the following is valid in an Earth-fixed coordinate system.

$$\mathbf{u}^{m+1} = \nabla\varphi^{m+1} \qquad \text{in } \Omega_{\mathrm{pot}} \tag{3.38}$$

$$\mathbf{u}^{m+1} = \mathbf{u}^{**} - \Delta t \nabla \tilde{p}^{m+1} \qquad \text{in } \Omega_{\mathrm{CFD}} \tag{3.39}$$

The velocity at next time-step on the intersection should be independent on which liquid domain it is calculated from. This leads to a condition on the temporary artificial velocity field $\mathbf{u}^{**}$ on the intersection, and will enter the right hand side of the Poisson equation for the pressure (equation 3.21).

$$\mathbf{u}^{**} = \nabla\varphi^{m+1} + \Delta t \nabla \tilde{p}^{m+1} \tag{3.40}$$

This can be combined with the time-discretized Bernoulli equation (3.37)

$$\begin{aligned}
\mathbf{u}^{**} &= \nabla\left(\varphi^m - \Delta t\left(\frac{1}{2}\left|\nabla\varphi^m\right|^2 + \frac{1}{\rho}p^{m+1} + gz\right)\right) + \Delta t\tilde{p}^m \\
&= \nabla\varphi^m - \Delta t\nabla\frac{1}{2}\left|\nabla\varphi^m\right|^2 - \frac{\Delta t}{\rho}\nabla p^{m+1} - \Delta t g\nabla z + \Delta t\nabla\tilde{p}^{m+1} \\
&= \nabla\varphi^m - \Delta t\nabla\frac{1}{2}\left|\nabla\varphi^m\right|^2
\end{aligned} \tag{3.41}$$

This equation replaces the temporary artificial velocity field values v^{**} from equation 3.18 and w^{**} from equation 3.19 on the intersection between the potential and viscous flow

domain, the locations are illustrated in Figure 3.7. Notice that the right hand side only contains values based on the present time-step and is therefore fully explicit. It does require the evaluation of the gradient of φ on the intersection, such that φ is required to exist inside the viscous domain. Meaning that the requirement for the presence of vorticity is somewhat stronger, and that it should not reach the cells that neighbours to the intersection. The higher order term $\nabla |\nabla\varphi|^2$ can be evaluated using the HPC method. Such that on the velocity nodes we need to evaluate the following,

$$\nabla |\nabla\varphi|^2 = 2\left[0, \frac{\partial\varphi}{\partial y}\frac{\partial^2\varphi}{\partial y^2} + \frac{\partial\varphi}{\partial z}\frac{\partial^2\varphi}{\partial y\partial z}, \frac{\partial\varphi}{\partial y}\frac{\partial^2\varphi}{\partial y\partial z} + \frac{\partial\varphi}{\partial z}\frac{\partial^2\varphi}{\partial z^2}\right] \tag{3.42}$$

Since we are aiming at solving a resonance problem, the phases between the terms becomes important and the terms on the intersection should be consistent within an explicit fourth-order Runge-Kutta scheme. (See the pseudocode in Appendix C.1.)

The next sections present details on how this works in both a body-fixed rotating coordinate system with nonlinear boundary conditions, and in an Earth-fixed coordinate system with linear boundary conditions.

3.4.1 Viscous - potential coupling in FVM

The first approach on coupling viscous and potential flow that was succesfully implemented was using FVM in both liquid domains. The coupling proved to be stable and reliable, however, as described earlier the wave dispersion and damping properties were not satisfactory when using the lower-order FVM in the potential flow domain.

Evaluation of the higher-order term in equation 3.42 is not possible in the coupling between the potential and viscous flow when the FVM is applied in both flow domains. Then equation (3.40) is again the starting point, but now the right hand side is approximated with a first order finite difference in space for the gradient terms. Therefore, let us say that we want to find u_w^{**}, then the current cell is a viscous flow cell and the west cell is a potential flow cell and u_w is the velocity node between these cells. The following will ensure a continuous normal velocity between a potential and a viscous flow cell, here discretized with a first order finite difference approximation.

$$u_w^{**} = \frac{\varphi_{\mathrm{P}}^{m+1} - \varphi_{\mathrm{W}}^{m+1}}{\delta y} + \Delta t\left(\frac{\tilde{p}_{\mathrm{P}}^{m+1} - \tilde{p}_{\mathrm{W}}^{m+1}}{\delta y}\right) \tag{3.43}$$

Here $\varphi_{\mathrm{P}}^{m+1}$ is not an unknown in the viscous domain, and similarly p_{W}^{m+1} is not an unknown in the potential domain. To change variables the time-discretized Bernoulli equation (3.37) is used, and equation 3.43 becomes

$$u_w^{**} = \frac{\varphi_{\mathrm{P}}^{m} - \varphi_{\mathrm{W}}^{m}}{\delta y} - \frac{\Delta t}{2}\frac{(\nabla\varphi_{\mathrm{P}}^{m})^2 - (\nabla\varphi_{\mathrm{W}}^{m})^2}{\delta y}, \tag{3.44}$$

which is equivalent to the result from equation (3.41). Note here that φ_{P}^{m} is a potential flow value on the previous time-step inside the viscous domain.

To ensure a continuous tangential velocity between potential and viscous cells, it is again required that equation (3.40) is valid. Now it is assumed that both the current and west cell is within the viscous flow domain, however, both the two neighbouring cells above is within the potential domain. Here both $\varphi_{\mathrm{P}}^{m+1}$ and $\varphi_{\mathrm{W}}^{m+1}$ are not unknowns within

the viscous domain. The derivation is similar as for the continuous normal velocity, the following expression then ensure continuous tangential velocity

$$\begin{aligned} u_w^{**} &= \frac{\varphi_{\mathrm{P}}^{m+1} - \varphi_{\mathrm{W}}^{m+1}}{\delta y} + \frac{\Delta t}{\rho}\left(\frac{p_{\mathrm{P}}^{m+1} - p_{\mathrm{W}}^{m+1}}{\delta y}\right) \\ &= \frac{\varphi_{\mathrm{P}}^{m} - \varphi_{\mathrm{W}}^{m}}{\delta y} - \frac{\Delta t}{2}\frac{(\nabla\varphi_{\mathrm{P}}^{m})^2 - (\nabla\varphi_{\mathrm{W}}^{m})^2}{\delta y}. \end{aligned} \tag{3.45}$$

Again all equations in this section are expressed in the Earth-fixed coordinate system.

Additional cell-types than those illustrated in Figures 3.1, 3.2, 3.3 are created to handle the cells on the intersection, and to determine if the cells belongs to the potential or viscous flow domains. The viscous cells get an addition 1000 added to the cell-type, such that a FVM viscous cell in the middle of the liquid will have a cell-type of 1001.

In order to deal with the remeshing of the potential flow domain near the free surface, a method to deal with a non-rectangular mesh in a FVM was implemented. The first-order finite difference approximation of the derivative between the values at the cell centers are no longer the flux normal to the cell edges.

The following sections will describe the two numerical hybrid methods that are based on a coupling between HPC and FVM. First the semi-nonlinear hybrid method is presented and then the nonlinear hybrid method will be given.

3.5 Semi-nonlinear hybrid method

Given the numerical foundation for the hybrid method in the previous sections, an Earth-fixed approach with linear free-surface and body-boundary conditions is presented. The method is "semi-nonlinear" as the Navier-Stokes equations are nonlinear. To clarify the difference to the nonlinear hybrid method, here the governing equations are solved in an Earth-fixed coordinate system in both flow domains.

The basics of the semi-nonlinear hybrid numerical method is based on the work by Kristiansen and Faltinsen (2012), except that the FVM used in their method is replaced by the HPC method in the potential flow domain and that the equations of motion are solved for the rigid-body motions.

In the potential-flow domain that covers the top liquid layer close to the free surface and the outer regions away from the floating body, the linear acceleration potential

$$\psi = -\varphi_t \tag{3.46}$$

is solved for. Note the negative sign, this is for convenience in order to have the same sign as the pressure in the viscous domain. The linear acceleration potential ψ is coupled to the pressure p in the viscous flow domain through the linearized Bernoulli equation,

$$\psi = \frac{p}{\rho} + gz = \tilde{p} \tag{3.47}$$

It is beneficial to solve for ψ and not φ when solving for body motions, see summary on acceleration potential flow solutions in coupled liquid-body motion problems from Bandyk and Beck (2011). In our case the potential flow contribution to the force on the body is limited to the top layer close to the free surface. As a minimum we need 3 HPC nodes in

the vertical direction close to the free-surface layer. The rest of the hull is then adjacent to viscous flow FVM cells. Entire water columns further away from the hull are covered with potential-flow HPC cells, see the principal sketch in Figure 3.8.

Both the linear velocity potential φ and its time-derivative, i.e. the linear acceleration potential ψ satisfy Laplace equation (2.3) in the potential flow domain.

$$\nabla^2\psi = 0 \qquad \text{in } \Omega_{\text{pot}}. \tag{3.48}$$

The Laplace equation for ψ in the potential flow domain will be coupled with the momentum conservation equation for an incompressible Newtonian liquid in an inertial Earth-fixed coordinate system in the viscous flow domain equation (2.1),

The last step in Chorin's projection method is to solve a Poisson equation for the pressure in the viscous flow domain (see section 3.1.4),

$$\nabla^2\tilde{p} = \frac{1}{\Delta t}\nabla\cdot\mathbf{u}^{**} \qquad \text{in } \Omega_{\text{CFD}} \tag{3.49}$$

Equations (3.48) and (3.49) share the same operator ∇^2 and can then be coupled directly in one matrix system, and solved together within one matrix operation. The divergence-free liquid velocity field can after $\tilde{p}$ and ψ are found be updated as $\mathbf{u}^{m+1} = \mathbf{u}^m - \Delta t\nabla\psi^{\text{N}+1}$ in the potential flow domain (Ω_{pot}) and as $\mathbf{u}^{m+1} = \mathbf{u}^{**} - \Delta t\nabla\tilde{p}^{m+1}$ in the viscous flow domain (Ω_{CFD}). Again m is the time-step number. This gives a condition for $\mathbf{u}^{**}$ on the intersection $\mathbf{u}^{**} = \mathbf{u}^m$ that is much simpler to evaluate than the corresponding term in the nonlinear hybrid method. Since the semi-nonlinear method only matches pressure and normal velocity at the intersection, the method cannot guarantee continuous tangential velocity across the intersection. The staircase pattern as shown in Figure 3.6 and indicated in Figure 3.8 is introduced as an attempt to also force continuous tangential velocity, as described by Kristiansen and Faltinsen (2012). This is not a perfect approach, but it increases the stability of the solution. The thought is that the alternating normal direction will force both the normal and tangential velocity to be continuous. The effects of the staircase pattern are examined in more detailed when forced motions are studied in section 5.4.

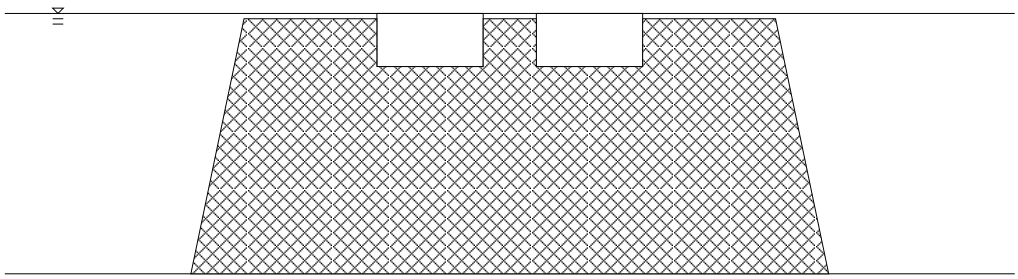

Figure 3.8: Overview on how to separate into a potential flow domain (Ω_{CFD}) (patterned area) and a viscous flow domain (Ω_{pot}) for the semi-nonlinear hybrid method with linear boundary conditions. Notice that there is only a thin potential flow domain near the mean free surface close to the body.

3.5.1 Boundary and initial conditions

The boundary conditions for the semi-nonlinear hybrid method are given in the following text. To achieve high computational performance the matrix system must not change with time, i.e. the discretization of the equation system remains fixed in time. This is achieved by using a constant mesh, which again requires us to satisfy the boundary conditions on the same interface every time-step. This can be done by using a linear perturbation of the free-surface conditions, i.e. we do a perturbation of the free-surface conditions around $z = 0$ using the wave elevation ζ as a small perturbation parameter, see for instance Faltinsen (1990).

The dynamic linear free-surface condition is an equation for the time evolution of the velocity potential φ on the mean free surface,

$$\frac{\partial \varphi}{\partial t} = -g\zeta \qquad \text{on } z = 0. \tag{3.50}$$

The kinematic linear free-surface condition will give an equation for the time evolution of the wave elevation ζ,

$$\frac{\partial \zeta}{\partial t} = \frac{\partial \varphi}{\partial z} \qquad \text{on } z = 0. \tag{3.51}$$

The relation between ψ and φ from equation (3.46) results in a value for ψ that will be used as a boundary condition on the free surface when solving the matrix system,

$$\psi = -\frac{\partial \varphi}{\partial t} = g\zeta \qquad \text{on } z = 0. \tag{3.52}$$

Notice from equation (3.51) that the z-derivative of φ is needed on the free surface, which means that after ψ is found in the potential flow domain we need to update φ in the upper potential flow domain close to the free surface ($\varphi^{m+1} = \varphi^m - \Delta t\, \psi^{m+1}$). This applies to at least the 3 upper rows of HPC nodes, such that $\frac{\partial \varphi}{\partial z}$ can be found using harmonic polynomials. Both free-surface conditions in equations (3.50) and (3.51) are evolved forward in time by using the common explicit fourth-order Runge-Kutta method. Note that a consequence of the current first-order finite difference relation between φ and ψ, is that there will phase lag between ψ and φ of half a time-step.

An equivalent approach inside the moonpool gap domain, is to stretch the viscous domain up to the free-surface and apply a similar linear free-surface condition here. From Faltinsen (2005), the linear kinematic and dynamic free-surface conditions are given as,

$$\frac{\partial \zeta}{\partial t} = w \quad \text{on } z = 0 \tag{3.53}$$

$$-p + 2\mu \frac{\partial w}{\partial z} = p_a \quad \text{on } z = \zeta \tag{3.54}$$

$$\mu \left(\frac{\partial u}{\partial z} + \frac{\partial w}{\partial x} \right) = 0 \quad \text{on } z = 0 \tag{3.55}$$

where μ is the dynamic viscosity of the liquid. If now the viscous shear stress on the free surface is assumed negligible, the equations can be further simplified. It is shown in Faltinsen (2005) that including the viscous terms in the free-surface boundary conditions

have a very small effect in linear free-surface problems for the relevant condition. This implies

$$\frac{\partial \zeta}{\partial t} = w \quad \text{on } z = 0 \tag{3.56}$$

$$p = -g\zeta \quad \text{on } z = 0. \tag{3.57}$$

Furthermore, it is believed that a small potential flow domain with only 3 potential-flow HPC cells in the vertical direction inside the gap is sufficient. In addition, we get a higher spacial accuracy with the HPC method in the potential flow domain, although it is not expected to be important inside the moonpool gap.

For the body-boundary condition we need to separate between the potential flow part and the viscous flow part at the body boundary. Similarly as the free-surface conditions, the body-boundary condition is applied on a surface that is constant in time. In the tangential direction of the wall a no-slip condition is imposed in the viscous flow domain, while in the potential flow domain a slip condition is used. Since we are not aiming at capturing the liquid flow inside the boundary layer, the difference between the no-slip and slip condition does not introduce a problem on the intersection between the two domains. However, it is not expect that this in general will be true, and especially not if the mesh density is increased to capture the detailed behaviour of the liquid flow inside the boundary layers.

Further, in the normal direction to the wall in both domains no liquid flux through the exact body boundary is required. In the potential flow domain the body-boundary condition can be found from the Euler's equations. These corresponds to the Navier-Stokes equations (2.1) with zero viscosity and the assumption of irrotational flow. These are linearized around the initial position of the hull by assuming that the rigid-body motions are small. The result is the following Neumann type body-boundary condition that is applied on the linear acceleration potential in the potential flow domain of the liquid,

$$\frac{\partial \psi}{\partial n} = -\left(\mathbf{a}_0 + \dot{\boldsymbol{\omega}}_0 \times \mathbf{r}\right) \cdot \mathbf{n} \qquad \text{on } S_{BP}, \tag{3.58}$$

where $\mathbf{n}$ is the unit normal vector of the hull pointing into the liquid, $\mathbf{a}_0$ is the 2D acceleration of the COG in sway and heave, $\dot{\boldsymbol{\omega}}_0$ is in 2D only nonzero for the roll acceleration $\ddot{\eta}_4$ and $\mathbf{r}$ is the position vector of a point on the body relative to the COG.

A similar Neumann type body-boundary condition is applied for the pressure $\tilde{p}$ in the viscous flow domain, which can be derived from the Navier-Stokes equations (2.1) following the same assumptions as for the potential flow part, i.e.

$$\frac{\partial \tilde{p}}{\partial n} = -\left(\mathbf{a}_0 + \dot{\boldsymbol{\omega}}_0 \times \mathbf{r}\right) \cdot \mathbf{n} \qquad \text{on } S_{BV}. \tag{3.59}$$

Both equation (3.58) and equation (3.59) represent an in-out flow through the initial position of the ship. We emphasize that S_{BP} or S_{BV} do not change with time and remain fixed at the initial position of the ship, see Figure 3.9.

In linear potential flow theory, it is usual to require that the body-boundary conditions are valid at the mean position of the ship. This may not be the case with the present semi-nonlinear hybrid method, due to nonzero drift force which together with the mooring system causes a mean offset of the body. Therefore we specify that the body-boundary conditions are valid at the initial position of the ship.

The outer wall and bottom boundary conditions are zero flux and a zero pressure gradient. (See later for conditions on the wavemaker and the numerical beach.)

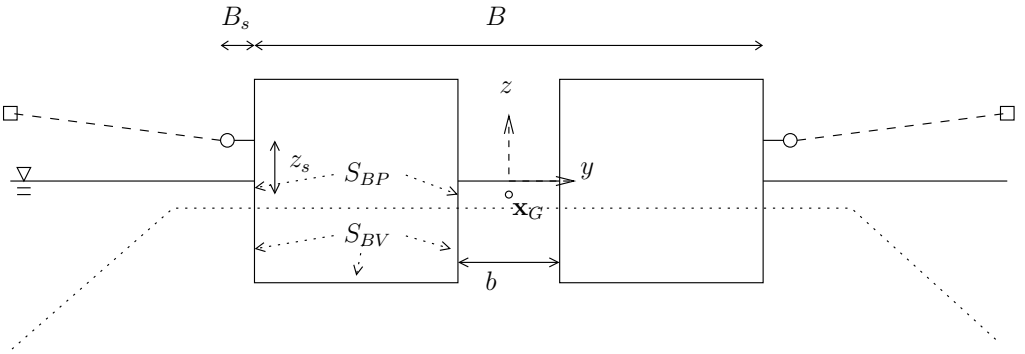

Figure 3.9: Numerical setup of the semi-nonlinear hybrid method. $\mathbf{x}_G$ is the center of gravity, B is the total width of the hull, b is the width of the moonpool gap, B_s is the length of the screw connecting the hull to the mooring line, z_s is the vertical distance from the screw to the center of gravity, S_{BP} is the potential flow part of the hull surface and S_{BV} is the viscous flow part of the hull surface. The dotted line indicate where the intersection between the potential and viscous flow is.

The initial conditions are simply still water with the body at rest.

3.5.2 Equations of motion

In two dimensions it is sufficient to consider rigid-body motion in three degrees of freedom; sway η_2, heave η_3 and roll η_4. The equations of motion due to Newton's second law in an inertial coordinate system are:

$$\begin{aligned} m\ddot{\eta}_2 &= F_y, \\ m\ddot{\eta}_3 &= F_z, \\ I\ddot{\eta}_4 &= M. \end{aligned} \tag{3.60}$$

Here m is the body mass, I is the moment of inertia about the center of gravity of the body $\mathbf{x}_{\mathrm{G}} = (y_{\mathrm{G}}, z_{\mathrm{G}})$, F_y and F_z are the external horizontal and vertical forces and M is the external roll moment about the COG (positive counter clockwise). The external forces and moment can further be decomposed to:

$$\begin{aligned} F_y &= \rho \int_{S_{BP}} \psi\, n_2 \,\mathrm{dS} + \rho \int_{S_{BV}} \tilde{p}\, n_2 \,\mathrm{dS} - K_{22}\,\eta_2 - K_{24}\,\eta_4 \\ F_z &= \rho \int_{S_{BP}} \psi\, n_3 \,\mathrm{dS} + \rho \int_{S_{BV}} \tilde{p}\, n_3 \,\mathrm{dS} - C_{33}\,\eta_3 \\ M &= \rho \int_{S_{BP}} \psi\, n_4 \,\mathrm{dS} + \rho \int_{S_{BV}} \tilde{p}\, n_4 \,\mathrm{dS} - K_{42}\,\eta_2 - (K_{44} + C_{44})\,\eta_4 \end{aligned} \tag{3.61}$$

where n_2 and n_3 are components of the normal vector $\mathbf{n}$ and n_4 is the first component of the vector $\mathbf{r} \times \mathbf{n}$. The restoring forces coefficients due to the spring mooring system can be

found as; for sway $K_{22} = k_s$, for the coupling between sway and roll $K_{24} = K_{42} = -k_s\, z_s$ and for roll $K_{44} = B'\, F_{pre}$. The restoring spring coefficient in roll K_{44} is found from geometrical considerations and by assuming that the total pre-tension is much larger than the change in the total tension due to a small rotation η_4, see Fredriksen (2008). Here k_s is the total spring stiffness constant in N/m and z_s is the vertical distance from the center of gravity to where the mooring lines are connected to the hull. Note that we use $B' = 2B + 2B_s + b$, where B is the breadth of one side hull, $B_s = 0.03$m is the screw connection between the body and the mooring line and b is the width of the moonpool gap.

The hydrostatic linear restoring coefficients that are associated with the change in the buoyancy force are: for sway $C_{22} = 0$, for heave $C_{33} = \rho\, g\, (2B)$ and for roll $C_{44} = \rho\, g\, V_{2\mathrm{D}}\, (z_b - z_G) + \frac{2}{3}\rho\, g \left(\left(B + \frac{b}{2}\right)^3 - \left(\frac{b}{2}\right)^3 \right)$. Here $V_{2\mathrm{D}}$ is the displaced volume of the two side hulls per meter in x-direction of the wave flume, and z_b is the vertical center of buoyancy. Note that both the potential flow part S_{BP} and the viscous flow part S_{BV} of the hull surface are constant in time.

In the viscous flow domain the pressure $\tilde{p}$ nodes are not on the cell edge where the pressure on the body should be evaluated, but in the middle of the FVM cell. We use the gradient as defined in equation (3.59) to extrapolate the solution of $\tilde{p}$ from the cell center to the cell edge where the hull surface is.

Note that since we are not solving for the viscous shear stresses in the boundary layer, we will also neglected viscous shear forces on the hull, i.e. we neglect viscous shear stresses on the form $\tau = \mu \frac{\partial u}{\partial n}\,|_{\mathrm{hull}}$. Also other viscous shear stresses are neglected. To include viscous shear stresses on the hull it would have been necessary to resolve the velocity gradient in the boundary layer, this could have been achieved by decreasing the mesh size close to the hull. An in-out flow analysis of the boundary layer in Kristiansen (2009), gave negligible difference in the total body forces and resulting rigid-body motion. However, this only accounts for the effect the boundary layer has on the pressure, in addition comes the viscous shear forces. The experimental setup considered there had similar dimensions as the experimental setup under consideration here. Also a simple implementation of τ in our code had the same negligible result. Note that both the effect the boundary layer has on the pressure and the viscous shear force are expected to be equally small Faltinsen and Timokha (2009).

To solve the equations in (3.60), the equations of motion are first converted from a set of second order differential equations, to a set of twice as many first order differential equations by introducing the velocities in the three degrees of freedom as a second set of unknowns. To gain a stable solution in time, it is on both sides of the equations for each degree of freedom added a term proportional to the acceleration in that degree of freedom. These acceleration terms will be multiplied by the infinite-frequency added mass $(A^*_{\mathrm{jj}}(\infty))$. On the right hand side of the equations the accelerations are approximated with values from the present time-step. This procedure is similar to what was done by Kristiansen (2009) and Shao (2010). Such that the updated equations of motion will look like, here

still given as a set of second order differential equations

$$\begin{aligned} \ddot{\eta}_2^{m+1} &= \frac{F_y + A_{22}^*(\infty)\ddot{\eta}_2^m}{m + A_{22}^*(\infty)}, \\ \ddot{\eta}_3^{m+1} &= \frac{F_z + A_{33}^*(\infty)\ddot{\eta}_3^m}{m + A_{33}^*(\infty)}, \\ \ddot{\eta}_4^{m+1} &= \frac{M + A_{44}^*(\infty)\ddot{\eta}_4^m}{I + A_{44}^*(\infty)}. \end{aligned} \tag{3.62}$$

The equations of motion are time-stepped forward in time using the explicit first order Euler method, but solutions of the free-surface conditions and the combined Laplace/Poisson equation are still solved using the fourth-order explicit Runge-Kutta method. The overall accuracy of the method thus remains first order in time.

3.5.3 Wave generation and absorption

There are a few options on how to generate incoming waves in a numerical wave tank. One choice is to model the physical hinged-type wavemaker from the wave flume to fully recreate the waves achieved in the wave flume. Another option is to specify a known analytical velocity potential φ_{in} on the free surface and on the wavemaker wall. Here it is chosen to input a known linear acceleration potential ψ_{in} for first order waves on the left wall and the equivalent value for φ_{in} for the dynamic free-surface condition and ζ_{in} for the kinematic free-surface condition. The method can easily be extended to a known velocity potential of any order.

Within the left damping zone close to the wavemaker we add damping terms $\nu_w(\varphi - \varphi_{in})$ and $\nu_w(\zeta - \zeta_{in})$ to the respective dynamic and kinematic free-surface boundary conditions, where ν_w is the user defined damping coefficient with dimension $1/s$. By applying this approach the reflected waves from the structure are damped out, but the incoming waves are kept unchanged. In the other damping zone, on the right side of the numerical wave tank, the added damping terms to the free-surface conditions are simply $\nu_w\varphi$ and $\nu_w\zeta$. This is equivalent to the numerical beach known as the Orlanski's condition (Orlanski (1976)), and used by Clement (1996) among others. The damping zone is divided in two parts, closest to the hull there is a smooth ramp-up zone from $\nu_w = 0$ to $\nu_w = 1.6$, in the other part closest to the walls the damping coefficient value is kept constant $\nu_w = 1.6$. Here 1.6 is the value chosen for ν_w in all simulations in this work instead of making the damping coefficient depending on the wave period. We have here chosen to make the length of the smooth ramp-up zone from $\nu_w = 0$ to $\nu_w = 1.6$ dependent on the wave length. The length of this ramp-up zone has been made long enough such that most of the wave amplitude have decayed before reaching the constant zone.

The main reason for not choosing to implement the physical hinged-type wavemaker is to save simulation time. A reason is that a finer mesh will be needed close to the wavemaker if the physical wavemaker was implemented. Also the physical length of the numerical wave tank must equal the physical wave flume. The drawback by choosing to input a first order velocity potential on the free-surface is that time-series results from the experimental programme cannot be compared against numerical calculation. It is only the steady-state values that can be compared, as the transient response of the structure will be different. However, we are able to compare time-series values with the nonlinear hybrid

method presented in the next section, where an implementation of a physical wavemaker would not be possible/beneficial. This is due to that the equation system is solved in a body-fixed coordinate system, and a physical wavemaker far away from the body would require a complicated re-meshing scheme.

3.6 Nonlinear hybrid method

With the nonlinear hybrid method we aim at satisfying all boundary conditions as exactly as possible, both on the free-surface and on the surface of the freely floating body. However, note that there is an exception. We do not aim at capturing the liquid behaviour inside the boundary-layer or turbulence flow at any scale. It was early in the development phase chosen to solve the nonlinear hybrid method using a body-fixed coordinate system with origin in the center of gravity and following the rigid-body motions of the body. The main benefit is that we avoid re-meshing close to the body due to the rigid-body motions. Instead, we have to re-mesh close to the free surface due to the rigid-body motions. However, it has not complicated the algorithm too much, as a re-meshing scheme is necessary in an Earth-fixed coordinate system due to that the free-surface waves are traced up to exact free-surface profile. We will come back to the benefits of using a body-fixed coordinate system later.

The difference in the governing equations between the Earth-fixed and body-fixed coordinate system have been described in the previous chapter. We will in the present chapter describe how they are numerically solved.

As for the semi-nonlinear method, the Chorin's fractional step method is used to solve the Navier-Stokes equation in the body-fixed coordinate system (2.6). The additional terms on the right hand side related to the body-fixed coordinate system are solved during a sub-step along with the advection and diffusion steps. The last step is to solve a Poisson equation for the pressure $\nabla^2 p = \frac{\rho}{\Delta t}\nabla \cdot \mathbf{u}_r^{**}$. The pressure p in the viscous flow domain in equation (2.6) is coupled to the absolute velocity potential φ, where the absolute velocity is seen in the Earth-fixed coordinate system and defined as $\mathbf{u} = \nabla\varphi$, see equation (2.5). The Laplace equation (2.3) is used to solve for φ.

The initial conditions are also here simply still water with the body at rest.

3.6.1 Body-boundary conditions

Similar as in the semi-nonlinear hybrid method it is needed to separate between body-boundary conditions in the potential flow domain, and body-boundary conditions in the viscous flow domain.

The body-boundary condition on the pressure in the viscous flow domain for solving the Poisson equation is found by evaluating equation (2.6) on the viscous part of the hull surface S_{BV}, and noting that $\partial^b \mathbf{u}_r/\partial t = 0$ and $\mathbf{u}_r = 0$ on S_{BV}. The result is

$$\frac{\partial p}{\partial n} = \rho\left[\mathbf{g} - \mathbf{a}_0 - (\boldsymbol{\omega}_0 \times \mathbf{u}_0) - (\dot{\boldsymbol{\omega}}_0 \times \mathbf{r}) - \boldsymbol{\omega}_0 \times (\boldsymbol{\omega}_0 \times \mathbf{r})\right] \cdot \mathbf{n} \qquad \text{on } S_{BV}. \tag{3.63}$$

Here the normal vector $\mathbf{n}$ now change direction with the motion of the body, and remains fixed in the body-fixed coordinate system. Similarly the condition for the temporary artificial velocity field on the body,

$$\mathbf{u}_r^{**} = \left[\mathbf{g} - \mathbf{a}_0 - (\boldsymbol{\omega}_0 \times \mathbf{u}_0) - (\dot{\boldsymbol{\omega}}_0 \times \mathbf{r}) - \boldsymbol{\omega}_0 \times (\boldsymbol{\omega}_0 \times \mathbf{r})\right] \Delta t \qquad \text{on } S_{BV}. \tag{3.64}$$

The body boundary condition for the absolute velocity potential φ in the potential flow domain,

$$\frac{\partial \varphi}{\partial n} = [\mathbf{u}_0 + \boldsymbol{\omega}_0 \times \mathbf{r}] \cdot \mathbf{n} \qquad \text{on } S_{BP}. \tag{3.65}$$

Here the potential-flow part of the hull surface S_{BP} will change with time, as the body-boundary condition is applied up to the exact free surface. Note that this is the equivalent of requiring the relative normal velocity to be zero on the body surface $\mathbf{u}_r \cdot \mathbf{n} = 0$. Similarly as in the semi-nonlinear hybrid method, we have not seen any problems on the intersection by requiring a no-slip condition in the viscous flow domain, and a slip condition in the potential flow domain. However, this cannot expected to be true if the mesh density is increased close to the hull surface.

3.6.2 Re-meshing

At every time-step the free-surface nodes are moved in z-direction to the new position based on time-integration of the free-surface conditions. Due to the body-fixed coordinate system, it will also look like the bottom of the wave flume is moving with time. However, to simplify the re-meshing algorithm we keep the bottom of the numerical wave tank fixed in the body-fixed coordinate system. This simplification will for large roll angles result in that the free surface in the far-field will collide with the "artificial" numerical bottom. The free-surface will far away behave as the distance from the center of gravity times the roll angle. The bottom boundary condition is changed from requiring zero liquid flux through the bottom, to requiring that the absolute liquid velocity is zero at the instantaneous position of the artificial bottom. This is somewhat in contradiction to the free-surface condition, when the "artifical" numerical bottom approaches the free-surface.

An input to the nonlinear hybrid method is an estimate on the largest roll angle η_4^{Max} expected during a simulation needed. From this estimate it is pre-defined within the code which HPC nodes to be moved and corresponding cells that needs to be re-meshed between time-steps. The parameter η_4^{Max} then gives us a limit on the maximum roll angle that can be tolerated within the current simulation. For roll angles close to η_4^{Max} the distance between HPC nodes will become small. When the roll angle is increased above η_4^{Max}, then some HPC nodes will enter the viscous flow FVM domain, and some HPC nodes will overlap with other HPC nodes that are fixed in time with respect to the body-fixed coordinate system. The consequence is that the simulation will break down. Here the coordinates of the FVM cells in the viscous flow FVM domain are fixed in time with respect to the body-fixed coordinate system.

The simplification in how the bottom boundary is handled also limits η_4^{Max}. The numerical implementation does not handle the case when the free surface intersects the artificial bottom. However, η_4^{Max} can be increased by either decreasing the length or increasing the water depth of the numerical wave tank. Since the change of water depth would change the dispersion properties of the free-surface waves the preferred option is to change the length of the numerical wave tank. Figure 3.10 shows details on how η_4^{Max} is defined, and its relation to the intersection between the potential flow and viscous flow domains.

The re-meshing algorithm for the nonlinear hybrid method then works as follows:

- In the initialization of the simulation, find for each free-surface node how many HPC nodes in the vertical column that shall be re-meshed each time-step, N_{RZ}.

- At every sub time-step, move the free-surface node in z-direction to the new wave elevation, based on equation (2.12).
- Move in z-direction the below neighbouring node a fraction $\frac{N_{RZ}-1}{N_{RZ}}$ of the free-surface node wave elevation.
- Move in z-direction the second below neighbouring node a fraction $\frac{N_{RZ}-2}{N_{RZ}}$ of the free-surface node wave elevation.
- Continue until node N_{RZ} below the free surface.
- Use the new coordinates to update the matrix system for the solution of the Laplace equation part of the matrix system.

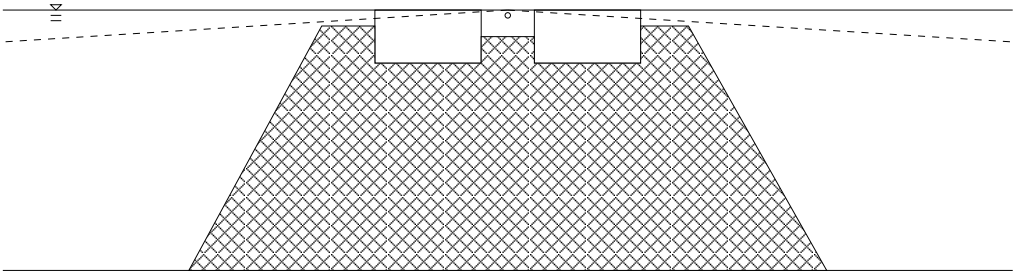

Figure 3.10: Illustration that shows the limitations in how to construct a mesh for the nonlinear hybrid method. The circle in the middle of the structure represent the position of the center of gravity. The dotted line represents η_4^{Max} line in the potential flow domain. The patterned area represents the viscous flow domain (Ω_{CFD}).

3.6.3 Intersection between viscous and potential flow domain

Details on the matching requirements in an Earth-fixed coordinate system can be found in section 3.4. It is here updated to reflect that it is used in a body-fixed rotating coordinate system.

The time-discretized Bernoulli's equation for the pressure in an inviscid liquid flow in a body-fixed rotating coordinate system is given as,

$$\frac{p^{m+1}}{\rho} = -\frac{\varphi^{m+1}-\varphi^{m}}{\Delta t} - \frac{1}{2}\left|\nabla\varphi^{m}\right|^2 + \left[\mathbf{u}_0 + \boldsymbol{\omega}_0 \times \mathbf{r}\right]\cdot\nabla\varphi^{m} - \mathbf{g}\cdot\mathbf{r}_{ef}. \tag{3.66}$$

Note it is changed due to that the time derivative $\partial\varphi/\partial t$ changes between the two coordinate systems. Here $\mathbf{r}_{ef}$ is the shortest distance from the evaluation point to the undisturbed free surface, equivalent to the vertical distance between a point and the undisturbed free surface in the Earth-fixed coordinate system. The total term $\rho\mathbf{g}\cdot\mathbf{r}_{ef}$ is then the hydrostatic pressure in the liquid. Here the gravitational term $\mathbf{g}$ changes in time with the angular roll motion, $\mathbf{g} = g\left[0, \sin(\eta_4), \cos(\eta_4)\right]$. Equation 3.66 is used to exchange variables from φ to p on the intersection.

The second requirement is that the liquid particle velocity on the intersection should be independent of which flow domain it is calculated from, i.e. from the velocity potential in the potential flow domain or from the pressure in the viscous flow domain. In the potential flow domain the relative liquid velocity is found as $\mathbf{u}_r = \nabla\varphi^{m+1} - (\mathbf{u}_0 + \boldsymbol{\omega}_0 \times \mathbf{r})$ and in the viscous flow domain as $\mathbf{u}_r = \mathbf{u}^{**} - \frac{\Delta t}{\rho}\nabla p^{m+1}$. By requiring the liquid particle velocity to be continuous across the intersection we can find the temporary artificial velocity field on the intersection as

$$\mathbf{u}^{**} = \nabla\varphi^m - \Delta t\nabla\left(\frac{1}{2}\left|\nabla\varphi^m\right|^2 - \left[\mathbf{u}_0 + \boldsymbol{\omega}_0 \times \mathbf{r}\right]\cdot\nabla\varphi^m + \mathbf{g}\cdot\mathbf{r}_{ef}\right) - \left(\mathbf{u}_0 + \boldsymbol{\omega}_0 \times \mathbf{r}\right). \quad (3.67)$$

Notice that all terms are valid for the present time-step. Equation (3.67) is applied for $\mathbf{u}^{**}$ on the intersection in the viscous flow domain for both the tangential and the normal velocities to the intersection line. Due to the higher-order spatial accuracy of the HPC method the nonlinear terms in equation (3.67) can be calculated. Since equation 3.67 contains a term multiplied with the time-step size Δt, the implementation should be consistent with the explicit fourth-order Runge-Kutta method along with the other equations that are integrated in time.

To fully understand the coupling between the potential and viscous flow domains, we will illustrate it by writing out the equations that are input to the matrix system. Two examples will be considered. The first is how to set up the FVM equation as used in the viscous flow domain. The second is how to set up the HPC equation as seen in the potential flow domain.

The first example is seen from the FVM side. The starting point is the discretized Poisson equation (3.24)

$$\begin{aligned} &\frac{p_{\mathrm{E}} - p_{\mathrm{P}}}{\delta y}\delta z - \frac{p_{\mathrm{P}} - p_{\mathrm{W}}}{\delta y}\delta z + \frac{p_{\mathrm{N}} - p_{\mathrm{P}}}{\delta z}\delta y - \frac{p_{\mathrm{P}} - p_{\mathrm{S}}}{\delta z}\delta y \\ = \;& \frac{1}{\Delta t}\left(v_e^{**}\delta z - v_w^{**}\delta z + w_n^{**}\delta y - w_s^{**}\delta y\right), \end{aligned} \quad (3.68)$$

where the potential domain is on the west (left) side, and the viscous domain is on the east (right) side, meaning that we need to replace p_{P} and v_w^{**} in equation (3.68). This approach will guarantee a continuous normal liquid velocity between the two domains.

$$\begin{aligned} &\frac{p_{\mathrm{E}} - p_{\mathrm{P}}}{\delta y}\delta z - \frac{p_{\mathrm{P}} + \frac{\varphi_{\mathrm{W}}}{\Delta t}}{\delta y}\delta z + \frac{p_{\mathrm{N}} - p_{\mathrm{P}}}{\delta z}\delta y - \frac{p_{\mathrm{P}} - p_{\mathrm{S}}}{\delta z}\delta y \\ = \;& \frac{1}{\Delta t}\left(v_e^{**}\delta z + w_n^{**}\delta y - w_s^{**}\delta y\right) \\ - \;& \frac{\delta z}{\Delta t}\left[\frac{\partial\varphi_{\mathrm{W}}}{\partial y} - \Delta t\left(\left(\frac{\partial\varphi_{\mathrm{W}}}{\partial y} - \dot{\eta}_2\right)\frac{\partial^2\varphi_{\mathrm{W}}}{\partial y^2} + \left(\frac{\partial\varphi_{\mathrm{W}}}{\partial z} - \dot{\eta}_3\right)\frac{\partial^2\varphi_{\mathrm{W}}}{\partial y\partial z} - v_0\right)\right] \\ + \;& \frac{\delta z}{\delta y}\left(-\frac{\varphi_{\mathrm{W}}}{\Delta t} + \frac{1}{2}\left|\nabla\varphi_{\mathrm{W}}\right|^2 - \left[\mathbf{u}_0 + \boldsymbol{\omega}_0 \times \mathbf{r}\right]\cdot\nabla\varphi_{\mathrm{W}}\right) \end{aligned} \quad (3.69)$$

Here, φ_{W} is not at a valid node inside the potential HPC domain. Meaning that the value of φ_{W} is interpolated based on the nearest four neighbouring HPC φ values. A similar approach is implemented to guarantee a continuous tangential liquid velocity at the intersection. If, for instance, also the north and south neighbouring cells are within the viscous flow domain, then the velocity nodes w_s and w_n are tangential to the intersection.

If now w_s and w_n satisfy equation (3.67), we require that also the tangential liquid velocity at the intersection is continuous. We do not need to replace p_{S} or p_{N}, since they are values within the viscous pressure domain.

After the solution of the matrix system for p in the viscous domain and φ in the potential flow domain are found, the velocities are time-stepped either based on the viscous flow solution or the potential flow solution. However, notice on the intersection in the viscous flow domain it is here assumed that vorticity has not reached the intersection.

From the potential flow side on the intersection, the starting point is the discretized equivalent of equation (3.32)

$$c_{1,1}\varphi_1 + c_{1,2}\varphi_2 + c_{1,3}\varphi_3 + c_{1,4}\varphi_4 + c_{1,5}\varphi_5 + c_{1,6}\varphi_6 + c_{1,7}\varphi_7 + c_{1,8}\varphi_8 - \varphi_9 = 0. \tag{3.70}$$

(See how the local numbering of the HPC cell is defined in Figure 3.4). If now the 8th HPC node (lower right corner) is within the viscous domain, equation (3.66) is used to exchange the variable φ_8 to a pressure node value p_8.

$$\begin{aligned} & c_{1,1}\varphi_1 + c_{1,2}\varphi_2 + c_{1,3}\varphi_3 + c_{1,4}\varphi_4 + c_{1,5}\varphi_5 + c_{1,6}\varphi_6 + c_{1,7}\varphi_7 - c_{1,8}\Delta t p_8 - \varphi_9 \\ = \;& c_{1,8}\left(-\varphi_8 - \Delta t\left[\frac{1}{2}\left|\nabla\varphi_8\right|^2 - \left[\mathbf{u}_0 \cdot + \boldsymbol{\omega}_0 \times \mathbf{r}\right] \cdot \nabla\varphi_8 + \mathbf{g}\cdot\mathbf{r}_{ef}\right]\right) \end{aligned} \tag{3.71}$$

Here all values on the right hand side is from the present time-step. However, p_8 is not at a valid node in the viscous domain. The value of p_8 needs to be interpolated based on the neighbouring values at the center of the FVM cells.

3.6.4 Smoothing

The spatial derivative terms in the free-surface conditions (2.12) and (2.15) are for φ found using the HPC method, while for ζ the derivatives are found from a fourth-order polynomial fitted from the neighbouring ζ values.

For simulations with low forward velocity, an instability on the free surface with saw-tooth behaviour was experienced. This happened both upstream and downstream of the body. To achieve a more stable numerical solution, a 5-point Chebychev smoothing originally from Longuet-Higgins and Cokelet (1976) was applied on the free-surface elevation ζ. The variable mesh size scheme from Koo et al. (2004) is here implemented. The smoothing algorithm is performed every Nth time step, where N is given in the input-file to the simulation. A sensitivity study of the smoothing algorithm has been performed and will be presented later. It was found sufficient to apply the smoothing algorithm only in the near-field of the body, one hull length to each side. The reason is that the smoothing algorithm has a damping effect on the free-surface waves, which is undesired when solving for body-motions due to incoming waves.

The smoothing algorithm is applied on the free surface in the outgoing wave domains, and not on the free surface inside the moonpool gap. The reason for not applying the 5-point Chebychev smoothing algorithm to the free surface inside the gap, was that it caused a continuous growth of the first sloshing mode. Instead inside the gap an artificial damping around the average free-surface value of the nodes inside the gap at the previous time-step is applied to remove any sloshing modes from the solution.

It is believed that the main reason for the saw-tooth instability is from the advective terms in the free-surface boundary conditions. It is, however, for the downstream side

also observed a small instability when vorticity reaches the intersection. Especially for higher wave steepness, vorticity reaches the intersection, and the smoothing algorithm is used on the free surface to stabilize the solution.

Two other approaches were tried and not found sufficient. The first was to discretize the advection terms in the free-surface condition with upwind values, which provided some numerical damping to the incoming waves. The second approach was to try a three-point low-pass filter used by Shao (2010) among others, $\zeta_j = c\,\tilde{\zeta}_{j-1} + (1-2c)\,\tilde{\zeta}_j + c\,\tilde{\zeta}_{j+1}$, where $\tilde{\zeta}$ is the free-surface value before smoothing and j is the numbering of the free-surface nodes, with increasing values in positive y-direction. Furthermore, c is the strength of the filter.

3.6.5 Equations of motion

Newton's second law is applied to calculate the rigid-body motion in three degrees of freedom, equivalent to procedure described for the semi-nonlinear hybrid method (equation (3.60)). However, the procedure is changed compared to the semi-nonlinear method to reflect that the equations are solved in a body-fixed coordinate system, see details in section 2.1.1 on how to change the time-derivatives in the equations of motion to a body-fixed coordinate system. The equations of motion in a body-fixed coordinate system are given as,

$$\begin{aligned} m\,(\ddot{\eta}_2^* - \dot{\eta}_4\dot{\eta}_3^*) &= F_y, \\ m\,(\ddot{\eta}_4^* + \dot{\eta}_4\dot{\eta}_2^*) &= F_z, \\ I\ddot{\eta}_4 &= M. \end{aligned} \tag{3.72}$$

Here F_y and F_z are the forces in y- and z-directions in the body-fixed coordinate system respectively. Furthermore, $\ddot{\eta}_2^*$ and $\ddot{\eta}_3^*$ are the accelerations of the center of gravity in y- and z-directions of the body-fixed coordinate system respectively. M is the moment around the center of gravity, positive anti-clockwise.

The resulting forces in y- and z-directions and the moment around the center of gravity can then be found as,

$$\begin{aligned} F_y &= \int_{S_{BP}} p\,n_2\,\mathrm{dS} + \int_{S_{BV}} p\,n_2\,\mathrm{dS} - m\,g\,\sin(\eta_4) + F_y^s, \\ F_z &= \int_{S_{BP}} p\,n_3\,\mathrm{dS} + \int_{S_{BV}} p\,n_3\,\mathrm{dS} - m\,g\,\cos(\eta_4) + F_z^s, \\ M &= \int_{S_{BP}} p\,n_4\,\mathrm{dS} + \int_{S_{BV}} p\,n_4\,\mathrm{dS} + M^s. \end{aligned} \tag{3.73}$$

Here, the integration surface S_{BP} will change with time, while S_{BV} remains constant in time. The spring contributions F_y^s, F_z^s and M^s are based on the exact elongation of the springs and angle of each mooring line, where both ends of the mooring lines are allowed to change, such that we can simulate towing of a freely floating object by the mooring system. Similar as in the semi-nonlinear hybrid method, the pressure p in the viscous domain is extrapolated from the cell centers to S_{BV}. This is achieved by the use of the body boundary condition in equation (3.63).

As before, the pressure in the potential flow domain is found from Bernoulli's equation. It is here changed to reflect that the HPC nodes attached to the body is moving in z-direction in the body-fixed coordinate system. The pressure from the Bernoulli equation then becomes,

$$\frac{p}{\rho} = -\frac{d^g\varphi}{dt} + w_n\frac{\partial\varphi}{\partial z} - \frac{1}{2}\left|\nabla\varphi\right|^2 + (\mathbf{u}_0 + \boldsymbol{\omega}_0 \times \mathbf{r}) \cdot \nabla\varphi - gz_e. \tag{3.74}$$

Here $\frac{d^g}{dt}$ is the time-derivative when following a z-moving HPC mesh node with velocity w_n in the body-fixed coordinate system, that is solved numerically by a first order finite difference approximation. Equation (3.74) is integrated along S_{BP} by locally fitting a fourth-order polynomial through the HPC nodes.

The method of adding the infinite frequency added mass term to solve the equations of motion as in the semi-nonlinear hybrid method has been tried and found not sufficient for solving the equations of motion in the nonlinear hybrid method. The solution has been to solve the equations of motion by an iteration scheme each time-step. It is however, coupled to the iterative solver of the matrix system, such that the computational cost is kept down.

For the acceleration terms in equation (2.6), accelerations from the present time-step are used as an initial guess for building the right hand side of the matrix system. Then one single iteration on the solution of matrix system by the iterative matrix solver BICGSTAB is performed, and an updated pressure field is found and used to solve the equations of motion. If then the difference between the new accelerations and the old accelerations of the rigid-body are less than a pre-set tolerance we continue to next time-step. If not we find a new guess on the accelerations and redo the above steps. The new guess is an average of the previously iterations. Note that the convergence tolerance is by this approach moved from the matrix system to the rigid-body accelerations. There is implemented a safety feature if the difference between the new acceleration and the previous acceleration increases compared to the previous iteration. The matrix system is then iterated until convergence for a given guess of the accelerations, and the new accelerations are found.

It was tried to set up a boundary value problem for the acceleration potential ψ for the potential flow domain, but it was found that it did not increase the convergence rate. Due to that the boundary conditions had to be generated from the solution of the boundary value problem for φ, it required the solution of two matrix system for each iteration step. This might be because a major part of the hull surface is within the viscous flow domain.

3.6.6 Time-step size

The requirements for the time-step Δt size from section 3.1.5 are still valid for the nonlinear hybrid method in a body-fixed coordinate system. However, here it is taken as a requirement on the relative liquid velocity $\mathbf{u}_r$. In the body-fixed coordinate system the largest relative velocity $\mathbf{u}_r$ can due to the roll motion be expected to occur far away from the body, either in the lower left or lower right corner of the wave tank. The mesh size is larger far away, but anyway the CFL criteria (equation 3.25) may be reached in the far-field. The value used for the CFL criteria have been 0.5 for all simulations.

3.6.7 Advantages and disadvantages of a body-fixed coordinate system

Conventionally numerical wave tanks have been posed in an Earth-fixed coordinate system.

To numerically simulate forced oscillations of a semi-submerged body with low forward velocity, an alternative was to solve all equations in the Earth-fixed coordinate system and generate a incoming current in the numerical wave tank. It requires quite long simulation time to generate a steady current. Furthermore, the initial conditions start a standing wave (seiching) in the wave flume. In order to satisfy the body-boundary condition exactly, a complicated re-meshing scheme is required. In principle a new mesh must be generated each time step close to the body surface. With a changing mesh close to the body, a numerical scheme that is able to handle a changing mesh inside the viscous domain must be implemented. Various methods on how to handle this are available in the literature. Usually this includes various interpolation techniques, and higher-order methods are complicated to implement. It is also thought to be out of the scope of this work to investigate a broad variety of viscous methods to use on moving meshes. Another even more complicated approach would have been to simulate low forward velocity in the Earth-fixed coordinate system.

The alternative experimental approach was also to generate a current in the wave flume. The main reason for not following this path was that the circulation system was untested and that concerns about the design of the circulation system were raised. Meaning that there were uncertainties in the vertical current profile and the turbulence intensity of the incoming flow on the model.

Some limitations of the body-fixed approach should also be mentioned. What if we want to simulation the behaviour of two ships moored together side by side? On which of the two ships do we attach the body-fixed coordinate system? What do we do with the other ship?

Even though the body-fixed solution is suitable for the rigid-body motion of one ship, the method is not easy to extend to other physically related problems. The method is therefore not suitable to study the rigid-body motions of a ship moored close to a terminal, as done by Kristiansen (2009). This is true even though an extension of the current nonlinear hybrid method to this problem only requires that we implement a wall close to the body. In a body-fixed coordinate system this will behave like a moving wall close to the body, in order to achieve this a re-meshing scheme has to be applied. Then a fixed viscous mesh approach is no longer sufficient. The wall will be so close to the hull edges such that a potential flow approximation close to the wall may not be sufficient.

For the motion of a second body in the proposed nonlinear hybrid method, an option is to implement a re-meshing scheme close to the second body. However, by doing this the benefits with the proposed nonlinear hybrid method is somehow lost, and a moving mesh in the viscous domain will be needed. Then the entire problem is perhaps best solvable in an Earth-fixed coordinate system. Another option that could be investigated is to split it into two separate body-fixed domains, and match the pressure and velocities at an intersection between the two domains. Preferably this matching should be done in a potential flow domain.

3.7 Matrix solution methods

Some preliminary studies were early performed to investigate which matrix solver that would be most efficient to solve the proposed numerical problem. The search were limited to a few selected iterative solvers from SPARSEKIT and Saad (2003), and a direct band-solver from LAPACK. It was without the use of advanced code profiling techniques found that the bottleneck of our numerical method was related to solving the matrix system. No parallel solvers were tried.

It was found from Kristiansen and Faltinsen (2012) that for small and linear problems, the band-solver from LAPACK was the fastest. The band-solver is a direct matrix solver that take advantage of the low bandwidth of the sparse matrix system. For the semi-nonlinear method it only needs to be inverted once at the beginning of the simulation. Furthermore, at every time-step the inverse matrix M^{-1} can be multiplied with the right hand side. Note that it is due to computational memory requirements not desirable to use this method for problems with many unknowns.

For the nonlinear hybrid method the biconjugate gradient stabilized method (BICGSTAB) from SPARSEKIT and Saad (2003) is used. In order to speed-up the computations an incomplete LU (ILU) factorization of the initial matrix is used as preconditioner. A new ILU preconditioner matrix is created if the number of iterations increases above $N_{\max}$, where $N_{\max}$ is given in the input-file to the simulations. Often large mesh deformations due to large roll angles will create the need for a new preconditioner matrix. Since the matrix is depending on the time step size, two preconditioner matrices are held in the computational memory, where the first is valid for half the time step size, i.e. the two first sub-steps in the fourth-order explicit Runge-Kutta method. The second preconditioner matrix is valid for the two last time-steps. Meaning also that the preconditioner matrices must be changed if the time step size changes in the simulation.

Note that the aim of the present study has not been to investigate all available direct and iterative solvers for the numerical method presented here. The generalized minimal residual method (GMRES) from SPARSEKIT was also tried and found to be equivalent to the chosen BICGSTAB routine.

For fast convergence of an iterative scheme, it is important to have a good first guess of the solution. Therefore, the previous solution is corrected by the first order finite difference gradient and used as an initial guess on the solution at the next time step to the iterative solver.

3.8 Code development environment

In order to set up an efficient and user friendly code development environment the following tools have been chosen.

All the pre- and post-processing of the results are done with scripts in Matlab. The pre-processing have been generation of input files for the numerical codes. The post-processing have been more complex, i.e. a set of scripts have been generated to read various output values from the numerical simulations:

- Script to read and visualize liquid properties such as velocity, divergence and vorticity.

- Visualizations of the mesh and how it is re-meshed in time.
- Visualizations of the free surface and the rigid-body motion in time.
- Scripts to find steady-state values of time series.
- Scripts to loop over a large amount of simulations and generate response amplitude operator values for different parameter variations, and compare them with experimental values.

The programming language have been Fortran, and the compiler has been the Intel Fortran Compiler for Linux. The main part of the Fortran code development has been performed in Eclipse with the Photran add-on. The Subversion revison control system has been used daily on the entire code base.

Chapter 4

Experimental programmes

In order to get validation data for the hybrid methods developed here, two experimental programmes have been performed. They are two-dimensional experiments of a moonpool section in a wave flume. The first experimental set-up was with forced oscillation with low forward velocity, the second experimental set-up was with a spring-moored floating moonpool section subjected to incoming regular waves. In the following sections both the experimental programmes will be described in detail.

4.1 Forced heave oscillation with low forward velocity

Our motivation was to continue the experimental programme started by Kristiansen and Faltinsen (2012), and perform parameter variations using an automatic control system for the job. Most effort was in Kristiansen and Faltinsen (2012) put on performing forced heave oscillation without forward velocity.

The experiments were performed in a wave flume at the Marine Technology Centre at NTNU in Trondheim. The wave flume is 12m long, 0.6m wide and with a 1.0m water depth. In both ends there where parabolic beaches with their upper position located just below (1mm) the free surface. Since the beaches occupied lengths of approximately 2.5m each, the usable rail length for the carriage was 5.6m. This fact together with that we needed our experiments to reach a steady-state piston-mode oscillation amplitude limited the carriage velocity (U) that could be used. We define a Froude number based on the total length of the model including the moonpool gap as,

$$\mathrm{Fn} = \frac{U}{\sqrt{g\,(2B+b)}} \tag{4.1}$$

where B is the breadth of one hull, and $b = 0.18$m is the moonpool gap width. We have found that using a model of total length 0.9m, limits the forward carriage velocity to Fn$= 0.08$. The dimensions of each section were breadth $B = 0.36$m, 0.585m wide in the transverse tank direction and with variable draft. It implies that there is a gap of 0.0075m between each end of the model and the tank wall. (See Figure 4.1 for a sketch of the experimental set-up and Figure 4.2 for a picture from the experiment). The only difference to the experimental set-up in Kristiansen and Faltinsen (2012) is that the vertical actuator was replaced with a actuator more suitable for the job. The previous actuator was over-dimensioned. This was done to reduce the top weight on the carriage

and allowed for easier movement of the carriage in the length direction of the wave flume.

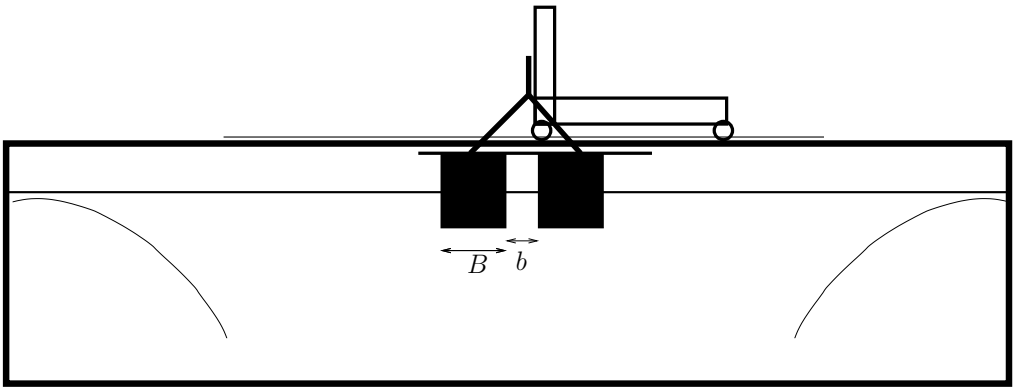

Figure 4.1: Principle sketch of forced oscillation experimental test set-up, with a carriage on top of a glass covered wave flume with a parabolic beach at each end. Note that the drawing is not in scale.

The following five parameters were possible to vary during the test programme: oscillation frequency, oscillation amplitude, draft, carriage velocity and moonpool inlet edge profiles. In total between 6000 and 7000 tests were planned. To be able to perform this extensive test programme an automated set-up was designed in Labview by Fredrik Dukan. The automated set-up allowed that experiments could be performed without anyone present. The only thing not automated was the wave gauge calibration process, such that we were at the experimental location at least once a day to check the calibration factor of the wave gauges. The automatic control system was configured to start the carriage from one side of the tank, and smoothly accelerate the carriage up to the wanted velocity while the heave oscillations also smoothly started. When the carriage reached the other end, it smoothly slowed down and waited until the waves had died out. After waiting for 200 seconds it returned to the starting position with the same heave oscillation amplitude, frequency and carriage velocity. In this manner, the same experiment was repeated twice, before a new heave oscillation amplitude, frequency or carriage velocity were tested. The waiting period of 200 seconds was chosen by observation of the measured wave elevation, of the time needed for the waves to dissipate. However, the circulation in the tank which was set up by the forward moving model might not have stopped. This means that when the model started moving in the opposite direction it might be influenced by the residual global flow. We should also consider that the presence of the seiching mode of the tank will result in a horizontal current at the middle of the tank, which also will influence the relative velocity between the model and the water. A seiching amplitude of 1mm will give a horizontal current at the middle of tank of 2.7% of the forward velocity at Froude number $\mathrm{Fn} = 0.04$. The seiching amplitude for carriage velocities of Froude number $\mathrm{Fn} = 0.08$ was found from the wave gauges to at most be 0.5mm. The wave gauges were then around 2m away from the end of the tank.

The model was equipped with four capacitance wave gauges, two in the moonpool gap and one on each side. The wave gauges in the moonpool gap were located 6.0cm

from the hull on each side. The wave gauge on the left was 26.5cm from the model side, and the wave gauge on the right was 21.0cm from the other model side. All four wave gauges were mounted on the rig and was then forced to move with the forward velocity and heave oscillation. All wave amplitudes presented in this work are therefore given from a body-fixed point of view.

Figure 4.2: Picture of the experimental set-up without appendages. Here the model is located close to left beach. To change the hull to include appendages, only the gray profiles of the moonpool edges are exchanged with corresponding appendage profiles.

4.1.1 Experimental error sources in forced experiments

The rails and the glass walls were not perfectly aligned, such that the model had to be smaller than necessary. From trial and error we found that the model had to be 1.5cm smaller than the width of the tank to minimize the contact between the model and the glass wall. Due to this gap we have a 3D effect in the experiments that are difficult to estimate. Visually we could at higher velocities observe vorticity being shed from the small gap between the glass and hull, into the moonpool gap, and behind the second hull. Since we still had some contact between the glass and the hull, the forward motion was influenced due to a varying friction in the length direction of the tank. The connection between the two glass windows was at some locations uneven, and the cause of the varying friction. The control system managed to counteract and minimize this, but it cannot be neglected as an error source.

Another error source is the control system for the carriage and heave actuator. It was not able to reach the desired heave oscillation amplitude, but on average around 90% of the desired heave amplitude. For a test series with a desired heave amplitude of 10.0mm, the actual heave amplitude became 9.1mm. It may not be characterized as an error source since we know the amplitude after the test, but since the control system did not perform

as expected we mention it as an potential error source. The results will be presented using the dimensionless equivalent to the forced heave amplitudes η_{3a} of 2.3mm, 4.5mm and 9.1mm, while it in reality was a small variation of the heave amplitude during each tests series with fixed heave amplitude. The values in the figures are corrected for this, but the title/legend of each figure uses the average value. Note, it was still found that the forced heave amplitude was steady for each experimental test.

A third error source in the experiments is reflections from the beaches. The velocity of the carriage is much lower than the group velocity of the outgoing waves. Note that for both higher carriage velocity and longer periods the steady-state piston-mode amplitude is found close to the beach at the end of the wave flume. Such that waves generate upstream of the structure and if not fully dissipated by the beach and reflected back to the structure, they might influence the piston-mode amplitude when the steady-state condition is evaluated. When the possible reflected wave reaches the structure is then dependent on the period of oscillation and forward velocity.

When accelerating the structure in any direction, a transient effect will be generated. The transient effect will generate outgoing waves, but it will also excite the natural piston-mode and the sloshing modes inside the moonpool gap. For the forward velocity case it means that the odd sloshing modes inside the moonpool may be excited, which mainly means that the first sloshing mode will be excited at its resonance frequency. For the forced heave oscillation case without forward velocity, the transient start-up results in an excitation of the piston-mode at the piston-mode resonance frequency. The piston-mode motion at the resonance frequency will decay due to wave radiation and viscous dissipation. The sloshing mode communication with the water outside the moonpool will be low, and not affected by flow separation at the moonpool edges. Since also boundary layer dissipation is small, the sloshing mode decays slowly. The first sloshing mode natural period is $T_s = 0.48$s for the 18cm wide moonpool.

The raw signal from the wave gauges was band-pass filtered to remove frequencies above 1.9Hz and below 0.5Hz. This will remove all higher harmonics, including the first natural sloshing mode. An inspection of the frequency spectrums computed by FFT of the raw wave gauge signals, shows negligible traces of nonlinearities. We chose to take the amplitudes from the experiments as half of the distance from the wave crests to the wave troughs over a steady or near-steady interval in time.

It was after the first week of continuous experiments discovered that the connection between the model and the actuator had some loose screws. To avoid any uncertainties related to this, all experiments that had been performed was redone and results from the first experiments have not been used further in the post processing analysis. Throughout the rest of the experiments, checks were regularly done to make sure that all screws were tightly fixed.

The electrical engine controlling the forward velocity of the carriage was mounted to a rubber band that was fixed to both ends of the wave flume. Due to the elasticity in the rubber band there is a small uncertainty in the position of the carriage, because the position of the carriage was measured by the engine itself, and the number of revolutions the wheel performed on the rubber band. The error is believed to be largest during the acceleration phases, and not when the carriage is at constant velocity. This is also the main reason for not considering studies with forced sway motion, because the total inertia of the set-up on the carriage gives a large force during acceleration on the rubber band that causes some uncertainties in the position.

4.1.2 Examples of time-series

Figures 4.3 and 4.4 show examples of time-series history based on the same period and amplitude of oscillation and forward velocity. The only difference is that the carriage velocity is in the opposite direction. In Figure 4.3 it is moving from left to right. In the upper right of both Figures is a plot showing the synchronization signal. This is a signal sent from the Labview control system to the Catman logging system. Here the voltage value represents different stages throughout the tests. 0 represents the waiting period before the test starts, 1 represents the acceleration phase, 2 is the constant velocity and constant amplitude phase, 3 is the de-acceleration phase and 4 represents the end of the test. Between the tests the signal will return back to 0. This was implemented since the forced heave motion, carriage velocity and wave gauges were not logged with the same data acquisition system. In the acceleration and de-acceleration phases the heave motion is smoothed with a $\cos^2$ function, to minimize the transient effect.

The wave gauges presented as ζ_2 and ζ_5 are measuring outgoing waves and ζ_4 and ζ_6 are measuring the water elevation inside the moonpool gap. Note that they are all fixed to the model, i.e. all wave gauge measurements are relative to the vertical heave motion of the model. A conversion back to the Earth-fixed frame was attempted, but a small phase difference between the two signals was still present, even with the synchronization system in place.

The steady-state results will be given in section 5.1.

4.2 Floating moonpool body in incident waves

A second series of two-dimensional experiments were performed during the fall of 2012, with the focus on freely-floating rigid-body motions. The location for floating experimental programme was the same as for the forced heave oscillation experiments with low forward velocity. However, the set-up was somewhat changed. The left beach on Figure 4.1 was removed to allow use of the wavemaker that is mounted behind it. It is a flap type wavemaker hinged 5cm above the bottom of the wave flume.

The hull model differs from the model used in the forced heave oscillation experiments. However, the draft-to-breadth and moonpool gap-to-breadth ratios were kept. The previous rig was too high and heavy to be used for floating motions. Among other things it had an unrealistic GM (metacentric height). Therefore, a new rig was constructed to better fit the dimensions of the wave flume, and with better control of the center of gravity and moment of inertia. The chosen dimensions for the new model was two hollow hulls of $20 \times 20 \times 59$cm, connected with a 10cm moonpool gap between the two side hulls using two aluminum L-profiles. The model was ballasted with weights strapped tight to the inside of the model, such that the model floated with a 10cm draft. It is referred to Table 4.1 for accurate values of the model test set-up and Figure 4.6 for a picture from the experiments. To gain as high as possible natural period in roll, the weights were placed as far away as possible from the center of gravity inside the hulls. We did this to avoid that the natural period in roll was in the same range as the heave or moonpool piston-mode natural periods. Lines were connected on each side of the hull to restrain the model from drifting. At the end of these lines, springs were connected, such that the model was free to move in sway, heave and roll. Between the hull and the springs each line went through a pulley, such that the springs were connected vertically to the roof,

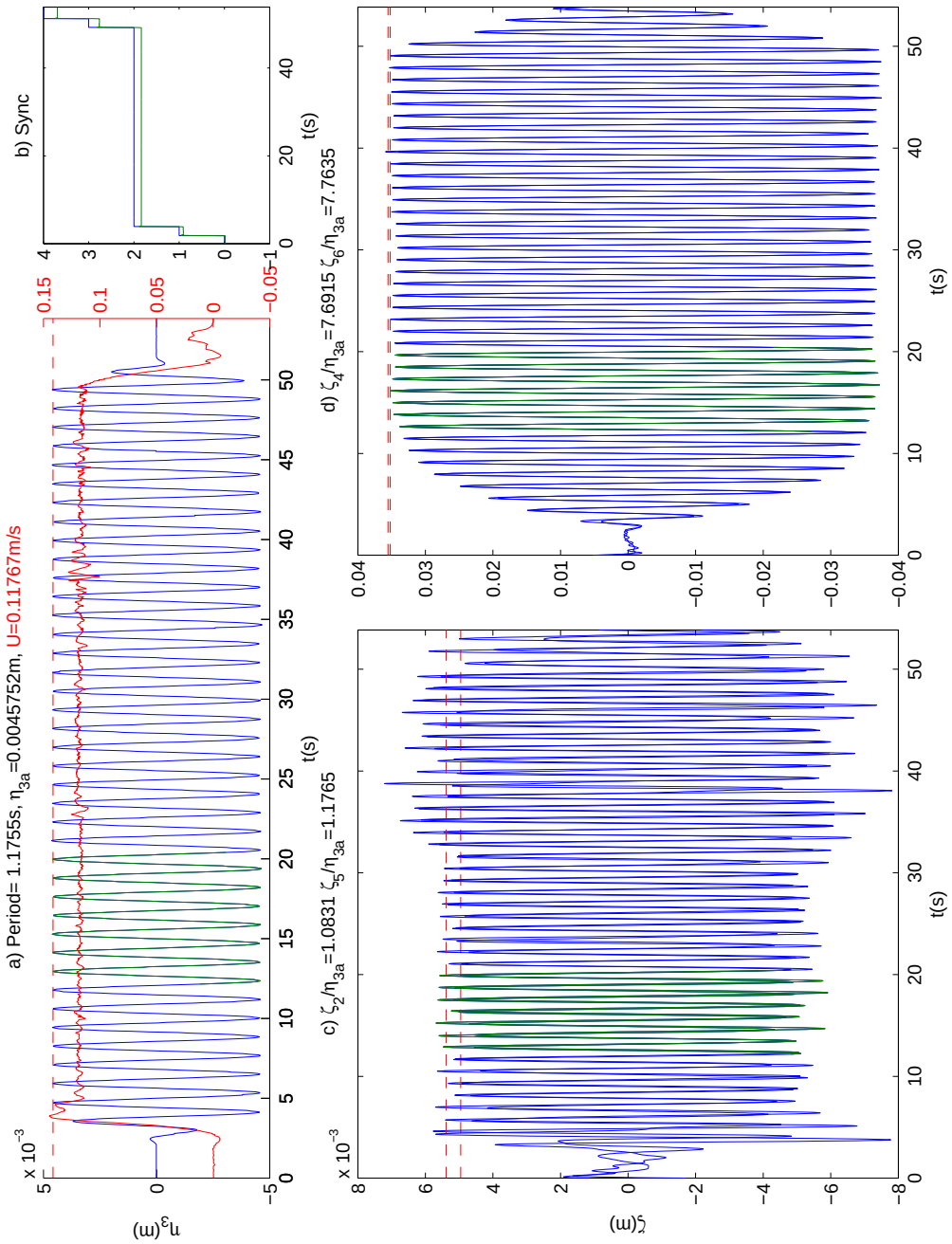

Figure 4.3: Example of recorded experimental time-series data. The red line in a) represents the carriage velocity, with scales given on the right axis in (m/s), the blue line in a) shows the heave position. The two lines in b) represents the synchronization signal between the two recording systems. In c) is the outgoing wave measurements on both sides. In d) is the two measured wave elevations inside the moonpool. Further, the red dotted lines represents the amplitude values extracted from the time-series in green.

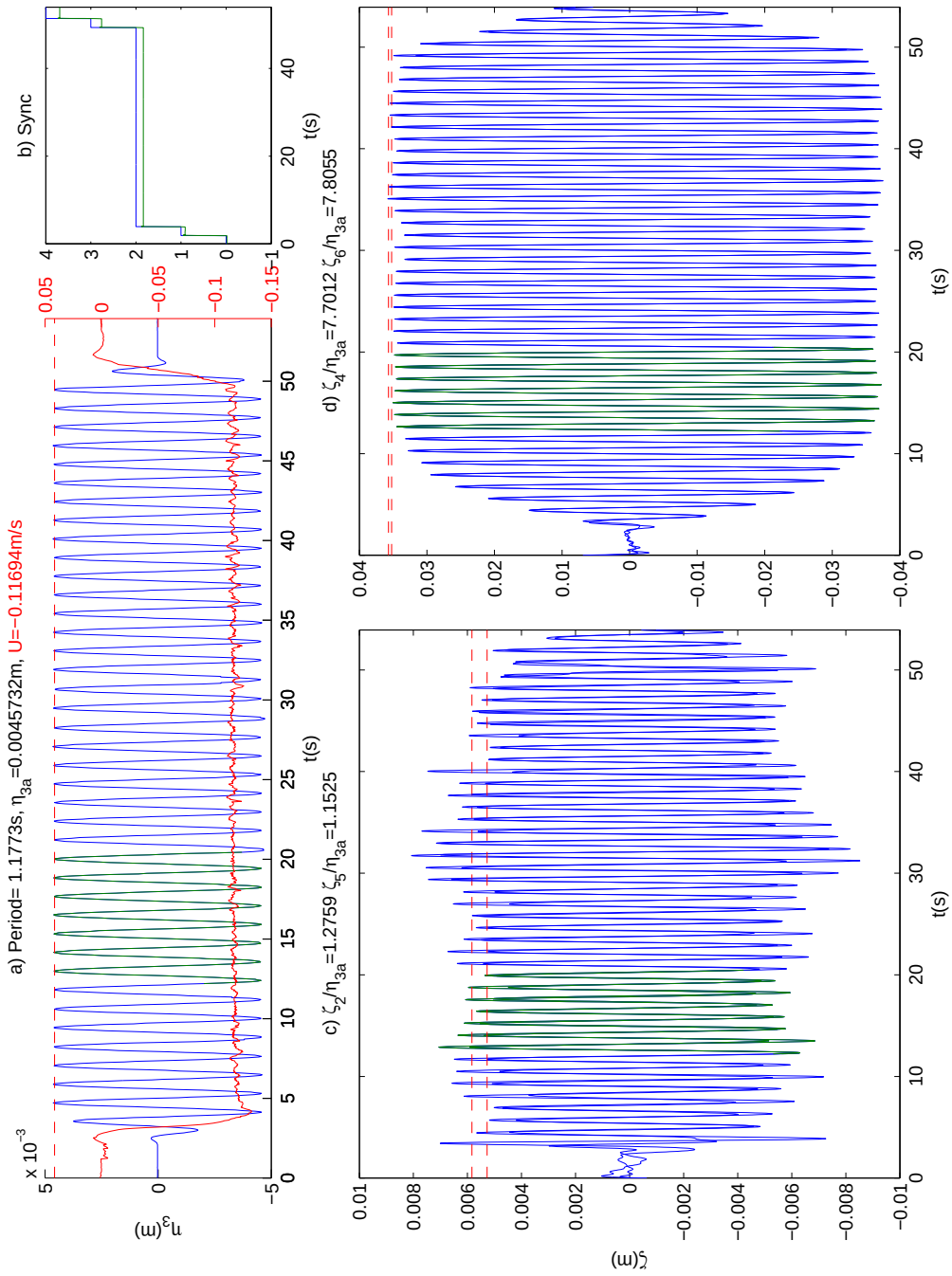

Figure 4.4: Example of recorded experimental time-series data, see Figure 4.3 for description.

see Figure 4.5. The natural period in sway was 3.2s. The springs were not horizontally connected to the model, but had an angle of around 5 degrees, such that some stiffness in heave due to the springs was introduced. This angle also gave a small, but negligible coupling between heave and the other degrees of freedom.

The floating experimental programme was performed for 35 different wave periods and 3 different wave height-to-wave length ratios (wave steepnesses) (1/60, 1/45 and 1/30). The experiments with the highest wave steepness were repeated once. Prior to the experiments a wave calibration series was performed without the model in the wave flume. After the four experimental test-series with a 0.10m moonpool gap were performed, the model was modified to have a 0.08m gap. A new test-series with wave steepness 1/60 were then performed. Neither the radius of gyration r_{xx} nor the center of gravity were experimentally checked for this configuration. It is, however, a reasonable approximation that the radius of gyration is decreased with 0.01m. Since both boxes are moved 0.01cm towards to center, the only thing that does not change location is the aluminum L-profile on top. The mass of the aluminum L-profiles was in total 1282g, that is 5.6% of the total mass of the model. The center of gravity is assumed unchanged.

Since the automatic control system developed for the forced heave oscillation study was not controlling the behaviour of the wavemaker, the period and amplitude of oscillation were manually changed between each individual test. The experimental routines were the following. Each test-series was performed with constant wave steepness and gradually increasing wave period. First the calibration of the wave gauges and copper tapes was done. Then we started the Catman logging system and logged continuously throughout the entire test-series with all the 35 wave periods in one data file. After entering the first wave period and amplitude into the wavemaker control system we could start the wavemaker. The wavemaker was stopped after generating waves for $30 - 35$seconds. While waiting for the waves to die out we entered the new wave period and amplitude into the wavemaker control system. After about 4 minutes the waves had died out and the wavemaker could be started again with a new period and amplitude. The time it took for the waves to decay was longer for shorter period waves, due to that they were almost fully reflected by the model. By following the previous steps, the experiments with all 35 wave periods were performed. At the end, we stored the data file from the Catman data logging system with the proper file-name. The repeated test-series with wave steepness 1/30 were also documented with a video camera.

We did separate tests to ensure that the frictional coefficient in each individual pulley was low enough such that it did not matter for the motion of the model, i.e. such that any hysteresis effect in the mooring system could be considered negligible.

Three acceleration sensors were used to measure position in 3 degrees of freedom. Two of them measured acceleration in body-fixed heave direction. They were placed on opposite sides of the hull. The third measured acceleration in body-fixed sway direction. To find roll acceleration the acceleration from the heave accelerometers were subtracted from each other and divided by the distance between them. The heave acceleration at COG was found by taking the average values from the two heave accelerometers. The body motions were found by first band-pass filtering away frequencies below 0.5 and above 4 times the incoming wave frequency. The band-pass filtered signal was then integrated twice to obtain position. Finally, the sway acceleration at COG was found by correcting the measured sway acceleration with the contribution from roll acceleration and the changing direction of gravity based on the roll position.

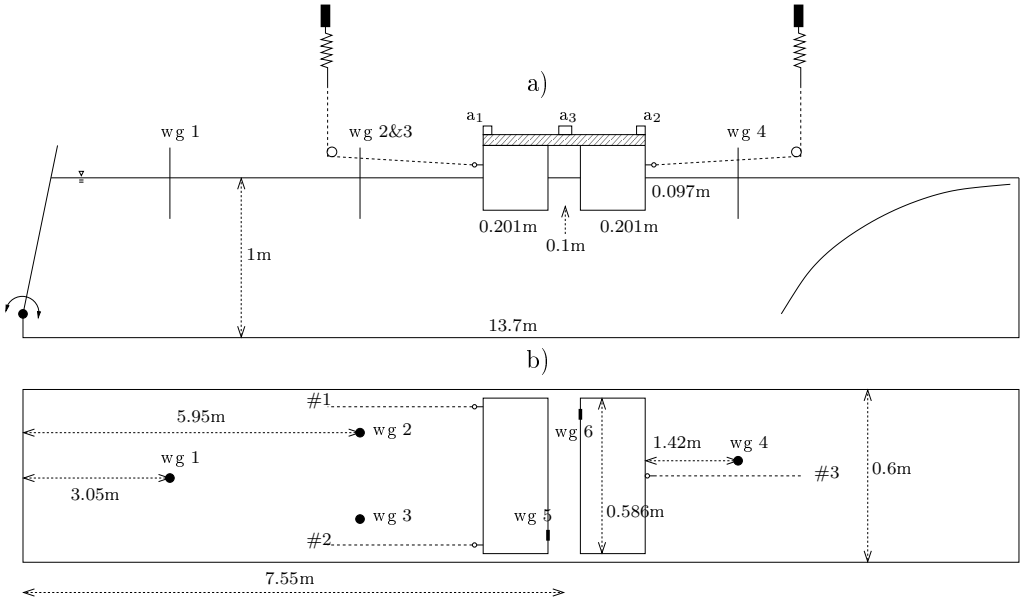

Figure 4.5: Sketch of the floating experimental set-up. a) Side view of the wave flume, b) top-view of the wave flume. Note that the figure is not in scale. Here wg1-6 are the locations of the wave gauges, where wg5 and wg6 are glued to the hull. Furthermore, a_1-a_3 are the locations of the accelerometers.

Model draft d (m)			0.097
Breadth of each side hull B (m)			0.201
Moonpool gap width b (m)			0.10(0.08)
Width in transverse direction (m)			0.586
Mass (kg)			22.885
Radius of gyration r_{xx}(m)			0.18
Center of gravity from the bottom (m)			0.091
Spring constants (N/m)	#1 43.7	#2 42.5	#3 88.2
Pre-tensions (N)	#1 7.5	#2 7.5	#3 15
Line connection height above WL on hull (m)			0.05
Line angle (deg)			~ 3
Length between hull and left pulley (m)			2.1
Length between hull and right pulley (m)			2.0

Table 4.1: Dimensions and properties of the model test set-up used in the floating experimental programme.

Four capacitance wave gauges were used to measure the wave field outside the model. Three wave gauges were placed between the wavemaker and the model. The distance between the first wave gauge and the wavemaker was 3.05m. The second and third wave gauge were placed in parallel 5.95m away from the wavemaker. The midpoint of the model was placed 7.55m away from the wavemaker. The fourth and last wave gauge was placed between the model and the parabolic beach, 1.42m away from the midpoint of the model, see Figure 4.5.

To measure the wave elevation inside the moonpool, copper tape was glued on the inside of each side hull. This allowed us to measure the wave elevation on two locations inside the moonpool gap, one location on each side hull. It was found that using conventional capacitance wave gauges inside the moonpool gap would influence the inertia properties of the model too much, such that copper tape was found to be the best available method to measure the wave elevation inside the moonpool gap. However, there was much more drift in the recorded wave elevation from the copper tape than from the other conventional wave gauges. It is also possible that the meniscus effect is different on conventional wave gauges and the copper tape. There may occur a very thin "run-up" on the hull which is detected by the copper tape. This type of run-up is not described by our theory and is of concern in e.g. sloshing.

The position of the center of gravity and the moment of inertia of the model were determined by Marintek personnel by following standard procedures in commercial testing. They performed free decay tests in air where the model was hinged at two different positions. The oscillation frequency was measured by laser, such that the natural period at the two hinge locations was determined within an accuracy of milliseconds. This was only performed for the model with 10cm moonpool gap.

Figure 4.6: Picture of the floating experimental set-up.

4.2.1 Error sources in the floating experiments

In addition to the usual error sources, such as error in calibration factor and the measurement equipment a few additional error sources are identified. Although the waves were calibrated before the model test started, we did not obtain the required wave steepness. On average the waves were 10% higher than what was expected from the inputs. However, since the incoming wave amplitude is known the results presented herein accounts for this. The degree of non-linearity is then somewhat different from that used in the numerical simulations because of different wave height-to-wave length ratios.

The properties of the waves generated by a hinged type wavemaker are not fully reflected in the numerical simulations. Second and other higher-order effects in the generated waves are not captured in the numerical simulations, which also applies in the nonlinear hybrid method. In both hybrid methods the incoming wave profile is specified by a known linear velocity potential on the free surface and the incoming wall boundary. The difference this represents are thought to be negligible, since only first order motions and how they are affected by the wave steepness are of interest herein.

Friction from the pullies should preferably be modelled as a Coulomb friction, i.e. the friction force is approximated as a friction coefficient times the normal force. This has not been implemented as the friction was found to be negligible from individual tests of each pulley.

The model covers 98% of the width of the wave flume, in total there is a possible ~ 1.5cm gap between the model and the glass. The reality is therefore 3D flow effects at the ends which influence the pressure at the ends. In addition there are viscous shear-forces at the gap between the glass and the model to be accounted for. In accordance with Faltinsen (1990) and Jonsson (1980) laminar flow can be assumed on a smooth surface with oscillating flow if the Reynolds number defined as $Re = U_{\text{lm}}^2/\omega\nu$ is less than 10^5. Here U_{lm} is the maximum tangential velocity just outside the boundary layer, ν and ω are the kinematic viscosity coefficient and circular frequency of oscillation, respectively. It is found that laminar flow can be assumed for all variations of wave period and amplitude that are experimentally tested. The known solution of the Stokes second order problem for laminar flow can be used to approximate the influence of the viscous stress between the model and the water inside the narrow gap between the model and the glass. Solutions to this problem can be found in White (2006) and other textbooks. The oscillating boundary layer thickness is estimated to be at most $\delta_{bl} = 6.5\sqrt{\frac{\nu}{\omega}} \leq 3$mm, which is less than the narrow gap in the model tests. The wet surface area A_g towards the glass is 0.08m^2, and the viscous stress force is at most $F_\tau/U_M = \sqrt{\rho\omega\mu}A_g \leq 0.20$Ns/m. Here U_M is the maximum absolute velocity of the model and μ is the dynamic viscosity of the liquid. This is negligible when comparing this to the forces measured by the force rings in the end of the mooring lines.

The parabolic beach was adjusted before the start of the experimental programme such that the top of the beach was 2-3mm below the free surface. However, the wave flume had a small leakage, and some reflection in the repetition tests was found during data processing. The reason could be that these tests were performed some days after the other tests, and that the water level had decreased 1-2mm. This resulted in more reflections of the longest waves for periods above 1.0s. It is referred to results from the repetition test in section 5.3.7.

The time-derivative of the acceleration signal is a quantity called "jerk", and that

makes it easier to identify spikes in a time-series, see Boore and Bommer (2005). The jerk has the dimensional property m/s^3, and it is convenient to use when trying to identify contact between the walls and the model. It has previously been used by Kristiansen (2010) when analyzing a similar experiment with a floating circular cylinder in the same wave flume. By going through all time-series for the jerk derived from all three accelerometers, it was for some of the periods above 1.2s found that contact between the model and the wall might have happened. Another reason for the high jerk in these time-series could be that the cables going from the model to the measuring system limited the motion.

Asymmetry in the wavemaker and small gaps on each side of the wavemaker in transverse direction generated some transverse waves in the wave flume. Visually the second transverse mode was observed for some of the lower wave periods. The wave period of the second transverse mode is 0.62s. Even though the first transverse mode was not visually observed we should be careful when analyzing the results around this period, which is 0.87s.

Chapter 5

Results

In this chapter the focus is on results from the two experimental programmes presented in chapter 4, and the two numerical hybrid methods presented in chapter 3. Discussions about the physical results and the comparison between the experimental and numerical work will be given. Emphasis is on topics that contribute to the increased physical understanding of the moonpool resonance phenomena for both fixed and floating structures.

The only results that were obtained with the first hybrid methods using FVM in both the viscous and potential flow domain were presented in Fredriksen et al. (2012) and will not be given or discussed any further here. A detailed description on why the HPC method was preferred over the FVM to solve the Laplace equation in the potential flow domain was given in the numerical theory chapter 3.

First results from the two-dimensional experimental programme with forced heave oscillation of a moonpool section with and without forward velocity are presented and compared against the semi-nonlinear and nonlinear numerical hybrid methods. The focus is here put on the wave field including the piston-mode amplitude behaviour due to forced oscillations, and not on the hydrodynamic forces on the moonpool section. The experimental programme setup was described in 4.1.

Secondly, results from an experimental and numerical study of a two-dimensional freely floating moonpool section in incoming regular waves are presented and results are discussed. The experimental programme setup was described in chapter 4.2. Based on the validity gained by comparing the experimental and numerical results, additional numerical results with appendages and with low forward velocity are presented.

At the end we will come back to forced oscillations, but with a focus on local pressure and water flow details from the two hybrid methods. This is to help in the understanding and explanation of the difference in results obtained by the semi-nonlinear and the nonlinear hybrid method as well as to understand which physical effects that are needed to model numerically to fully describe the problem considered.

The results will as long as appropriate be presented in a dimensionless manner, based on Froude scaling and geometric similarity. This is done for convenience since the physical dimensions in the two experimental setups were different, and it is then easier to do comparison between the results from the experimental programmes. The moonpool width b is chosen as the main length parameter in scaling the results. This means that the dimensionless oscillation period will become $T^* = T\sqrt{g/b}$, the dimensionless water depth $h^* = h/b$, the dimensionless draft $d^* = d/b$ and the dimensionless forcing heave amplitude $\eta_{3a}^* = \eta_{3a}/b$. The dimensionless oscillation period T^* will be used for both the dimensionless

wave period and the dimensionaless forced oscillation period. An exception is the Froude number which is dimensionless using the total width of the structure, and the incoming wave height is dimensionless by the wave length to obtain the wave steepness. One should note that the only dimensionless parameter that is different between the two experimental programmes and possibly important for the results was the dimensionless water depth. The differences this causes are investigated in section 5.3.10, where the added mass and potential-flow damping in heave and roll for the two experimental setups are numerically simulated and compared. The dimensionless wave flume lengths are also different, but the influence is thought to be negligible, as long as the wave flume is long enough to obtain steady-state conditions. This matters in the floating experimental set-up due the fact that reflections from the wavemaker cannot be damped out. The reason is that the control system for the wavemaker does not include software to absorb reflected waves. Another secondary influence from the difference in dimensionless wave flume length is the possible influence of the seiching mode of the tank, which will occur at different dimensionless periods between the two setups. The latter factor will also apply to any influence from the transverse sloshing modes of the wave flume.

5.1 Forced heave oscillation with low forward velocity

During the development phase of the numerical code, the first milestone was to do forced heave oscillations without forward velocity with the semi-nonlinear and nonlinear hybrid methods, and validate it against experiments performed by Kristiansen and Faltinsen (2012) and the experiments described in section 4.1. Before this, separate parts of the code were validated against selected cases from the literature. The viscous FVM part was checked against lid-driven cavity flow problem presented by Ghia et al. (1982). Furthermore, similar validation studies as in Berthelsen and Faltinsen (2008) were performed for a square with sharp edges in oscillating flow in infinite fluid, where both the added mass and drag coefficients were checked.

The complete numerical hybrid methods were not validated against anything prior to the studies presented here. However, good results based on a similar code by Kristiansen and Faltinsen (2012) have previously been achieved.

As an introduction to the rest of the chapter, some idealized considerations of the vortex shedding in the moonpool of the forced oscillation set-up will be discussed. For the forced heave oscillation case without forward velocity the problem can be considered as symmetric about the mid-line of the moonpool gap, as long as the excitation amplitude is sufficiently small to avoid asymmetry in the shed vorticity pattern due to instabilities in the flow. However, the problem is asymmetric with a low forward velocity of the hull. A few questions and assumptions then arise, with the strength of the shed vorticity being a function of the local fluid velocity at any sharp edge. Let us for the moment assume that the shed vorticity is concentrated in thin free shear layers without diffusion. Furthermore, we discuss the free-shear layer separating from one corner and define the time rate of change of circulation $\partial\Gamma/\partial t = \pm 0.5U_s^2$, see Faltinsen (2005). Γ is the circulation around a closed curve C in the liquid domain that encloses the shed vorticity and is equal to the integrated vorticity inside C. Furthermore, U_s is the separation velocity just outside of the boundary layer, at the corner. The latter consideration assumes a thin boundary layer. The low forward velocity of the body will influence the local velocity at the edges of

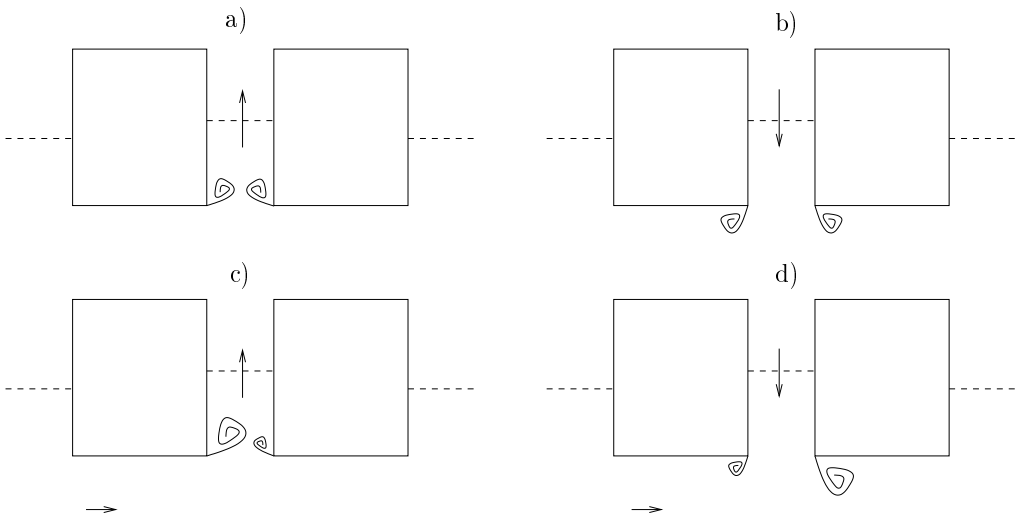

Figure 5.1: Symmetric vorticity shedding for zero forward velocity case in a) and b). Asymmetric vorticity shedding for the low forward velocity case in case c) and d).

the moonpool. At the beginning of the oscillation cycle, when the wave amplitude inside the moonpool is increasing, the velocity introduced by the piston-mode oscillation will on the leading edge have the same direction as the undisturbed incoming velocity. Due to the higher local velocity we will expect that more vorticity is being shed from this edge. The opposite will happen on the trailing edge of the moonpool entrance. Here the local induced flow from the increasing piston-mode amplitude will have opposite flow direction as the undisturbed incoming velocity, and weaker vorticity is generated from this edge, see Figure 5.1 c). Half a period later in the oscillation cycle the situation is turned around. The piston-mode amplitude is now decreasing and the vorticity shed from the leading edge is now lower than that shed from the trailing edge, see Figure 5.1 d). Due to the mentioned effects, how will the viscous damping of the piston-mode amplitude change due to low forward velocity or incoming current? The above discussion will be dependent on the ratio between the forward velocity and the local liquid velocity due to the moonpool behaviour. In the above discussion we have neglected the effect of vorticity shed from the leading edge of the hull. This vorticity will influence the local flow around the entrance of the moonpool gap. The assumptions about the magnitude of vorticity above might not be correct, with a sharp leading corner.

Some of the results in this section have previously been published in Fredriksen et al. (2014).

5.1.1 Parameter variation

In order to put the results from the extensive experimental programme into system, the following tables present the first section of the parameter study performed in the experimental program. Here the combination of three different drafts, 3 different forward velocities, 3 different heave forcing amplitudes, 3 different appendage profiles (see Figure

5.2) and a suitable number of oscillation periods for each case (see Table 5.1 for a overview on the different parameters tested in Figures 5.3-5.11). Table 5.2 gives an overview on how each of the Figures 5.3-5.11 are subdivided into 9 different sub-figures.

Edge profile / d^*	Sharp corner	Appendage #1	Appendage #2
0.833	Fig. 5.3	Fig. 5.6	Fig. 5.9
1.0	Fig. 5.4	Fig. 5.7	Fig. 5.10
1.167	Fig. 5.5	Fig. 5.8	Fig. 5.11

Table 5.1: Overview of figure numbers where results from the given combination of edge profile and draft are given. Appendage #1 has dimensions 18mm width by 9mm height and appendage #2 has dimensions 27mm width by 18mm height. The appendage #1 cover 20% of the moonpool gap, while appendage #2 cover 30% of the moonpool gap, see Figure 5.2. The moonpool gap width b are for all cases 0.18m.

Fn / η^*_{3a}	0.00	0.04	0.08
0.0128	a	b	c
0.0250	d	e	f
0.0506	g	h	i

Table 5.2: Overview of how the velocity and heave amplitude variation in Figures 5.3-5.11 are organized. The letters a-i refer to different parts in the figures.

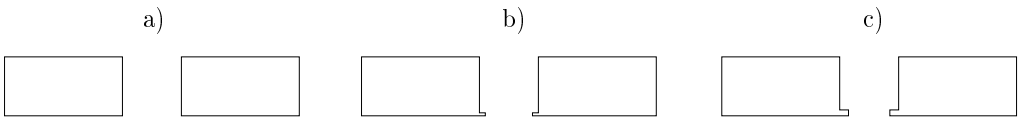

Figure 5.2: Overview of appendage edge geometries that were tested. a) sharp edge profile, b) appendage profile #1 where each appendage dimensions were 18mm width by 9mm height and c) appendage profile #2 where each appendage dimensions were 27mm width by 18mm height. The moonpool gap width b are for all cases 0.18m.

5.1.2 Numerical setup

The meshes for the numerical hybrid method for the forced oscillation simulations are constructed as follows: Note that the discussion here are based on values with real dimensions and are valid only for the forced heave oscillation with and without forward velocity study. For all simulations the horizontal cell size around the hull was 0.01m, which means that there were 36 cells in the horizontal direction over each hull and 18 cells across the moonpool. This mesh size extends 1.2 hull lengths or 0.3 wave lengths away from the hull depending on what is shortest in upstream direction. In the downstream direction

of the hull, the mesh size is constant for 1.5 hull lengths or 0.42 wave lengths away from the hull also depending on what is shortest. Outside this area the mesh size gradually increases to 30 cells for each wave length. In the damping zone the mesh size increases even further. Note that the horizontal mesh size is then constant in the vertical column, as we are limited to rectangular cells. The wave length considered here is without current effects, but with the effect of water depth.

In the vertical direction the mesh used depends on the draft and the expected piston-mode amplitude to occur during the simulation. Generally the vertical mesh size is 30% smaller than the horizontal mesh size around the hull. The mesh is kept constant until 0.5 times the draft below the bottom of the hull, then gradually increasing until the bottom of the tank, with a total number of 60 cells in vertical direction. Also here the vertical mesh size is kept constant for each horizontal row. A problem in using an easy mesh generation method as this, is that the aspect ratio of the cells far away from the body (vertically or horizontally) becomes high (or low). In addition it should be noted that the mesh resolution does not aim at capturing the behaviour of the water flow inside the boundary layers attached to the hull.

The numerical beach zone starts, at both sides, four wave lengths (without current) away from the body and increases smoothly over one wave length to its maximum value (0.8), and is kept at this value for another three wave lengths before the end of the tank. The total length of the numerical domain is 16 wave lengths in addition to the length of both hulls including the moonpool.

The time-step size Δt is chosen to be the lowest of 0.5 times the Courant–Friedrichs–Lewy (CFL) number ($\Delta t = 0.5\delta y/v$ or $\Delta t = 0.5\delta z/w$) or 120 time-steps per oscillation period $\Delta t = T/120$.

The height of the potential flow domain in the nonlinear hybrid method inside the moonpool is for all drafts and appendages set to be 0.03m for 2.3mm heave amplitude, 0.06m for 4.5mm heave amplitude and 0.075m for 9.1mm heave amplitude. These values are based on what is observed from the experiments presented in chapter 4.1, and included a safety margin to allow over-prediction of the moonpool amplitude in the numerical simulation.

The wave profile in the moonpool gap should be almost horizontal when the sloshing modes are not present. The sloshing modes will be excited by transient effects in the start-up. These transient sloshing modes are damped out by a numerically added artificial damping around the space average value of the wave profile inside the moonpool gap each time-step. This is done in a similarly way as for the damping applied in the numerical beach. Physically the only damping source of the sloshing modes is through the boundary layers on the glass walls and on the side hulls. The damping ratio ξ on the first sloshing mode for the forced oscillation experimental setup for the boundary layer flow is found from Faltinsen and Timokha (2009) to be $\xi = 0.0014$. It is believed that the artificial damping added in the numerical method inside the moonpool gap is larger than what will be in reality due to boundary layer damping.

The mesh is changed inside the moonpool gap when the appendages are considered. There are 2 cells over both the length and height of the appendage for the small appendage profile (#1). For the large appendage profile (#2) there is 3 cells in horizontal direction and 4 cells in the vertical direction across the appendage. The remaining part of the mesh is equal to the sharp-edge case.

In the cases with zero forward velocity, the intersection between the potential and

viscous flow domains are ordered in a staircase pattern on both sides of the hull. However, with forward speed we need to allow for vorticity transport away from the hull in the down-stream direction. Therefore the staircase pattern on the down-stream side of the hull is replaced with a horizontal intersection stretching all the way down to the end of the numerical wave tank.

5.1.3 Numerical limitations in the nonlinear hybrid method

For higher heave amplitudes η_{3a}^*, the ratio between the piston-mode amplitude and the draft increases. This requires a larger potential flow domain due to re-meshing strategy of the potential flow domain close to the free surface. This means that, while the amount of vorticity increases, we have to decrease the viscous domain inside the gap. The consequence is increased probability that vorticity will reach the numerical intersection between the viscous and the potential flow domain. Therefore, our numerical method is limited to free shear layers that stay below the level of the wave trough in the body-fixed coordinate system. (See results from the sensitivity tests of the height of the potential domain inside the moonpool in Figure 6.3.)

The following discussion is used to justify that vorticity is likely to be transported to the intersection. The vorticity separated from the trailing edge on the downstream side will grow with increasing current velocities, up to a point where the flow separation will cause a "dry transom stern". By "dry transom stern" the analogy is made to what happens for high-speed semi-displacement and planing vessels. However, the dry flow separation case is not relevant here, as it will happen for much higher Froude numbers than what we consider (Fn $> 0.3 - 0.4$ Faltinsen (2005)). However, for velocities lower than for dry separation the vorticity will reach the numerical intersection between the potential flow and viscous flow domains, and later the vorticity will in the experiments reach the free surface. This is the reason for not being able to simulate with much larger forward velocity than Fn$= 0.08$ in the nonlinear hybrid method.

5.1.4 Results from forced oscillations

First a comprehensive comparisons between the two numerical hybrid methods and the experimental results for the parameter variations presented in Tables 5.1 and 5.2 will be given. Note that there is not experimental results for all variations given in Tables 5.1 and 5.2, however, the numerical hybrid method results are given for all parameter combinations. There are only semi-nonlinear hybrid method results for the cases without forward velocity.

A first check of the quality of the experimental and numerical results is to compare the natural period of the piston-mode resonance with results given in the literature.

Faltinsen et al. (2007) provided accurate calculations of the natural periods for the piston-mode resonance, based on non-separated potential flow without current for case a) without appendages. Based on their results the natural period for the 3 different drafts are $T_{15} = 1.125$s, $T_{18} = 1.179$s and $T_{21} = 1.233$s. The observed natural periods from experiments for forced heave motion without forward velocity were $T_{15} = 1.13$s, $T_{18} = 1.18$s and $T_{21} = 1.23$s, and thus corresponds well to the results from Faltinsen et al. (2007), see corresponding dimensionless values in Table 5.3. The natural periosd are from the experimental programme taken where the maximum moonpool response

occur. Other approximate formulas for estimating the piston-mode natural period exist, a practical and useful theory for approximating the natural frequency of the piston-mode for zero current is given by Molin (2001),

$$\omega_0 = \sqrt{\frac{g}{d}\frac{1}{1+\frac{b}{\pi d}\left(\frac{3}{2}+\ln\frac{B_T}{2b}\right)}} \tag{5.1}$$

where B_T is the total breadth of the body. It has many times been observed that the actual length of B_T should be taken somewhat larger that the total breath of the body Maisondieu et al. (2001).

Source / d^*	Faltinsen et al. (2007)	Molin (2001)	Experiments
0.833	8.31	7.95	8.34
1.0	8.70	8.36	8.71
1.167	9.10	8.74	9.08

Table 5.3: Comparison of dimensionless natural periods T^* between literature results and experimental results.

The natural periods were found not to change much when introducing low forward velocity to the problem; it might have decreased a few percent when comparing the zero Froude number cases with the 0.08 Froude number cases.

The asymptotic value when T $\rightarrow$ 0s for the outgoing wave amplitude should approach 0, that corresponds to 1 in the body-fixed results in Figures 5.3-5.11. This is due that the high-frequency free-surface condition can be approximated as $\varphi = 0$, which does not allow for wave solutions. The convergence of the results towards the asymptotic values are not clear from Figures 5.3-5.11, since the dimensionless periods given are far from the asymptotic values. Inside the moonpool the asymptotic value when T $\rightarrow$ 0s can be different from zero, due to that $\varphi = 0$ allows vertical motion of the free surface.

As a first estimate on the influence of turbulent diffusion in our problem, we simulated with our nonlinear hybrid method cases where we increased the dynamic viscosity ν from 10^{-6}kg/(ms) to 10^{-4}kg/(ms) in the fluid. We increased ν to simulate that there exists turbulent diffusion due to eddy viscosity at scales smaller than what we capture with our mesh density. An increase in ν will result in an increase in the boundary layer thickness, that will increase the damping of the piston-mode motion. For $\nu = 10^{-6}$kg/(ms) we have seen that the damping contribution from the boundary layer is small, this may not be the case with $\nu = 10^{-4}$kg/(ms). For the lowest heave amplitude ($\eta^*_{3a} = 0.0128$) we see a decrease in the piston-mode motion, around 10% at resonance. However, for the highest heave amplitude ($\eta^*_{3a} = 0.0506$) the piston-mode response is not much affected by increasing the dynamic viscosity. This could be a result of that we for some areas in the water have a turbulent mixing of vorticity, and thus a higher diffusion/cancellation of vorticity which would lead to a smaller damping of the moonpool piston-mode resonance. One should remember that free vorticity is turbulent at very low Reynolds number (see chapter 6 in Faltinsen and Timokha (2009)).

5.1.5 Effect of changing draft on moonpool amplitude

The vertical position of the body was easily changeable in the experimental setup. This allowed for easy testing of three different draft configurations as described in Table 5.1.

The effect of changing the draft is in practice negligible for the maximum value of the piston-mode amplitude, as seen by comparing Figures 5.3-5.5 for the case a) with sharp edge profile, Figures 5.6-5.8 for case b) with small appendages and Figures 5.9-5.11 for case c) with large appendages. A simplistic view on this is that the heave motion displaces a certain amount of water which is proportional to the beam of the section. During resonance a large part of that water goes into the moonpool. How large the piston-mode amplitude becomes is then dependent on the ratio between the width of the moonpool and the length of the two side hulls, and not much affected by the draft. I.e. the ratio between the volume of the moonpool and the displacement of the hull remains constant and is independent of the draft. The situation may be different if the hull sides are no longer vertical, and the ratio between the moonpool volume and the displacement of the hull changes for different draft configurations.

The draft changes the piston-mode natural period, such that for a given period the moonpool response is changed. For deeper drafts the natural period of the piston-mode motion increases. Meaning that the piston-mode motion could be either higher or lower when changing the draft for a given oscillation period.

For the numerical simulation using the semi-nonlinear and nonlinear hybrid methods, it is numerical beneficial with larger drafts. As the intersection between the potential and viscous flow domains will be further away from the edges of the hull, and there is lower probability that the vorticity will reach the intersection. For the setups simulated in this section, it is not experienced any vorticity at the intersection for the cases without forward speed. However, for the cases with low forward speed, the sensitivity study showed that the moonpool amplitude is sensitive to the location of the intersection between viscous and potential flow. (See the convergence and sensitivity study in section 6.2.)

5.1.6 Effect of appendages at the moonpool inlet

Only simple appendage geometries that are possible to simulate with the hybrid methods were experimentally tested. This allowed only rectangular shapes as illustrated in Figure 5.2 to be tested. It was not the ambition of this study to find the optimal solution of the moonpool edge geometry to damp out the moonpool motion, or any other moonpool damping devices.

There is a major increase in the damping of the moonpool motion when comparing sharp edges to appendages, this is accordance with Graham (1980) who found that the strength of shed vorticity decreases with increasing interior apex angle. However, there is not much difference between the two different appendages configurations that were tested. The appendages have two effects, it is from the experiments seen that they increase the natural period. From the case without appendages to the case with large appendages (#2) the natural period is increased by 3%. The second effect is the increase in the strength of shed vorticity, as more water is being pushed through a more narrow entrance, and the fluid velocity at the edge is larger.

The numerical results for appendage configuration #1 compare better with experiments than the numerical results for appendage configuration #2 (see Figures 5.6-5.11).

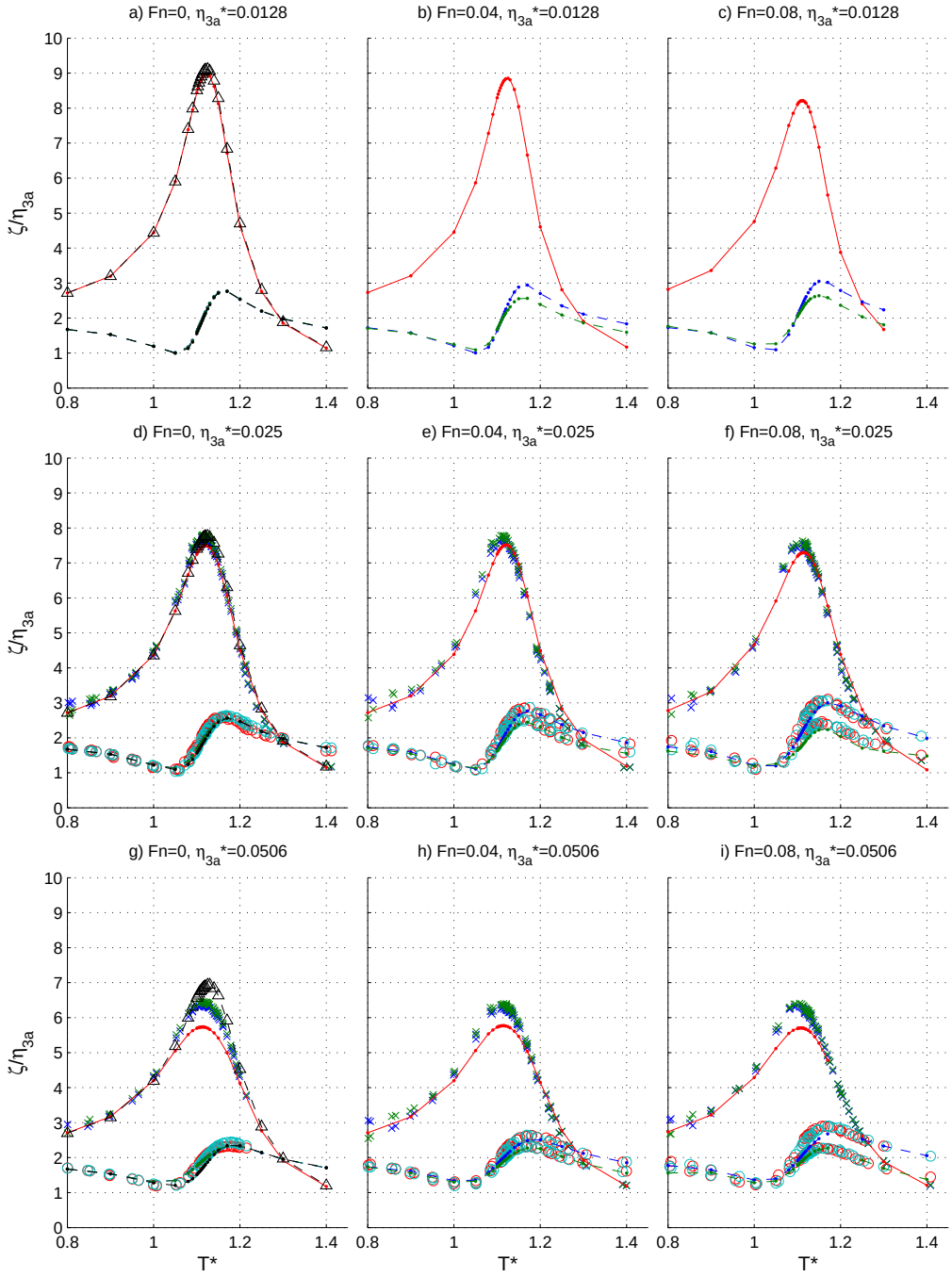

Figure 5.3: Moonpool gap and outgoing wave amplitude operators for different forcing amplitudes η_{3a} and Froude numbers for the set-up with rectangular side hulls (without appendage) with $d^* = 0.833$. See caption in figure 5.4 for description of symbols.

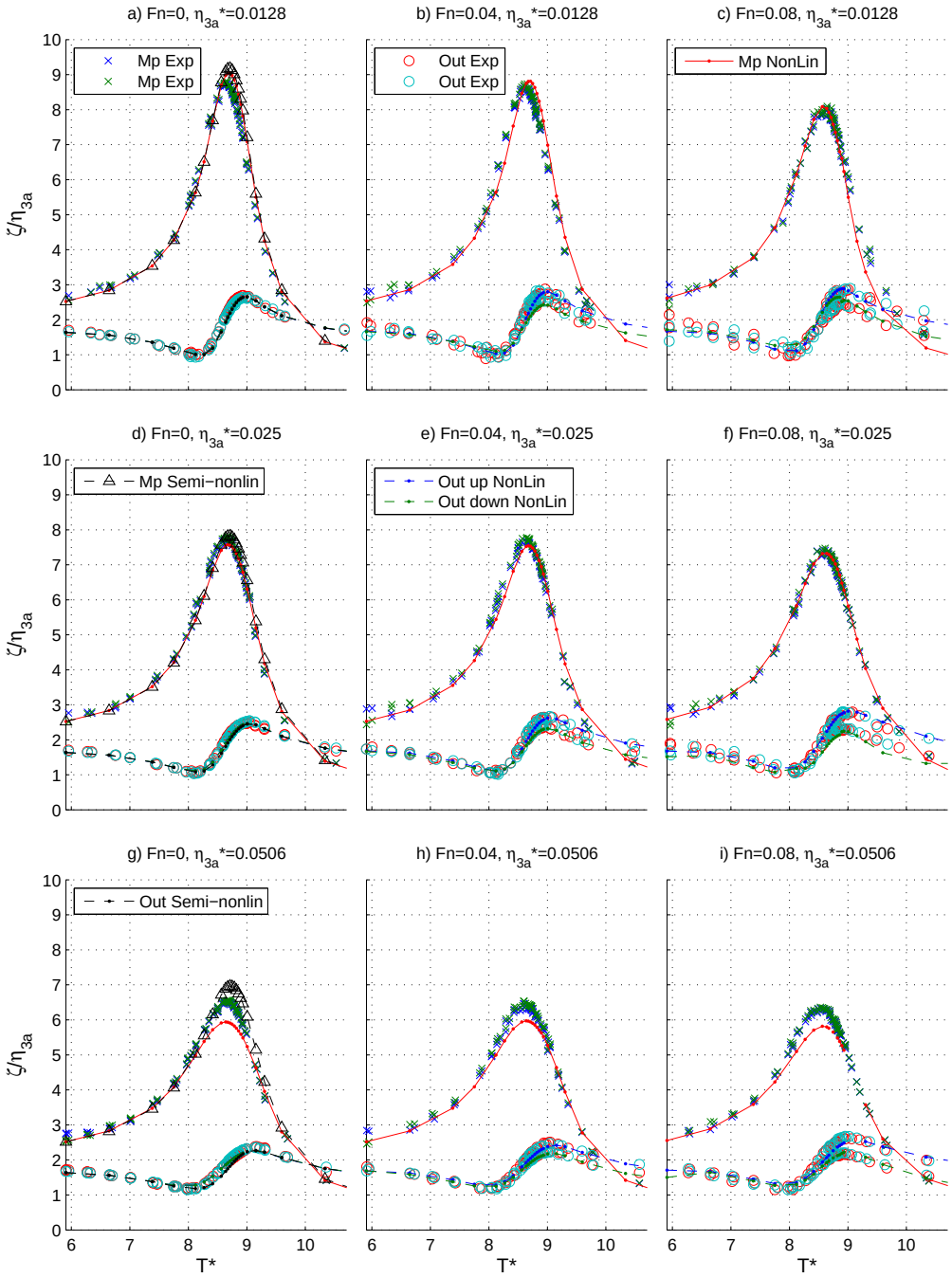

Figure 5.4: Moonpool gap and outgoing wave amplitude operators for different forcing amplitudes η_{3a} and Froude numbers for the set-up with rectangular side hulls (without appendage) with $d^* = 1.0$. Experimental (Exp) results for dimensionless moonpool gap amplitudes (Mp) in x and x, dimensionless outgoing waves in o and o. Nonlinear numerical results for moonpool gap amplitude in dotted(.) line, upstream waves (Out up) in dashed dotted(.) line , downstream waves (Out down) in dashed dotted(.) line. Semi-nonlinear numerical results for moonpool gap amplitude in dashed line with △ and outgoing waves in dashed dotted(.) line. Results are given in the body-fixed coordinate system.

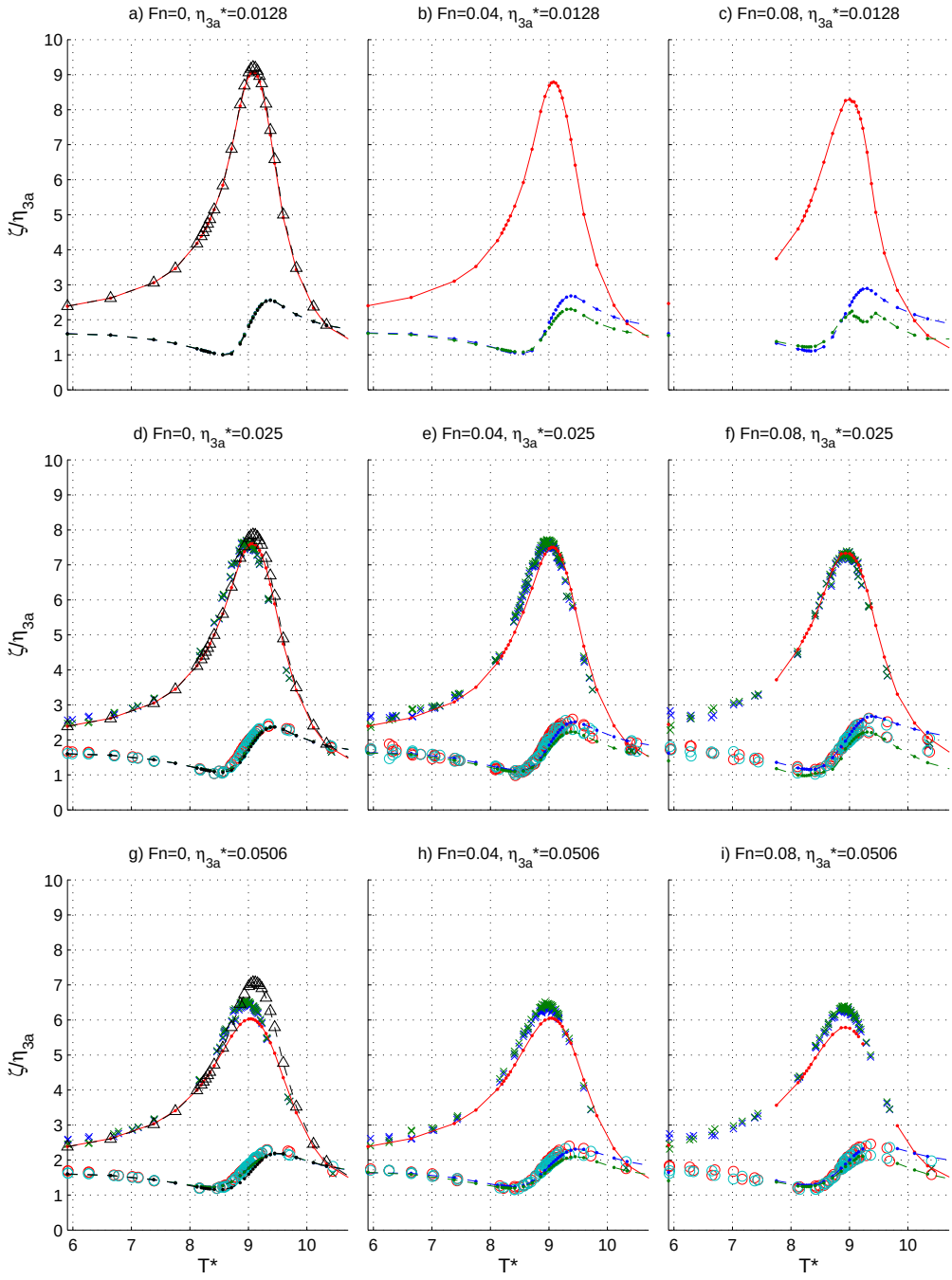

Figure 5.5: Moonpool gap and outgoing wave amplitude operators for different forcing amplitudes η_{3a} and Froude numbers for the set-up with rectangular side hulls (without appendage) with $d^* = 1.167$. See caption in figure 5.4 for description of symbols.

Here the two numerical hybrid methods results and experimental results differ in both amplitude and the predicted period of maximum response. The mesh is almost identical for the two cases and the intersection is at the same location, so there must be some physical effect our numerical method does not capture. The same physical effect should be almost negligible in the setups with sharp edges and appendages #1, and have a small effect on the flow field with appendages #2. The following explanation is proposed, without further studies. For appendage configuration #2 the edges are closer to each other than they are for appendage #1, such that the vorticity created at one edge is more likely to influence the vorticity created at the other edge. Meaning that there could be turbulent mixing of vorticity in the experiments for the largest appendage that is not well captured by our numerical viscous method. Further studies by using a viscous model that include the effect of turbulence is needed to fully answer this question.

The appendages also have a decreasing effect in linear potential-flow theory on the piston-mode moonpool amplitude. There is a 13% decrease in the maximum piston-mode moonpool amplitude when going from the sharp edge case to appendage #1 in linear potential flow theory results, see Figure 5.17. In the experimental programme the same reduction was around 40%. Also the potential flow theory results show large differences between the two appendages profiles.

The dimensionless natural periods of the piston-mode oscillation from the experimental programme are given in Table 5.4 and from the nonlinear hybrid method in Table 5.5. The natural periods are taken when the piston-mode response has a maximum from the experimental test-series without forward velocity and forced heave amplitude $\eta^*_{3a} = 0.025$.

Edge profile / d^*	Sharp corner	Appendage #1	Appendage #2
0.833	8.34	8.4	8.6
1.0	8.71	8.8	8.9
1.167	9.08	9.1	9.3

Table 5.4: Measured dimensionless natural periods for the different moonpool sections from experimental results.

Edge profile / d^*	Sharp corner	Appendage #1	Appendage #2
0.833	8.26	8.49	8.70
1.0	8.68	8.88	9.08
1.167	9.08	9.26	9.45

Table 5.5: Dimensionless natural periods for the different moonpool sections from the nonlinear hybrid method results.

In "Recommended Practice DNV-RP-H103 Modelling and Analysis of Marine Operations" a formula for engineering use that estimates the natural period T_0 of the moonpool

piston-mode resonance with changing moonpool gap cross-section is given as follows

$$T_0 = \frac{2\pi}{\sqrt{g}} \sqrt{\int_{-D}^{0} \frac{A(0)}{A(z)} dz + \frac{A(0)}{A(-D)} \cdot \kappa \sqrt{A(-D)}}, \tag{5.2}$$

where κ is a coefficient to account for the added mass of the vertical oscillation of the water column inside the moonpool, and is found to be between 0.45 and 0.47 for rectangular sections. Further, $A(z)$ is the cross-sectional area of the moonpool for a given depth z. The estimated dimensionless natural periods based on equation 5.2 are given in Table 5.6. Here the value of κ is chosen to be 0.46. These values are above what are given in Table 5.4, but equation (5.2) still serves as a good first estimate on the piston-mode natural period due to appendages. The relative difference for the difference in the natural periods between the sharp edge case and the cases with appendages are similar to what is seen in Table 5.4.

Edge profile / d^*	Sharp corner	Appendage #1	Appendage #2
0.833	8.70	9.01	9.26
1.0	9.07	9.37	9.61
1.167	9.53	9.72	9.95

Table 5.6: Predicted dimensionless natural periods for the different moonpool sections based on equation (5.2).

5.1.7 Effect of low forward velocity on the moonpool amplitude

In this section a review of the results with regards to the difference in the moonpool motion due to low forward velocity will be given. By taking Figure 5.4 as an example the low forward carriage velocity has a minor damping effect on the piston-mode amplitude. A decrease in the piston-mode amplitude of $5-7\%$ from Fn$=0.0$ to Fn$=0.08$ is observed, while for other appendage/draft configurations no change/decrease is observed.

We can in Figure 5.12 see how the moonpool amplitude is changing with respect to the carriage velocity for two different forcing heave amplitudes. Note the uncertainty increases for higher Froude numbers, due to the short physical length of the wave flume, meaning that a steady-state condition may not have been reached. Unfortunately the desired oscillation period of 1.18s ($T^* = 8.711$) was not reached by the control system, but on average the oscillation period was 1.19s ($T^* = 8.785$), with a small variation of the oscillation period between the tests. A linear fit of the results are performed and shown in Figure 5.12. It results in the following the two equations for the maximum moonpool amplitude as function of Froude number,

$$\frac{\zeta_{gap}}{\eta_{3a}} = 7.5814 - 4.7372\text{Fn} \tag{5.3}$$

for $\eta^*_{3a} = 0.0250$ and,

$$\frac{\zeta_{gap}}{\eta_{3a}} = 6.1950 - 1.5210\text{Fn} \tag{5.4}$$

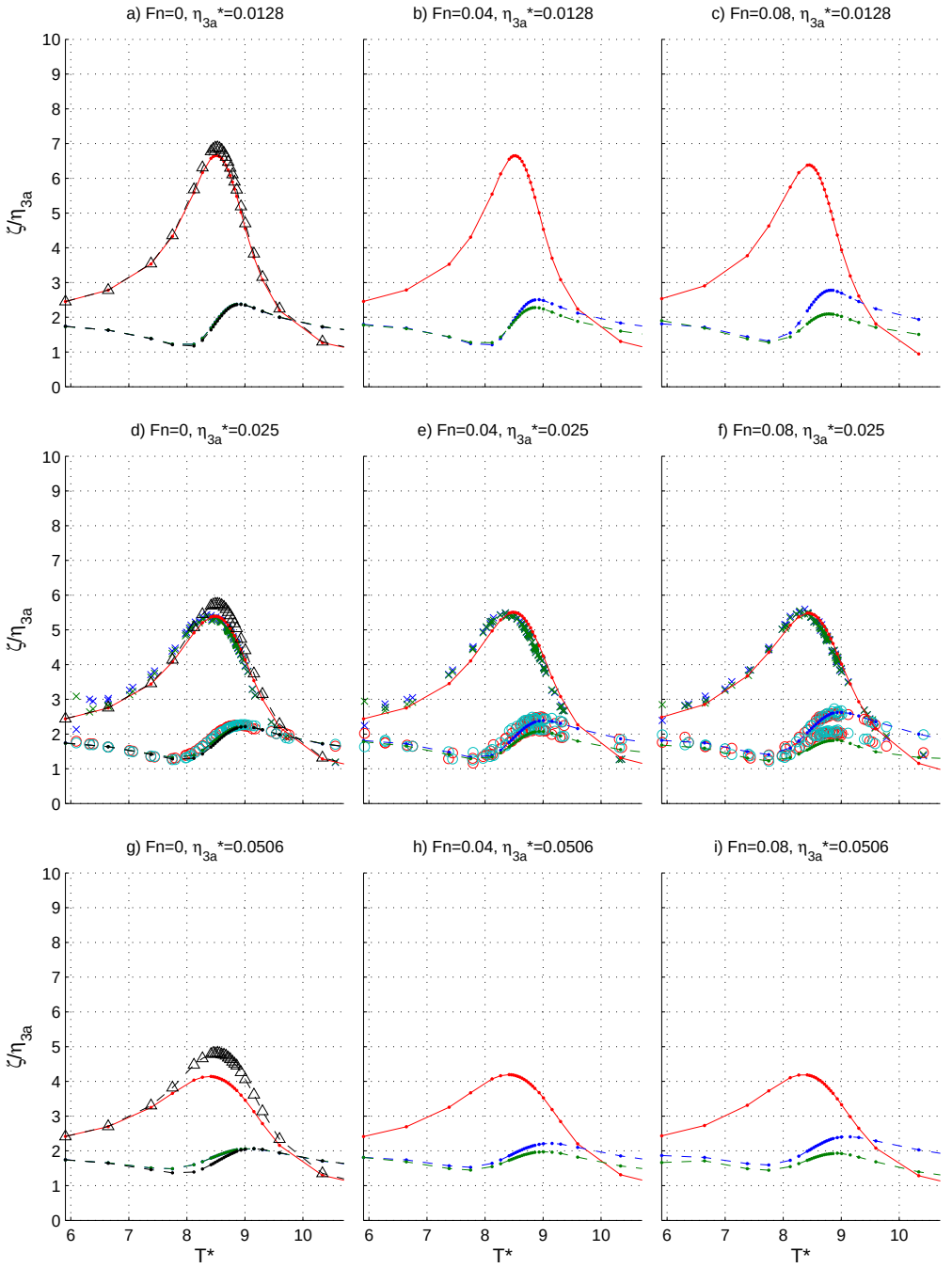

Figure 5.6: Moonpool gap and outgoing wave amplitude operators for different forcing amplitudes η_{3a} and Froude numbers for the set-up with appendage #1 (18x9mm) with $d^* = 0.833$. See caption in figure 5.4 for description of symbols.

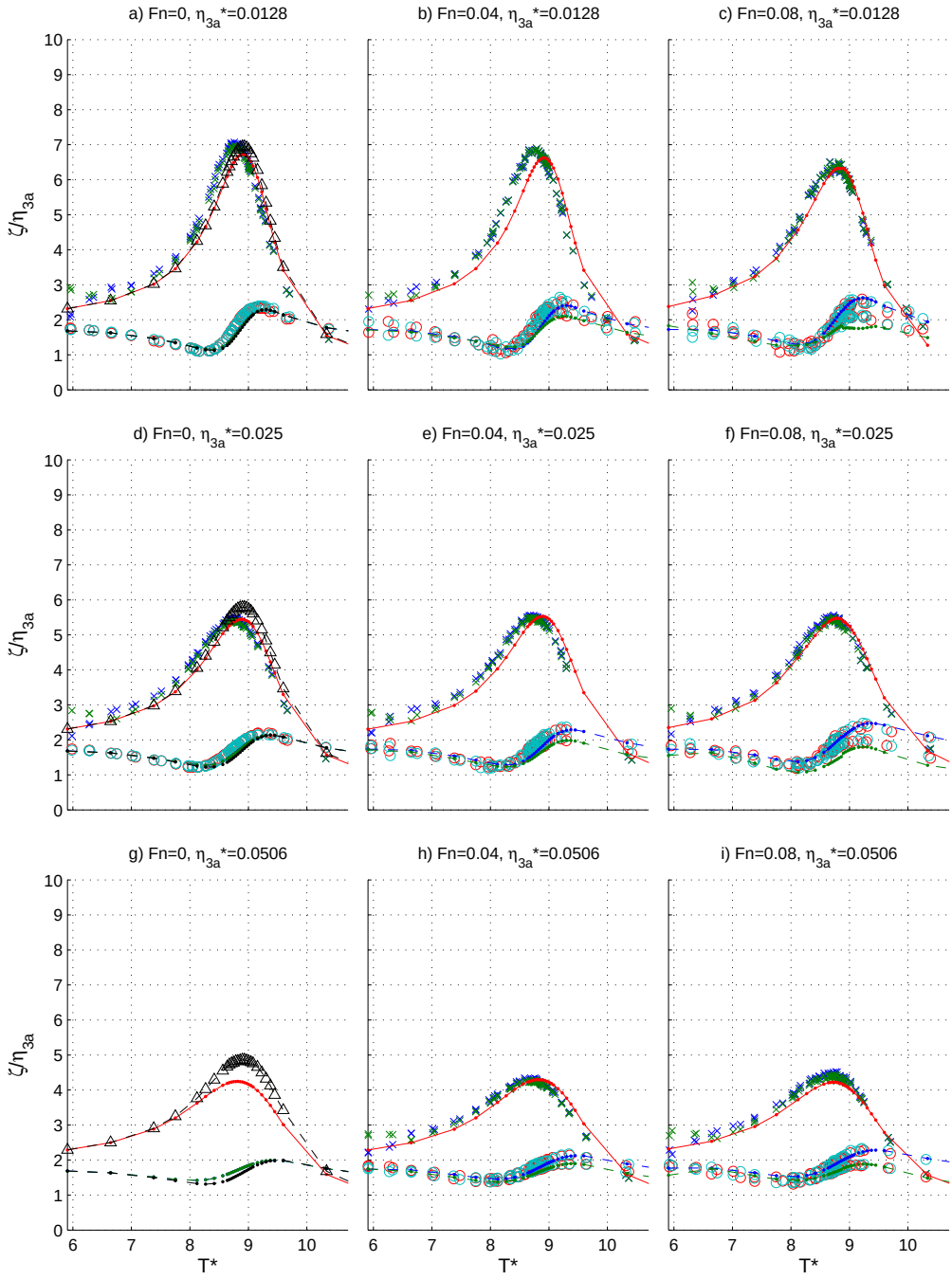

Figure 5.7: Moonpool gap and outgoing wave amplitude operators for different forcing amplitudes η_{3a} and Froude numbers for the set-up with appendage #1 (18x9mm) with $d^* = 1.0$. See caption in figure 5.4 for description of symbols.

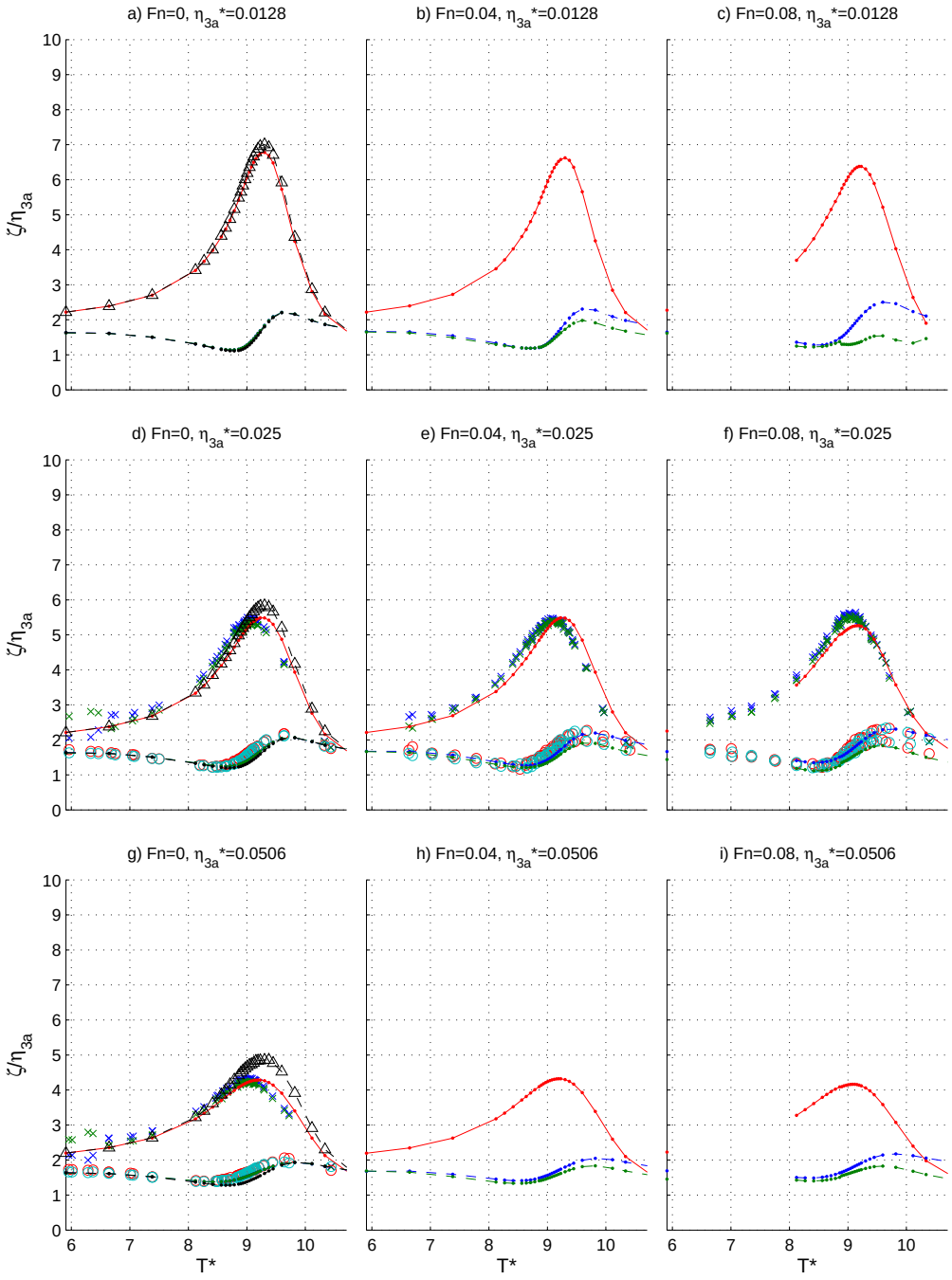

Figure 5.8: Moonpool gap and outgoing wave amplitude operators for different forcing amplitudes η_{3a} and Froude numbers for the set-up with appendage #1 (18x9mm) with $d^* = 1.167$. See caption in figure 5.4 for description of symbols.

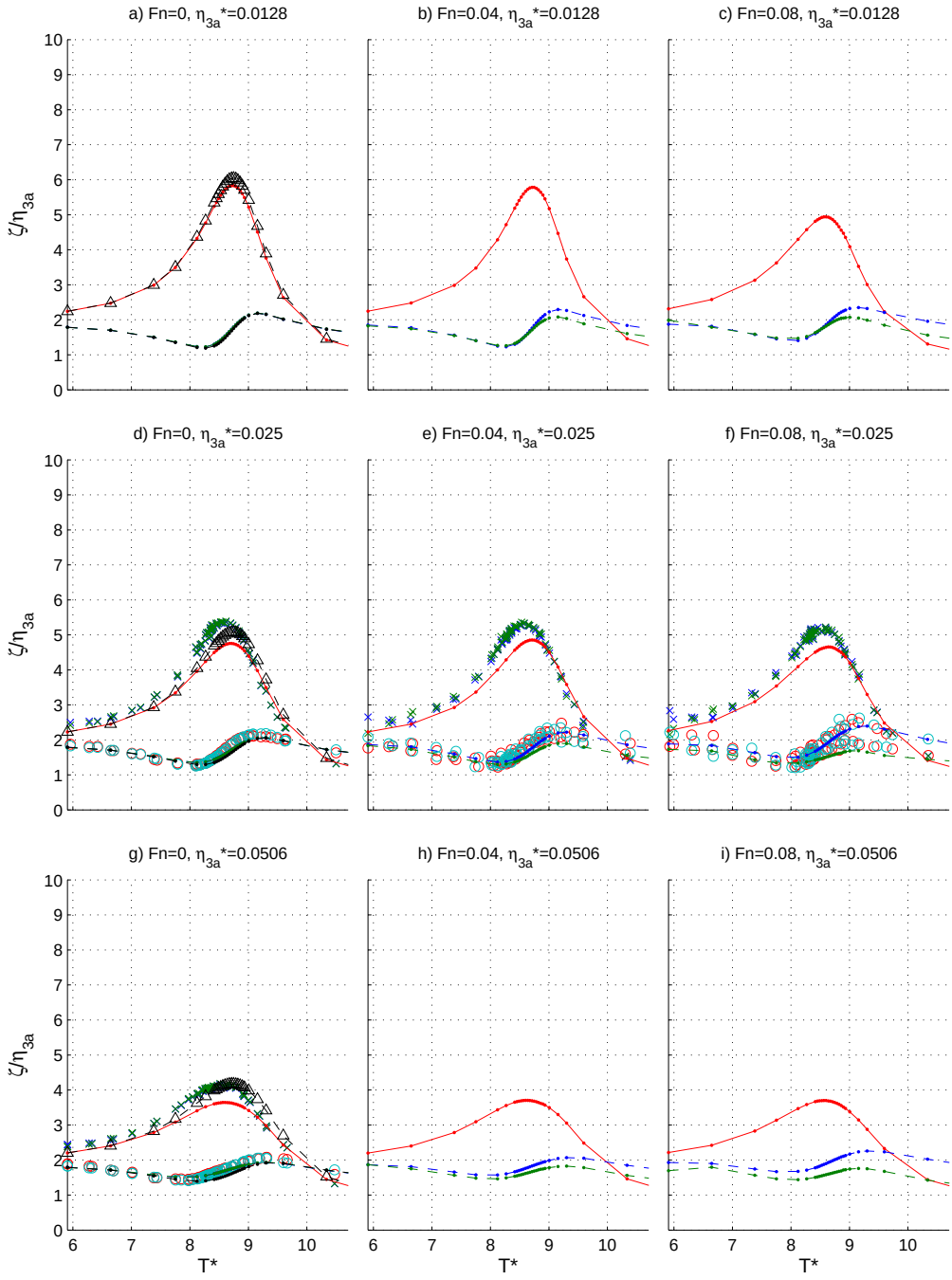

Figure 5.9: Moonpool gap and outgoing wave amplitude operators for different forcing amplitudes η_{3a} and Froude numbers for the set-up with appendage #2 (27x18mm) with $d^* = 0.833$. See caption in Figure 5.4 for description of symbols.

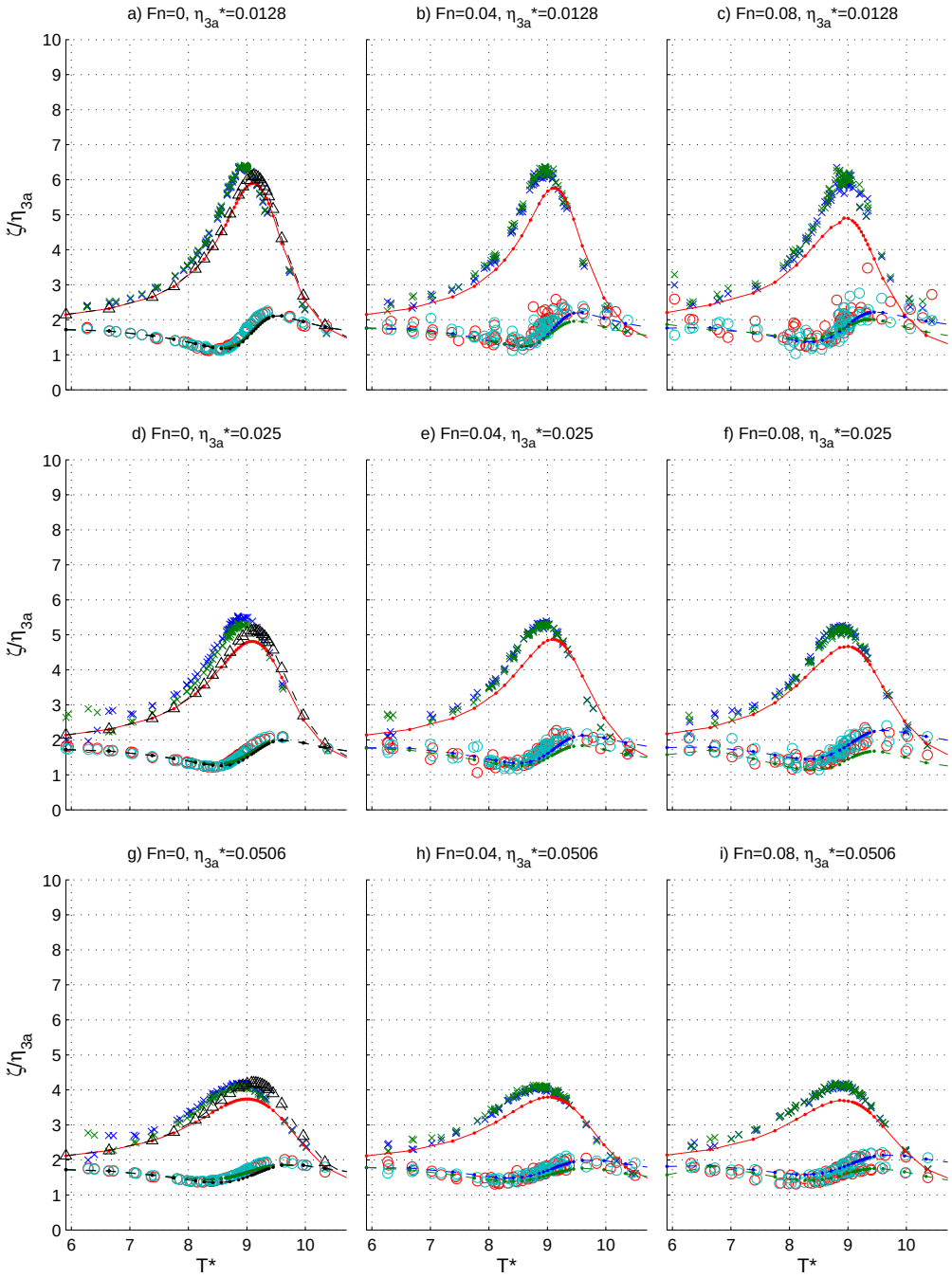

Figure 5.10: Moonpool gap and outgoing wave amplitude operators for different forcing amplitudes η_{3a} and Froude numbers for the set-up with appendage #2 (27x18mm) with $d^* = 1.0$. See caption in Figure 5.4 for description of symbols.

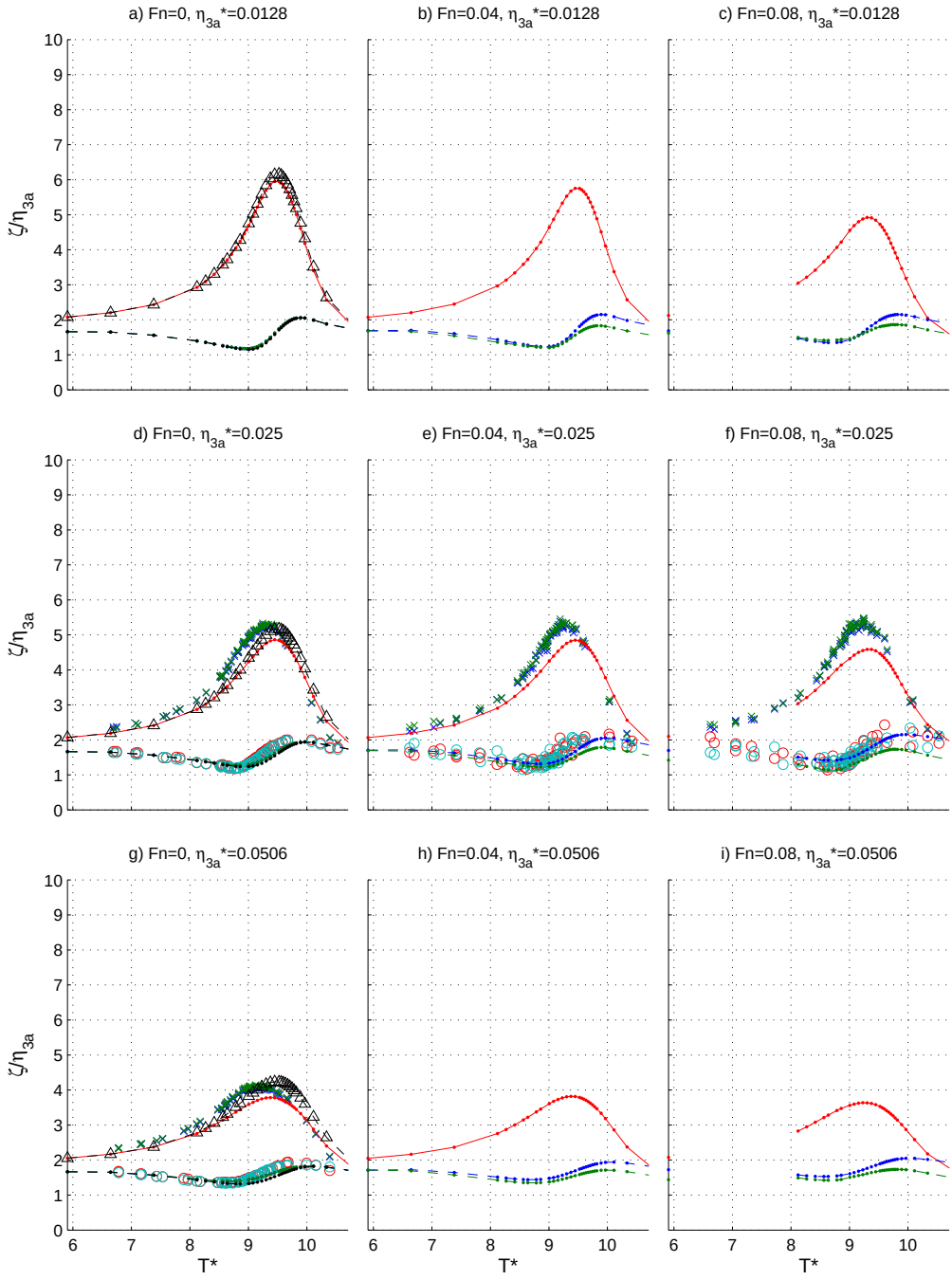

Figure 5.11: Moonpool gap and outgoing wave amplitude operators for different forcing amplitudes η_{3a} and Froude numbers for the set-up with appendage #2 (27x18mm) with $d^* = 1.167$. See caption in Figure 5.4 for description of symbols.

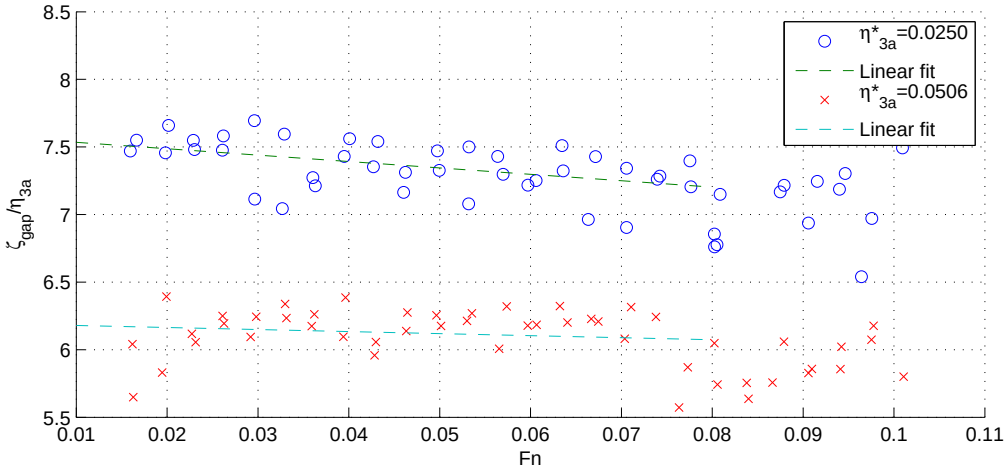

Figure 5.12: Dimensionless moonpool amplitudes in a body-fixed view as a function of Froude number for constant dimensionless heave amplitudes η^*_{3a} of 0.0250 and 0.0506. The dimensionless oscillation period $T^* = 8.785$. The experimental set-up is without appendages and $d^* = 1.0$.

for $\eta^*_{3a} = 0.0506$. Both equations are valid for Froude numbers between 0.00 and 0.08 and for the dimensionless heave oscillation period $T^* = 8.785$.

By studying velocity plots from our numerical simulations using the nonlinear hybrid method with low forward velocity (see examples in Figure 5.13), we see that the leading edge on the upstream side hull creates a wake which make the relative liquid velocity at the moonpool gap entrance almost zero. In effect, the water in the moonpool is free to oscillate nearly without the influence of forward velocity. This may explain the negligible influence of low forward velocity on the moonpool behaviour. In addition also the free-vorticity flow that develops at the leading edge will easily become turbulent, which again influences the diffusion of vorticity that will not be captured by our laminar viscous model.

Numerical simulations with Froude number 0.12 were tried, but were unsuccessful due to vorticity reaching the interface between potential and viscous flow, such that reliable results were not obtained.

An experimental test-series with carriage velocity of Fn= 0.1 is given in Figure 5.14 for the case without appendages and a draft of $d^* = 1.0$. Due to the limited length of the carriage rails, the total duration of the experiments is only around 20sec, including the acceleration and de-acceleration phases. This might not be enough time to reach steady state for longer periods, and for periods around the natural piston-mode period. The results are quite surprising, i.e. the moonpool response has increased compared to the results presented in Figure 5.4 for lower Froude numbers.

The group velocity of the outgoing waves are for all periods larger than the forward velocities tested here, meaning that there will be outgoing waves on both sides. According to pp. 239-240 in Faltinsen (2005) upstream waves will exist when the dimensionless number $\tau_w = \omega_e U/g < 0.25$, where ω_e is the angular frequency of encounter. The situation is expected to change when there is only outgoing waves on one side, meaning that the piston-mode motion might change.

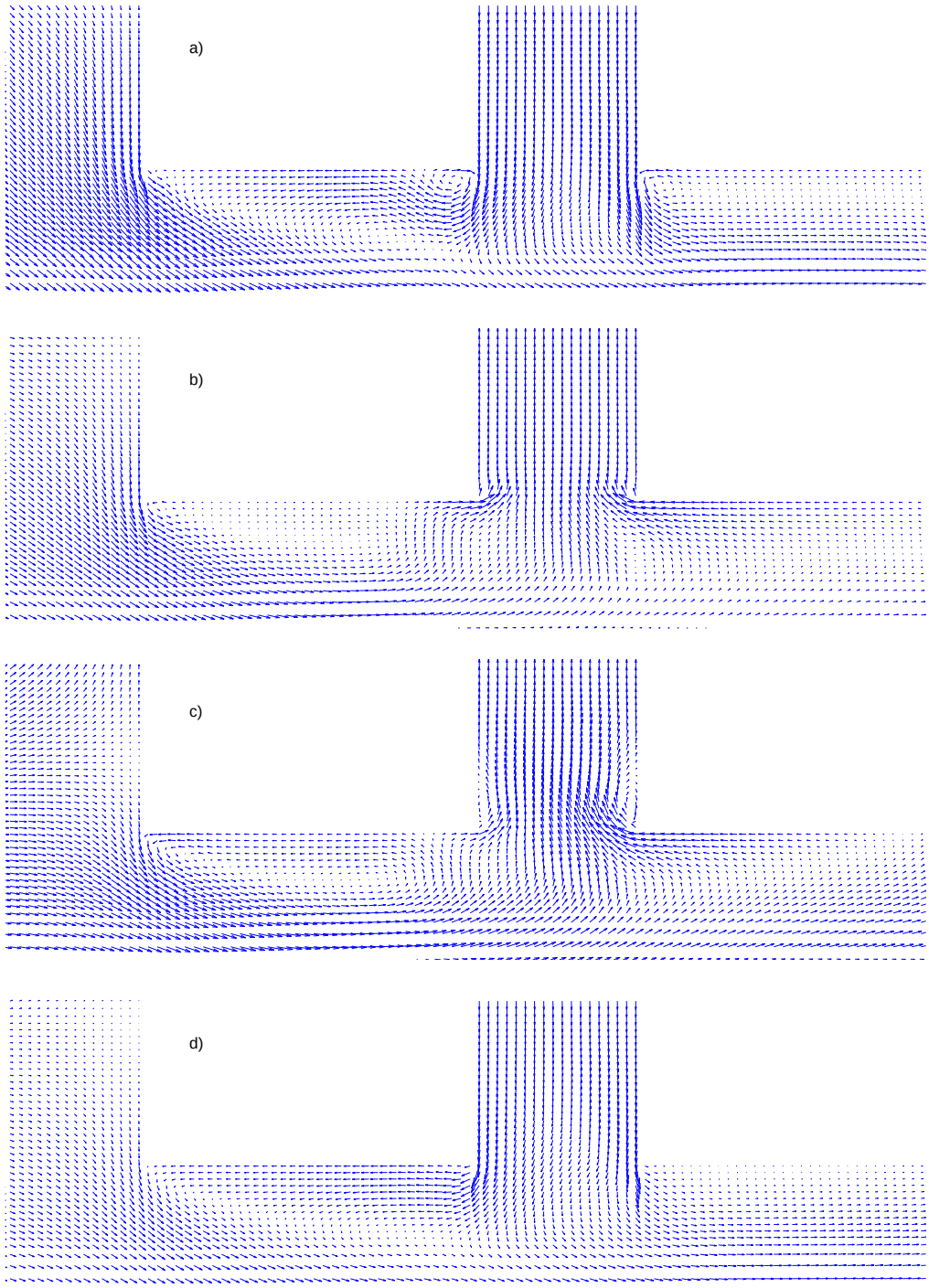

Figure 5.13: Examples on how the leading edge wake influence the flow field at the moonpool entrance. The case here is from Figure 5.4 with Fn = 0.04, $\eta^*_{3a} = 0.0250$ and $T* = 8.6743$. a) is at the start of an oscillation when the boxes are moving upwards, b) is at the top position, c) is at middle position moving downwards, d) is at the bottom position. Velocity arrows are given in the body-fixed coordinate system. The simulation results are from the nonlinear hybrid method.

The upstream outgoing wave is for all cases found to be larger than the downstream wave. The numerical prediction of the outgoing waves is in good agreement with the experimental results.

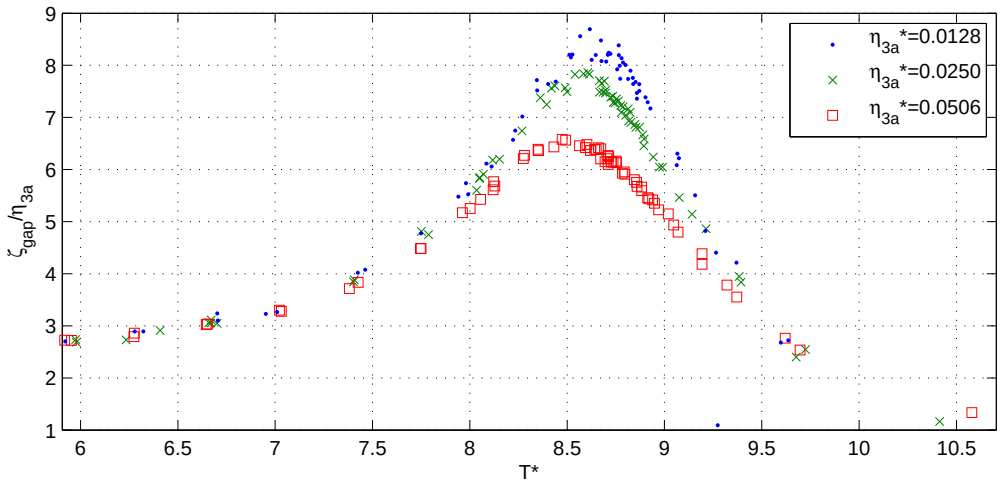

Figure 5.14: Experimental results for the measured moonpool gap amplitude divided by the forced heave motion amplitude for Fn= 0.1, without appendages and $d^* = 1.0$ (18cm) draft.

5.1.8 Effect of heave amplitude on the moonpool amplitude

In this section a review of the results with regards to the difference in the moonpool motion due to changing forced heave oscillation amplitude are given. Figures 5.15 and 5.16 show how the piston-mode moonpool amplitude is depending on the forced heave oscillation amplitude. Figure 5.15 is for $d^* = 0.833$, Fn= 0.04 and without appendages, while Figure 5.16 is for $d^* = 1.0$, Fn= 0.04 and all appendages options. In both figures each heave amplitude is tested for 5 different oscillation periods around the resonance piston-mode period. The similarities between the two figures show again how independent the piston-mode moonpool amplitude is of the draft of the hull. For all experimental tested heave amplitudes the wave elevation inside the moonpool gap never reached the lower entrance of the hull. A nonlinear effect is expected to occur when the piston-mode motion reaches the lower entrance of the hull for higher heave forcing amplitudes than experimentally tested. This effect has not been investigated in the present experimental and numerical work.

As expected, the ratio between the piston-mode amplitude and the heave amplitude at resonance decreases as the heave amplitude increases. This is due to a quadratic increase in the strength of the shed vorticity. However, strictly speaking quadratic dependency on heave velocity cannot be assumed, but on local relative fluid velocity on hull edges.

The sub-figure in the upper right corner of Figure 5.15 illustrates how the heave oscillation period is varying during the experiment. This period variation is also valid

for the results showed in Figure 5.16. There is therefore some scattering in the results because of the variation of the heave oscillation period.

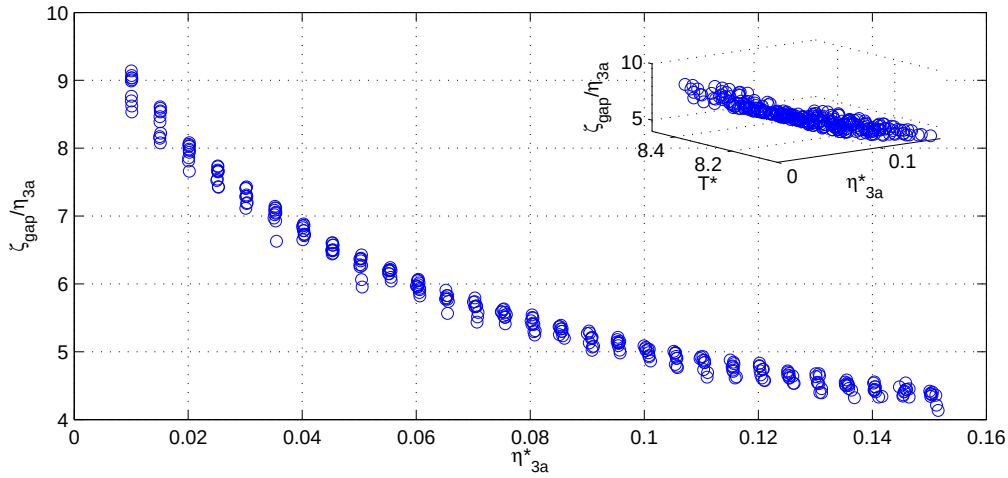

Figure 5.15: Dimensionless moonpool wave amplitudes in the body-fixed view as function of forced heave oscillation amplitudes. For the case without appendages and $d^* = 0.833$cm draft. Each heave amplitude is tested for 5 different oscillation periods.

5.1.9 Linear potential-flow theory results

Since linear potential-flow theory is often used for engineering applications, it is of practical interest to compare results against linear potential-flow theory. The results here has been obtained by using the present coupling between the HPC and the FVM method, but with the use of linear potential-flow theory in both domains. A more comprehensive discussion regarding the physical differences between linear potential-flow theory and what is observed in experiments will be given later, where the discussion will contain interpretation of the results from both the semi-nonlinear and the nonlinear hybrid methods.

It has been the topic of many publications before the difference between potential flow theory and the physical reality. In Figure 5.17 the large difference for the moonpool problem is again confirmed. The piston-mode motion is over-estimated due to the neglection of vorticity separation from the lower moonpool entrance.

An important physical result to notice from the potential-flow results in Figure 5.17 is the significant decrease in the moonpool amplitude due to the presence of appendages. Meaning that it is not only that the presence of appendages increase the vorticity separation and therefor decrease the moonpool amplitude, there is also a potential-flow effect reducing the moonpool amplitude.

5.1.10 Phase angle

Typical behaviour of the phase angle (α) between the heave acceleration and the moonpool motion is given in Figure 5.18. The example that is illustrated is without appendages, $d^* =$

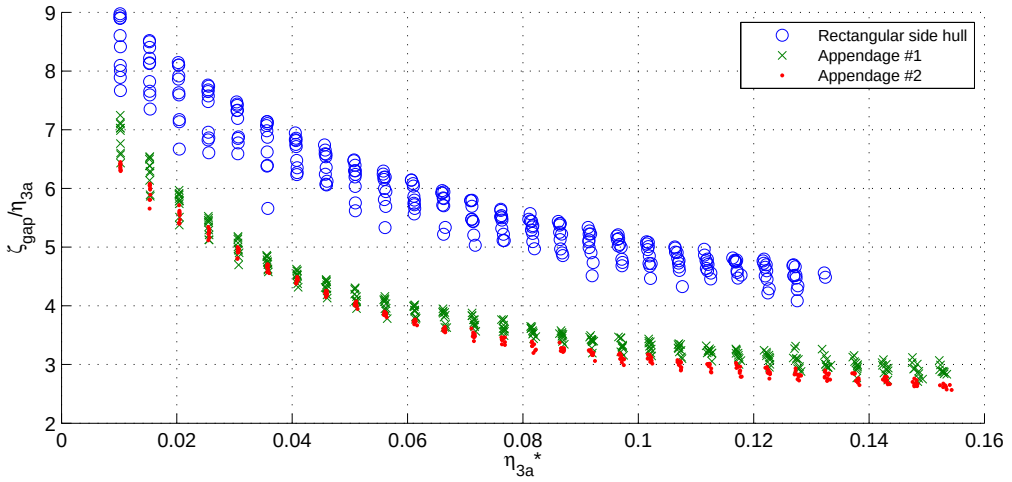

Figure 5.16: Dimensionless moonpool amplitudes in a body-fixed view as a function of forced heave amplitude. For all cases with and without appendages, with forward velocity Fn= 0.04. Each heave amplitude is tested for 5 different oscillation periods.

1.0 (18cm) draft, $\eta_{3a}^* = 0.025$ (4.5mm) oscillation amplitude and zero forward velocity. This corresponds to the phase angle of the results in sub-figure d) of Figure 5.4. The phase angle goes through 90° around the piston-mode resonance. Furthermore, for periods below the piston-mode resonance period, the heave and moonpool motions are out of phase. For periods above the piston-mode resonance period they are in phase.

Figure 5.18 also illustrates the main reason for showing all results from the forced heave oscillations experimental programme in a body-fixed view. There is an offset between the numerically predicted phase angle, and the measure phase angle from the experimental programme. It is clear that the measurements from the experimental programme contain an error. When analysing the experimental data it was found that there is a time lag between the heave signal and the wave gauge signal, such that the wave gauge measurements could not be converted back to the Earth fixed coordinate system. Since the wave gauges are mounted to the model and follow the motion of the body in both sway and heave, the measured wave gauge signal would need to be corrected with the measured heave position.

5.1.11 Overall agreement for forced oscillation study

The validity and limitations of the numerical method in predicting the moonpool response due to forced heave oscillations have been presented. With the limitations given in the numerical hybrid method, the results compare quite well with experiments (see Figures 5.3-5.11). The nonlinear hybrid method simulations for higher heave amplitudes somewhat over-predict the damping of the piston-mode amplitude, while it for lower amplitudes are in good agreement with the experimental results. As an example in Figure 5.4 the difference in the predicted piston-mode amplitude for the lowest heave forcing amplitude $\eta_{3a}^* = 0.0128$ is less than 2%, and for the highest heave forcing amplitude $\eta_{3a}^* = 0.0506$ the

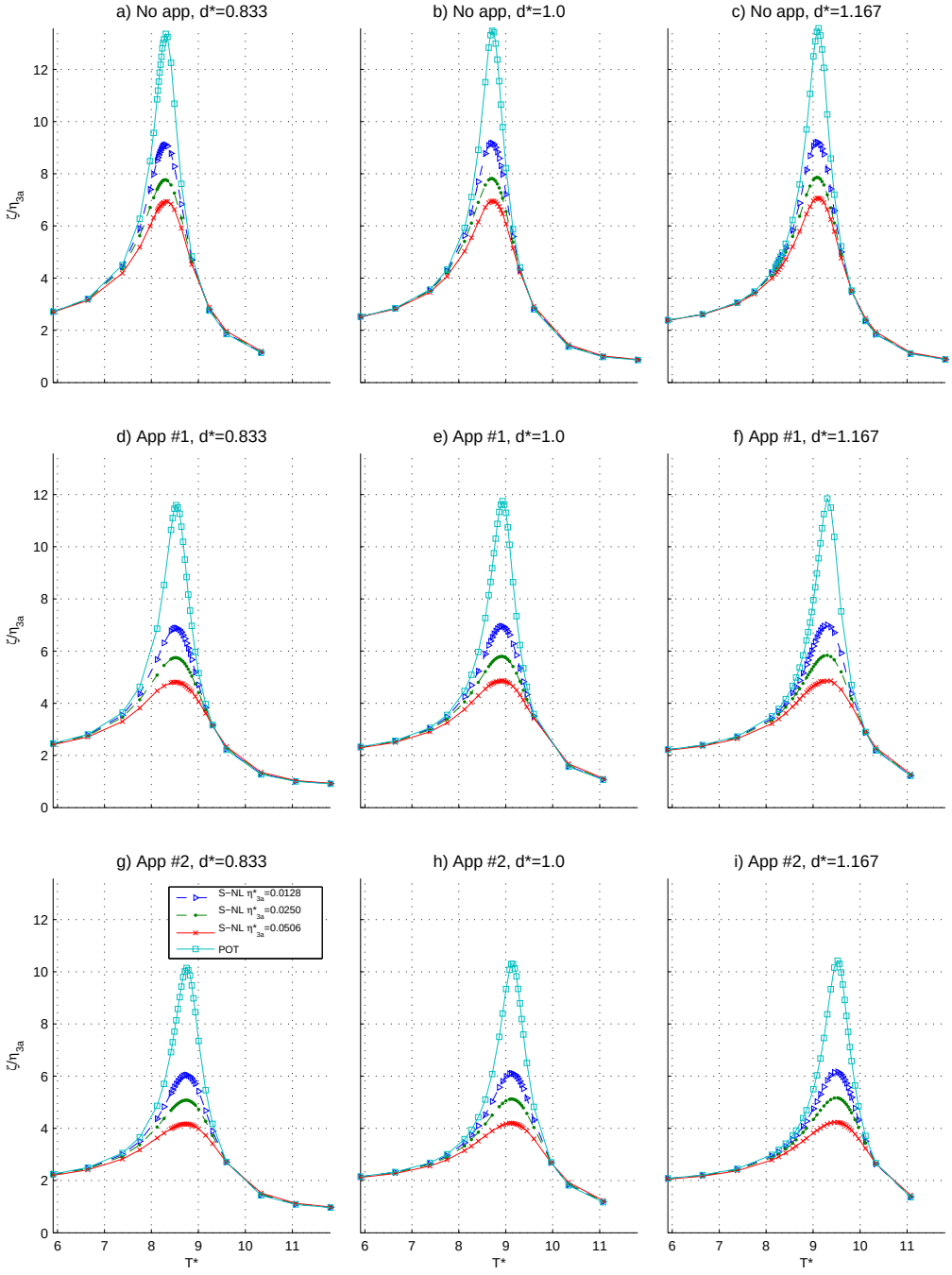

Figure 5.17: Dimensionless moonpool amplitudes in a body-fixed view comparison of linear potential flow theory (POT) with the semi-nonlinear (S-NL) simulations for all appendages and draft configurations versus dimensionless oscillation period. The semi-nonlinear results are the same as presented in Figures 5.3-5.11.

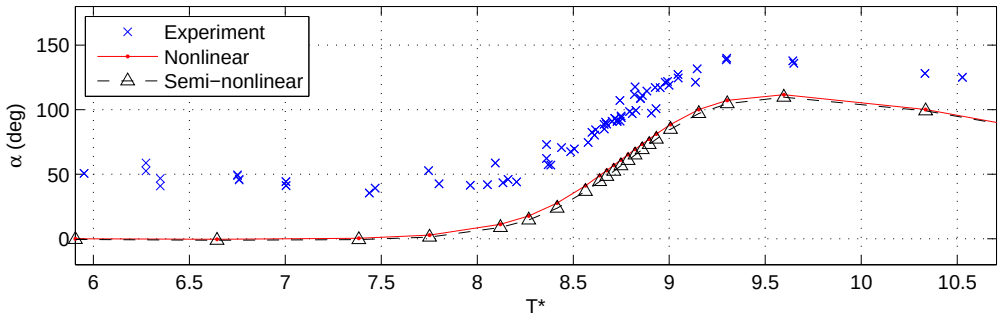

Figure 5.18: Phase angle α between heave acceleration and moonpool motionversus the dimensionless oscillation period T^*.

relative difference is around 7% at the piston-mode resonance period.

Piston-mode amplitude results from the semi-nonlinear hybrid method are higher than the nonlinear hybrid results for all zero current cases. Furthermore, it over-predicts the piston-mode response for higher heave amplitudes. It is believed that the reason for this is that the potential flow domain in the semi-nonlinear results can be minimized to only contain the top layer close to the free surface, while the potential flow domain in the nonlinear hybrid method needs to be larger due the re-meshing algorithm of the free-surface. The reason is that the implementation does not allow the viscous flow domain to change size in time. Notice that also the semi-nonlinear results are different from the experiments for appendage #2.

More comments regarding the applicability of the semi-nonlinear and the nonlinear hybrid methods will be given when the local pressure and flow details are studied due to forced oscillations in section 5.4. It is then with emphasis on the different results produced by the two hybrid methods, especially for the roll motion.

5.2 Linear potential-flow frequency-dependent hydrodynamic coefficients

The linear potential-flow frequency-dependent coefficients $A_{ii}(\omega)$ and $B_{ii}(\omega)$ are computed by the time-domain code, where the time-domain simulations are performed until steady-state conditions. However, steady-state conditions occur much later in the potential flow case due to low damping, such that the numerical beach needs to be carefully tuned to avoid the influence of reflecting waves from the ends of the numerical wave tank.

Four different cases are simulated for each frequency. The first three are forced motion in each of the three degrees of freedom, and a fourth with incoming waves on a fixed ship. The first three determines the hydrodynamic added mass and potential-flow damping coefficients, while the fourth gives the wave excitation forces F^{ex}. The dimensionless water depth is here changed to $h^* = 10$, while all results presented until now has been for $h^* = 5.56$. For each case the resulting steady-state hydrodynamic forces are obtained. The effect of the two different water depths on the added mass and potential-flow will be

given later in section 5.3.10.

Hydrodynamic coefficients for the setup without appendages and forward velocity, for the dimensionless draft $d^* = 1.0$ will be given in the following sections.

5.2.1 Added mass and potential-flow damping

It has been shown by many authors before that the added mass and potential-flow damping coefficients in heave for the moonpool problem are highly frequency dependent, particular around the piston-mode resonance frequency. See Faltinsen et al. (2007) for added mass and potential damping coefficients for two-dimensional moonpool sections, where their case 1 corresponds to the case considered in this work with $d^* = 1.0$, $h^* = 10$ and without appendages. Their result will be compared against what has been achieved in our work in section 5.3.10.

Forced sway oscillations give the coefficients $A_{22}(\omega)$, $B_{22}(\omega)$ and the moment in roll due to motion in sway results in the coefficients $A_{42}(\omega)$ and $B_{42}(\omega)$. Here the added mass $A_{ij}(\omega)$ are force coefficients 180° out of phase with acceleration of the body and $B_{ij}(\omega)$ are force coefficients 180° out of phase with velocity of the body.

I.e. it is assumed that the hydrodynamic forces from forced oscillations have the following form,

$$F_{kj}(t) = -A_{kj}(\omega)\,\ddot{\eta}_j(t) - B_{kj}(\omega)\,\dot{\eta}_j(t). \tag{5.5}$$

Here $F_{kj}(t)$ is the hydrodynamic force in k-direction due to oscillatory motion in j-direction. Unsteady forces and moments due to hydrostatic pressure and the instantaneous wetted surface are not included. The hydrodynamic added mass and potential-flow damping coefficients are found by evaluating the following integrals,

$$A_{kj}(\omega) = -\frac{\int_0^{nT} F_{kj}(t)\,\ddot{\eta}_j(t)\,dt}{\int_0^{nT} \ddot{\eta}_j(t)^2\,dt}, \tag{5.6}$$

$$B_{kj}(\omega) = -\frac{\int_0^{nT} F_{kj}(t)\,\dot{\eta}_j(t)\,dt}{\int_0^{nT} \dot{\eta}_j(t)^2\,dt}. \tag{5.7}$$

Here nT indicates that it should be integrated over whole periods. Note that these coefficients are very sensitive to the phase of the acceleration and velocity. Even though the forced motion is prescribed, it is not clear due to the time-integration method which time-step for velocity and acceleration to apply for the integration in equations (5.6) and (5.7). It is found that the velocity in the middle of two time-steps is the best approximation of the force in phase with velocity. The roll moments are calculated around the point in the middle of the hull at the mean free-surface (z=0).

The resulting dimensionless added mass and potential-flow damping coefficients are given in Figure 5.19. A first observation is that the results confirm that the sway motion is coupled to the roll motion, while the heave motion is uncoupled to both sway and roll motion. The situation will be different with forward velocity.

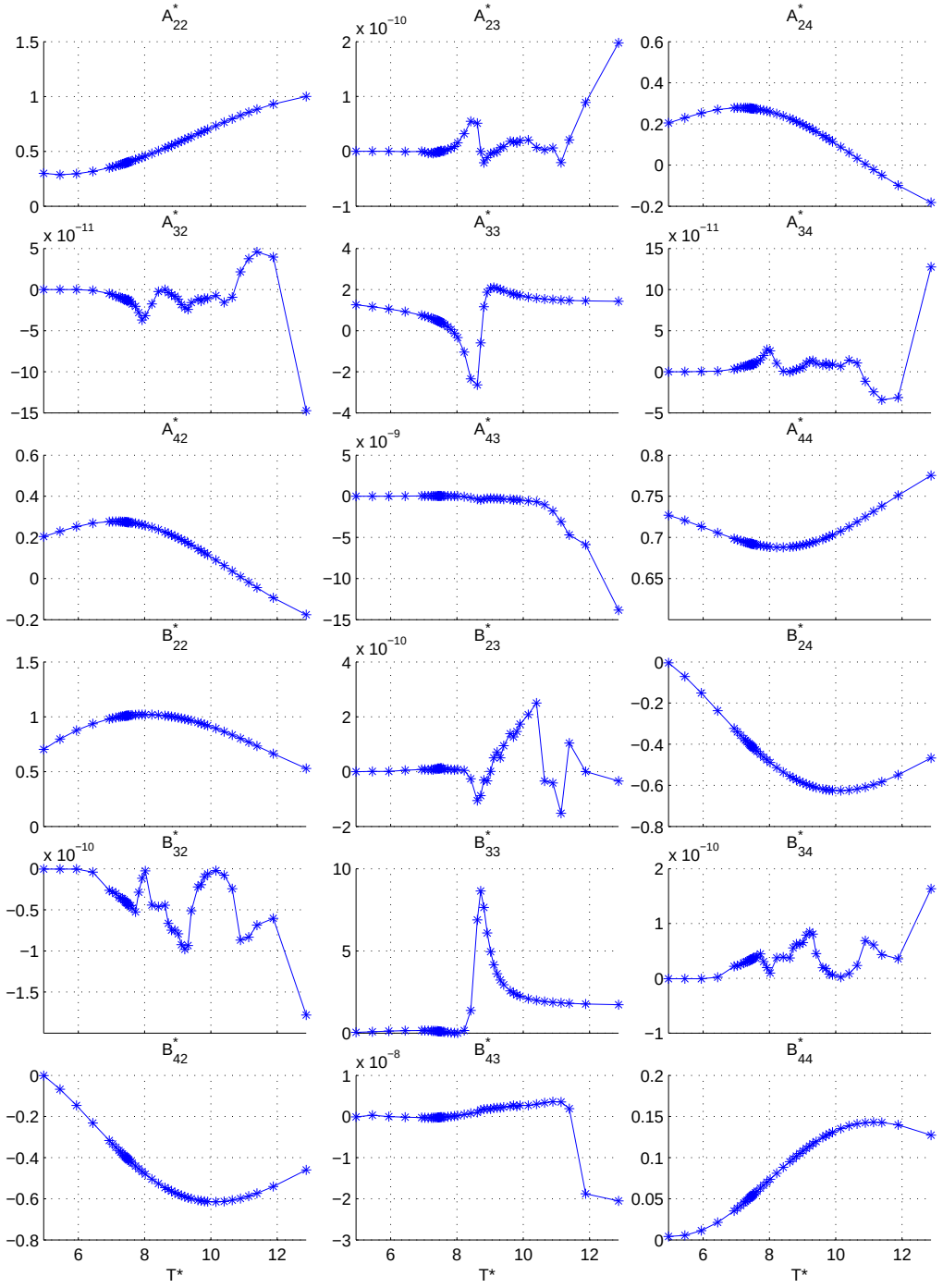

Figure 5.19: Dimensionless added mass and potential-flow damping coefficients versus the dimensionless oscillation period T^* for the monpool section without appendages and dimensionless draft $d^* = 1.0$ based on linear potential flow. The dimensionless water depth is $h^* = 10$.

The dimensionless parameters in Figure 5.19 are defined as:

$$A^*_{22} = \frac{A_{22}}{m}, \quad A^*_{33} = \frac{A_{33}}{m}, \quad A^*_{24} = \frac{A_{24}}{dm}, \quad A^*_{42} = \frac{A_{42}}{dm}, \quad A^*_{44} = \frac{A_{44}}{I} \tag{5.8}$$

$$B^*_{22} = \frac{B_{22}}{m\sqrt{g/(2B+b)}}, \quad B^*_{33} = \frac{B_{33}}{m\sqrt{g/(2B+b)}}, \quad B^*_{24} = \frac{B_{24}}{dm\sqrt{g/(2B+b)}},$$

$$B^*_{42} = \frac{B_{42}}{dm\sqrt{g/(2B+b)}}, \quad B^*_{44} = \frac{B_{44}}{I\sqrt{g/(2B+b)}} \tag{5.9}$$

When the hydrodynamic added mass, potential damping, linear hydrostatic restoring force coefficients and wave excitation forces are known, the equations of motion in the frequency domain can be approximated as a complex 3 by 3 matrix, by assuming $\eta_j = \eta_{ja} \exp(i\omega t)$ and $F^{ex'}_j = F^{ex}_j \exp(i\omega t)$.

$$\left(-\omega^2 \left[\mathbf{M} + \mathbf{A}(\omega)\right] + i\omega \left[\mathbf{B}(\omega)\right] + \left[\mathbf{C}\right]\right) \begin{bmatrix} \tilde{\eta}_{2a} \\ \tilde{\eta}_{3a} \\ \tilde{\eta}_{4a} \end{bmatrix} = \begin{bmatrix} \tilde{F^{ex}}_{2a}(\omega) \\ \tilde{F^{ex}}_{3a}(\omega) \\ \tilde{F^{ex}}_{4a}(\omega) \end{bmatrix} \tag{5.10}$$

where

$$\left[\mathbf{M} + \mathbf{A}(\omega)\right] = \begin{bmatrix} (M + A_{22}(\omega)) & 0 & k\left(-Mz_G + A_{24}(\omega)\right) \\ 0 & (M + A_{33}(\omega)) & 0 \\ \left(-Mz_G + A_{42}(\omega)\right)/k & 0 & (I + A_{44}(\omega)) \end{bmatrix} \tag{5.11}$$

$$\left[\mathbf{B}(\omega)\right] = \begin{bmatrix} B_{22}(\omega) & 0 & kB_{24}(\omega) \\ 0 & B_{33}(\omega) & 0 \\ B_{42}(\omega)/k & 0 & B_{44}(\omega) \end{bmatrix} \tag{5.12}$$

$$\left[\mathbf{C}\right] = \begin{bmatrix} K_{22} & 0 & kK_{24} \\ 0 & C_{33} & 0 \\ K_{42}/k & 0 & C_{44} + K_{44} \end{bmatrix} \tag{5.13}$$

and $\tilde{\eta}_{2a} = \eta_{2a}/\zeta_a$, $\tilde{\eta}_{3a} = \eta_{3a}/\zeta_a$, $\tilde{\eta}_{4a} = \eta_{4a}/(k\,\zeta_a)$. And $\tilde{F}^{ex}_2 = F^{ex}_2/\zeta_a$, $\tilde{F}^{ex}_3 = F^{ex}_3/\zeta_a$, $\tilde{F}^{ex}_4 = F^{ex}_4/(k\,\zeta_a)$.

The undamped equation of motion with no forcing can be rewritten to look like

$$\left[\mathbf{C}\right]\left[\mathbf{M} + \mathbf{A}(\omega)\right]^{-1} - \lambda_i(\omega)\left[\mathbf{I}\right] = 0 \tag{5.14}$$

where $\lambda_i(\omega) = \omega_i(\omega)^2$ and $[\mathbf{I}]$ is the 3 by 3 identity matrix. Equation (5.14) represents a frequency dependent eigenvalue problem. By setting the determinant of this matrix to zero we find the natural periods of the system. Due to that the coefficients are frequency dependent, we will find 3 artificial natural frequencies ω_i for each frequency dependent hydrodynamic added mass coefficients. The real natural frequencies are found when the artificial natural frequencies are equal to the frequency used for the frequency dependent added mass and damping coefficient $\omega_n = \omega_i(\omega_n)$, see Figure 5.20. Based on the frequency dependent added mass coefficients, inertia and hydrostatics of the moonpool section, three undamped natural dimensionless periods in heave are found [7.4, 8.7 and 9.9]. Where the middle one is the piston-mode natural period, as seen in the previous section with forced heave oscillations and given in Table 5.4. The corresponding potential damping-to-critical

damping ratios for the three natural heave periods are [0.02, above 1.0 and 0.3]. We will come back to the discussion about natural periods when analysing the results from the floating experimental and numerical work.

To find these undamped natural periods we have made the assumption that the hydrodynamic force can be split in two as in equation (5.5), and that the term proportional to the velocity can be neglected. This is a somewhat controversial assumption, it is an assumption about something that cannot be achieved in reality. However, an analogy to a simple mass-spring system can then be made. The presence of damping terms less than 5% of the critical damping is not significant in the prediction of the natural period of the spring mass system. The practical point must be that one of the undamped natural periods corresponds to a pronounced peak in the response curve.

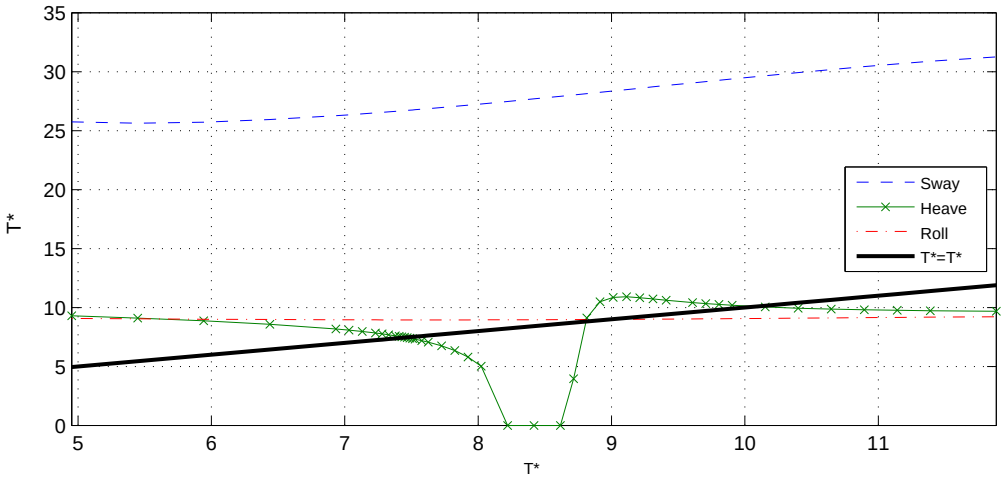

Figure 5.20: Illustration of calculation of the undamped natural period. What is refered to as Sway, Heave and Roll are the solutions of $\lambda_i(\omega)$ in equation (5.14). The natural periods are found where the black line intersects the other lines.

5.2.2 Wave exciting forces and moment by linear potential flow

To help in the discussion and understanding of the floating experimental results, the linear potential-flow wave exciting forces and moment are given in Figure 5.21, where the moment is calculated around the center-line at $z = 0$. The linear potential-flow wave exciting forces and moment amplitudes can according to Newman (1962) be related to the linear potential-flow wave radiation damping for corresponding modes, for instance the heave wave excitation force amplitude is related to heave damping. The latter fact can be used as a test to check that our calculations are performing as expected.

To foresee some of the coming results from the floating experimental programme, we notice that the linear potential-flow wave excitation force amplitude in heave has a minimum around $T^* = 7.9$. We will come back to the heave cancellation later when studying time-series results from the floating experimental programme. (See the discussion related to Figure 5.30.)

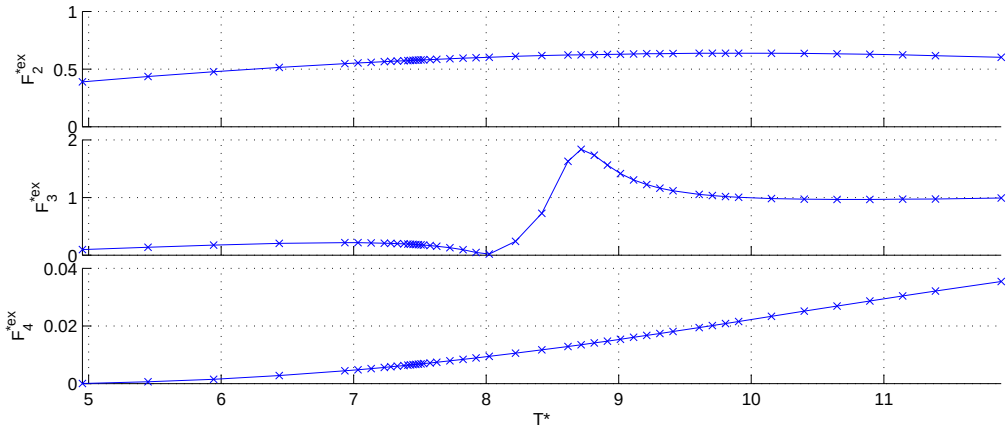

Figure 5.21: The dimensionless linear potential-flow wave exciting forces and moments amplitudes in sway (F_2^{*ex}), heave (F_3^{*ex}) and roll (F_4^{*ex}) versus the dimensionless wave period T^* for the two-dimensional monpool section without appendages. The dimensionless water depth is $h^* = 10$.

Here the dimensionless wave exciting forces and moment amplitudes are defined as:

$$F_2^{*ex} = \frac{F_2^{ex}}{\rho g \zeta_a (2B+b)^2}, \quad F_3^{*ex} = \frac{F_3^{ex}}{\rho g \zeta_a (2B+b)^2} \quad \text{and} \quad F_4^{*ex} = \frac{F_4^{ex}}{\rho g \zeta_a (2B+b)^3}. \tag{5.15}$$

5.3 Freely-floating body in incoming regular waves

All studies presented until now has been with forced oscillations or with incoming waves on a fixed 2D moonpool section. Here a spring-moored freely floating 2D moonpool section subjected to incoming regular waves will be studied, corresponding to the experimental programme described in section 4.2.

Since numerical results here will be compared against the floating experimental programme described in section 4.2, the dimensions here are different than in the study with forced heave oscillations. However, the ratios between the moonpool gap width, the hull draft ($d^* = 1.0$) and the hull width are kept. The water depth in the wave flume was kept constant at 1.0m for both cases. Meaning that the finite-water effect will be different, and the dimensionless water depth to draft ratio has increased from $h^* = 1.0/0.18 = 5.556$ to $h^* = 1.0/0.1 = 10$. The corresponding difference in added mass and potential damping will be checked.

The additional capability added to the hybrid methods used to study the freely-floating problem compared to the forced heave oscillation studies is the coupling with the equations of motion for the rigid-body motion of the moonpool section. One validation test has been performed to check that the equations of motion are solved correctly. This was free heave decay tests against data from Yeung (1982) for the linear potential flow version of the code. No other verification tests have been performed to check that the equations of motion are solved correctly in the two hybrid methods, other than the studies presented in the following sections.

Further, an experimental repetition test of the highest wave steepness 1/30 is performed, and an experimental test-series with a smaller moonpool gap of 8cm is given.

As the numerical hybrid method does not include any turbulence modelling, there is an uncertainty connected to the lack of turbulence modelling in the present work. Although the mesh could be made fine enough to capture details at the lowest turbulence scale, it will still be an open question about the 3D behaviour of turbulence and other 3D effects in the experimental setup. In the forced heave oscillation study, the effect of turbulent cancellation of vorticity was thought to be the main reason for the discrepancies between the numerical hybrid method results and the experimental results for the setup with the largest appendages. Another discussed issue was at forward velocity when the leading edge vorticity influences the vorticity generated at the moonpool entrance edges. With a freely-floating body in incident waves, can we expect that our numerical method without any turbulence model to accurately agree with experimental results?

Some of the results in this section have previously been published in Fredriksen et al. (2015).

5.3.1 Numerical setup

The numerical setup and the properties of the mesh used in the study in this section are somewhat different from before, and will be described here.

In between the wavemaker and the model the horizontal mesh resolution is set to 30 cells over a wave length. The mesh size gradually changes and becomes equal to the mesh size across the hull. This applies from either half a wave length or two times the length of one side hull, depending on what is longest. In the horizontal direction the number of FVM cells across one side hull is set to be 30 (mesh size = 0.0067m). The mesh size is kept constant across the moonpool gap, i.e. 15 cells across the gap.

The mesh is symmetric relative to the center-plane of the hull, except that in the numerical beach the mesh size is increasing. The numerical beach starts three wave lengths after the hull, and is 4 wave lengths long. The total length of the numerical wave tank in addition to the length of the hull is 14 wave lengths, and therefore different for each wave period.

In the z-direction the mesh resolution is constant from $z = 0$ until half the hull draft below the bottom, using 20 cells across the draft of the body (mesh size 0.005m), then gradually increasing until the bottom of the tank. A total number of 60 cells in the z-direction are used.

Because of limitations in the implemented numerical hybrid method, only rectangular cells can be used in the viscous flow domain. The HPC potential flow domain has no such limitations. However, to simplify the re-meshing scheme the HPC nodes in the same liquid column will all have the same y-coordinate. Figure 5.22 shows an example of a mesh used in the semi-nonlinear hybrid simulation and Figure 5.23 shows an example from the nonlinear hybrid simulation.

The following discussion applies to the nonlinear hybrid method. To avoid having a changing mesh in time in the viscous flow domain, the intersection between the potential and viscous flow domains needs to be below what is the expected minimum z-coordinate value of the free-surface elevation in the simulation. At every time-step the free-surface nodes are moved in the z-direction to the new position of the free surface. Parts of the HPC mesh are then either stretched or compressed, as exemplified in Figure 5.23. There

are three challenges related to this re-meshing strategy. One is related to large roll angles, the second is related to large moonpool piston-mode motions and the third is related to the viscous flow domain around the hull edges where flow separation occurs. To satisfy these challenges we are required to create a mesh with as large as possible viscous flow domain around the body, while still allowing the potential flow domain enough area to follow the free surface in time in the body-fixed coordinate system.

For the mesh inside the moonpool gap, an estimate of the expected moonpool piston-mode amplitude should be given and used to create the intersection between the potential flow and viscous flow domains. For the mesh outside the vessel the limiting factor is the expected roll amplitude η_4^{Max} in the simulation. This is illustrated in Figure 5.23, where η_4^{Max} can be interpreted from the top figure. The expected moonpool wave amplitude and roll amplitude are inputs to the simulation with a safety margin. The simulation will break down if the achieved roll motion in the simulation is higher than the input value η_4^{Max}.

The meshes in the semi-nonlinear hybrid simulations are equal for all three wave steepness cases, but different for each wave period as described above. The intersection between potential and viscous flow is created as close as possible to the free surface, in order to minimize the potential flow domain. The HPC solution of the potential flow domain should contain at least 3 rows of nodes, to accurately propagate the free-surface waves.

The three different meshes used to obtain results for three different wave steepnesses 1/60, 1/45 and 1/30 with wave period T=0.95s are presented in Figures 5.23-5.25. Different meshes are created for other wave periods and wave steepnesses, based on the criteria described above. Notice that due to higher η_4^{Max} for the three cases in Figures 5.23-5.25, the water depth changes. Therefore, the finite-water effect on the waves changes. It is, however, for the longest waves at 1.2s a ratio between the water depth and the wave length around 0.45. A usual rule of thumb is that the waves start feeling the bottom when the water depth is half the wave length, such that we are for the longest waves just within this limit. However, the waves around the natural periods remains more or less unchanged due to finite-water depth effects. The added mass and potential-flow damping properties will also change due to different water depths. This change is again small, see results in section 5.3.10, where the differences in the dimensionless added mass and potential damping between the two experimental setups are checked.

The waves will be propagated from the left end of the numerical wave tank to the middle where the structure is located. We will therefore refer to the left hand and the right hand sides of the moonpool gap when discussing the measurements of the moonpool wave elevation.

5.3.2 Results with free-floating structure

The main results from the floating experimental programme are given in Figure 5.26 and Figure 5.27 and compared with the two numerical hybrid methods. In general, the agreement is good, in particular for the nonlinear hybrid method. The moonpool wave amplitude comparisons are reasonable, with some over-prediction on the right hand side of the gap, while some under-prediction on the left side. One of the reasons can be the quality of the measurements, keeping in mind that they are based on the copper tape glued onto the model. The semi-nonlinear hybrid method results suffer some notable discrepancies

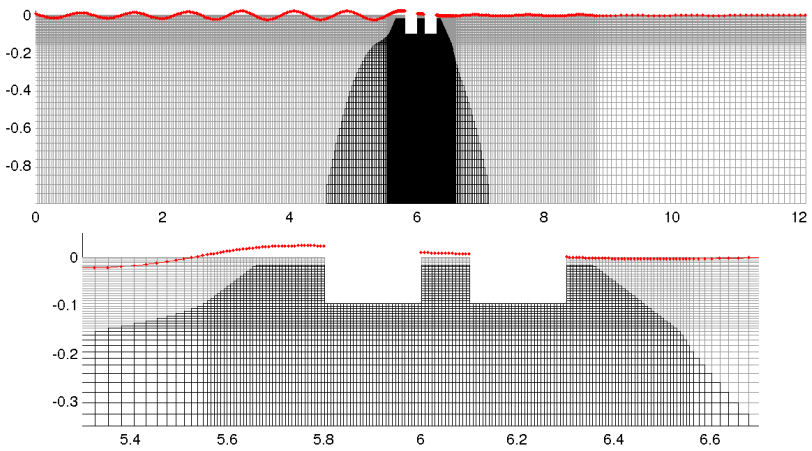

Figure 5.22: Example of mesh use in the semi-nonlinear hybrid method simulation, the wave period is $T = 0.73$s. Gray cells belong to the potential flow domain, and black cells to the viscous flow domain. The mesh on the top illustrates the entire numerical wave tank. One should observe the difference in scales on the y- and z-axis. The bottom mesh is a close-up of the mesh close to the hull, here the scale ratio is correct. The free surface is shown in both meshes.

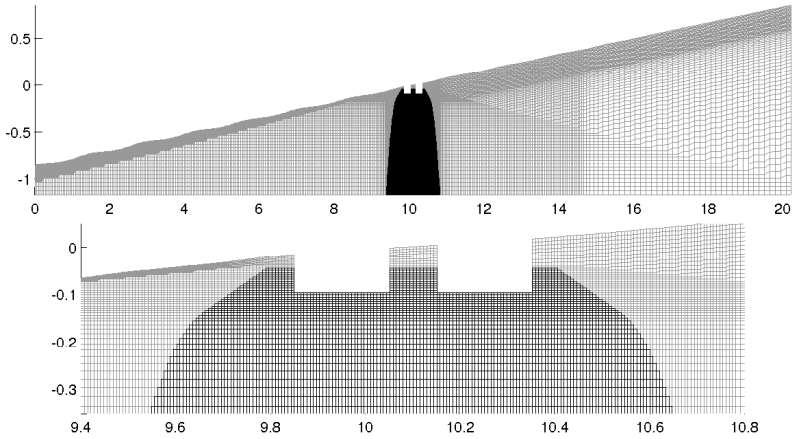

Figure 5.23: Example of body-fixed mesh at a specific time-step used in the nonlinear simulation in the body-fixed coordinate system. The wave period is $T = 0.95$s and wave steepness 1/60. η_4^{Max} is set to 5.5°. Gray cells belong to the potential flow domain, and black cells to the viscous flow domain (Ω_{CFD}). The mesh on the top illustrates the entire numerical wave tank. One should observe the difference in scales on the y- and z-axis. The bottom mesh is a close-up of the mesh close to the hull, here the scale ratio is correct.

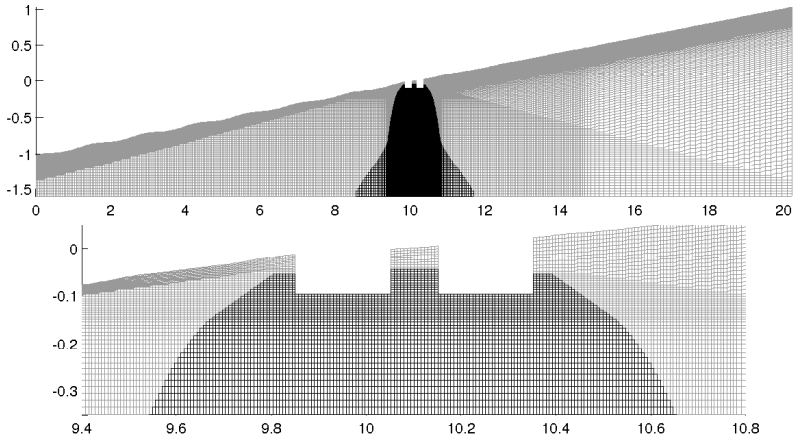

Figure 5.24: Example of body-fixed mesh at a specific time-step used in the nonlinear simulation in the body-fixed coordinate system. The wave period is $T = 0.95$s and wave steepness 1/45. η_4^{Max} is set to 7.5°. See Figure 5.23 for further description.

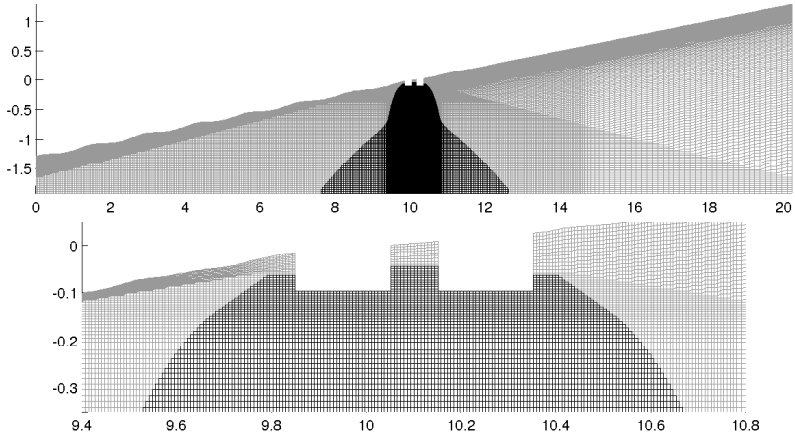

Figure 5.25: Example of body-fixed mesh at a specific time-step used in the nonlinear simulation in the body-fixed coordinate system. The wave period is $T = 0.95$s and wave steepness 1/30. η_4^{Max} is set to 9.0°. See Figure 5.23 for further description.

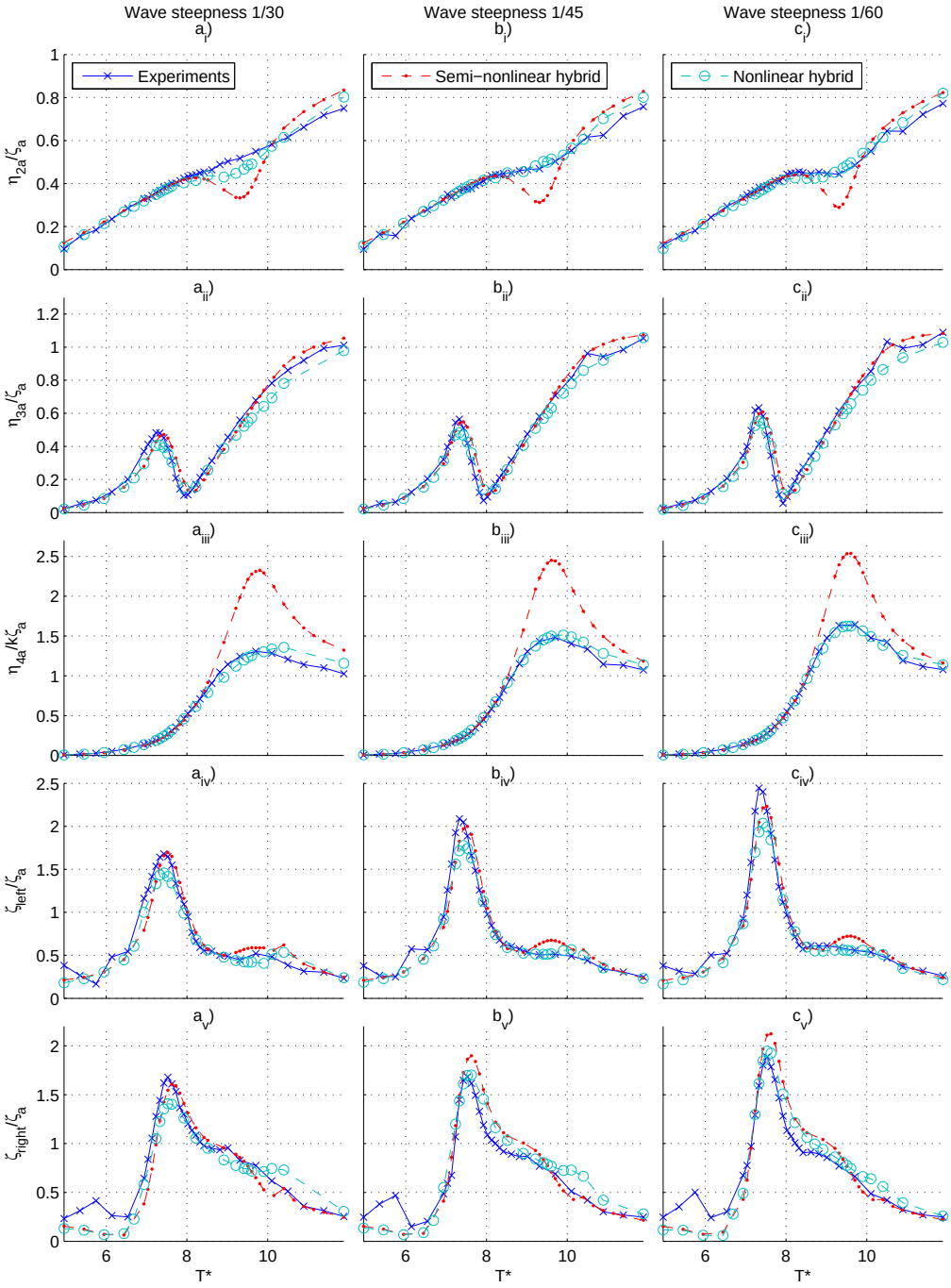

Figure 5.26: Comparison of numerical and experimental results of rigid-body motion amplitudes (η_{2a}, η_{3a}, η_{4a}) and free-surface amplitudes on the left ζ_{left} and right ζ_{right} of the moonpool for 3 different wave steepnesses versus wave period. ζ_a =incident wave amplitude. k =wave number.

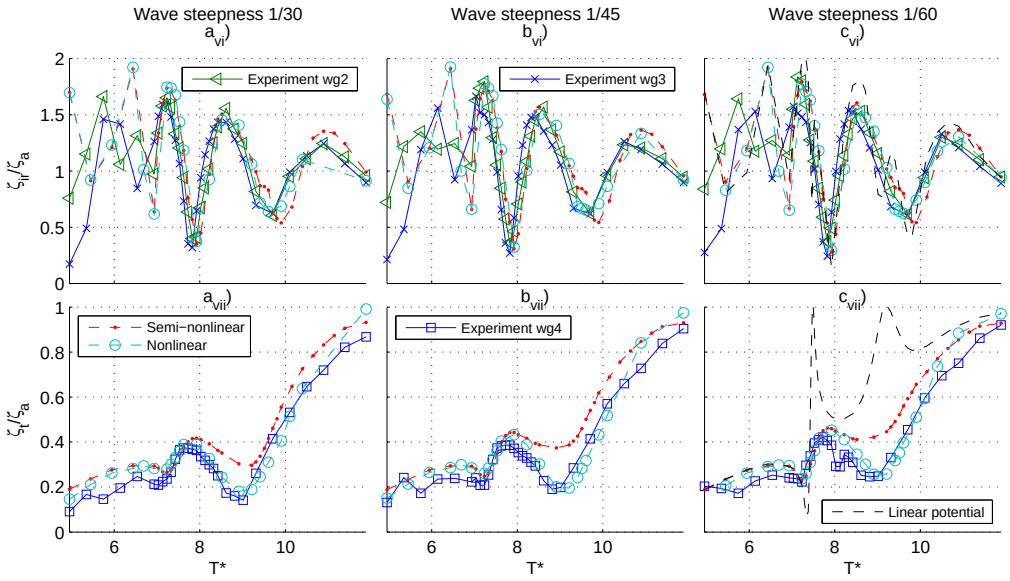

Figure 5.27: Comparison of numerical and experimental results of the measured wave field for 3 different wave steepnesses. The combination of the incoming and reflected wave ζ_{ir} is measured by wave gauges 2 and 3 (wg2 and wg3) that are mounted in parallel between the wavemaker and the hull. The transmitted wave ζ_t is measured by wave gauge 4 (wg4) that is mounted between the hull and the beach.

compared to the experiments. The roll amplitude is at resonance over-predicted by up to a factor 2 depending on the wave steepness. This also has a clear effect on the sway motion. Away from the frequency range around the roll resonance, the sway motion compares quite well. The heave motion is well predicted. A minor discrepancy is that the period of local maximum is over-predicted by about $2-3\%$.

A comparison of the measured wave field in the wave flume is given in Figure 5.27. The agreement is good for the nonlinear hybrid method, while the semi-nonlinear results differ around the roll resonance. A combination of the incoming waves from the wavemaker and the reflected waves from the structure will be measured by wave gauges 2 and 3, see results in Figure 5.27(vi). Wave gauges 2 and 3 are located in parallel between the wavemaker and the hull, see Figure 4.5 for detailed overview of the experimental set-up. The wave gauges 2 and 3 are placed away from any zero nodes of the lowest transverse sloshing modes, and positioned to ensure that any sloshing mode will influence the two wave gauges differently. For wave gauge 4 it is only the transmitted wave that is measured, assuming the reflection from the beach is negligible. The wave measurements from the nonlinear hybrid method are taken for a fixed point in the body-fixed coordinate system, while the wave gauges in the experiments were fixed to the tank. Meaning that evaluation point of the wave gauges in the nonlinear hybrid method will change with time in the Earth-fixed coordinate system. It can from the two parallel wave gauges (2 and 3) be seen some differences between the measured wave field for small periods around the second transverse natural sloshing period of the wave flume, see Figure 5.27 row (vi). The transverse wave is also seen to influence the wave elevation inside the moonpool gap for small wave periods ($T^* \sim 6$), see Figure 5.26 rows (iv) and (v).

The nonlinear hybrid method results for wave steepness 1/60 are different from the two other wave steepnesses with respect to how they were obtained. For the simulations with the two highest wave steepnesses the initial simulations broke down before steady-state conditions were obtained. To avoid this break-down the 5-point Chebychev smoothing algorithm was applied on the entire free surface. The simulations were then stable, but the smoothing algorithm had a large damping effect on the incoming free-surface waves. To avoid this the smoothing algorithm is only applied on the free surface close to the hull, one hull length in each direction, see results in Figure 5.26 for the two highest wave steepnesses (a) and (b). The damping effects on the incoming waves are therefore minimized, see further sensitivity studies in section 6.3.

A curious effect to notice is that there is no resonance behaviour at the piston-mode natural period at $T^* = 8.7$ in any of the results in Figure 5.26. From the corresponding case with forced oscillation in Figure 5.4 the piston-mode resonance was $T^* = 8.7$.

Also when considering incoming waves on a fixed moonpool structure (the diffraction problem) the piston-mode resonant period is found to be $T^* = 8.7$, see Figure 5.28. However, for the floating problem there is no sign of a resonant piston-mode motion around $T^* = 8.7$. This is similar as the results from McIver (2005), who found that within linear potential-flow theory at steady state the main contributions from the diffraction and the radiation potentials on the piston-mode are 180° out of phase around the piston-mode natural period for a freely floating body.

The following brief explanation will illustrate what is found by McIver (2005). In linear

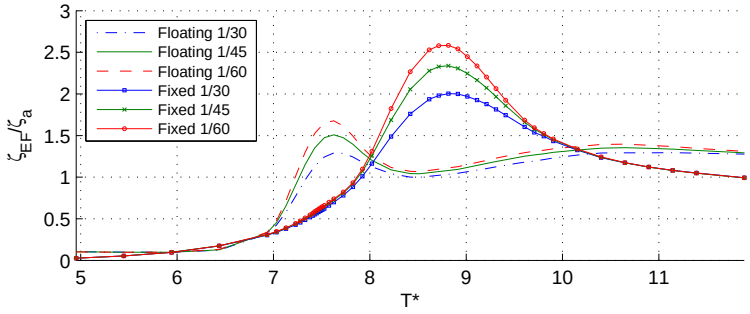

Figure 5.28: Comparison of the piston-mode amplitude in the Earth-fixed coordinate system ζ_{EF} due to incoming waves with different steepnesses on a fixed and a floating moonpool section versus dimensionless wave period. The results are from the semi-nonlinear hybrid method. Not supported with experimental results.

potential flow theory the velocity potential can be split into the following components.

$$\varphi = \varphi_i + \varphi_d + \sum_{j=2,3,4} \varphi_j \tag{5.16}$$

where φ_j are the radiation potentials found from forced oscillations of the structure in direction j, and from where the added mass and potential damping is calculated. Further φ_i is the velocity potential associated with the incoming wave. φ_d is the diffraction potential associated with the wave field generated by the presence of the structure in incoming waves, i.e. the diffraction problem is solved using the body-boundary condition $\partial\varphi_d/\partial n = -(\partial\varphi_i/\partial n)$. In the moonpool problem, the main contributions from φ_d and φ_3 will cancel around the piston-mode natural period.

To ensure that the piston-mode resonance in general is canceled, a few additional numerical studies with different moonpool widths and drafts were simulated. It was found that the results were consistent with results in Figure 5.26.

After the first peak in heave at $T^* = 7.4$, the moonpool wave motion becomes in phase with the heave response (see the phase angle α in Figure 5.29a), where α is defined as the phase angle between the heave acceleration of COG and the moonpool wave motion. This causes a decrease in the heave response; the moonpool wave response decreases the heave motion. This is illustrated in Figure 5.30. The heave motion builds up faster than the moonpool wave response. After the initial build-up phase the moonpool wave response is still increasing while the heave response starts decreasing. The initial heave response is thus larger than the steady-state response. This is not only related to the viscous simulations, but also the potential flow calculations capture this effect. It means that the moonpool works as a heave minimization device. The steady-state linear potential wave excitation force were given in Figure 5.21 and confirm the minimum heave motion around $T^* = 7.9$.

The phase angle β between heave and roll motion is given in Figure 5.29b. For low periods, heave and roll are 180° out of phase, causing high local heave motion on the side hull facing the incoming waves. Similarly the combined heave and roll motion has a cancellation effect on local heave on the aft side hull. For higher periods (stiffness

dominated) the heave and roll motion are 90° out of phase, meaning that the hull motion is in phase with the incident wave motion. The snapshots from Figure 5.31 show how the phase angle between the heave and roll motion affects the hull motion. For instance, there is a cancellation effect on the trailing hull around $T^* = 7.4$. Basically it is a visualisation of the results from Figure 5.29, the snapshots are given for 10 equally spaced time instances throughout one period at steady-state.

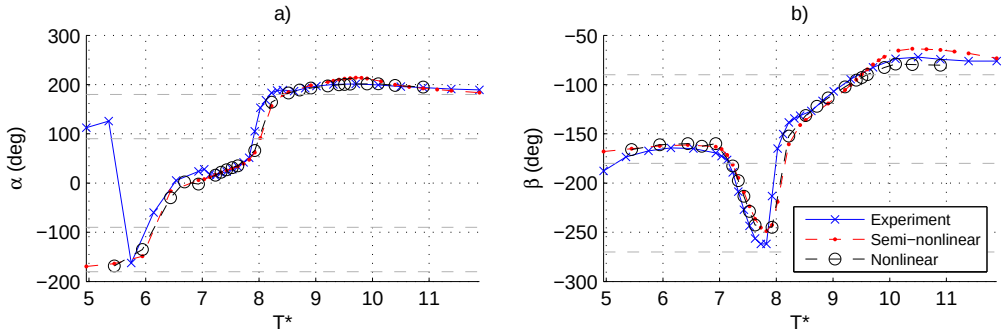

Figure 5.29: **a)**: phase angle α between heave acceleration and moonpool wave motion (from copper tape on right side of the moonpool gap). **b)**: phase angle β between heave and roll acceleration. Wave steepness 1/60.

There has not been identified any significant interaction effects between either the sway or roll motions and the moonpool motion. However, the sway and roll motion should be expected to excite sloshing modes within the moonpool gap, but for the present set-up the first sloshing mode natural period is 0.36s ($T^* = 3.6$).

For the nonlinear hybrid method results, the conclusions are different from the semi-nonlinear hybrid method results. The roll motion is in good agreement with the experimental results. In the semi-nonlinear simulation, the maximum roll amplitude is 7.6° for wave steepness 1/60, while the corresponding result is 4.8° in the nonlinear simulation. One conclusion that can be drawn is that much less vorticity is being shed in the semi-nonlinear hybrid method compared to the nonlinear hybrid method. Figure 5.32 illustrates that there is a difference between the semi-nonlinear and the nonlinear hybrid method, here the liquid velocity vectors around the outer edges are shown from both the semi-nonlinear and the nonlinear hybrid method simulations. The figure shows a close-up of the two outer hull edges and illustrates that the shed vorticity structures generated in the nonlinear hybrid method are significantly larger than in the semi-nonlinear hybrid method. We will come back to a detailed investigation of the differences between the semi-nonlinear and the nonlinear hybrid method, by investigating the damping caused by forced oscillations.

The semi-nonlinear hybrid method approach has been proven to work well for predicting the piston-mode motion in forced heave oscillation tests (see the previous chapters and Kristiansen and Faltinsen (2012)). There the relative liquid motion is dominated by the water (piston-mode) motion. A detailed investigation of the shed vorticity structures during forced heave oscillations will be given and discussed later.

A 2D freely floating vessel close to a terminal was investigated by Kristiansen and

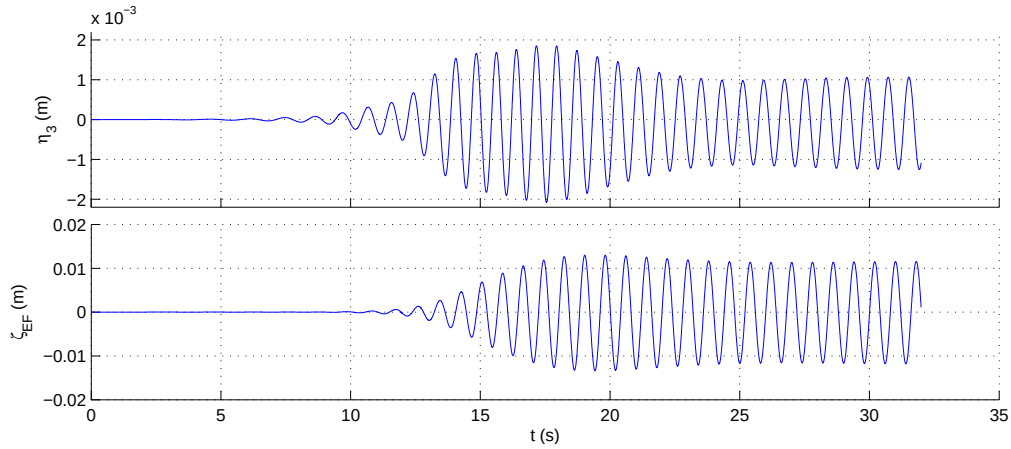

Figure 5.30: Time-series example illustrating how the heave motion excites the piston-mode motion, and later how the heave motion is reduced as a consequence of the piston-mode motion inside the moonpool gap by means of a semi-nonlinear simulation, with wave period $T^* = 7.9$ ($T = 0.8$s) and 1/60 wave steepness. ζ_{EF} space-averaged wave elevation inside the moonpool in the Earth-fixed coordinate system.

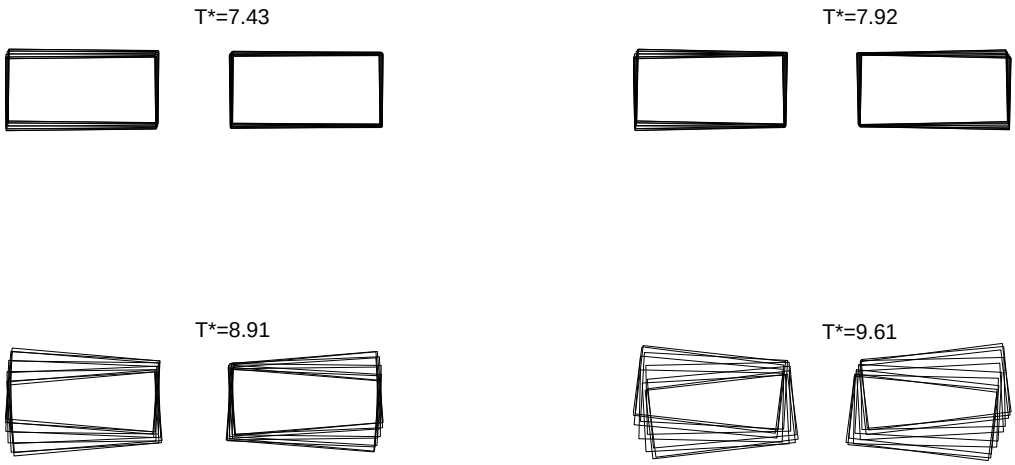

Figure 5.31: Snapshots taken from the steady state response for 4 different wave periods from the semi-nonlinear hybrid method calculation for wave steepness 1/60. $T^*/10$ between each snapshot.

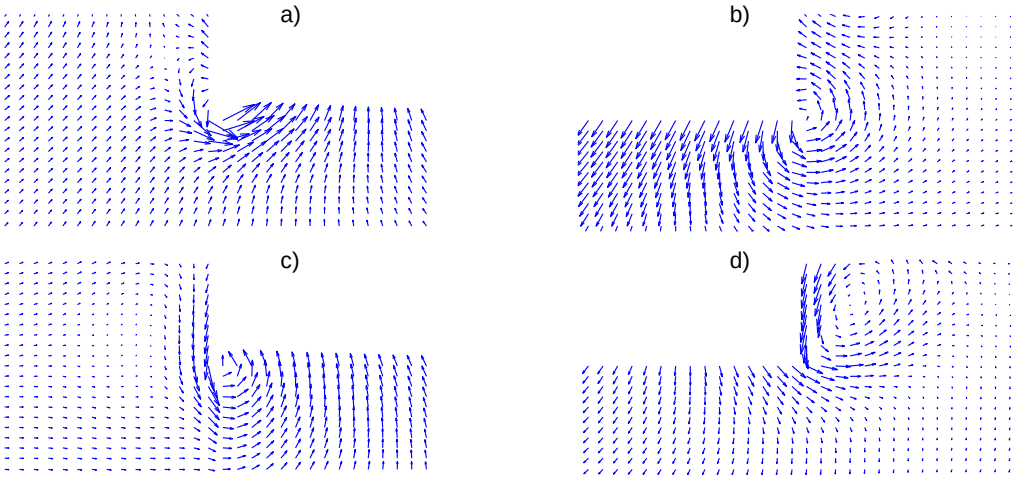

Figure 5.32: Liquid velocity vectors in the Earth-fixed coordinate system from the semi-nonlinear hybrid method in a) and b), and from the nonlinear hybrid method in c) and d). Left: close-ups of the left bilge of the left box. Right: close-ups of the right bilge of the right box. The wave period in both simulations is $T = 0.96$s, and steepness of incoming wave is 1/60.

Faltinsen (2010) using both numerical and experimental methods. Their numerical work was motivated by the question: what is the main cause to the discrepancies between linear potential-flow theory and what was measured? (1) Flow separation or (2) nonlinear boundary conditions. Our findings are consistent with the results from Kristiansen and Faltinsen (2010) for pure heave and piston-mode motion, i.e. that flow separation is the main reason for the difference between linear potential-flow theory and experimental measurements. It is in prediction of the roll motion more complicated, due to the poor results from the semi-nonlinear hybrid method in predicting the roll motion. A few additional physical related explanations are investigated to explain the difference. It is still thought that the flow separation from the edges is the most influencing reason, and the change in the pressure field due to that. The first effect to investigate is the change from a linear body-boundary condition to an exact body-boundary condition in a body-fixed coordinate system. The separation point will in both cases always be on the sharp edges of the body. For the linear case it will be fixed in space, and an in-out flow through the nearby non-moving body-boundaries is disturbing the pressure around the edges. For the body-exact case the separation point will be the physically correct point. The second effect to investigate is the importance of the nonlinear non-viscous terms. Meaning, what happens at the intersection in the semi-nonlinear hybrid method where the nonlinear non-viscous terms are not communicated between the two domains. Any inaccuracies at the intersection in the semi-nonlinear hybrid method means that nonlinear effects are important in the potential flow domain. Then it is a question if this can be traced back to free-surface or body-boundary nonlinearities. Further studies with forced sway, heave and roll motion will be presented later, with a closer look at local pressure and flow details around the edges around the hull.

5.3.3 Comparison with potential-flow theory

As pure linear potential flow theory is used in many engineering applications, results are presented in Figure 5.33a together with results from the semi-nonlinear hybrid method and experiments with wave steepness 1/60. These results are obtained by solving for linear potential flow in the whole water domain using the present semi-nonlinear code. All motions are over-predicted around resonance by the potential-flow theory. The sway resonance at 3.2s is not shown. The large over-prediction of the resonant heave and piston-mode motions by linear potential-flow theory shows the importance of flow separation at the lower moonpool entrance in the floating 2D moonpool problem. The roll motion is further over-predicted by a factor 2 in this case. The damping from flow separation is considered to be the main reason for this difference. The damped natural roll period is predicted to be 4% lower in the pure potential flow case than what is predicted by the semi-nonlinear hybrid method.

The comparison of the outgoing waves is given earlier in Figure 5.27c$_{vi}$. It is seen a big change in the transmitted wave before and after the first natural heave period and that the linear potential-flow solution over-predicts the transmitted wave from the structure. Meaning that the presence of shed vorticity influences the generation of free-surface waves. It is for this case connected to the amplitude of the piston-mode inside the moonpool gap and the piston-mode ability to generate outgoing waves. The combination of the incoming and reflected wave is on the other hand in good compliance with the experimental results.

5.3.4 Low forward velocity

Due to the benefits gained by employing a body-fixed coordinate system, the nonlinear hybrid method is suitable of simulating a towing of a free-floating body in incident regular waves. The nonlinear hybrid method is applied to the same physical set-up as in the floating experiments, while adding towing of the hull in both head and following seas using Froude number 0.04, where the Froude number is defined based on the total length of the hull, including the moonpool gap, as defined in equation (4.1). We numerically move the ends of the springs on both sides of the hull to enforce forward motion of the hull. The hull will therefore experience a frequency of encounter, which is different from the wave frequency seen in the Earth-fixed coordinate system.

The wave steepness is kept constant at 1/60 where the wave lengths are calculated based on the stationary case. This means that for the same period of encounter, the waves in head seas will be higher than the waves for zero Froude number. In Figure 5.33b results with low forward velocity are compared against the nonlinear simulations without forward velocity. The Froude number dependency is relevant for considering the effect of combined waves and current.

Potential flow results for a semi-submerged circular cylinder with low forward velocity were presented by Zhao and Faltinsen (1998). They noticed that the predicted maximum response in heave occurred at a frequency slightly different from the zero velocity case, due to coupling with sway at non-zero forward velocity. This is also true for the lowest heave natural period in Figure 5.33b. The maximum response occurs for a slightly higher period in following seas, and for a slightly lower period in following seas. The trend in the numerical simulations with low forward velocity is that the rigid-body motion is amplified with low forward velocity in head seas, and smaller in following seas. This is similar to

the results from Zhao and Faltinsen (1998), although it can be noted that their results show that for higher periods than used in Figure 5.33b the sway motion will be higher for following seas and lower in head seas.

The roll motion is clearly affected although not dramatically: it is increased in head seas, and decreased in following seas. The moonpool wave amplitude is only decreased by $2-3\%$ due to forward velocity, which is consistent with findings from forced heave oscillations with low forward velocity.

For the forced heave oscillation case with low forward velocity the intersection between potential and viscous flow could be stretched horizontally to the end of the numerical wave tank. This only leaves the top fluid layer to be re-meshed due to the outgoing wave and allows the vorticity to be transported down the numerical wave tank. For the floating case this is no longer possible due the roll motion (as described earlier), and the intersection between the potential and viscous flow have to be equal for the stationary case and the forward velocity case. This means similar meshes as in Figure 5.23 are used for the simulations with low forward velocity. Meaning that vorticity transported away from the hull will easily reach the intersection between potential and viscous flow on the downstream side. However, the dissipation of vorticity is quite high with use of the linear upwind method for solving the advection step, which limits the amount of vorticity reaching the intersection.

Notice, that the simulations with low forward velocity did not converge with the same accuracy as the numerical results with a stationary hull due to vorticity reaching the interface between potential and viscous flow, see the convergence study in section 6.3.

5.3.5 Comparison with single hull

To put the rigid-body motions of the moonpool hull in some perspective, a comparison to the rigid-body motions of a single mono-hull is given here. The dimensions used for the single hull are equal to the moonpool hull, but with a closed moonpool gap. The mass is increased correspondingly, and the inertia is changed by keeping the radius of gyration constant ($r_{xx} = 0.18$m). The comparison of all three rigid-body motions and the wave field is given in Figure 5.34.

Three differences can be observed for the rigid-body motions of the hull, first the additional heave resonance introduced by the moonpool, second the increased roll natural period without moonpool, and last, the cancellation effect in heave in the moonpool case. The increased roll natural period is mostly an effect of increased inertia and change of the metacentric height. It is further clear that the moonpool has a significant effect on the rigid-body motions.

The presence of the moonpool also influences the reflected and transmitted wave, see the two bottom sub-figures in Figure 5.34.

Since the semi-nonlinear hybrid method over-predicts the roll motion around resonance (see Figure 5.26), it is also expected that the single hull results in Figure 5.34 are affected and over-predicted. However, the qualitative differences explained above are still thought to be valid.

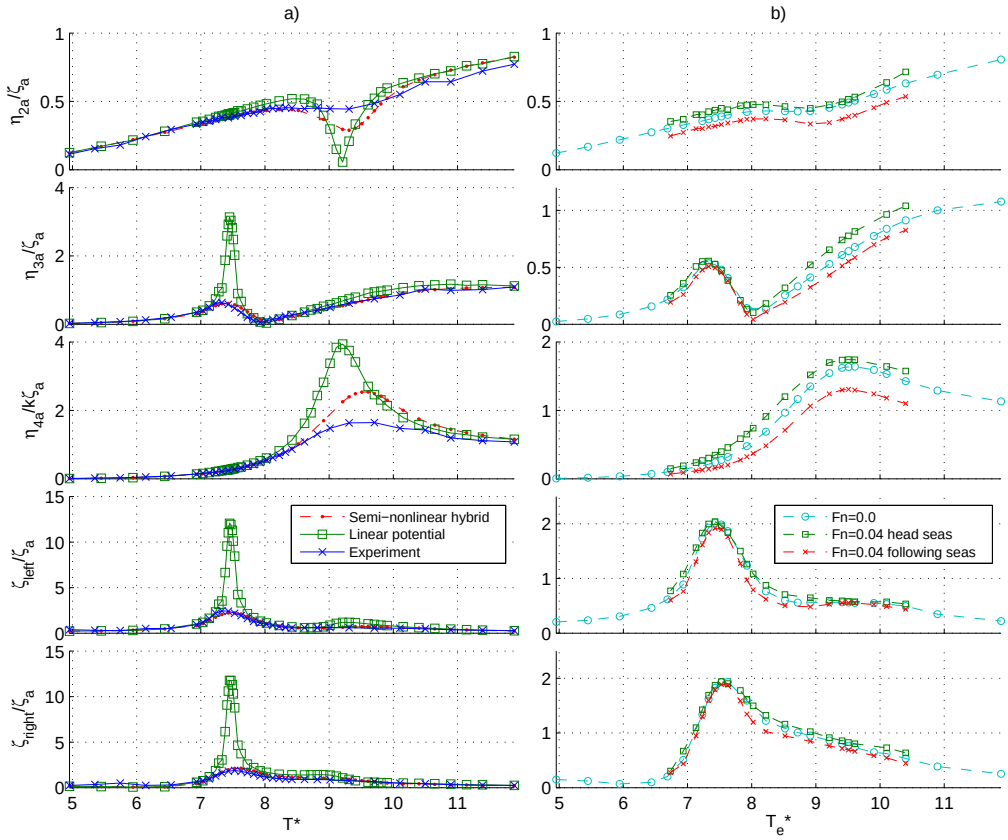

Figure 5.33: In **a)**: Comparison between linear potential flow theory, the semi-nonlinear hybrid method and experimental data. In **b)** Results from the nonlinear hybrid method with low forward velocity in head and following seas. T_e^* is the wave period of encounter. All simulations in both **a)** and **b)** are with wave steepness 1/60.

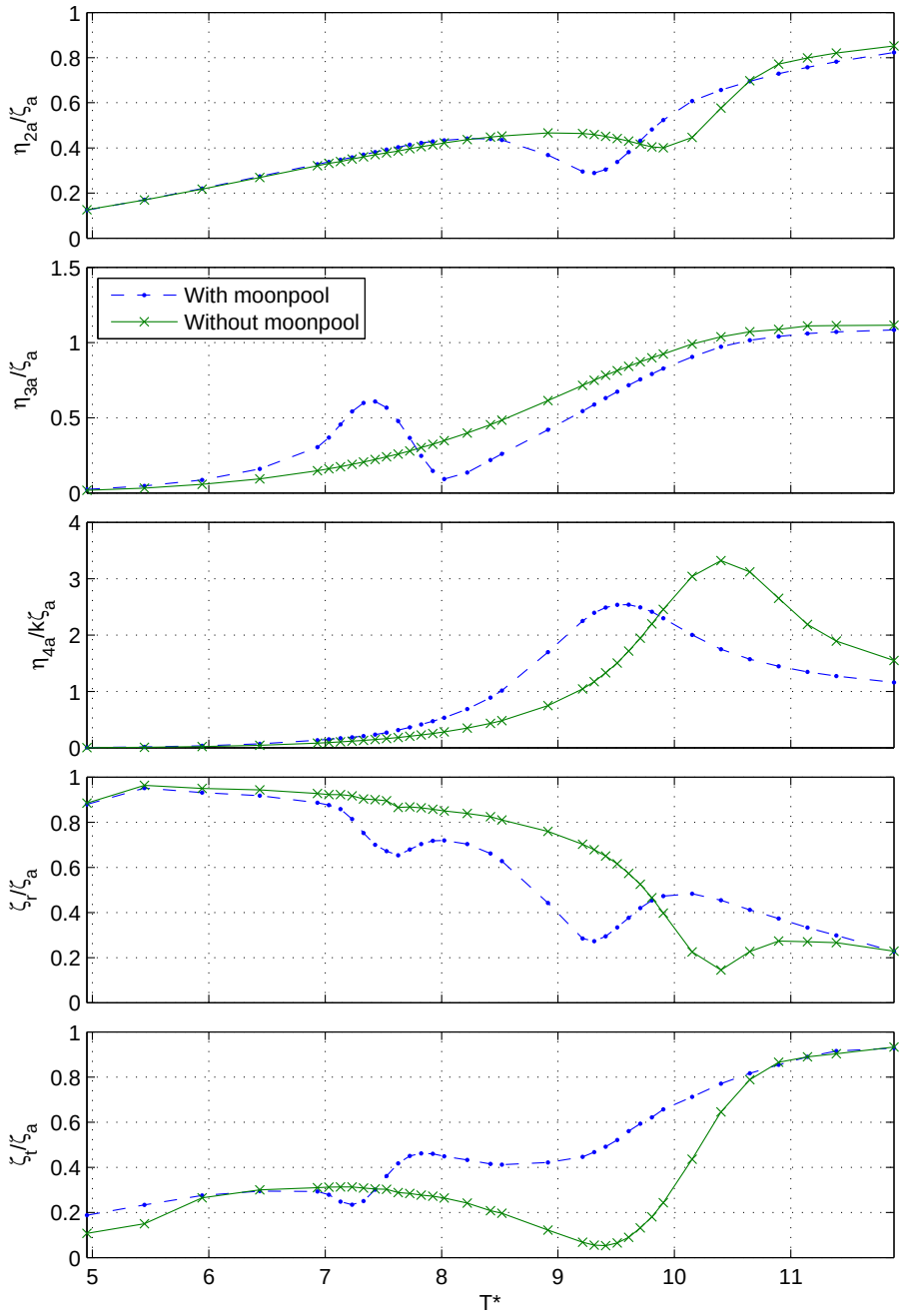

Figure 5.34: Comparison of the rigid-body motion response amplitudes, reflected wave amplitudes (ζ_r) and transmitted wave amplitudes (ζ_t) between a hull with and without a moonpool subjected to waves with steepness 1/60 using the semi-nonlinear hybrid method.

5.3.6 Appendages in the moonpool inlet

The influence of appendages at the moonpool inlet on the rigid-body motion and piston-mode behaviour in waves is studied by use of the semi-nonlinear hybrid method for three wave steepnesses (1/30, 1/45 and 1/60), see Figure 5.35. There are no experimental tests to validate the result.

The numerical setup with appendages has the following dimensional properties. The appendages are horizontal and rectangular with dimensions 1.0cm wide by 0.5cm high, and are placed on each side of the moonpool gap entrance. The appendages then cover 20% of the width of the moonpool gap, and extend 5% of the draft in the vertical direction. This is equivalent to appendage configuration #1 from the forced heave oscillation study.

The sway and roll motions were not influenced by the appendages and therefore not given in Figure 5.35. The first heave natural period is increased compared to the square opening case, and the resonance top is wider. For the moonpool wave amplitude, the appendages has a significant damping effect; the piston-mode amplitude is reduced by $20-30\%$ at resonance. This can partly be explained by a reduced inlet opening causing larger flow velocities at the lower moonpool entrances. Further, the strength of the shed vorticity is increased due to a lower effective interior angle relative to the rectangular section. This is in accordance with results from the forced heave oscillation study and Kristiansen and Faltinsen (2012). Note that for the forced heave oscillation study it was found a decrease in the piston-mode amplitude using appendages in the linear potential flow solution.

The appendages also change the cancellation frequency in heave, and the minimum heave response at the cancellation frequency is increased. The corresponding piston-mode resonance period from the forced heave oscillation set-up are given in Table 5.4 as $T^* = 8.8$, the results in Figure 5.35 are consistent with the conclusion from before. There are no signs of resonance behaviour in the freely-floating problem at the piston-mode resonance period.

The comparison between the forced heave oscillation experiments and the hybrid methods showed that the numerical methods were unable to accurately capture the moonpool motion for the largest appendage (#2), see section 5.1.6. The reason for the difference is thought to be that our numerical viscous method does not deal with turbulent mixing of vorticity. It is unclear how this will affect the results seen in Figure 5.35 and actually all results with the floating body. However, since there is good agreement between the nonlinear hybrid method and experimental data, it is thought to be a secondary effect. This conclusion may not be actual for a floating body with appendages, since we have no experimental validation data to support the conclusion either way.

5.3.7 Experimental repetition test

A few days after the three experimental test-series with 1/30, 1/45 and 1/60 wave steepness were performed, a test-series with 1/30 wave steepness was repeated. Prior to this the location of the model in the wave flume was changed; the model was moved closer to the wavemaker. This was done to improve the video-recording capabilities of the experiments. The reason was that the previous position of the model was behind a large steel beam, which blocked the video camera view. Also the anchors to the roof and the pullies had to be moved the same distance. The consequence of this was that the pre-tension

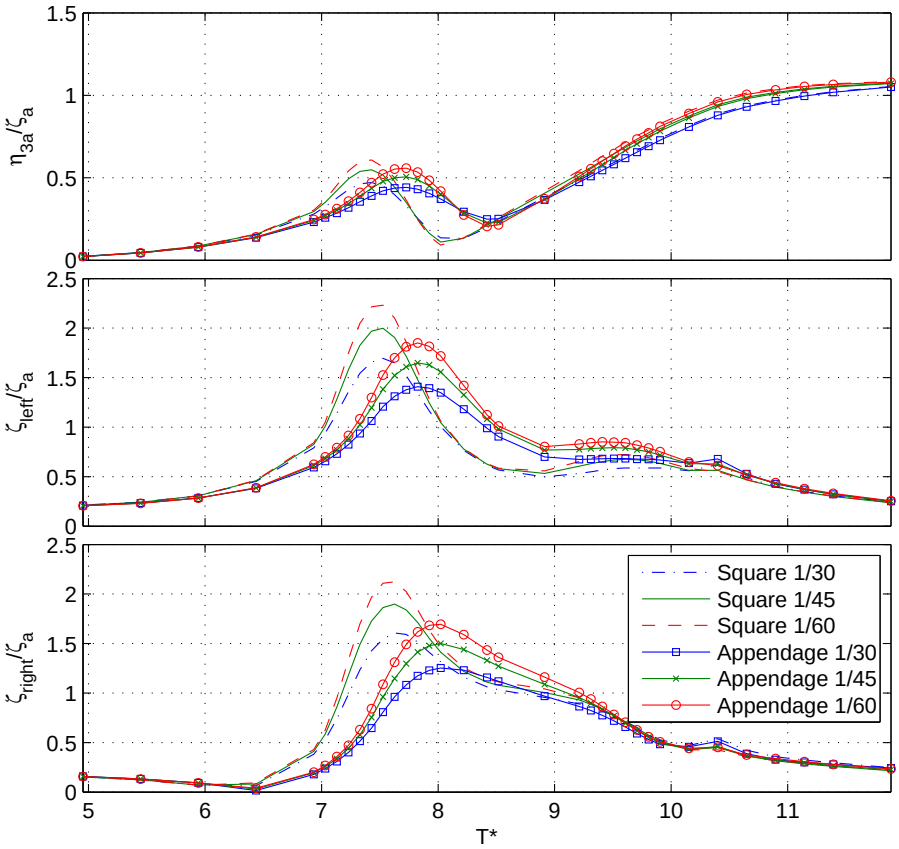

Figure 5.35: Comparison of the heave η_{3a} and moonpool piston-mode response at left-side ζ_{left} and right-side ζ_{right} of the moonpool with and without appendages for 3 different wave steepnesses using the semi-nonlinear hybrid method.

might have changed. The pre-tension has a restoring effect in roll, such that the roll motion might have been influenced. Everything else about the repetition test is the same as the original test.

As the model was moved closer to the wavemaker, reflections from the wavemaker returned sooner, and the steady-state condition became shorter. It was also found that the wave flume had a small leakage resulting in a different position of the beach relative to the free surface. The latter fact gave some reflections from the beach. In total there is some reflections for the higher wave periods, (see results in Figure 5.36a).

There is also a difference seen in the right moonpool wave gauge. Here it is believed that the repetition test is more correct, as it would fit better with the trend from the 1/45 and 1/60 tests, see Figure 5.26. The original results do not show much decrease in the ratio ζ_{right}/ζ_a, between the 1/45 and the 1/30 tests. Meaning that there could be an error in the calibration factor for the first original test of wave steepness 1/30.

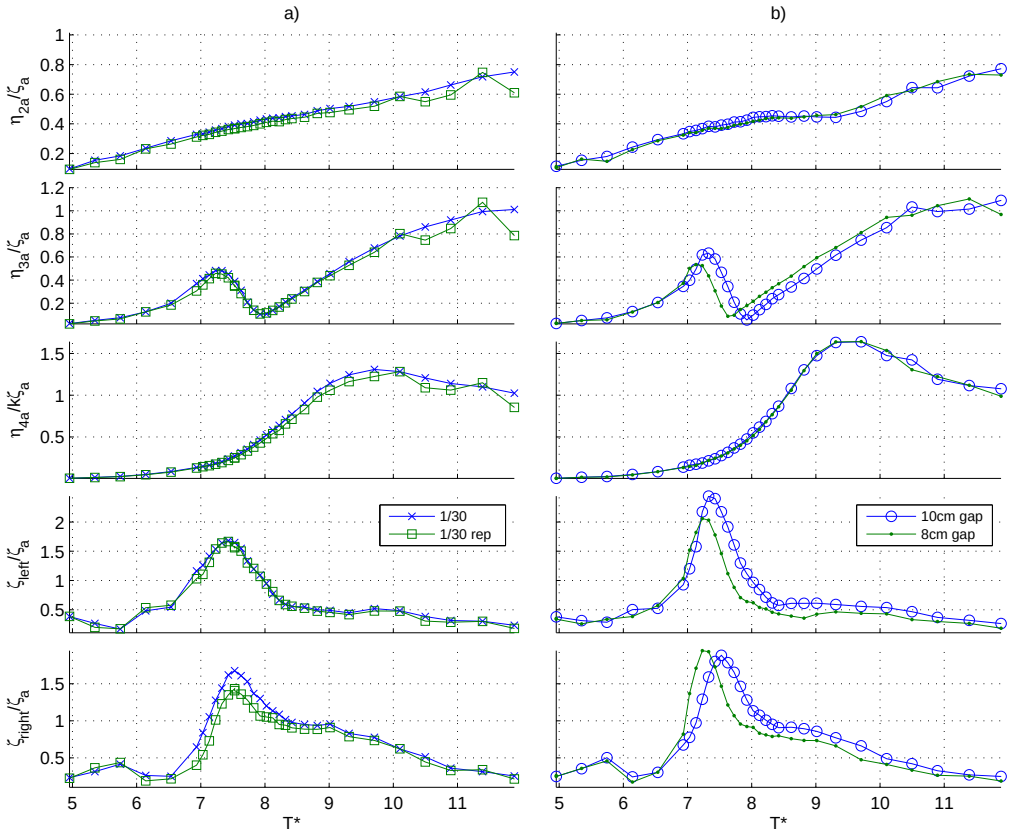

Figure 5.36: In **a)**: Experimental results for wave steepness 1/30, with repetition test. In **b)**: Experimental results for comparison between 8cm gap and 10cm gap with 1/60 wave steepness.

5.3.8 Smaller moonpool gap

In the end of the experimental programme it was decided to do an additional test with smaller width of the moonpool gap. The aim was to investigate the influence of the moonpool width on the behaviour of the structure and the moonpool. The moonpool width of the model was relatively easy to change. However, since the total length of the structure became 2cm shorter, the pretension in the mooring lines had to be adjusted. Meaning that there might be a small difference in the pre-tension between the two tests. Note that the wave period in Figure 5.36b) for the 8cm gap case is dimensionless by the same factor as the 10cm gap case, i.e. by 10cm.

There is a small difference in the right moonpool wave amplitude between the two tests, only the period of maximum wave response have changed. While the difference is larger for the left moonpool wave amplitude, here both the maximum response period and amplitude has changed. The moonpool wave amplitude is smaller for the 8cm moonpool gap case.

The main difference between the two set-ups is the decrease in the heave motion at the first heave natural period. This is in-line with the obvious conclusion that the rigid-body motion will approach the single body behaviour when the gap width is decreased.

5.3.9 Effect of changing draft

The results from forced heave oscillations showed that the piston-mode amplitude were independent on the draft of the hull. Since there is no resonant effect at the piston-mode natural period, this may not be the case for the floating body. Therefore the effect of changing the draft is here checked by the use of the nonlinear hybrid method for two additional dimensionless drafts with wave steepness 1/60. See results in Figure 5.37. In the numerical calculations the radius of gyration is kept constant, and the position of the centre of gravity is fixed with regards to the mean free-surface. Basically every parameter except for the mass, the draft and the moment of inertia is unchanged. The consequence is that all natural periods will change. We are however, only interested in comparing the maximum value of the wave elevation inside the moonpool gap.

The results in Figure 5.37 are consistent with the forced heave oscillation study with different drafts, the maximum moonpool gap amplitude is quite independent of the draft. However, there is a small increase on the left side of the moonpool for the lowest draft $d^* = 0.833$ in Figure 5.37 compared to the two other numerical cases. The results in Figure 5.37 shows once again that there is no sign of a resonant response ot the piston-mode resonance period as given in Table 5.4.

5.3.10 Difference in added mass and damping for the floating and forced oscillation cases

Due to different dimensionless water depths in the experimental setups, the finite-water depth effects can possibly influence the added mass and potential-flow damping differently for the two setups. The added mass and potential-flow damping coefficients for heave are presented in Figure 5.38, and roll in Figure 5.39. It is as expected seen some difference for the higher periods, however, the difference is small around the natural periods in heave and roll. Two dimensionless water depths h^* are presented, where $h^* = 10$ corresponds to

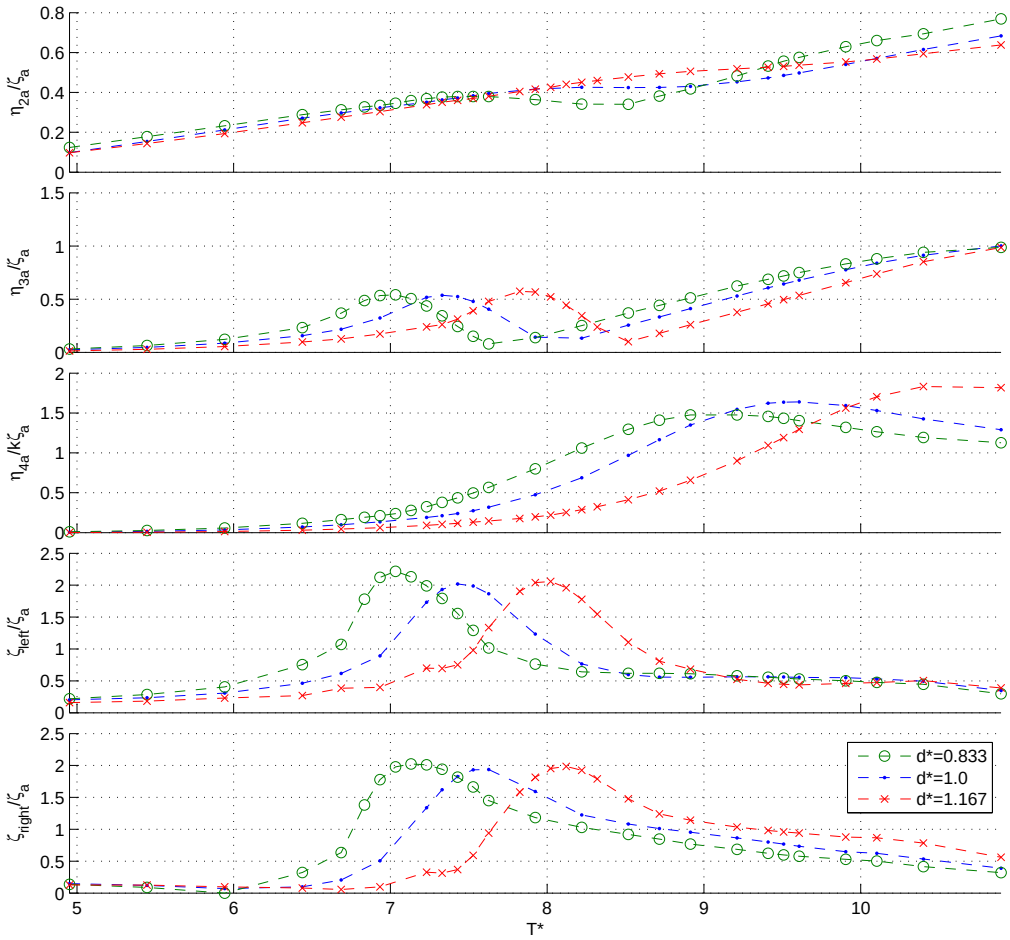

Figure 5.37: Effect of changing draft on the rigid-body and moonpool motions, simulations are performed by the nonlinear hybrid method.

the floating experimental setup and $h^* = 5.56$ corresponds to the forced heave oscillation with low forward velocity experimental setup. The larger water depth corresponds to the case from Faltinsen et al. (2007) which are given in Figure 5.38 and the comparison towards our results are good.

Since the different water depths have a small influence on the added mass and potential-flow damping coefficients in Figures 5.38 and 5.39, it was decided not to check the influence of the water depth changes in the nonlinear hybrid method. There the water depth had to be changed due to limitations in η_4^{Max}, and therefore the numerical water depth was larger from what was tested experimentally, and the dimensionless water depth exceeded $h^* = 10$.

The added mass and potential-flow damping coefficients in Figure 5.38 and Figure 5.39 are obtained by the same approach as the added mass and potential-flow damping coefficients in section 5.2.1.

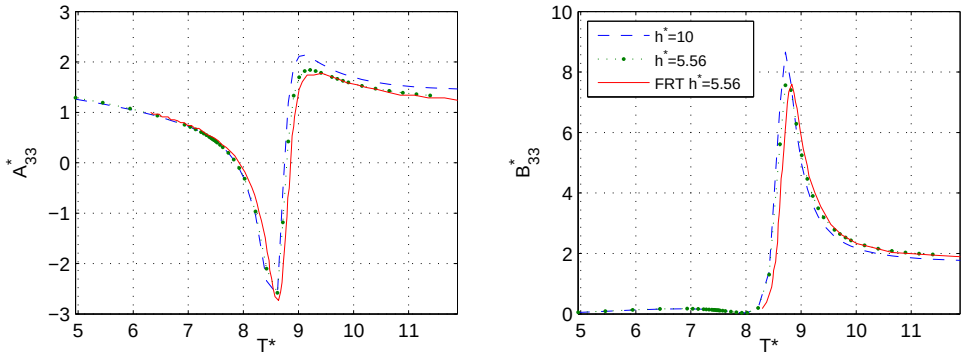

Figure 5.38: Dimensionless added mass and potential damping in heave for two different water depths corresponding to the dimensionless water depths in the two experimental programmes. Numerical results from Faltinsen et al. (2007) (FRT) are also given.

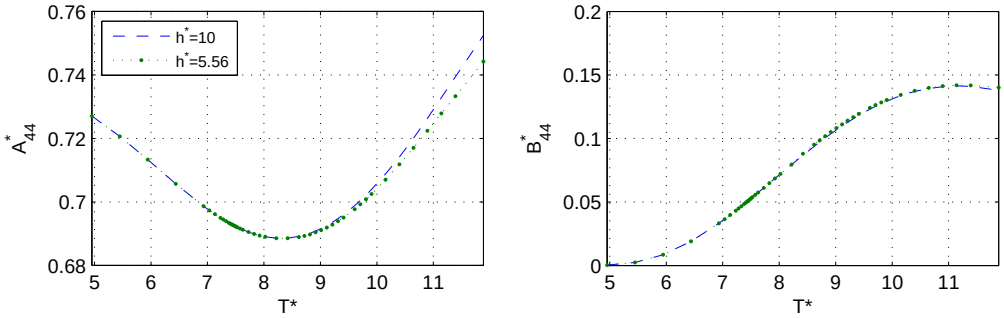

Figure 5.39: Dimensionless added moment of inertia and potential damping in roll for two different water depths corresponding to the dimensionless water depths in the two experimental programmes.

5.4 Damping from forced oscillations

The previous sections about forced heave oscillations studies were focused on the piston-mode amplitude and the comparison with experiments. In this section focus will be on the local and global pressure details between the two hybrid methods in order to study the differences seen in Figure 5.26. That means we want to further investigate the shortcomings of the semi-nonlinear hybrid method to capture roll motions, as shown in Figure 5.26. A detailed comparison of the damping moment about COG (180° out of phase with the roll angular velocity) due to forced roll about COG has been performed using both hybrid methods, see Figure 5.40a.

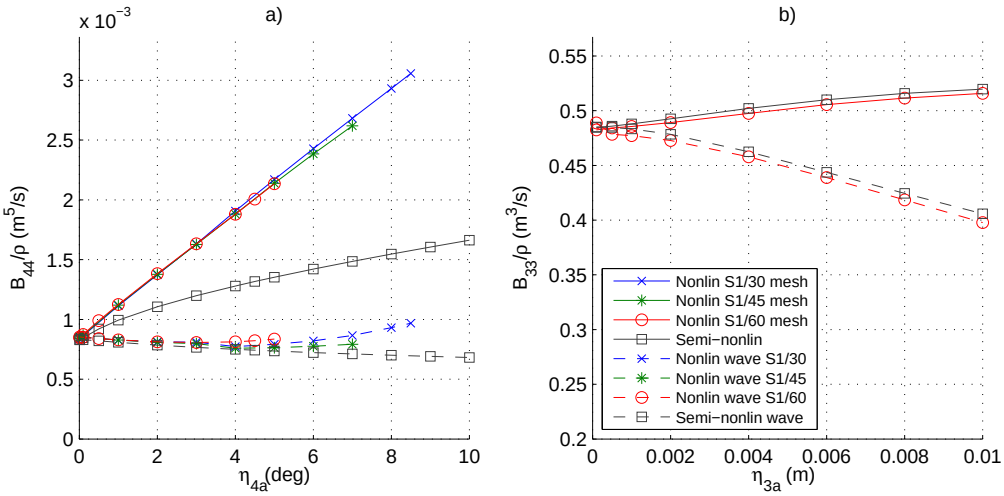

Figure 5.40: Linearized damping coefficients for different forcing amplitudes from the semi-nonlinear and nonlinear hybrid methods for forced roll oscillation in **a)**, and forced heave oscillation in **b)**. The period is $T^* = 9.51$ ($T = 0.96$s) for all simulations.

In Figure 5.40a the nonlinear hybrid method results are obtained from three different meshes, these corresponds to the meshes used for the 1/30, 1/45 and 1/60 wave steepness cases in Figure 5.26. Note, it is not the meshes that are different. It is where the intersection between the potential and viscous flow domain is located. The meshes are created such that the 1/60 mesh may at maximum simulate roll angles up to 5.0°. Further the 1/45 mesh may at maximum simulate 7.0° and the 1/30 mesh may at maximum simulate 8.5°. This is corresponding to the maximum roll angles found from the experimental programme including a safety factor to allow over-prediction in the numerical method. See illustrations on how the different meshes are created in Figures 5.23-5.25. For the semi-nonlinear hybrid method results in Figure 5.40a the same mesh is used for all simulations.

From the forced roll oscillations the corresponding linear roll damping coefficient B_{44} has been calculated. The simulations are performed for forced roll oscillation with different roll amplitudes (see Figure 5.40a) for a period around the natural roll period $T^* = 9.5$ ($T = 0.96$s). The results for forced roll oscillation are somewhat surprising; the trend is

different for the semi-nonlinear and the nonlinear case. Results for the zero degree limit are similar and equal to the wave radiation damping due to outgoing waves. The wave radiation damping is calculated from energy of outgoing waves. The nonlinear hybrid method has a clear linear dependence of B_{44} on the roll amplitude, which is not present in the semi-nonlinear hybrid method. Even for small roll angles there is a significant difference between the semi-nonlinear and the nonlinear hybrid method.

The findings in Figure 5.40a) agree with the results from Braathen (1987) or Braathen and Faltinsen (1988), who found that vortex shedding had a secondary effect on the wave radiation damping in roll. The latter effect is associated with small far-field flow due to local vorticity at the body edges. Furthermore, it was found by Braathen (1987) or Braathen and Faltinsen (1988) that the presence of free-surface waves had an important effect on the shed vorticity generation and eddy-making damping. Note here that Braathen (1987) compared results using a rigid free-surface condition and a nonlinear free-surface condition. It will later be presented simulations with a rigid free-surface condition in a body-fixed coordinate system, and the resulting damping coefficient.

The roll damping coefficients up to forced oscillations with 4 degrees roll are almost equal between the three different meshes used in the nonlinear hybrid method. Above 4 degrees there is seen a small difference between the predicted B_{44}, even though there is a higher possibility of vorticity reaching the intersection between the potential and viscous flow domain for the meshes generated to simulate higher roll angles the damping coefficients remains linear with the roll amplitude. Such that the pressure on the hull is not very sensitive to the inaccuracies on the intersection between the potential and viscous flow domain. However, this is not true for simulations with roll angles above 7 degrees. After some time the inaccuracies grow as vorticity is reaching the intersection between the potential and viscous flow, up to a point when the simulation breaks down.

The difference between the total damping and the wave radiation damping in the nonlinear hybrid method is mainly due to vortex shedding, i.e. eddy making damping. It is a well-known fact that viscous shear stresses have a small influence on roll damping. The eddy-making damping depends on the instantaneous positions, velocities and strengths of shed vorticity. The latter fact can be qualitatively indicated by using a thin free-shear layer and boundary layer method as presented by Faltinsen and Pettersen (1987). The derivation using a thin free-shear layer can be found in Appendix B. It follows then that the motion of the separation points as it is accounted for in the nonlinear method cause a different expression for the amount of shed vorticity.

In the semi-nonlinear simulation with wave steepness 1/60, the roll amplitude is 7.6° at roll resonance and the heave amplitude is 4.5mm at the first heave resonance. However, in the nonlinear simulation the roll amplitude is 4.9° at roll resonance and the heave amplitude is 3.9mm at the first heave resonance, see Figure 5.26. If we further assume a one degree of freedom system $\eta_{ja}\left(-\omega^2\left[A_{jj}(\omega)+m_{jj}\right]+i\omega B_{jj}(\eta_{ja})+C_{jj}\right)=F_j$, and that the inertia and hydrostatic restoring force terms cancel each other at resonance, the relation between the response and the damping coefficient from Figure 5.40 should be constant, i.e. $C_j=\eta_{ja}B_{jj}(\eta_{ja})$ should be independent if it is calculated in the semi-nonlinear or nonlinear hybrid method. For the heave case there is a 2.5% difference in C_3, and for the roll case there is a 11.4% difference in C_4 between the semi-nonlinear and nonlinear hybrid method. The latter discussion only proves that there is consistency between damping and the time-domain rigid-body response.

When studying the damping in heave B_{33} (see Figure 5.40b) due to forced heave

oscillations with the same oscillation period as in Figure 5.40a), we find that the agreement between the two hybrid methods are significantly better. However, here damping due to shed vorticity is of secondary importance, and the total damping is dominated by wave radiation damping. The predicted heave motion response in Figure 5.26 are also almost equal between the two hybrid methods for the given period.

The relation between the importance of viscous damping compared to wave radiation damping is depending on the oscillation period. It is seen a higher influence of viscous damping when studying forced oscillations in heave around the first natural heave period. The heave damping coefficient B_{33} is then also different for the two hybrid methods, see Figure 5.41. The difference between the two hybrid methods is similar as to that seen in Figure 5.40a). The damping coefficient B_{33} has a clear linear dependence on the heave amplitude in the nonlinear method.

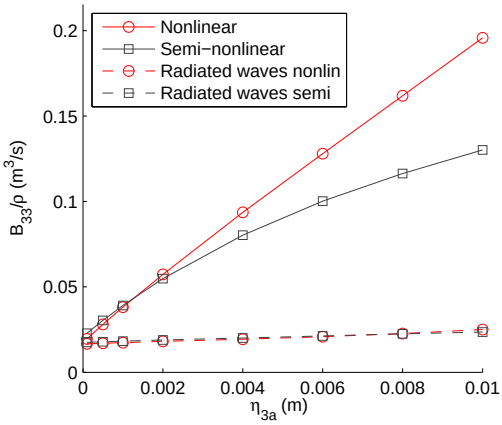

Figure 5.41: Linear damping coefficients for different forcing amplitudes from the semi-nonlinear and nonlinear hybrid methods for forced heave oscillations for period $T^* = 7.43$ $T = 0.75$s.

In order to better understand the shortcomings of the semi-nonlinear hybrid method, the local pressure distribution on the hull is compared with the nonlinear hybrid method. Figure 5.43 compares the pressure at the outer edges of the hull due to forced roll oscillation of 3 degrees, Figure 5.42 show the location of the pressure points. Furthermore, Figure 5.44 compares of the pressure at the moonpool edge and the outer edge of the hull due to forced heave oscillation of 0.008m. It is the dynamic pressure value from the cell closest to the edge that is given. By dynamic pressure it is meant the total pressure without the effect of hydrostatics and atmospheric pressure.

For the forced roll oscillation case of 3° with oscillation period of $T^* = 9.51$ ($T = 0.96$s) in Figure 5.43 a difference between the two hybrid methods is seen for point 1 on the vertical side of the edge. However, the dynamic pressure is for point 2 on the horizontal side of the edge quite equal for the two hybrid methods. By inspecting the vorticity plots from the simulation in Figure 5.45, a much stronger vortex is generated on the left side of the hull in the nonlinear hybrid method. The situation is quite equal to what is illustrated in the right part of Figure 5.32. The larger vortex creates a drop in the pressure. A similar behaviour is not seen when vorticity is created beneath the hull. For

this situation the amount of vorticity created in the two hybrid methods are similar, and then also the pressure.

The pressures in Figures 5.43 and 5.44 should be viewed together with the vorticity plots given in Figures 5.45 and 5.46. There it is given 6 different comparisons between the semi-nonlinear and the nonlinear hybrid method equally distributed over a period at steady-state.

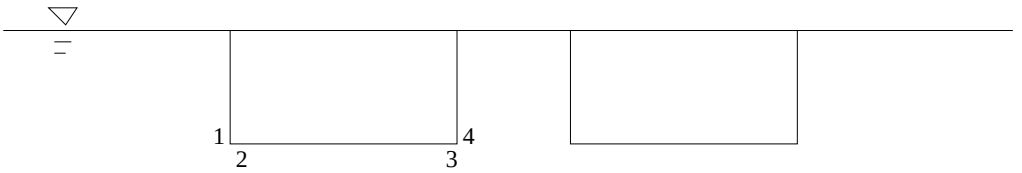

Figure 5.42: Location of the dynamic pressure points given in Figures 5.43 and 5.44. It is the dynamic pressure in the FVM cell closest to the edge that is used.

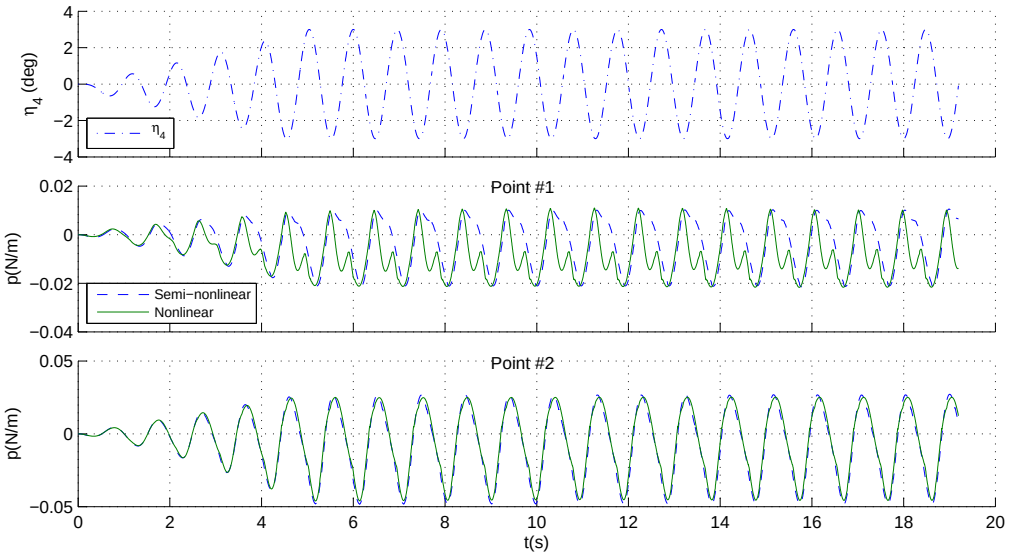

Figure 5.43: Dynamic pressure during forced roll oscillation, with oscillation period of 0.96s, and roll oscillation amplitude of $\eta_{4a} = 3°$, for points 1 and 2 given in Figure 5.42. The roll position is given in the top sub-figure.

In Figure 5.45 an important difference between the semi-nonlinear and the nonlinear hybrid methods can be discovered. In all vorticity illustrations from the semi-nonlinear method, an artificial vorticity can be seen at the intersection between potential and viscous flow close to the hull. The corresponding vorticity illustrations from the nonlinear hybrid method show no sign of the same artificial vorticity. The origin of the artificial vorticity can be one of the following two reasons. (1) That the nonlinear non-viscous

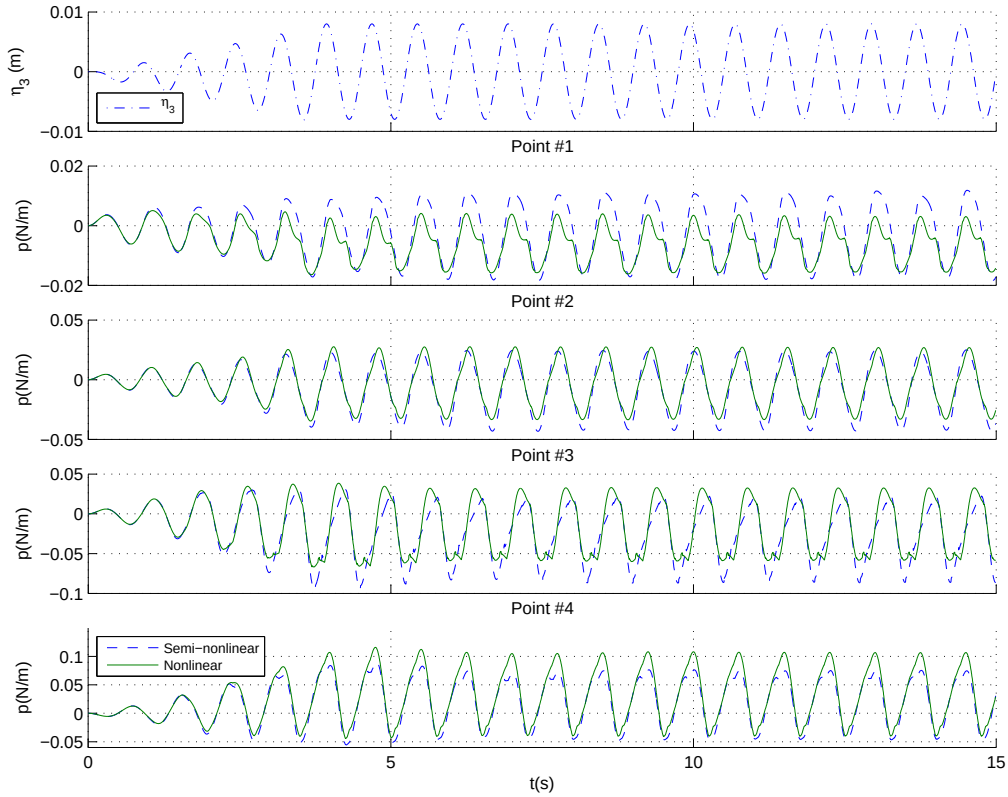

Figure 5.44: Dynamic pressure during forced heave oscillation, with oscillation period of 0.75s, and heave oscillation amplitude of $\eta_{3a} = 0.008$m, for points 1-4 given in Figure 5.42. The heave position is given in the top sub-figure.

terms in the governing equations are not communicated between the two domains, due to that the potential flow domain is linearized. (2) That the body-boundary conditions in the semi-nonlinear hybrid methods generate vorticity at the hull surface. Due to this observation it cannot in general be concluded that nonlinearities in the potential flow domain are unimportant. If this means that free-surface nonlinearities are important is still an unanswered question. Further studies with the two different body-boundary conditions in viscous liquid only will be given in next section.

The consequence of not matching the contribution from the nonlinear advection terms on the intersection is that the normal velocity and pressure are continuous across the interface, while the tangential velocity at the interface is discontinuous. The result is artificial local vorticity on the viscous flow side of the intersection. The latter fact was also observed by Greco et al. (2013) in their studies with a domain decomposition method involving linear potential flow and the Navier-Stokes equations.

For the forced heave oscillation case $\eta_{3a} = 0.008$m with oscillation period of $T^* = 7.43$ ($T = 0.75$s) in Figure 5.44. The corresponding vorticity illustrations are given in Figure 5.46. Although the vorticity distribution looks similar between the two hybrid methods in Figure 5.46 the corresponding pressure are still somewhat different, as in Figure 5.44. More notably, there is no sign of the artificially generated vorticity in the semi-nonlinear hybrid method. Instead it appears from the vorticity illustrations that the semi-nonlinear hybrid method is better than the nonlinear hybrid method, due that vorticity reaches the intersection between potential and viscous flow in the nonlinear hybrid method (see time-instances (iv)-(vi) in Figure 5.46). The vorticity is accumulated below the intersection while the piston-mode is rising, but it disappears when the piston-mode is decaying. Furthermore, in time-instances (i)-(iii), there are no signs of vorticity at the intersection in the nonlinear hybrid method. Meaning that the vorticity is not generated at the intersection in the nonlinear hybrid method. It is only limited in vertical direction inside the moonpool. Based on observations in section 5.1 the limitation on vorticity in vertical direction inside the moonpool has low influence on the piston-mode and its damping due to vorticity separation from the moonpool edges.

The reason for that artificial vorticity is not generated in the semi-nonlinear hybrid method with forced heave oscillation is thought to be that the liquid velocity is mainly normal to the intersection.

We should note the difference between absolute vorticity and relative vorticity: The vorticity in the semi-nonlinear hybrid method is calculated from the absolute velocity $\mathbf{u}$ as seen in the Earth-fixed coordinate system, while the vorticity in the nonlinear hybrid method is calculated from the relative velocity $\mathbf{u}_r$ as seen in the body-fixed coordinate system. The relative vorticity ($\nabla \times \mathbf{u}_r$) in the nonlinear hybrid method, is different from the absolute vorticity ($\nabla \times \mathbf{u}$). This can be found by the following consideration: By starting with equation (2.5), the difference between the absolute vorticity and the relative vorticity is found as,

$$\begin{aligned} \nabla \times \mathbf{u}_r &= \nabla \times (\mathbf{u} - \mathbf{u}_0 - \boldsymbol{\omega}_0 \times \mathbf{r}) \\ &= \nabla \times \mathbf{u} - 2\dot{\eta}_4. \end{aligned} \tag{5.17}$$

This means that the difference between the absolute and the relative vorticity is depending on the angular roll velocity. It is the absolute vorticity that will be presented in Figure 5.45.

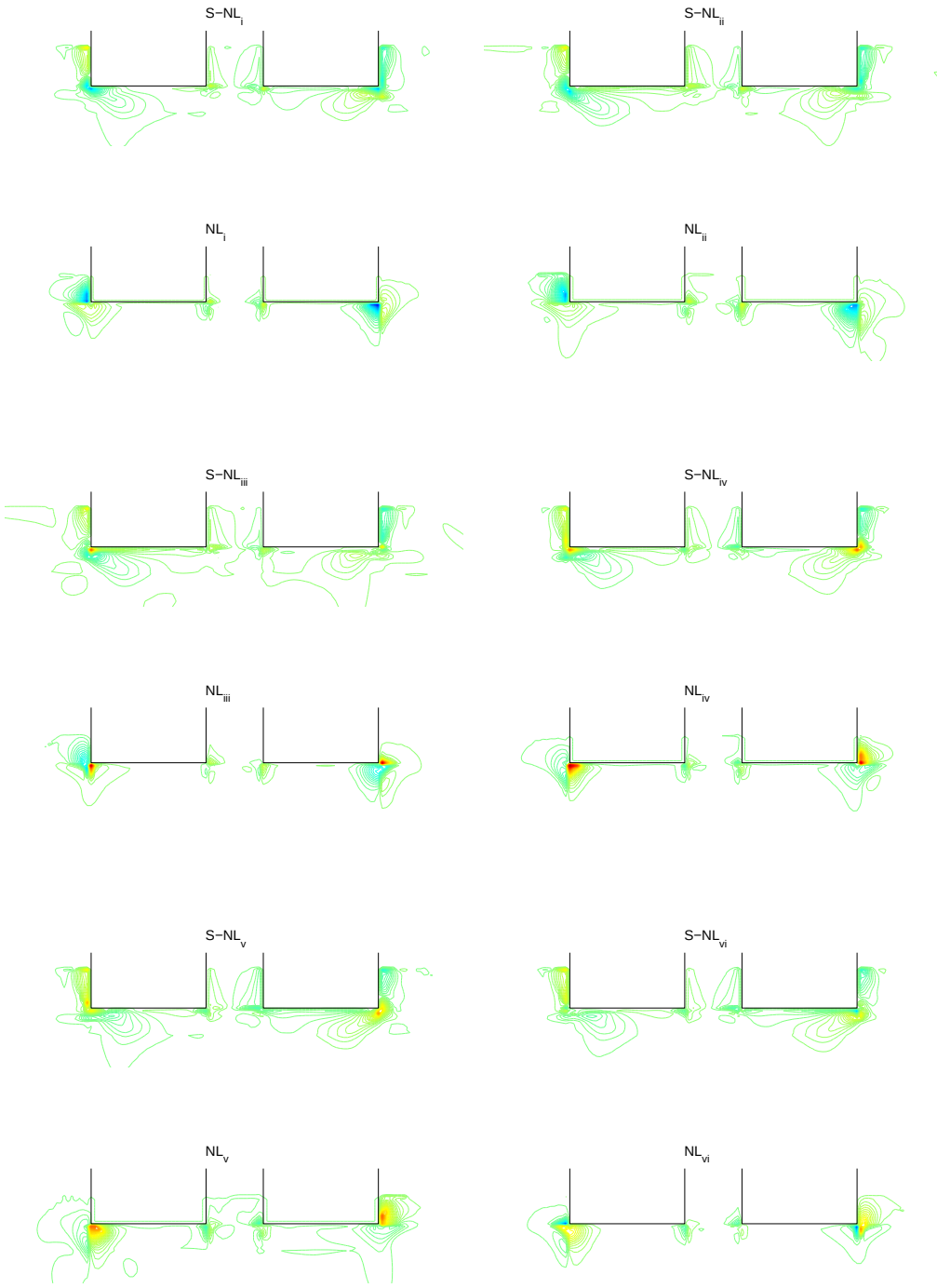

Figure 5.45: Absolute vorticity in the flow from both the semi-nonlinear (S-NL) and the nonlinear (NL) hybrid method. Roll oscillation period is $T^* = 9.5$s and roll amplitude is 3°. The 6 cases are equally spaced over a period at steady state. The colour scale ranges from negative vorticity in blue to positive vorticity in red, and passes through cyan, yellow and orange.

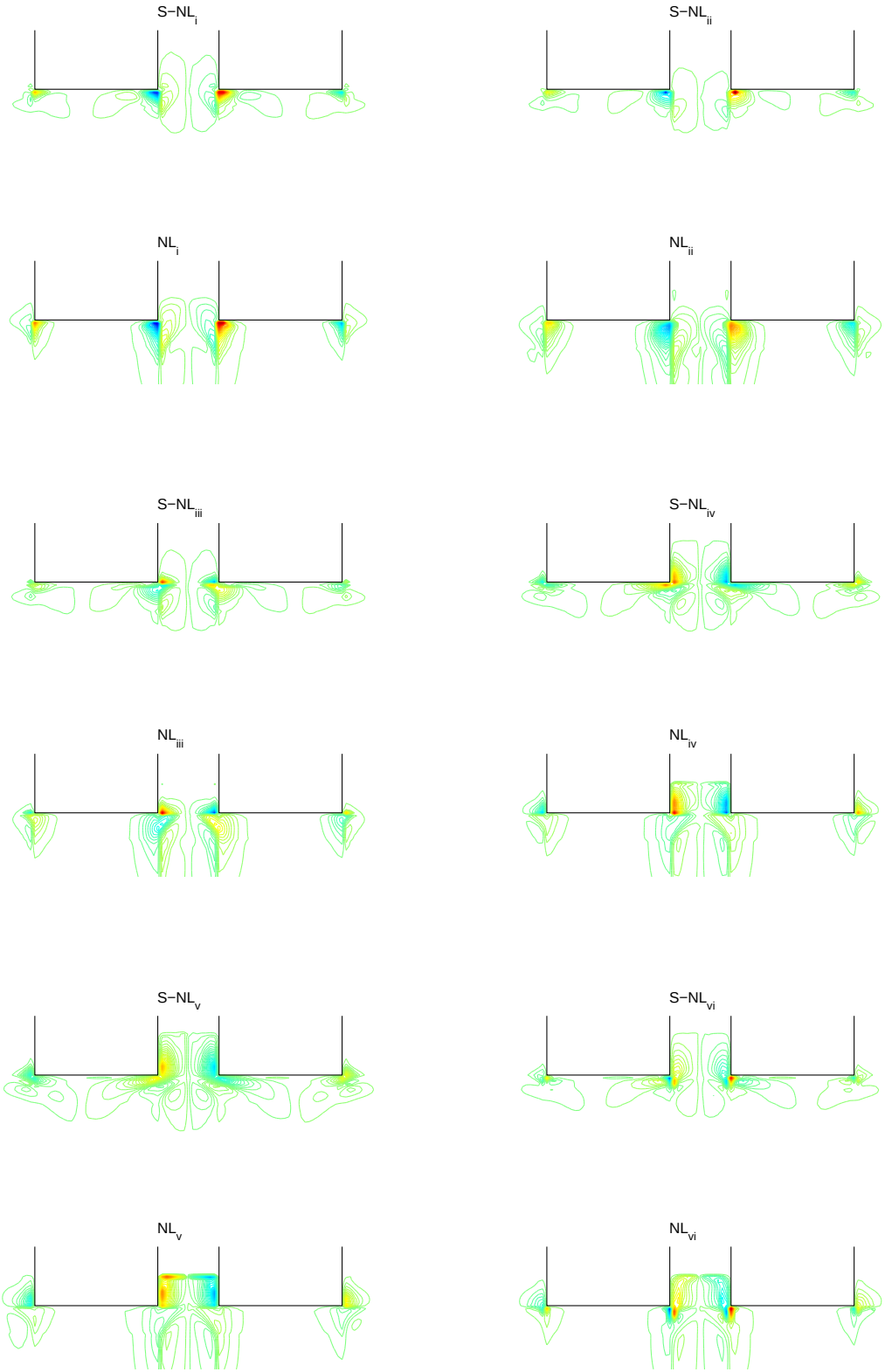

Figure 5.46: Absolute vorticity in the flow from both the semi-nonlinear (S-NL) and the nonlinear (NL) hybrid method. Heave oscillation period is $T^* = 7.4$ (T= 0.75s) and heave amplitude is 0.008m. The 6 cases are equally spaced over a period at steady state.

It is from vorticity illustrations of forced sway oscillation in Figure 5.47 quite clear that the nonlinear non-viscous terms on the intersection creates artificial vorticity. It is not seen any clear difference between artificial vorticity created at the horizontal intersection close to the hull or at the intersection with the staircase pattern.

Two attempts on improving the semi-nonlinear method were made. The first attempt was to add the higher-order terms from the Bernoulli's equation to the condition on the intersection between potential and viscous flow, while still solving for the linear acceleration potential ψ in the potential flow domain. This approach required that the solution of φ was found on the intersection to accurately evaluate the higher order terms. The second attempt was therefore to include the higher order term from the Bernoulli's equation, while solving for the linear velocity potential φ in the potential flow domain. These simulations based on these two attempts became more unstable than the original semi-nonlinear hybrid method, and no steady-state solution could be obtained. Since both the body-boundary and free-surface boundary conditions in the potential flow domain are linearized, there is still an inconsistency in the solution. It is therefore found that the usage of the semi-nonlinear method should be done with care, although good results have been obtained with the semi-nonlinear method for the forced heave case.

5.4.1 Damping from viscous flow

Since the results from the forced oscillation study with a surface piercing structure are inconclusive with regards to the importance of the body-boundary conditions (BBC) for the semi-nonlinear hybrid method due to inconsistency between non-viscous terms on the intersection between potential and viscous flow further investigations are performed. To remove the uncertainty it is here performed a similar study with the body submerged in viscous fluid without a free surface. The body dimensions used here are 0.5m wide by 0.2m high. That means the body is mirrored around the free surface and the moonpool is removed. It means that forced angular oscillation of a rectangle with a width divided by height ratio of 2.5 is studied. The height of the liquid domain is 2m, to resemble that the free surface is mirrored. The width of the domain is set to 5m, i.e. ten times larger than the width of the structure. The body is placed in the middle.

The results in Figure 5.48 show how the two different body-boundary conditions are influencing the force in phase with the roll angular velocity. The main differences between the two cases here are that the Navier-Stokes equations are solved in an inertial coordinate system with linear body-boundary conditions, and that the Navier-Stokes equations are solved in a non-inertial coordinate system with exact body-boundary conditions. Only for small roll angles $\eta_{4a} < 0.5°$ the predicted viscous damping are in the same magnitude.

The meshes used in the two numerical cases are equal, which was not the case of the previous study with forced roll oscillations in the two hybrid methods. There the intersection between the two domains where at different locations in the two hybrid methods.

It should also be considered that the outer wall conditions are different. In both the Earth-fixed and body-fixed coordinate system the outer walls remains fixed with the coordinate system. The correct approach would have been to re-mesh close to the outer walls in the body-fixed coordinate system. As discussed earlier, the reason for this is to avoid re-meshing in the viscous domain. It means that some of the difference between the results in Figure 5.48 can be due to the difference in the outer wall boundary conditions. However, this is thought to be small compared to the difference due to the body-boundary

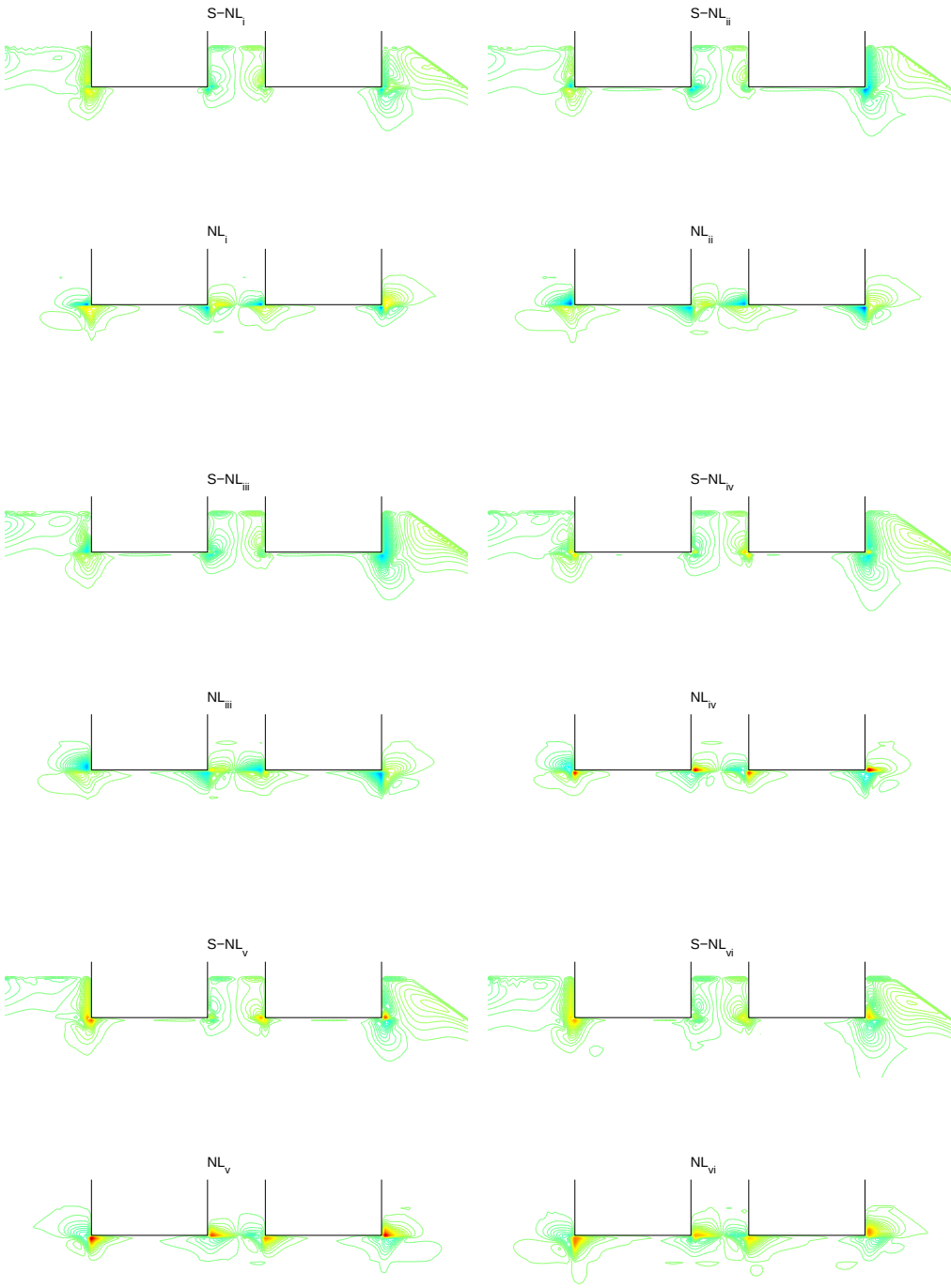

Figure 5.47: Absolute vorticity in the flow from both the semi-nonlinear (S-NL) and the nonlinear (NL) hybrid method. Sway oscillation period is $T^* = 7.4$ (T= 0.75s) and sway amplitude is 0.008m. The 6 cases are equally spaced over a period at steady state.

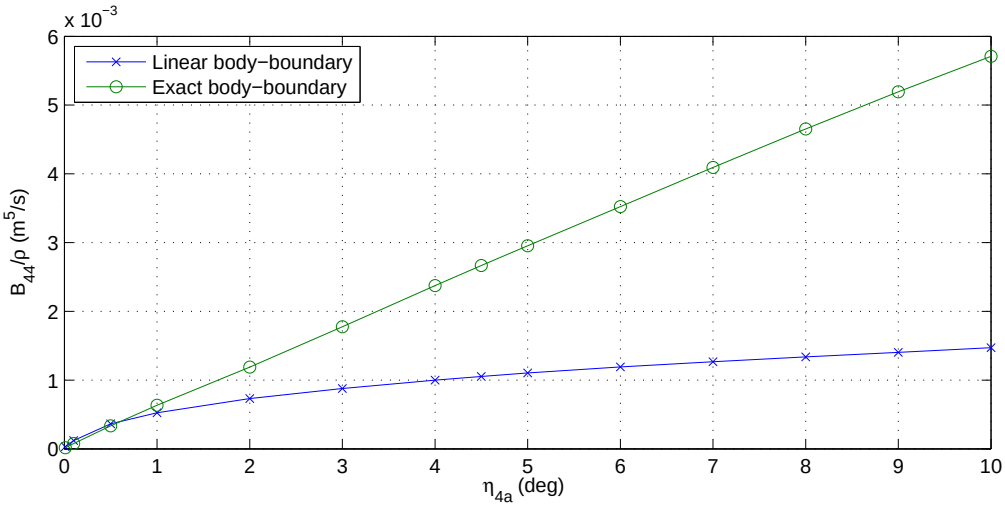

Figure 5.48: Roll damping from forced angular oscillation of a rectangular cross-section in infinite viscous fluid by using linear body-boundary conditions in an Earth-fixed coordinate system and by using exact body-boundary conditions in a body-fixed coordinate system.

conditions. The reason is that the outer wall is far away from the body.

Results from the forced roll oscillation study in viscous fluid are given in Figure 5.48. The trend in the results are similar as those in 5.40, which proves that the difference between the linear and the exact body-boundary conditions can explain most of the difference between the semi-nonlinear hybrid method results and the experimental results in Figure 5.26. However, we cannot answer if it is due to the position of the edges where vorticity is shed or if is it due to the vorticity created along the hull surfaces, that is the main reason for the low damping created in the semi-nonlinear hybrid method.

From Figure 5.49 the largest artificial vorticity is created along the centre line of the hull. This can be related to that the in-out flow body-boundary condition changes sign here, see equation (3.59). Meaning that the liquid flow through the hull surface on two neighbouring cells will have opposite direction causing local vorticity.

Note here that it is the pressure in the FVM cell closest to the hull edge that is used to generate the results in Figure 5.48. This is not valid for all the other results presented in this thesis, where the pressure gradient is used to extrapolate to values at the hull surface.

Based on the results in Figure 5.48 a first estimate on the importance of free-surface nonlinearities in the floating experimental setup can be made. The damping from the outgoing waves in the semi-nonlinear hybrid method is extracted from Figure 5.40, and half the damping predicted in infinite viscous fluid by using linear body-boundary conditions (Figure 5.48) is added and the result is presented in Figure 5.50. Note that the roll damping contribution from the moonpool edges are not included in the studies with infinite viscous fluid. Meaning that a small difference can be expected due to that. Since the two results in Figure 5.50 are quite close, it means that it is mostly the linear body-boundary conditions in the semi-nonlinear method that explain the large difference between the

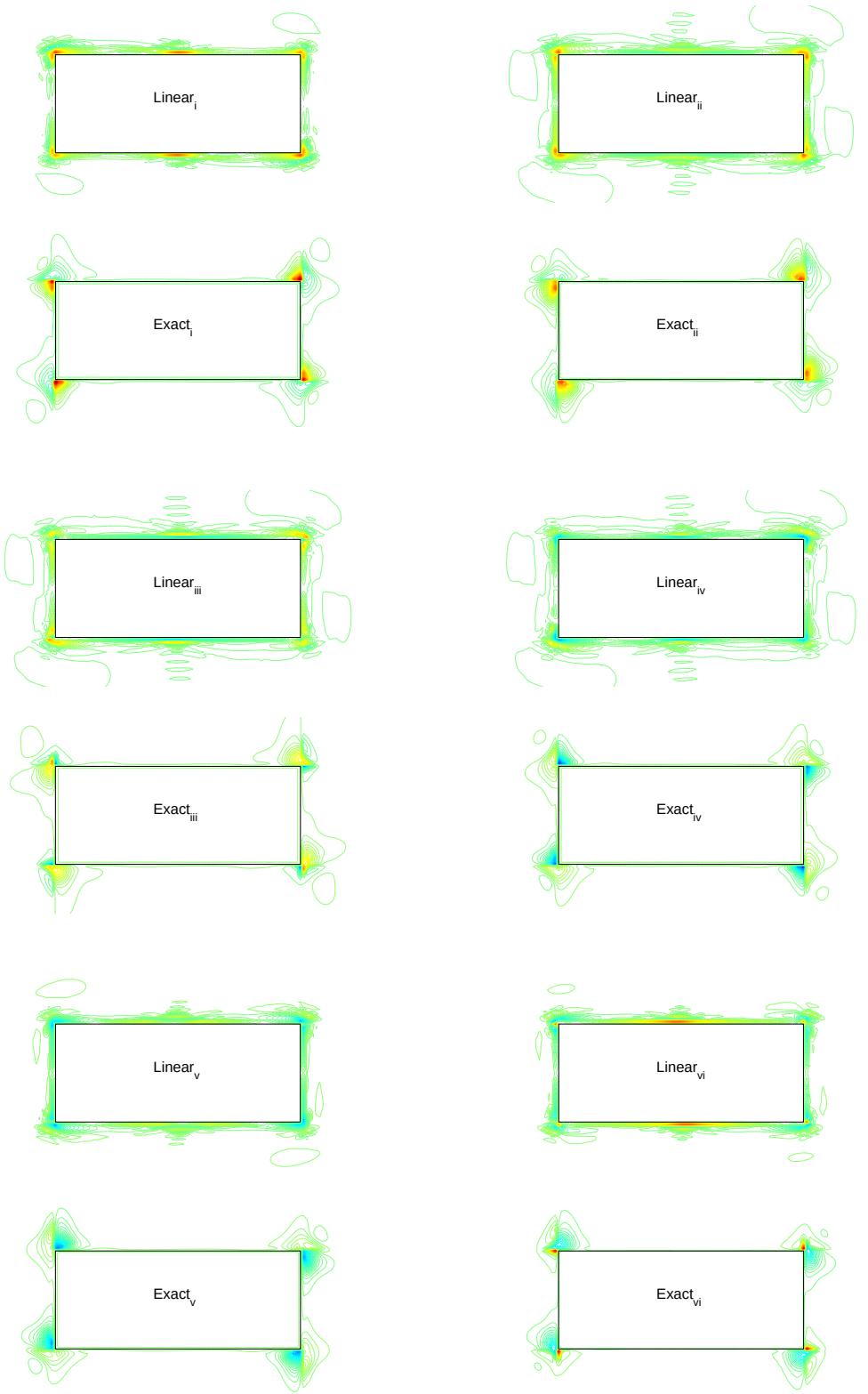

Figure 5.49: Absolute vorticity for forced roll oscillation in viscous fluid, with roll amplitude of 3° by using linear body-boundary conditions in an Earth-fixed coordinate system and exact body-boundary conditions in a body-fixed coordinate system.

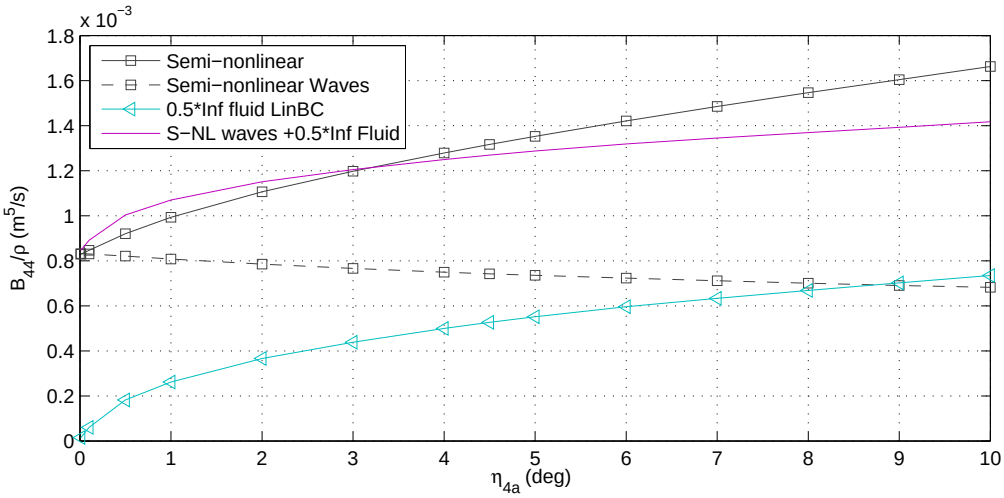

Figure 5.50: Comparison of the total damping in roll predicted by the semi-nonlinear hybrid method, with an approximate result where damping from outgoing waves is added to half the damping from forced oscillation in viscous flow. For oscillation period $T^* = 9.51$.

semi-nonlinear and nonlinear hybrid method in Figure 5.26. Further, the same study is done for the nonlinear hybrid method results from Figure 5.40, and the exact body-boundary conditions results from Figure 5.48. The result is presented in Figure 5.51. Here the approximate approach is almost equal to the nonlinear hybrid method results. However, there are some differences for higher roll angles.

To confirm that the results seen in Figures 5.50 and 5.51 are general and not only valid at the natural roll period simulations with two additional periods $T^* = 7.43$ and $T^* = 8.22$ are performed. The results are presented in Figure 5.52. The results for all three tested oscillation periods are consistent, and it is therefore assumed that the difference between the two body-boundary conditions is somewhat general.

5.4.2 Rigid free surface

Simulations with a rigid free surface have been performed in order to compare the results to those given by Braathen (1987), who compared result using a rigid free surface with results using a nonlinear free-surface condition. In general it can be expected that the result will differ between the rigid free-surface and the double body flow in infinite fluid. The simulations with rigid-free surface are performed with an open gap, and a rigid free-surface condition inside the moonpool.

Note that it is not totally accurate to call it here a rigid free-surface condition. The proper rigid free-surface boundary condition is to satisfy no fluid flux vertically in the Earth-fixed coordinate system on the mean free surface. It is here instead used that there should be no fluid flux in z-direction of the body-fixed coordinate system, which is a good approximation for small roll angles, but has an error increasing with larger roll angles.

The result when using a rigid free-surface condition from Figure 5.53 is comparable to

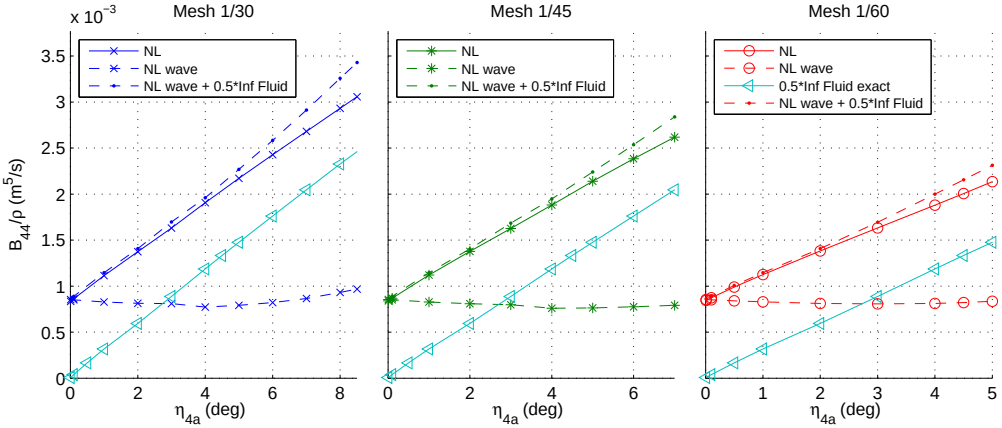

Figure 5.51: Comparison of the total damping in roll predicted by the nonlinear hybrid method, with an approximate result where damping from outgoing waves is added to half the damping from forced oscillation in viscous flow. For oscillation period $T^* = 9.51$.

the results with infinite fluid from Figure 5.51. The results confirm that for the present setup with the given dimensions the free-surface waves has a small influence on vortex shedding and associated eddy-making damping from the corners of the hull. There is a 8% difference between the results for forced roll oscillation of 6.0° in Figure 5.53, which may be related to the free surface influence on vortex shedding.

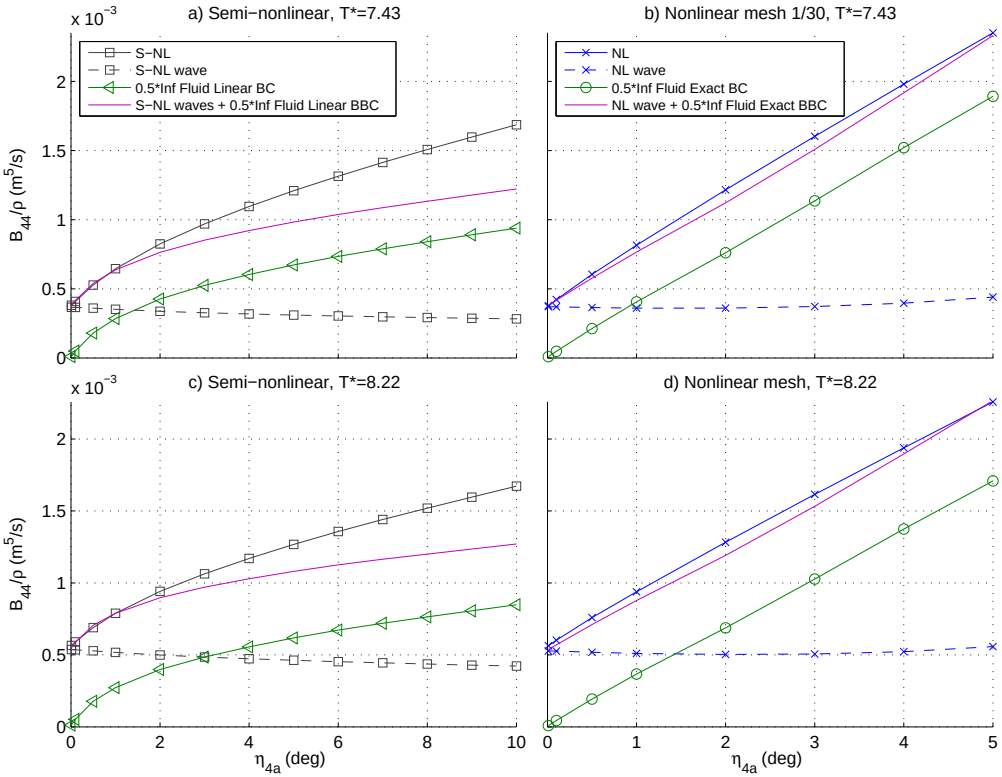

Figure 5.52: Comparison of the total damping in roll predicted by the semi-nonlinear hybrid method (in **a)**) and **c)**) and nonlinear hybrid method (in **b)** and **d)**), with an approximate result where damping from outgoing waves is added to half the damping from forced oscillation in viscous flow.

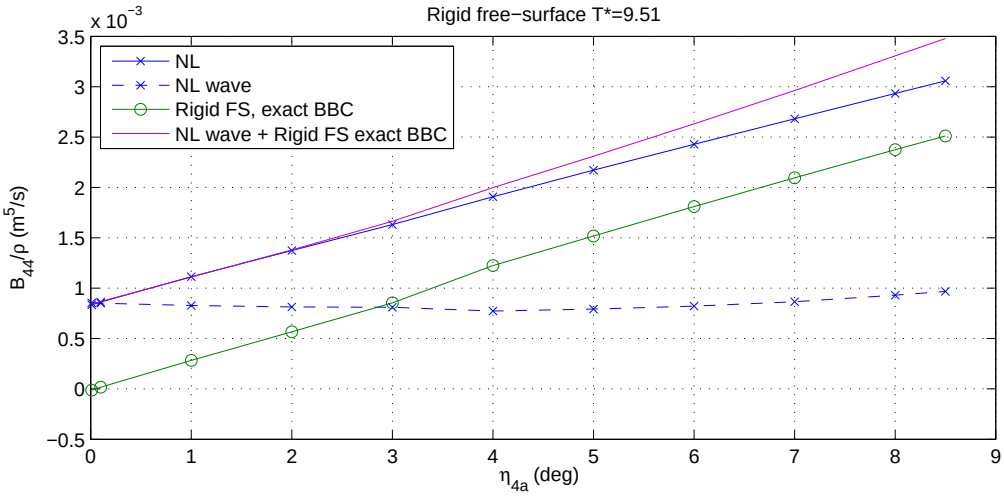

Figure 5.53: Comparison of the total damping in roll predicted by the semi-nonlinear hybrid method, with an approximate result where damping from outgoing waves is added to the damping from forced roll oscillation with a rigid free surface. For oscillation period $T^* = 9.51$.

Chapter 6

Convergence and sensitivity studies

To gain additional confidence in the two numerical hybrid methods, a comprehensive convergence and sensitivity study of some selected parameters have been performed. Ideally the numerical hybrid methods results should be independent of parameters related to the intersection between the potential and viscous flow domains. However, since they represent two different physical representations of the liquid fluid flow, it is expected that the location of the intersection can possibly influence the overall calculated liquid motion and pressure.

Three separate convergence studies have been performed. The first is dedicated to propagation of waves and the second is dedicated to forced heave oscillations with and without forward speed using the nonlinear hybrid method. Furthermore, the third is dedicated to the study with a spring-moored floating body in incoming regular waves.

6.1 Wave propagation

It has throughout this thesis been stated that the HPC method propagates waves with high accuracy. See Figure 6.1 for two examples on how the steady state wave amplitude develops throughout the numerical wave tank. The results in Figure 6.1a) are found by using linear free-surface conditions, and the results in Figure 6.1b) are found by using nonlinear free-surface conditions. In both cases the horizontal discretization of the free surface is 30 HPC cells for each wave length. Both results show that the change in wave amplitude after 11 wave length is less than 0.5%.

6.2 Forced heave oscillations with the nonlinear hybrid method

During the development phase it was identified four parameters that were possible candidates to influence the results, and identified as important to evaluate the sensitivity of. These four parameters are mesh size, size of the potential flow domain inside the moonpool gap, time-step size and smoothing size on the free surface. Convergence is studied for all appendage configurations with draft $d^* = 1.0$ (18cm), $\eta_{3a} = 0.025$ (4.5mm) heave amplitude and two Froude numbers (Fn = 0.00 and Fn = 0.08). We have chosen five different forcing periods around the piston-mode natural period for each case. The pa-

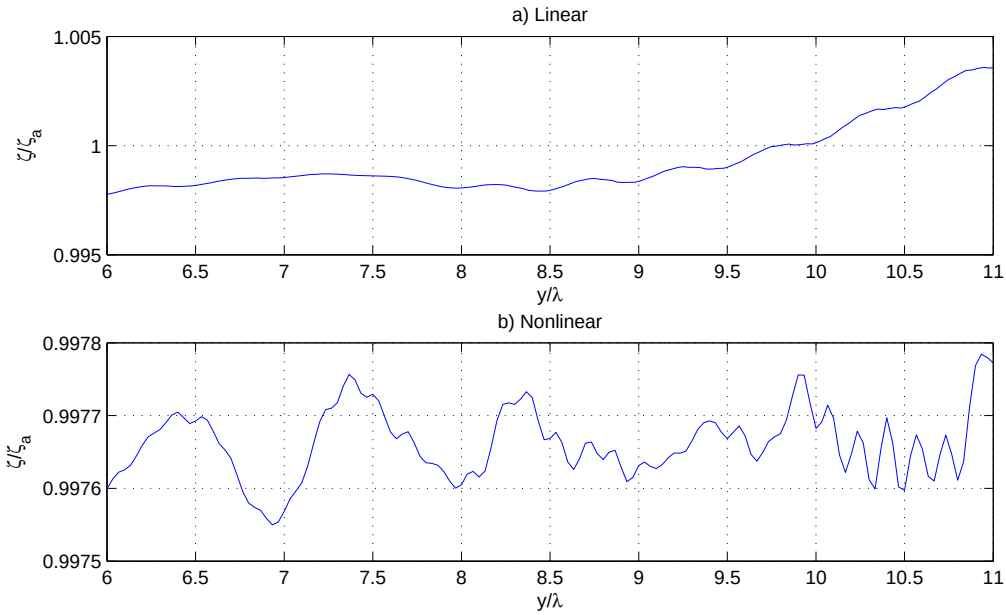

Figure 6.1: Wave propagation accuracy with 30 HPC cells for each wave length λ, using: **a**) linear free-surface conditions, **b**) nonlinear free-surface conditions. Here ζ is the steady-state wave amplitude, and ζ_a is the incoming wave amplitude.

rameters are varied around the inputs used for the calculations in Figures 5.3-5.11, from here on called the "standard case" throughout this chapter. Figures 6.2-6.5 all have six sub-figures, in two rows and three columns. In the first row is convergence results for Fn = 0.00, and second row is results for Fn = 0.08. The first column contains results for the rectangular side hull profile (no appendage), second column for appendage #1 and third column for appendage #2, see Table 6.1.

App. / Fn	-	#1	#2
0.00	a	b	c
0.08	d	e	f

Table 6.1: Overview of appendages and forward velocities that are used in the convergence study in Figures 6.2-6.5. The letters a-f refer to different parts in the figures. See Figure 5.2 for description of the appendages.

The convergence and sensitivity results with low forward velocity should all be viewed keeping in mind that vorticity has reached the intersection between the potential and viscous flow domains. This means that the convergence results could show how the local inaccuracy at the intersection is affected by a change in mesh and/or time-step size and how this inaccuracy influences the piston-mode oscillation, and not how the changes in mesh and time-step size change the global flow field, and then the piston-mode oscillation.

6.2.1 Mesh density

The standard case used in results from Figures 5.3-5.11 is the one called 36 in Figure 6.2. By 36 it is meant that the length of one hull is divided into 36 equal cells in the horizontal direction. The corresponding number of cells in the vertical direction for the standard case are 25. The number of cells in the vertical direction are increased such that the aspect ratio is kept constant.

One observation from Figure 6.2 is that for smaller cells the piston-mode amplitude converges towards a higher value without appendages, but for the two cases with appendages the piston-mode amplitude converges towards a smaller value. However, the experimental results are higher than the numerical results. The behaviour of the water flow inside the boundary layer is with the decreased mesh size still not captured. It does neither capture the behaviour of the water flow at any turbulence scale.

6.2.2 Height of potential domain inside the mooonpool

Another parameter that the simulations are somewhat sensitive to is the height of the potential flow domain inside the moonpool gap from the free surface to the intersection between the potential domain and the viscous domain, see results in Figure 6.3. Similarly to the convergence study above we have varied the height of the potential flow domain inside the moonpool gap around the standard case, where the number of cells across one hull is 36, and the number of cells in the vertical direction of the hull is 25. The standard case had the intersection line at 0.06m below the free surface. The results should in principle not be sensitive to this parameter, except when vorticity reaches the

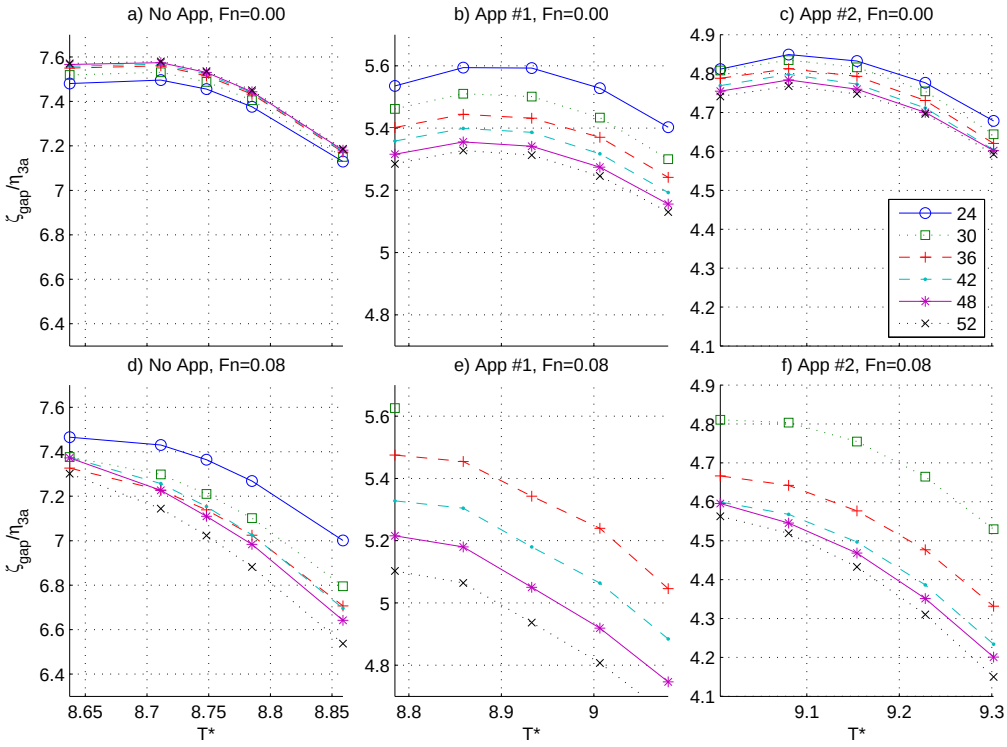

Figure 6.2: Convergence of the piston-mode amplitude with respect to the number of mesh-cells across one side hull, the number is indicated in the figure. Here 36 is the case corresponding to the "standard case" results in Figures 5.3-5.11. The number of cells in the vertical direction is varied respectively, to keep the aspect ratio $\delta z/\delta y$ constant. The upper row shows results with zero forward velocity, and the lower row shows results with forward velocity corresponding to Fn= 0.08.

intersection. For the cases with forward velocity (see Figure 6.3d-f), the $3-4\%$ difference in piston-mode amplitude is an indication on that vorticity has reached the intersection. For the cases without forward velocity the results are insensitive.

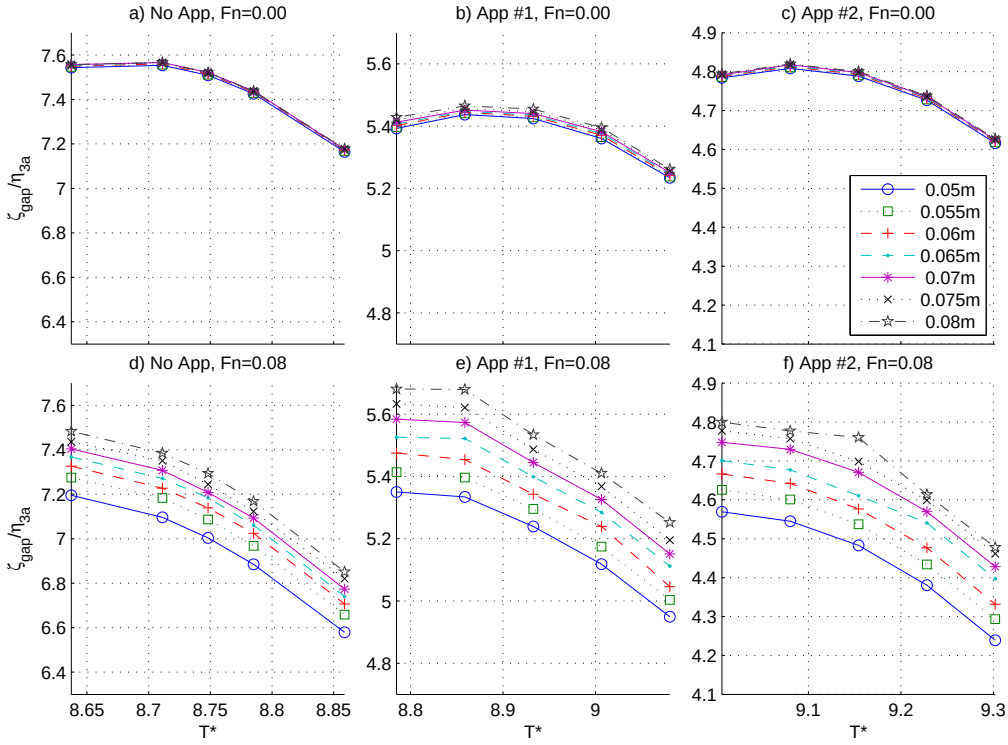

Figure 6.3: Sensitivity of the piston-mode amplitude with respect to the height of potential domain inside the moonpool gap, the height is indicated in the figure. Here 0.06m is the case corresponding to the "standard case" results in Figures 5.3-5.11. The upper row shows results with zero forward velocity, and the lower row shows results with forward velocity corresponding to Fn= 0.08.

6.2.3 Time-step size

If the CFL number is smaller than 0.5 the time-step will be set to $\Delta t = \mathrm{T}/120$ in all simulations presented in Figures 5.3-5.11. To justify this choice of time-step size a sensitivity analysis of the number of time-steps per oscillation period has been performed. We varied the number of time-steps per oscillation period from $\mathrm{N_T} = 80$ to $\mathrm{N_T} = 280$ with an increment of 40. Note that still the simulations will be limited by the CFL number criterion. Figure 6.4 shows good convergence for the zero Froude number case, but almost a 10% decrease in piston-mode amplitude for cases with forward velocity from $\mathrm{N_T} = 120$ to $\mathrm{N_T} = 240$. The latter means convergence away from the experimental results.

The convergence results are good for the cases without forward velocity.

Note here that the dependence on the time-step size is expected to be somewhat different here compared to the studies with a floating moonpool section. As the rigid-body motion here is prescribed, i.e. the equations of motion are not solved. Thus the dependency on the time-step size is expected to be different in the two cases.

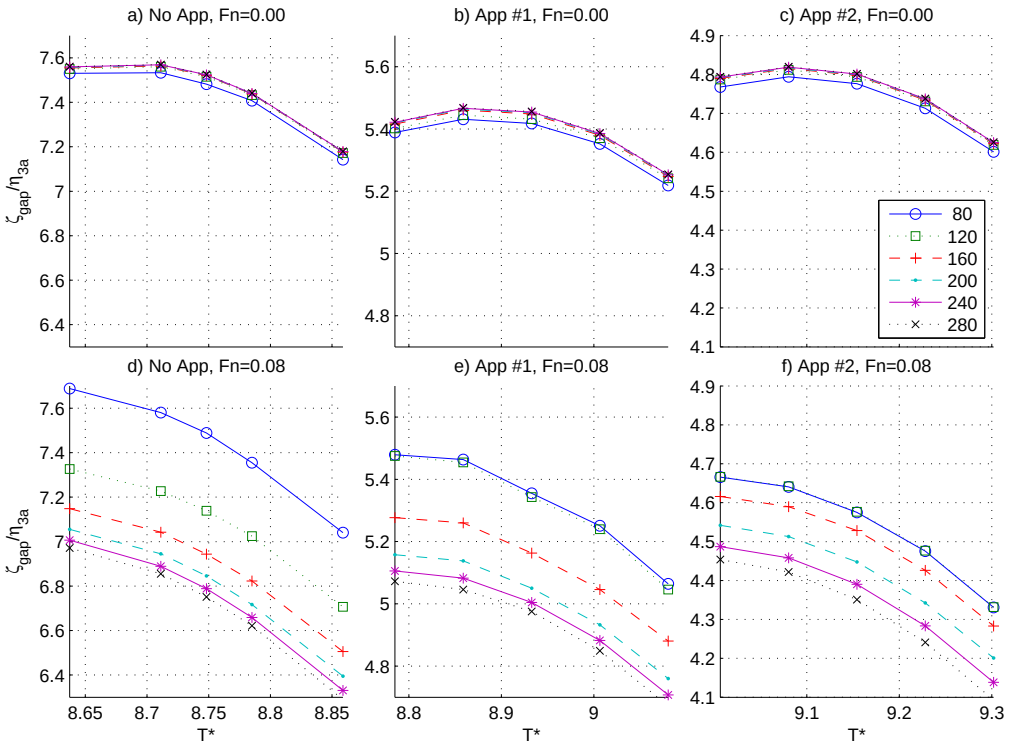

Figure 6.4: Convergence of the piston-mode amplitude with respect to the number of time-steps per period, the number is indicated in the figure. Here 120 is the case corresponding to the "standard case" results in Figures 5.3-5.11. The upper row shows results with zero forward velocity, and the lower row shows results with forward velocity corresponding to Fn= 0.08.

6.2.4 Smoothing of the free-surface description

In the standard simulations without forward velocity, we applied the smoothing operation 20 times per period, while for forward velocity cases 120 smoothing operations per period were used. Figure 6.5 shows that the moonpool amplitude results are insensitive to the smoothing algorithm, except for cases with forward velocity where the simulation breaks down at the downstream side for low number of smoothing operations per period.

The effect on smoothing will be different when studying rigid-body motions due to incoming waves with prescribed wave amplitude. The smoothing algorithm has a damping effect on wave propagation. The smoothing algorithm effect on the dispersion properties of the waves has not been studied, but it is thought to be negligible.

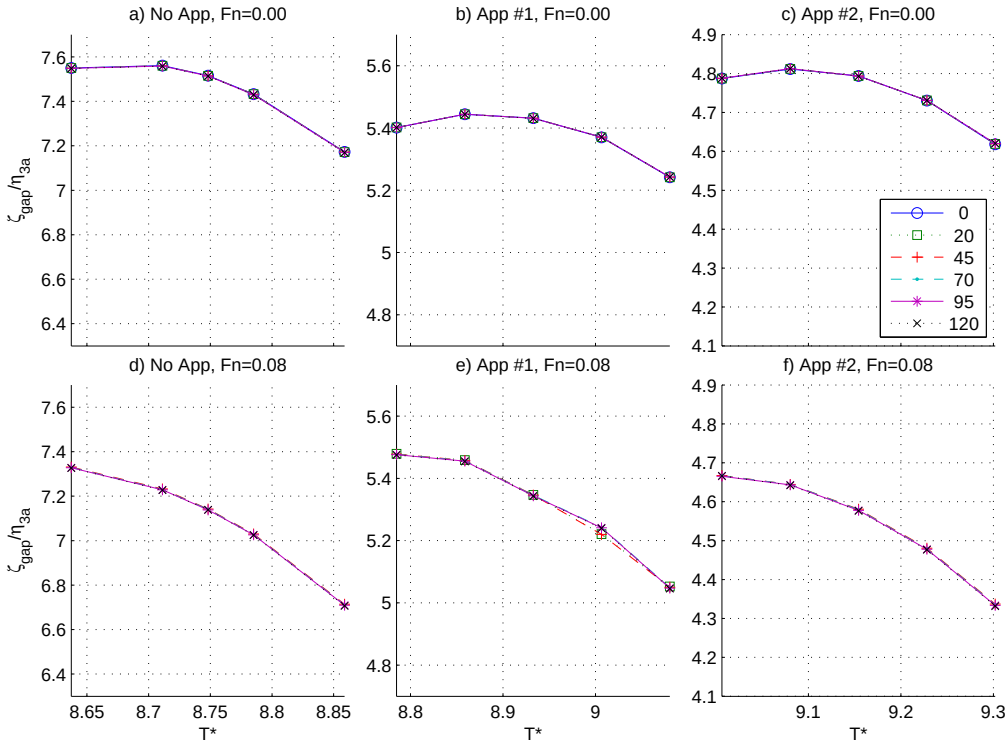

Figure 6.5: Sensitivity of the piston-mode amplitude with respect to the number smoothing operations per period. The upper row shows results with zero forward velocity, and the lower row shows results with forward velocity corresponding to Fn= 0.08.

6.3 Convergence for a freely floating body

Both the semi-nonlinear and the nonlinear hybrid methods with freely floating rigid-body motions are checked with regards to time-step size and mesh size. In addition, the nonlinear hybrid method is checked with regards to parameters related to the location of the intersection between the potential flow and viscous flow domains.

Even though the smoothing parameter was found to not influence the results for the forced heave oscillation study, it was concluded that the smoothing parameter influenced the propagation of gravity surface waves. A similar study of the smoothing parameter is therefore given here.

6.3.1 Convergence semi-nonlinear hybrid method

It is chosen to check convergence on the results for the largest wave steepness 1/30 from Figure 5.26, the results are thought to be valid for the two other wave steepnesses 1/45 and 1/60. Note that the wave period resolution is not the same as in Figure 5.26, i.e. convergence has only been checked for a chosen set of wave periods (10 in total). For convergence study results with regards to the time-step size see the right column of Figure 6.6, and the left column of Figure 6.6 for convergence study results with regards to the mesh size.

The numerical results are with regards to the time-step size converged for the base case with 200 time-steps per wave period. For the mesh size we see that around the roll natural period the response is decreasing for increasing mesh density, and they converge towards the experimental result.

Simulations are again limited by that the CFL-number should be smaller than 0.5.

Checks have been made to check that the solution of the equations of motion is independent of the choice of the artificial added mass term. This is true as long as it is in the order of the infinite frequency added mass.

6.3.2 Convergence nonlinear hybrid method

Two wave periods have been selected where convergence and sensitivity are checked. The first period is close to the first natural heave period $T^* = 7.5$, and the second period is close to the natural roll period $T^* = 9.6$. For both wave periods convergence and sensitivity are checked for both the stationary case with wave steepness 1/60, but also for towing in head seas with Fn= 0.04. In the latter case, the wave period refers to the wave period of encounter.

Four parameters are identified as relevant to check for convergence. In addition to the two parameters from the semi-nonlinear convergence study (mesh density and time-step size), η_4^{Max} (see Figure 5.23) and the height from the mean free surface to the intersection between the potential flow and the viscous flow domains are varied.

In Figure 6.7 the sensitivity/convergence study for the zero Froude number case with period $T^* = 7.5$ ($T = 0.76$s) is given. Similar sensitivity/convergence study for the forward velocity case with Froude number 0.04 in head sea with fixed period of encounter $T_{\text{e}}^* = 7.5$ ($T_{\text{e}} = 0.76$s) is given in Figure 6.8. The convergence study results around the roll natural period are given in Figure 6.9 for the zero Froude number case and Figure 6.10 for the head sea case. The convergence study lacks some data-points due to that

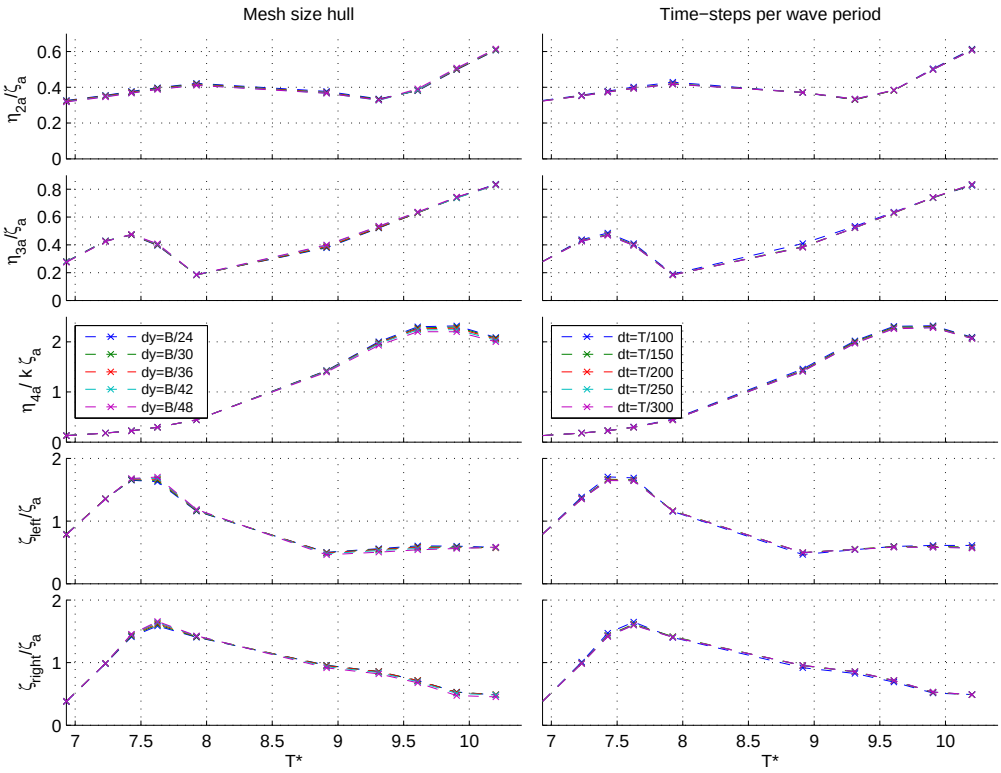

Figure 6.6: Convergence with respect to mesh resolution is given in the left column. Here the number in the figure corresponds to the number of cells across one hull in the horizontal direction (y-direction). The number of cells in z-direction are varied to keep the aspect ratio of the cells constant. 30 corresponds to the base case used in Figure 5.26. In the right column convergence is checked with respect to number of time-steps per wave period. 200 corresponds to the base case in Figure 5.26.

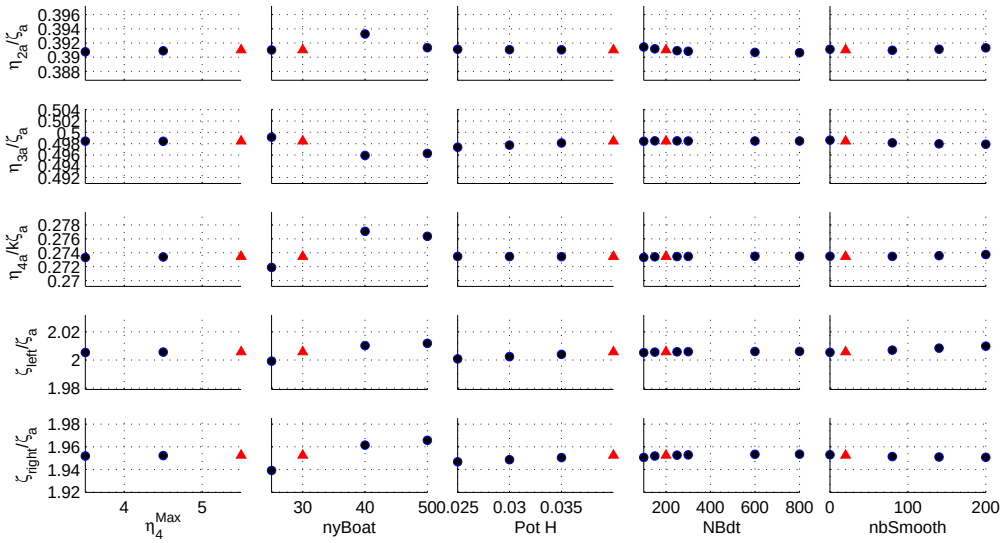

Figure 6.7: Fn = 0, $T^* = 7.5$ (T = 0.76s). red ▲: base case used in Figure 5.26. By *deglim* we mean η_4^{Max}, *nyBoat* is the number of cells across one side hull in length direction. *Pot H* is the height from the intersection between the two flow domains to the mean free surface. *NBdt* is the number of time-steps for each wave period.

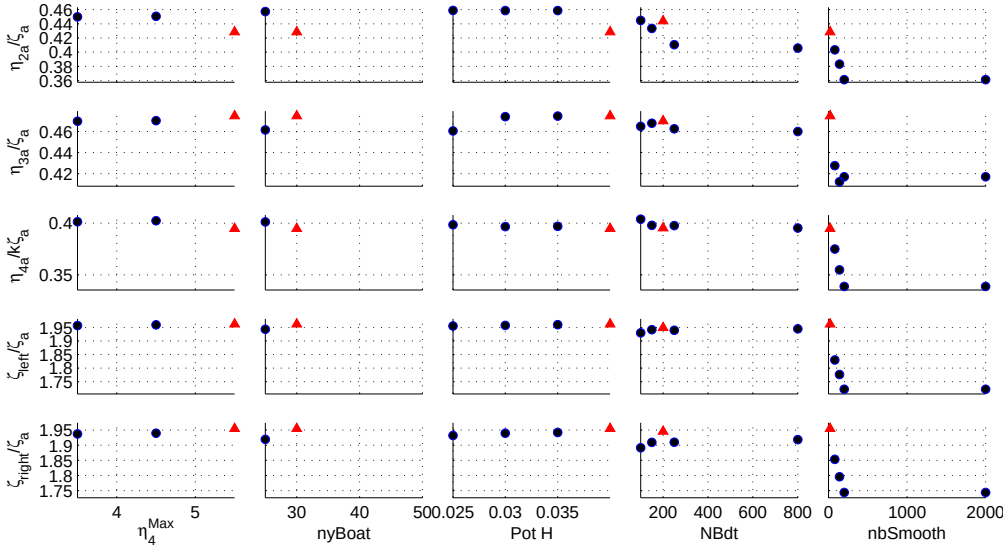

Figure 6.8: Fn = 0.04, $T_e^* = 7.5$ (T_e = 0.76s). red ▲: base case used in Figure 5.33b. Some of the numerical simulation for higher mesh density and smaller time-step crashed. See explanations in Figure 6.7.

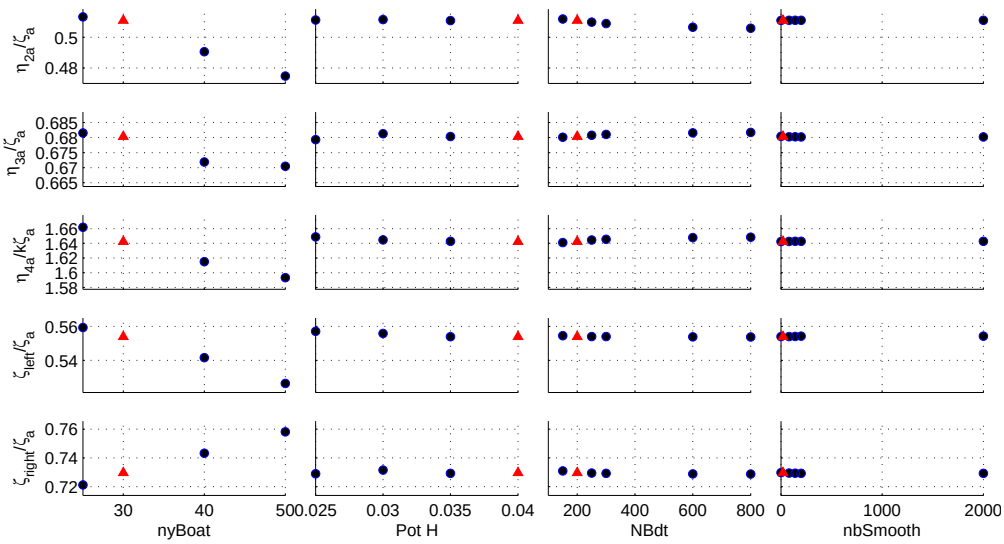

Figure 6.9: Fn = 0, $T^* = 9.6$ (T = 0.97s). red ▲: base case used in Figure 5.26. See explanations in Figure 6.7.

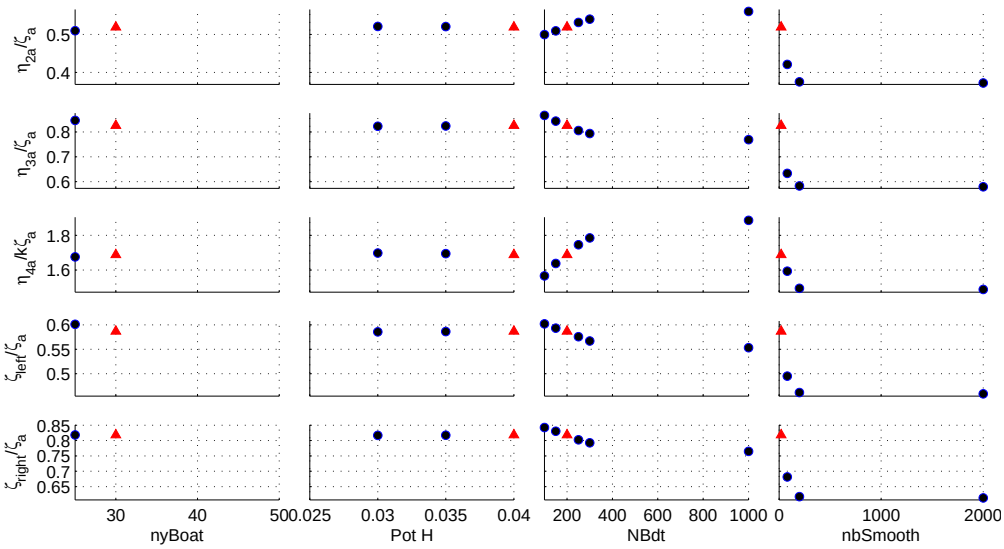

Figure 6.10: Fn = 0.04, $T_e^* = 9.6$ (T_e = 0.97s). red ▲: base case used in Figure 5.33b. Some of the numerical simulation for higher mesh density crashed. See explanations in Figure 6.7.

the simulations crashed. Results from Figure 5.33b) should be considered together with results from Figure 6.8 and 6.10.

The sensitivity/convergence study for the stationary case in Figure 6.7 and 6.9 are relatively independent on the parameters tested. Meaning that results in 5.26 are relatively close to convergence with regards to time-step and mesh size, and independent on the location of the intersection between potential and viscous flow.

For the towed case in head seas the results are more unreliable (see Figures 6.8 and 6.10), the same was found in the convergence study for forced heave oscillations with forward velocity.

For the dependency on the smoothing algorithm 2000 smoothing steps per wave period has been used as input value. Since the number of time-step per wave period is depending on the CFL-number, and unknown prior to the simulation, the use of 2000 will guarantee that the algorithm is performed once each time-step.

Separate checks have been performed to check the dependence on the intersection. The mesh created for simulations with wave steepness 1/30 has been used to calculate the results for waves with steepness 1/45 and 1/60. Similarly the mesh for wave steepness 1/45 has been used for simulating wave steepness 1/60. The differences between these meshes have been illustrated before, and it is a combination of the parameters η_4^{Max} and *Pot H*.

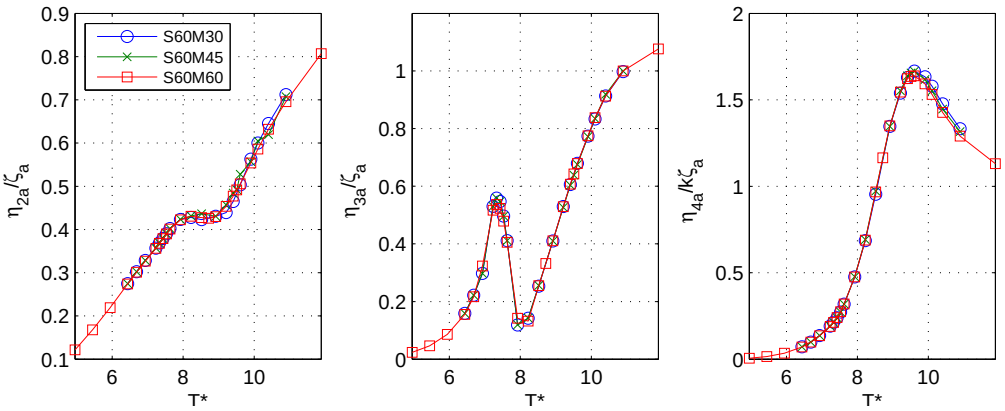

Figure 6.11: Meshes used for wave steepnesses 1/30 and 1/45 are used to generate results S60M30 and S60M45 for wave steepness 1/60. Results for wave steepness 1/60 from Figure 5.26 are also given as S60M60.

Chapter 7

Summary and further work

In the present work we have investigated properties of a two-dimensional ship section with moonpool in both vertically forced oscillations and freely-floating conditions. Special focus has been put on the resonant properties of the piston mode. By piston mode we mean the nearly vertically oscillating flow of the water inside the moonpool.

Two dedicated experimental programmes have been performed, where the first experimental programme involved an automized setup for studying forced heave oscillation with and without small forward velocity. Here two geometrical parameters, i.e. the draft and the edge profile at the moonpool's inlet were varied. In addition the forward carriage velocity and heave amplitude were varied. The second experimental setup was with a spring-moored two-dimensional moonpool section subjected to incoming regular waves, where three different wave steepness ratios were tested.

The experimental programmes have served as validation data for two numerical hybrid methods coupling potential and viscous flow. The water domain is divided in two strongly coupled domains, where the Navier-Stokes equations are solved in the viscous flow domain close to the hull edges where vorticity is expected to be generated. Furthermore, the HPC method is employed to solve the Laplace equation for the velocity potential in the outer potential flow domain enclosing the entire free surface. The two numerical hybrid methods are different in the way boundary conditions are treated. In the semi-nonlinear hybrid method linear free-surface conditions are applied in the potential flow domain. Linear body-boundary conditions are used in both the potential flow and viscous flow domains. On the intersection between the potential flow and the viscous flow domains both pressure and normal velocities are matched. However, tangential velocities are not guaranteed to be continuous across the intersection. In the nonlinear hybrid method the free-surface conditions are satisfied in a nonlinear manner and the body-boundary conditions are satisfied exactly. The latter is achieved by solving the governing equations in a body-fixed coordinate system. In addition, the tangential velocities are continuous across the intersection.

Three main studies have been presented, first a comprehensive study with both experimental and numerical studies of forced heave motions with and without forward velocity, secondly an experimental and numerical study of a spring-moored freely floating ship section. By the confidence gained by the good comparison both the numerical studies include some data without experimental validation. At last a detailed study of the flow and pressure details has been performed to determine the shortcomings of the semi-nonlinear hybrid method in prediction of the rigid-body roll motion.

7.1 Forced heave oscillation with low forward velocity

The main motivation behind this study was to investigate how a low current/low forward velocity influences the resonant piston-mode motion of a moonpool inside a 2D ship section. This was done by both numerical and experimental methods, and for current velocities up to Fn = 0.08. We found that within this range, the low current/low forward velocity had a slightly decreasing effect on the moonpool piston-mode behaviour. To what extent this fact depends on the moonpool gap width remains unknown.

In addition to the low forward velocity influence, we varied the moonpool edge profile, the draft and the heave amplitude. We tested 3 different edge profiles inside the moonpool gap. First we studied rectangular side hulls. Then we included two appendages in the moonpool inlet covering 20% and 30% of the moonpool gap area. The damping of the piston-mode is increased by using appendages compared to the rectangular side hull. For each of the 3 edge profiles we tested 3 different drafts, where the ratio between the draft and the total hull width was 1/6, 1/5 and 7/30. However, the change of draft had little influence on the maximum piston-mode response. It did change the period of maximum response of the system, such that for a given period the response was changed.

7.2 Freely-floating in incoming regular waves

In general, the two numerical hybrid methods predict the rigid-body and moonpool responses quite well. An exception is that the resonant roll motion is clearly over-predicted by the semi-nonlinear hybrid method, while the nonlinear hybrid method captures the roll motion well. The reason for this is eddy-making damping.

The moonpool behaviour has a clear effect on the rigid-body motions. The moonpool wave amplification factor is found to be around 2–2.5 times the incoming wave amplitude around resonance, depending on the wave amplitude. In comparison, pure linear potential flow theory predicts a factor of up to 10.

An important observation is that we cannot use the natural piston-mode period to calculate which period causes maximum piston-mode response of a free-floating body in incident waves. The linear potential flow response from the radiation and diffraction potentials is 180° out of phase at the natural piston-mode period, with the consequence that the piston-mode motion at the piston-mode natural period does not have any resonant behaviour. The maximum piston-mode response is found at the first resonant heave motion period in the vicinity of the piston-mode resonance.

7.3 Difference between the two hybrid methods

The shortcomings of the semi-nonlinear hybrid method in predicting the roll motion are investigated by a detailed study of the damping from forced roll oscillations with different forcing amplitudes. It is suggested that the main reason for the differences is that the body-boundary condition is linearized in the semi-nonlinear hybrid method.

In addition comes the inaccuracies at the intersection between the potential and viscous domain in the semi-nonlinear hybrid method, where the tangential velocity across the intersection is not continuous, with the consequence of local creation of artificial vorticity.

7.4 Recommendations for further work

To improve the confidence in the present hybrid method, additional case studies that are suitable to be numerically simulated using the present hybrid methods would be welcomed.

It was throughout the work attempts on developing a particular solution for the Poisson equation that could be combined with the harmonic solution of the Poisson equation by the HPC method. The particular solution was based on an integral for each viscous node over the entire viscous domain, and thus the solution became quite CPU expensive. Recently, Andrea et al. (2015) has generalized the HPC method to include the solution of the Poisson equation, this is achieved by including other polynomials than the original harmonic polynomials in the HPC method that gives a particular solution of the Poisson equation.

Improvement of the semi-nonlinear hybrid method by satisfying the body-boundary condition in a more exact manner, two main alternatives are then thought of:

- By still solving the governing equations in the Earth-fixed coordinate system and re-meshing the viscous domain close to the body.
- By solving the governing equations in the body-fixed coordinate system and linearizing the free-surface conditions in body-fixed coordinate system.

The motivation is that the body-boundary conditions were the main reason for the difference between the semi-nonlinear and experimental results for roll motion. Other improvements of the hybrid methods could include turbulence modelling and extension of the method to handle more general mesh types. Extension of the method into 3D would obviously be interesting.

With regards to the physical problem of moonpool resonance it is not fully clear how the results from this work are applicable in three dimensions on a real ship. How large is the difference between the piston-mode resonance period found from forced oscillations, to the period where maximum piston-mode response occur at a natural heave period for a freely floating ship?

It was not the ambition of this work to find the optimal ship design for reducing the moonpool motion. However, it is felt that this work would serve as a good basis for continuing on such a path.

Another application of the present nonlinear hybrid method is to study the total mean drift force, including both potential and viscous flow force contributions.

Appendix A

Conversion from Earth-fixed to body-fixed coordinate system

Details in this Appendix are given in (Faltinsen and Timokha 2009), and given here to understand how the Navier-Stokes equations and the equations of motion are converted from an Earth-fixed coordinate system to a body-fixed coordinate system.

First notice that the left hand side of equation (2.1) is the material derivative D/Dt, which expresses the time rate of change as a liquid particle is followed in space and time, i.e. a Lagrangian description. The challenge is now to convert the time-derivative from an inertial coordinate system (Earth-fixed coordinate system), to a noninertial coordinate system (body-fixed coordinate system). The derivation is started by expressing the position of the liquid particle relative to the inertial coordinate system by

$$\mathbf{r}'(t) = \mathbf{r}'_0(t) + \mathbf{r}(t). \tag{A.1}$$

Here $\mathbf{r}'_0(t)$ is the distance between the two coordinate systems expressed in the inertial coordinate system and $\mathbf{r}(t)$ is the radius vector of the position of the liquid particle with respect to the noninertial coordinate system. I.e. $\mathbf{r}(t) = x_1(t)\mathbf{e}_x(t) + y_1(t)\mathbf{e}_y(t) + z_1(t)\mathbf{e}_z(t)$, where $\mathbf{e}_i\,(i = x, y, z)$ are unit vectors of the noninertial coordinate system, and rotated relative to the inertial coordinate system. Meaning that the time derivative of $\mathbf{r}(t)$ becomes,

$$\begin{aligned} \frac{d\mathbf{r}(t)}{dt} &= \dot{x}_1(t)\mathbf{e}_x(t) + \dot{y}_1(t)\mathbf{e}_y(t) + \dot{z}_1(t)\mathbf{e}_z(t) \\ &+ x_1(t)\dot{\mathbf{e}}_x(t) + y_1(t)\dot{\mathbf{e}}_y(t) + z_1(t)\dot{\mathbf{e}}_z(t) \end{aligned} \tag{A.2}$$

that according to (Faltinsen 2005) can be rewritten to

$$\frac{d\mathbf{r}(t)}{dt} = \frac{d^b\mathbf{r}(t)}{dt} + \boldsymbol{\omega}_0(t) \times \mathbf{r}(t) = \mathbf{u}_r(t) + \boldsymbol{\omega}_0(t) \times \mathbf{r}(t), \tag{A.3}$$

where d^b/dt means that the unit vectors should not be time-differentiated. The time-derivative of the position of the fluid particle (equation A.1) can then be expressed as,

$$\frac{D\mathbf{r}'(t)}{Dt} = \mathbf{u}_0(t) + \mathbf{u}_r(t) + \boldsymbol{\omega}_0(t) \times \mathbf{r}(t), \tag{A.4}$$

where $\mathbf{u}_0(t) = d\mathbf{r}'(t)/dt$. The Lagrangian description of the Navier-Stokes equation (2.1) implies that

$$\frac{D\mathbf{u}(t)}{Dt} = \frac{D^2\mathbf{r}'(t)}{Dt^2} \tag{A.5}$$

which can by using the same procedure as above obtained to be

$$\begin{aligned} \frac{D^2\mathbf{r}'}{Dt^2} &= \mathbf{a}_0 + \boldsymbol{\omega}_0 \times \mathbf{u}_0 + \dot{\boldsymbol{\omega}}_0 \times \mathbf{r} + 2\boldsymbol{\omega}_0 \times \mathbf{u}_r \\ &+ \boldsymbol{\omega}_0 \times (\boldsymbol{\omega}_0 \times \mathbf{r}) + \mathbf{a}_r \end{aligned} \tag{A.6}$$

where $\mathbf{a}_0 = d^b\mathbf{u}_0/dt$ is the translatory acceleration of the body-fixed coordinate system and $\mathbf{a}_r = d^b\mathbf{u}_r/dt$ is the translatory relative acceleration. Notice that the notation has been simplified, meaning that $\mathbf{a}_0(t) = \mathbf{a}_0$ and similar for the other terms. In a numerical calculation we want to calculate the rate of change in time and space at fixed points. Then as a last step, an Eulerian description for the time-derivative of the relative fluid velocity is needed for fixed points in a body-fixed coordinate system

$$\mathbf{a}_r = \frac{d^b\mathbf{u}_r}{dt} = \frac{\partial^b\mathbf{u}_r}{\partial t} + \mathbf{u}_r \cdot \nabla\mathbf{u}_r. \tag{A.7}$$

Here $\frac{\partial^b\mathbf{u}_r}{\partial t} = \frac{\partial u_r}{\partial t}\mathbf{e}_x + \frac{\partial v_r}{\partial t}\mathbf{e}_y + \frac{\partial w_r}{\partial t}\mathbf{e}_z$ means the time-differentiation of a value for a fixed point in the body-fixed coordinate system, i.e. we do not time differentiate the unit vectors, as they do not vary with time relative to the body-fixed coordinate system. Furthermore, the spatial derivatives are invariant.

Appendix B

Thin free-vortex sheet model

It is from the results from the two hybrid methods suspected that the main explanation for the difference between the two methods is due to the different body-boundary conditions. We will here employ a thin free-vortex sheet model to explain the difference due to the different body-boundary conditions. The basis of the thin free-vortex sheet model can be found in (Faltinsen and Pettersen 1987). First diffusion of vorticity is neglected, and the flow outside the vortex sheets is described by potential flow theory. The force acting on the body due to flow separation can be related to the circulation Γ and the advection velocity of the vorticity. Where the circulation is defined as,

$$\Gamma = \oint_C \mathbf{u} \cdot d\mathbf{s} \tag{B.1}$$

The integration is along a closed curve C and can be related to $\varphi^+ - \varphi^-$. Here φ^+ and φ^- are the velocity potentials at each side of the free-shear layer. By employing Stokes's theorem to equation (B.1) we get that

$$\Gamma = \int_C \frac{\partial \varphi}{\partial s} ds. \tag{B.2}$$

If now the integration is around the complete structure and free-shear layer, the total circulation remains zero. For further description see for instance chapter 6.4 in (Faltinsen 2005).

Further, if we limit the closed curve C_1 to the vorticity separated from one corner during one oscillation cycle. We get

$$\Gamma_1 = \int_{C_1} \frac{\partial \varphi}{\partial s} ds. = \varphi^+ - \varphi^-, \tag{B.3}$$

note that the integration direction matter and here exemplified using the counterclockwise direction.

We can find $\partial\Gamma/\partial t$ by using the condition that the pressure is continuous across the vortex sheet, i.e. a zero pressure jump condition. Due to the change of the Bernoulli equation between the Earth-fixed and the body-fixed coordinate system, we get two different expressions for the zero pressure jump condition.

We will indicate the difference between the two hybrid methods by considering two examples with forced roll motion. See illustrations in Figure B.1 for example a) and

Figure B.2 for example b). Remember, it is the difference between linear body-boundary conditions in an Earth-fixed coordinate system and exact body-boundary conditions in a body-fixed coordinate system we are studying here.

B.1 Semi-nonlinear hybrid method

The zero pressure jump condition across a free shear layer (vortex sheet) in an Earth fixed coordinate system, is found by subtracting the pressure found from the Bernoulli equation on each side of the free shear layer

$$\frac{\partial}{\partial t}\left(\varphi^{+}-\varphi^{-}\right)+\frac{1}{2}\left[\left(\frac{\partial\varphi^{+}}{\partial y}\right)^{2}-\left(\frac{\partial\varphi^{-}}{\partial y}\right)^{2}+\left(\frac{\partial\varphi^{+}}{\partial z}\right)^{2}-\left(\frac{\partial\varphi^{-}}{\partial z}\right)^{2}\right]=0. \tag{B.4}$$

Example a)

Now let us study case a) illustrated in Figure B.1. Here vorticity is shed from the left edge (y_1, z_1) of the hull to the left and towards the free surface. The following body-boundary condition for forced roll motion η_4 on the vertical side of the body applies

$$\frac{\partial\varphi^{+}}{\partial y}=-\dot{\eta}_4\, z_1. \tag{B.5}$$

Continuous normal velocity across the free shear layer, implies

$$\frac{\partial\varphi^{+}}{\partial z}=\frac{\partial\varphi^{-}}{\partial z}. \tag{B.6}$$

Then the zero pressure jump condition in the Earth-fixed coordinate system valid for the semi-nonlinear hybrid method becomes,

$$\frac{\partial}{\partial t}\left(\varphi^{+}-\varphi^{-}\right)=-\frac{1}{2}\left(\dot{\eta}_4\, z_1\right)^2+\frac{1}{2}\left(\frac{\partial\varphi^{-}}{\partial y}\right)^{2}. \tag{B.7}$$

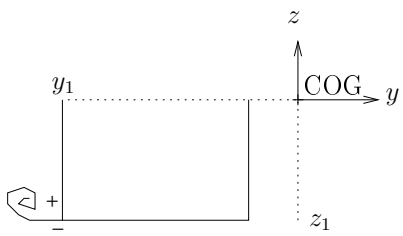

Figure B.1: Overview illustration example a).

Example b)

When vorticity is shed downwards from the left edge of the hull the following body-boundary condition applies, see illustration in Figure B.2

$$\frac{\partial \varphi^-}{\partial z} = \dot{\eta}_4 \, y_1. \tag{B.8}$$

Further, continuous normal velocity across the free shear layer in example b), implies

$$\frac{\partial \varphi^+}{\partial y} = \frac{\partial \varphi^-}{\partial y}. \tag{B.9}$$

The result is then for example b),

$$\frac{\partial}{\partial t}\left(\varphi^+ - \varphi^-\right) = -\frac{1}{2}\left(\frac{\partial \varphi^+}{\partial z}\right)^2 + \frac{1}{2}\left(\dot{\eta}_4 \, y_1\right)^2. \tag{B.10}$$

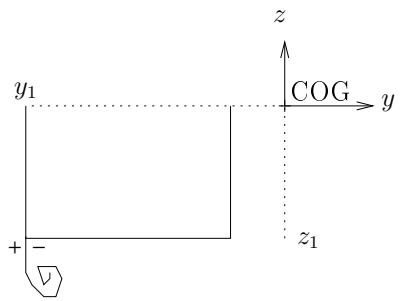

Figure B.2: Overview illustration example b).

B.2 Nonlinear hybrid method

The zero pressure jump condition across a free-shear layer in a body-fixed coordinate system with forced roll motion η_4 is given according to equation (2.60) in (Faltinsen and Timokha 2009),

$$\begin{aligned} \frac{\partial^*}{\partial t}\left(\varphi^+ - \varphi^-\right) \;&+\; \frac{1}{2}\left[\left(\frac{\partial \varphi^+}{\partial y}\right)^2 - \left(\frac{\partial \varphi^-}{\partial y}\right)^2 + \left(\frac{\partial \varphi^+}{\partial z}\right)^2 - \left(\frac{\partial \varphi^-}{\partial z}\right)^2\right] \\ &-\; \left[\left(-\dot{\eta}_4 \, z_1\right)\left(\frac{\partial \varphi^+}{\partial y} - \frac{\partial \varphi^-}{\partial y}\right) + \dot{\eta}_4 \, y_1\left(\frac{\partial \varphi^+}{\partial z} - \frac{\partial \varphi^-}{\partial z}\right)\right] = 0, \end{aligned} \tag{B.11}$$

where $\frac{\partial^*}{\partial t}$ means that we follow and time-differentiate a value of a fixed point in the body-fixed coordinate system. Note here that φ is the absolute velocity potential.

Example a)

The exact body-boundary condition in a body-fixed coordinate system for the forced roll motion example illustrated in Figure B.1 is,

$$\frac{\partial \varphi^+}{\partial y} = -\dot{\eta}_4 \, z_1. \tag{B.12}$$

The expression is equal to equation (B.5) due to that we solve for the absolute velocity potential.

Also the condition for continuous normal velocity across the free shear layer is equal to that in the semi-nonlinear hybrid method, i.e.

$$\frac{\partial \varphi^+}{\partial z} = \frac{\partial \varphi^-}{\partial z}. \tag{B.13}$$

The zero pressure condition for example a) using body-boundary condition as in the nonlinear hybrid method then becomes,

$$\frac{\partial^*}{\partial t}\left(\varphi^+ - \varphi^-\right) + \frac{1}{2}\left[(-\dot{\eta}_4 \, z_1)^2 - \left(\frac{\partial \varphi^-}{\partial y}\right)^2\right] - \left[(-\dot{\eta}_4 \, z_1)\left(-\dot{\eta}_4 \, z_1 - \frac{\partial \varphi^-}{\partial y}\right)\right] = 0. \tag{B.14}$$

Further simplification gives:

$$\frac{\partial^*}{\partial t}\left(\varphi^+ - \varphi^-\right) = \frac{1}{2}\left(\dot{\eta}_4 \, z_1\right)^2 + \dot{\eta}_4 \, z_1 \frac{\partial \varphi^-}{\partial y} + \frac{1}{2}\left(\frac{\partial \varphi^-}{\partial y}\right)^2. \tag{B.15}$$

Example b)

When vorticity is shed downwards the following body-boundary condition for forced roll motion in the nonlinear hybrid method we can write, see illustration in Figure B.2

$$\frac{\partial \varphi^-}{\partial z} = \dot{\eta}_4 \, y_1. \tag{B.16}$$

Again, continuous normal velocity across the free-shear layer gives,

$$\frac{\partial \varphi^+}{\partial y} = \frac{\partial \varphi^-}{\partial y}. \tag{B.17}$$

The final expression for the change of circulation due to an exact body-boundary conditions in the body-fixed coordinate system in example b) is,

$$\frac{\partial^*}{\partial t}\left(\varphi^+ - \varphi^-\right) = -\frac{1}{2}\left(\frac{\partial \varphi^+}{\partial z}\right)^2 + \dot{\eta}_4 \, y_1 \frac{\partial \varphi^+}{\partial z} - \frac{1}{2}\left(\dot{\eta}_4 \, y_1\right)^2. \tag{B.18}$$

B.3 Qualitative results

There are a couple of reasons why the differences seen between equations (B.7) and (B.15) for example a), and equations (B.10) and (B.18) cannot be quantified. First and most important is that the derivatives of φ is not equal in the two hybrid methods. Secondly the phases between the different terms are unknown without further investigations.

Appendix C

Pseudocode

C.1 Pseudocode for the Runge-Kutta implementation

An overview with the main details of the steps in the explicit fourth-order Runge-Kutta method is given here. Here ΔT is the main time-step size, based on the CFL-criteria or the input value.

$\Delta t(1) = \Delta T/2$
$\Delta t(2) = \Delta T/2$
$\Delta t(3) = \Delta T$
for $ii = 1 \rightarrow 4$ **do**
  for all CFD cells **do**
    $du(i)^*$ = advect $u(i)$
    $du(i)^{**}$ = diffuse $u(i)$ + body-fixed term
    if $ii < 4$ **then**
      $u^{**} = u(1) + \Delta t(i)\,(du(i)^* + du(i)^{**})$;
    end if
  end for
  for all HPC nodes on the FS **do**
    $df\zeta(i)$ = RHS of eq (2.12) based on $\zeta(i)$ and $\varphi(i)$
    $df\varphi(i)$ = RHS of eq (2.15) based on $\zeta(i)$ and $\varphi(i)$
    if $ii < 4$ **then**
      $\zeta(i+1) = \zeta(1) + \Delta t(i)\, df\zeta(i)$
      $\varphi(i+1) = \varphi(1) + \Delta t(i)\, df\varphi(i)$
    end if
  end for
  if $i < 4$ **then**
    Re-grid to $\zeta(i+1)$
    Update matrix system based on new grid
    Update $u^{**} = u_0 + \Delta t(i)\, intS(i)$ on the intersection
    Calculate RHS of equation (3.21) and apply boundary conditions
    Solve matrix system for p and φ
    Update $u(i+1) = u^{**} - \Delta t(i)\,\nabla p$ in Ω_{CFD}
    Update $intS(i+1)$ higher order terms in equation (3.67)
  end if

end for
for all CFD cells **do**
$u^* = u(1) + \frac{1}{6}\Delta T\ (du(1)^* + 2 \cdot du(2)^* + 2 \cdot du(3)^* + du(4)^*)$
$u^{**} = u^* + \frac{1}{6}\Delta T\ (du(1)^{**} + 2 \cdot du(2)^{**} + 2 \cdot du(3)^{**} + du(4)^{**})$
end for
for all HPC nodes on the FS **do**
$\zeta(1) = \zeta(1) + \frac{1}{6}\Delta T\ (df\zeta(1) + 2 \cdot df\zeta(2) + 2 \cdot df\zeta(3) + df\zeta(4))$
$\varphi(1) = \varphi(1) + \frac{1}{6}\Delta T\ (df\varphi(1) + 2 \cdot df\varphi(2) + 2 \cdot df\varphi(3) + df\varphi(4))$
end for
Re-grid to $\zeta(1)$
Update matrix system based on new grid
Update $u^{**} = u_0 + \frac{1}{6}\Delta T\ (intS(1) + 2 \cdot intS(2) + 2 \cdot intS(3) + intS(4))$ on the intersection
Calculate RHS of equation (3.21) and apply boundary conditions
Solve matrix system for p and φ
Update $u(1) = u^{**} - \Delta T\, \nabla p$ in Ω_{CFD}
Update $intS(1)$ higher order terms in equation (3.67)

C.2 Pseudocode for iterative procedure

The main steps in the iterative procedure are outlined here. The scheme is used at every step in the explicit fourth-order Runge-Kutta method.

Find ζ and φ on the free surface
Regrid and update matrix system
$\mathbf{a}_0 = \mathbf{a}_0^{\mathrm{N}}$ and $\dot{\boldsymbol{\omega}}_0 = \dot{\boldsymbol{\omega}}_0^{\mathrm{N}}$
while $tol > \varepsilon$ **do**
Calculate $\mathbf{u}^{**}$ based on $\mathbf{a}_0$ and $\dot{\boldsymbol{\omega}}_0$
Calculate $\frac{\rho}{\Delta t}\nabla \cdot \mathbf{u}_r^{**}$
Solve matrix system
Calculate forces on the body
Calculate accelerations $\mathbf{a}_0^*$ and $\dot{\boldsymbol{\omega}}_0^*$
$tol = |\mathbf{a}_0^* - \mathbf{a}_0| + |\dot{\boldsymbol{\omega}}_0^* - \dot{\boldsymbol{\omega}}_0|$
if $tol > \varepsilon$ **then**
New guess on $\mathbf{a}_0$ and $\dot{\boldsymbol{\omega}}_0$, based on average of $\mathbf{a}_0^*$ and $\dot{\boldsymbol{\omega}}_0^*$ from 6 previous iterations
else
$\mathbf{a}_0^{\mathrm{N}+1} = \mathbf{a}_0$ and $\dot{\boldsymbol{\omega}}_0^{\mathrm{N}+1} = \dot{\boldsymbol{\omega}}_0$
end if
end while

Bibliography

Aalbers, A. B. (1984). The water motions in a moonpool. *Ocean Engineering 11*, 557–579.

Andrea, B., L. Claudio, A. Matteo, G. Giorgio, and O. Faltinsen (2015). Generalized HPC method for the Poisson equation. *Journal of Computational Physics Under review*.

Bandyk, P. J. and R. F. Beck (2011). The acceleration potential in fluid–body interaction problems. *Journal of Engineering Mathematics 70*, 147–163.

Berthelsen, P. A. and O. M. Faltinsen (2008). A local directional ghost cell approach for incompressible viscous flow problems with irregular boundaries. *Journal of Computational Physics 227*, 4354–4397.

Bingham, H. B. and H. Zhang (2007). On the accuracy of finite-difference solutions for nonlinear water waves. *Journal of Engineering Mathematics 58*, 211–228.

Boore, D. M. and J. J. Bommer (2005). Processing of strong-motion accelerograms: needs, options and consequences. *Soil Dynamics and Earthquake Engineering 25*, 93–115.

Braathen, A. (1987). *Application of a vortex tracking method to the prediction of roll damping of a two-dimensional floating body*. Ph. D. thesis, NTH.

Braathen, A. and O. M. Faltinsen (1988). Interaction between shed vorticity, free surface waves and forced roll motion of a two-dimensional floating body. *Fluid Dynamics Research 3*, 190–196.

Buchner, B., A. van Dijk, and J. de Wilde (2001). Numerical multiple-body simulation of side-by-side mooring to an fpso. In *Proc. 11th Int. Offshore and Polar Eng. Conf.*

Campana, E., A. D. Mascio, P. G. Esposito, and F. Lalli (1995). Viscous-inviscid coupling in free surface ship flows. *International journal for numerical methods in fluids 21*, 699–722.

Chorin, A. J. (1968). Numerical solution of the Navier-Stokes equations. *Mathematics of Computation 22*, 742–762.

Clement, A. (1996). Coupling of two absorbing boundary conditions for 2D time-domain simulations of free surface gravity waves. *Journal of Computational Physics 126*, 139–151.

Colicchio, G., M. Greco, and O. M. Faltinsen (2006). A bem-level set domain-decomposition strategy for non-linear and fragmented interfacial flows. *International journal for numerical methods in engineering 67*, 1385–1419.

Dommermuth, D. G. and D. K. P. Yue (1987). Numerical simulations of nonlinear axisymmetric flows with a free surface. *Journal of Fluid Mechanics 178*, 195–219.

Faltinsen, O. M. (1990). *Sea Loads on Ships and Offshore Structures*. Cambridge University Press.

Faltinsen, O. M. (2005). *Hydrodynamics of High-Speed Marine Vehicles*. Cambridge University Press.

Faltinsen, O. M. and B. Pettersen (1987). Application of a vortex tracking method to separated flow around marine structures. *Journal of Fluids and Structures 1*, 217–237.

Faltinsen, O. M., O. Rognebakke, and A. N. Timokha (2007). Two-dimensional resonant piston-like sloshing in a moonpool. *Journal of Fluid Mechanics 575*, 359–397.

Faltinsen, O. M. and A. N. Timokha (2009). *Sloshing*. Cambridge University Press.

Ferziger, J. and M. Perić (2002). *Computational Methods for Fluid Dynamics*. Springer-Verlag GmbH.

Fredriksen, A. (2008). Ship motion in exposed harbor. Master's thesis, NTNU.

Fredriksen, A. G., T. Kristiansen, and O. M. Faltinsen (2012). Investigation of gap resonance in moonpools at forward speed using a non-linear domain-decomposition method. In *Proc. 27th International Workshop on Water Waves and Floating Bodies*.

Fredriksen, A. G., T. Kristiansen, and O. M. Faltinsen (2014). Experimental and numerical investigation of wave resonance in moonpools at low forward speed. *Applied Ocean Research 47*, 28–46.

Fredriksen, A. G., T. Kristiansen, and O. M. Faltinsen (2015). Wave-induced response of a floating 2D body with moonpool. *Phil. Trans. R. Soc. A 373*, 20140109.

Gaillarde, G. and A. Cotteleer (2005). Water motion in moonpools empirical and theoretical approach. Technical report, Maritime Research Institute Netherlands (MARIN), HMC Heerema.

Ghia, U., K. N. Ghia, and C. T. Shin (1982). High-Re solutions for incompressible flow using the Navier-Stokes equations and a multigrid method. *Journal of Computational Physics 48*, 387–411.

Graham, J. M. R. (1980). The forces on sharp-edged cylinders in oscillatory flow at low Keulegan-Carpenter numbers. *Journal of Fluid Mechanics 97*, 331–346.

Greco, M., G. Colicchio, and O. M. Faltinsen (2007). Shipping of water on a two-dimensional structure. part 2. *Journal of Fluid Mechanics 581*, 371–399.

Greco, M., G. Colicchio, C. Lugni, and O. M. Faltinsen (2013). 3D domain decomposition for violent wave-ship interactions. *Int. J. Numer. Meth. Engng 95*, 661–684.

Grilli, S. T. (2008). On the development and application of hybrid numerical models in nonlinear free surface hydrodynamics. In *Keynote lecture published in Proc. 8th Intl. Conf. on Hydrodynamic*.

Grilli, S. T., R. W. Gilbert, P. Lubin, S. Vincent, D. Astruc, D. Legendre, M. Duval, O. Kimmoun, H. Branger, D. Devrard, P. Fraunie, and S. Abadie (2004). Numerical modeling and experiments for solitary wave shoaling and breaking over a sloping

beach. In *Proceedings of The 14th International Offshore and Polar Engineering Conference*.

Heiden, H. J. V. D., P. V. D. Plas, A. E. Veldman, R. Luppes, and R. W. Verstappen (2013). Simulation of moonpool water motion. In *V International Conference on Computational Methods in Marine Engineering MARINE 2013*.

Hess, J. L. and A. M. O. Smith (1962). Calculation of non-lifting potential flow about arbitrary three-dimensional bodies. Technical report, Douglas Aircraft, Aircraft Division.

Huijsmans, R. H. M., J. A. Pinkster, and J. J. D. Wilde (2001). Diffraction and radiation of waves around side-by-side moored vessels. In *Proceedings of the Eleventh (2001) International Offshore and Polar Engineering Conference*.

Jonsson, I. G. (1980). A new approach to oscillatory rough turbulent boundary layers. *Ocean Engineering 7*, 109–152.

Kim, S.-H., M. Yamashiro, and A. Yoshida (2010). A simple two-way coupling method of bem and vof model for random wave calculations. *Coastal Engineering 57*, 1018–1028.

Koo, W., M. H. Kim, and A. Tavassoli (2004). Fully nonlinear wave-body interactions with fully submerged dual cylinders. In *International Journal of Offshore and Polar Engineering Vol. 14, No. 3, September 2004 (ISSN 1053-5381)*.

Kristiansen, D. (2010). *Wave Induced Effects on Floaters of Aquaculture Plants*. Ph. D. thesis, NTNU.

Kristiansen, T. (2009). *Two-Dimensional Numerical and Experimental Studies of Piston-mode Resonance*. Ph. D. thesis, NTNU.

Kristiansen, T. and O. M. Faltinsen (2008). Application of a vortex tracking method to the piston-like behaviour in a semi-entrained vertical gap. *Applied Ocean Research 30*, 1–16.

Kristiansen, T. and O. M. Faltinsen (2009). Studies on resonant water motion between a ship and a fixed terminal in shallow water. *Journal of Offshore Mechanics and Arctic Engineering 131*, 11.

Kristiansen, T. and O. M. Faltinsen (2010). A two-dimensional numerical and experimental study of resonant coupled ship and piston-mode motion. *Applied Ocean Research 32*, 158–176.

Kristiansen, T. and O. M. Faltinsen (2012). Gap resonance analyzed by a new domain-decomposition method combining potential and viscous flow. *Applied Ocean Research 34*, 198–208.

Kristiansen, T., T. Sauder, and R. Firoozkoohi (2013). Validation of a hybrid code combining potential and viscous flow with application to 3D moonpool. In *Proceedings of 32nd International Conference on Offshore Mechanics and Arctic Engineering, Nantes, France*.

Lee, C. H., J. S. Letcher, R. G. Mack, J. N. Newman, D. M. Shook, and E. Stanley (2002). Integration of geometry definition and wave analysis software. In *Proceedings of the 21st Conference on Offshore Mechanics and Arctic Engineering*.

Liang, H., O. M. Faltinsen, and Y.-L. Shao (2015). Application of a 2D harmonic polynomial cell (HPC) method to sloshing, singular flows and lifting problems. *Applied Ocean Research Submitted*.

Longuet-Higgins, M. S. and E. D. Cokelet (1976). The deformation of steep surface waves on water. I. A numerical method of computation. *Proceedings of the Royal Society of London. Series A, Mathematical and Physical Sciences 350*, 1–26.

Lu, L. and X. Chen (2012). Dissipation in the gap resonance between two bodies. In *Proc. 27th International Workshop on Water Waves and Floating Bodies*.

Lu, L., L. Cheng, B. Teng, and M. Zhao (2010). Numerical investigation of fluid resonance in two narrow gaps of three identical rectangular structures. *Applied Ocean Research 32*, 177–190.

Lu, L., B. Teng, L. Cheng, L. Sun, and X. B. Chen (2011). Modelling of multi-bodies in close proximity under water waves—fluid resonance in narrow gaps. *Science China Physics, Mechanics & Astronomy 54*, 16–25.

Lu, L., B. Teng, L. Sun, and B. Chen (2011). Modelling of multi-bodies in close proximity under water waves—fluid forces on floating bodies. *Ocean Engineering 38*, 1403–1416.

Maisondieu, C. and M. L. Boulluec (2001). Flow dynamics in a moon-pool experimental and numerical assessment. In *Proceedings of OMAE'01 20th International Conference on Offshore Mechanics and Arctic Engineering, Rio de Janeiro, Brazil*.

Maisondieu, C. and P. Ferrant (2003). Evaluation of the 3d flow dynamics in a moonpool. In *Proceedings of The Thirteenth (2003) International Offshore and Polar Engineering Conference*.

Maisondieu, C., B. Molin, O. Kimmoun, and L. Gentaz (2001). Simulation bidimensionnelle des écoulements dans une baie de forage : Etude des modes de résonance et des amortissements. In *8èmes Journées de l'Hydrodynamique*.

McIver, M. (1996). An example of non-uniqueness in the two-dimensional linear water wave problem. *Journal of Fluid Mechanics 315*, 257–266.

McIver, P. (2005). Complex resonances in the water-wave problem for a floating structure. *Journal of Fluid Mechanics 536*, 423–443.

McIver, P. and M. McIver (1997). Trapped modes in an axisymmetric water-wave problem. *Quarterly Jnl. of Mechanics & App. Maths. 50*, 165–178.

McIver, P. and M. McIver (2006). Trapped modes in the water-wave problem for a freely floating structure. *Journal of Fluid Mechanics 558*, 53–67.

McIver, P. and J. N. Newman (2003). Trapping structures in the three-dimensional water-wave problem. *Journal of Fluid Mechanics 484*, 283–301.

Molin, B. (2001). On the piston and sloshing modes in moonpools. *Journal of Fluid Mechanics 430*, 27–50.

Molin, B., F. Remy, A. Camhi, and A. Ledoux (2009). Experimental and numerical study of the gap resonances in-between two rectangular barges. In *13th Congress of Intl. Maritime Assoc. of Mediterranean*.

Molin, B., F. Remy, O. Kimmoun, and Y. Stassen (2002). Experimental study of the wave propagation and decay in a channel through a rigid ice-sheet. *Applied Ocean Research 24*, 247–260.

Newman, J. N. (1962). The exciting forces on fixed bodies in waves. *Journal of Ship Research 6*, 10–17.

Newman, J. N. (1999). Radiation and diffraction analysis of the McIver toroid. *Journal of Engineering Mathematics 35*, 135–147.

Ommani, B. (2013). *Potential-Flow Predictions of a Semi-Displacement Vessel Including Applications to Calm-Water Broaching*. Ph. D. thesis, NTNU.

Orlanski, I. (1976). A simple boundary condition for unbounded hyperbolic flows. *Journal of Computational Physics 21*, 251–269.

Paulsen, B. T., H. Bredmose, and H. B. Bingham (2014). An efficient domain decomposition strategy for wave loads on surface piercing circular cylinders. *Coastal Engineering 86*, 57–76.

Pauw, W. H., R. H. Huijsmans, and A. Voogt (2007). Advances in the hydrodynamics of side-by-side moored vessels. In *Proceedings of the 26th International Conference on Offshore Mechanics and Arctic Engineering, San Diego, California, USA*.

Saad, Y. (2003). *Iterative Methods for Sparse Linear Systems, Second Edition*. Society for Industrial and Applied Mathematics.

Shao, Y. (2010). *Numerical Potential-Flow Studies on Weakly-Nonlinear Wave-Body Interactions with/without Small Forward Speeds*. Ph. D. thesis, NTNU.

Shao, Y. and O. M. Faltinsen (2012a). Solutions of nonlinear free surface-body interaction with a harmonic polynomial cell method. In *Proc. 27th International Workshop on Water Waves and Floating Bodies*.

Shao, Y. and O. M. Faltinsen (2012b). Towards efficient fully-nonlinear potential-flow solvers in marine hydrodynamics. In *Proceedings of the 31 International Conference on Ocean, Offshore and Arctic Engineering, Rio de Janeiro, Brazil*.

Shao, Y. and O. M. Faltinsen (2013). Fully-nonlinear wave-current-body interaction analysis by a harmonic polynomial cell (hpc) method. In *Proceedings of the 32 International Conference on Ocean, Offshore and Arctic Engineering, Nantes, France*.

Shao, Y. and O. M. Faltinsen (2014). A harmonic polynomial cell (HPC) method for 3D Laplace equation with application in marine hydrodynamics. *Journal of Computational Physics 274*, 312–332.

Sphaier, S., F. Torres, I. Masetti, A. Costa, and C. Levi (2007). Monocolumn behavior in waves: Experimental analysis. *Ocean Engineering 34*, 1724–1733.

Sun, L., R. E. Taylor, and P. Taylor (2010). First- and second- order analysis of resonant waves between adjacent barges. *Journal of Fluids and Structures 26*, 954–978.

Torres, F. G. S., A. T. P. Alho, J. Joel S. Sales, S. H. Sphaier, and K. Nishimoto (2008). Experimental and numerical analysis of the behavior of a monocolumn with a moonpool. In *Proceedings of the ASME 27th International Conference on Offshore Mechanics and Arctic Engineering, Estoril, Portugal*.

van 't Veer, R. and H. J. Tholen (2008). Added resistance of moonpools in calm water. In *Proceedings of the ASME 27th International Conference on Offshore Mechanics and Arctic Engineering*.

Vekua, I. N. (1953). On the completeness of a system of harmonic polynomials in space. *Dokl. Akad. Nauk SSSR (NS) 90*, 495–498.

Wang, C. and G. Wu (2008). Analysis of second-order resonance in wave interactions with floating bodies through a finite-element method. *Ocean Engineering 35*, 717–726.

Wang, C., G. Wu, and B. Khoo (2011). Fully nonlinear simulation of resonant motion of liquid confined between floating structures. *Computers & Fluids 44*, 89–101.

White, F. M. (2006). *Viscous Fluid Flow*. McGraw-Hill.

Yang, S. H., Y. J. Yang, S. B. Lee, J. Do, and S. H. Kwon (2013). Study on moonpool resonance effect on motion of modern compact drillship. *Journal of Ocean Engineering and Technology 27*, 53–60.

Yeung, R. W. (1982). The transient heaving motion of floating cylinders. *Journal of Engineering Mathematics 16*, 97–119.

Yeung, R. W. and R. K. M. Seah (2007). On Helmholtz and higher-order resonance of twin floating bodies. *Journal of Engineering Mathematics 58*, 251–265.

Zhang, X. and P. Bandyk (2013). On two-dimensional moonpool resonance for twin bodies in a two-layer fluid. *Applied Ocean Research 40*, 1–13.

Zhang, X. and P. Bandyk (2014). Two-dimensional moonpool resonances for interface and surface-piercing twin bodies in a two-layer fluid. *Applied Ocean Research 47*, 204–218.

Zhang, Y. (2013). *A Numerical Wave Tank Based on Coupled Potential Flow–Viscous Flow Model*. Ph. D. thesis, Oregon State.

Zhang, Y., F. D. Pin, and S. C. Yim (2014). A heterogeneous flow model based on DD method for free surface fluid–structure interaction problems. *International Journal for Numerical Methods in Fluids 74*, 292–312.

Zhao, R. and O. M. Faltinsen (1998). Interaction between waves and current on a two-dimensional body in the free surface. *Applied Ocean Research 10, No 2*, 87 99.

Previous PhD theses published at the Departement of Marine Technology
(earlier: Faculty of Marine Technology)
NORWEGIAN UNIVERSITY OF SCIENCE AND TECHNOLOGY

Report No.	Author	Title
	Kavlie, Dag	Optimization of Plane Elastic Grillages, 1967
	Hansen, Hans R.	Man-Machine Communication and Data-Storage Methods in Ship Structural Design, 1971
	Gisvold, Kaare M.	A Method for non-linear mixed -integer programming and its Application to Design Problems, 1971
	Lund, Sverre	Tanker Frame Optimalization by means of SUMT-Transformation and Behaviour Models, 1971
	Vinje, Tor	On Vibration of Spherical Shells Interacting with Fluid, 1972
	Lorentz, Jan D.	Tank Arrangement for Crude Oil Carriers in Accordance with the new Anti-Pollution Regulations, 1975
	Carlsen, Carl A.	Computer-Aided Design of Tanker Structures, 1975
	Larsen, Carl M.	Static and Dynamic Analysis of Offshore Pipelines during Installation, 1976
UR-79-01	Brigt Hatlestad, MK	The finite element method used in a fatigue evaluation of fixed offshore platforms. (Dr.Ing. Thesis)
UR-79-02	Erik Pettersen, MK	Analysis and design of cellular structures. (Dr.Ing. Thesis)
UR-79-03	Sverre Valsgård, MK	Finite difference and finite element methods applied to nonlinear analysis of plated structures. (Dr.Ing. Thesis)
UR-79-04	Nils T. Nordsve, MK	Finite element collapse analysis of structural members considering imperfections and stresses due to fabrication. (Dr.Ing. Thesis)
UR-79-05	Ivar J. Fylling, MK	Analysis of towline forces in ocean towing systems. (Dr.Ing. Thesis)
UR-80-06	Nils Sandsmark, MM	Analysis of Stationary and Transient Heat Conduction by the Use of the Finite Element Method. (Dr.Ing. Thesis)
UR-80-09	Sverre Haver, MK	Analysis of uncertainties related to the stochastic modeling of ocean waves. (Dr.Ing. Thesis)
UR-81-15	Odland, Jonas	On the Strength of welded Ring stiffened cylindrical Shells primarily subjected to axial Compression
UR-82-17	Engesvik, Knut	Analysis of Uncertainties in the fatigue Capacity of

		Welded Joints
UR-82-18	Rye, Henrik	Ocean wave groups
UR-83-30	Eide, Oddvar Inge	On Cumulative Fatigue Damage in Steel Welded Joints
UR-83-33	Mo, Olav	Stochastic Time Domain Analysis of Slender Offshore Structures
UR-83-34	Amdahl, Jørgen	Energy absorption in Ship-platform impacts
UR-84-37	Mørch, Morten	Motions and mooring forces of semi submersibles as determined by full-scale measurements and theoretical analysis
UR-84-38	Soares, C. Guedes	Probabilistic models for load effects in ship structures
UR-84-39	Aarsnes, Jan V.	Current forces on ships
UR-84-40	Czujko, Jerzy	Collapse Analysis of Plates subjected to Biaxial Compression and Lateral Load
UR-85-46	Alf G. Engseth, MK	Finite element collapse analysis of tubular steel offshore structures. (Dr.Ing. Thesis)
UR-86-47	Dengody Sheshappa, MP	A Computer Design Model for Optimizing Fishing Vessel Designs Based on Techno-Economic Analysis. (Dr.Ing. Thesis)
UR-86-48	Vidar Aanesland, MH	A Theoretical and Numerical Study of Ship Wave Resistance. (Dr.Ing. Thesis)
UR-86-49	Heinz-Joachim Wessel, MK	Fracture Mechanics Analysis of Crack Growth in Plate Girders. (Dr.Ing. Thesis)
UR-86-50	Jon Taby, MK	Ultimate and Post-ultimate Strength of Dented Tubular Members. (Dr.Ing. Thesis)
UR-86-51	Walter Lian, MH	A Numerical Study of Two-Dimensional Separated Flow Past Bluff Bodies at Moderate KC-Numbers. (Dr.Ing. Thesis)
UR-86-52	Bjørn Sortland, MH	Force Measurements in Oscillating Flow on Ship Sections and Circular Cylinders in a U-Tube Water Tank. (Dr.Ing. Thesis)
UR-86-53	Kurt Strand, MM	A System Dynamic Approach to One-dimensional Fluid Flow. (Dr.Ing. Thesis)
UR-86-54	Arne Edvin Løken, MH	Three Dimensional Second Order Hydrodynamic Effects on Ocean Structures in Waves. (Dr.Ing. Thesis)
UR-86-55	Sigurd Falch, MH	A Numerical Study of Slamming of Two-Dimensional Bodies. (Dr.Ing. Thesis)
UR-87-56	Arne Braathen, MH	Application of a Vortex Tracking Method to the Prediction of Roll Damping of a Two-Dimension Floating Body. (Dr.Ing. Thesis)

UR-87-57	Bernt Leira, MK	Gaussian Vector Processes for Reliability Analysis involving Wave-Induced Load Effects. (Dr.Ing. Thesis)
UR-87-58	Magnus Småvik, MM	Thermal Load and Process Characteristics in a Two-Stroke Diesel Engine with Thermal Barriers (in Norwegian). (Dr.Ing. Thesis)
MTA-88-59	Bernt Arild Bremdal, MP	An Investigation of Marine Installation Processes – A Knowledge - Based Planning Approach. (Dr.Ing. Thesis)
MTA-88-60	Xu Jun, MK	Non-linear Dynamic Analysis of Space-framed Offshore Structures. (Dr.Ing. Thesis)
MTA-89-61	Gang Miao, MH	Hydrodynamic Forces and Dynamic Responses of Circular Cylinders in Wave Zones. (Dr.Ing. Thesis)
MTA-89-62	Martin Greenhow, MH	Linear and Non-Linear Studies of Waves and Floating Bodies. Part I and Part II. (Dr.Techn. Thesis)
MTA-89-63	Chang Li, MH	Force Coefficients of Spheres and Cubes in Oscillatory Flow with and without Current. (Dr.Ing. Thesis
MTA-89-64	Hu Ying, MP	A Study of Marketing and Design in Development of Marine Transport Systems. (Dr.Ing. Thesis)
MTA-89-65	Arild Jæger, MH	Seakeeping, Dynamic Stability and Performance of a Wedge Shaped Planing Hull. (Dr.Ing. Thesis)
MTA-89-66	Chan Siu Hung, MM	The dynamic characteristics of tilting-pad bearings
MTA-89-67	Kim Wikstrøm, MP	Analysis av projekteringen for ett offshore projekt. (Licenciat-avhandling)
MTA-89-68	Jiao Guoyang, MK	Reliability Analysis of Crack Growth under Random Loading, considering Model Updating. (Dr.Ing. Thesis)
MTA-89-69	Arnt Olufsen, MK	Uncertainty and Reliability Analysis of Fixed Offshore Structures. (Dr.Ing. Thesis)
MTA-89-70	Wu Yu-Lin, MR	System Reliability Analyses of Offshore Structures using improved Truss and Beam Models. (Dr.Ing. Thesis)
MTA-90-71	Jan Roger Hoff, MH	Three-dimensional Green function of a vessel with forward speed in waves. (Dr.Ing. Thesis)
MTA-90-72	Rong Zhao, MH	Slow-Drift Motions of a Moored Two-Dimensional Body in Irregular Waves. (Dr.Ing. Thesis)
MTA-90-73	Atle Minsaas, MP	Economical Risk Analysis. (Dr.Ing. Thesis)
MTA-90-74	Knut-Aril Farnes, MK	Long-term Statistics of Response in Non-linear Marine Structures. (Dr.Ing. Thesis)
MTA-90-75	Torbjørn Sotberg, MK	Application of Reliability Methods for Safety Assessment of Submarine Pipelines. (Dr.Ing.

		Thesis)
MTA-90-76	Zeuthen, Steffen, MP	SEAMAID. A computational model of the design process in a constraint-based logic programming environment. An example from the offshore domain. (Dr.Ing. Thesis)
MTA-91-77	Haagensen, Sven, MM	Fuel Dependant Cyclic Variability in a Spark Ignition Engine - An Optical Approach. (Dr.Ing. Thesis)
MTA-91-78	Løland, Geir, MH	Current forces on and flow through fish farms. (Dr.Ing. Thesis)
MTA-91-79	Hoen, Christopher, MK	System Identification of Structures Excited by Stochastic Load Processes. (Dr.Ing. Thesis)
MTA-91-80	Haugen, Stein, MK	Probabilistic Evaluation of Frequency of Collision between Ships and Offshore Platforms. (Dr.Ing. Thesis)
MTA-91-81	Sødahl, Nils, MK	Methods for Design and Analysis of Flexible Risers. (Dr.Ing. Thesis)
MTA-91-82	Ormberg, Harald, MK	Non-linear Response Analysis of Floating Fish Farm Systems. (Dr.Ing. Thesis)
MTA-91-83	Marley, Mark J., MK	Time Variant Reliability under Fatigue Degradation. (Dr.Ing. Thesis)
MTA-91-84	Krokstad, Jørgen R., MH	Second-order Loads in Multidirectional Seas. (Dr.Ing. Thesis)
MTA-91-85	Molteberg, Gunnar A., MM	The Application of System Identification Techniques to Performance Monitoring of Four Stroke Turbocharged Diesel Engines. (Dr.Ing. Thesis)
MTA-92-86	Mørch, Hans Jørgen Bjelke, MH	Aspects of Hydrofoil Design: with Emphasis on Hydrofoil Interaction in Calm Water. (Dr.Ing. Thesis)
MTA-92-87	Chan Siu Hung, MM	Nonlinear Analysis of Rotordynamic Instabilities in Highspeed Turbomachinery. (Dr.Ing. Thesis)
MTA-92-88	Bessason, Bjarni, MK	Assessment of Earthquake Loading and Response of Seismically Isolated Bridges. (Dr.Ing. Thesis)
MTA-92-89	Langli, Geir, MP	Improving Operational Safety through exploitation of Design Knowledge - an investigation of offshore platform safety. (Dr.Ing. Thesis)
MTA-92-90	Sævik, Svein, MK	On Stresses and Fatigue in Flexible Pipes. (Dr.Ing. Thesis)
MTA-92-91	Ask, Tor Ø., MM	Ignition and Flame Growth in Lean Gas-Air Mixtures. An Experimental Study with a Schlieren System. (Dr.Ing. Thesis)
MTA-86-92	Hessen, Gunnar, MK	Fracture Mechanics Analysis of Stiffened Tubular Members. (Dr.Ing. Thesis)

MTA-93-93	Steinebach, Christian, MM	Knowledge Based Systems for Diagnosis of Rotating Machinery. (Dr.Ing. Thesis)
MTA-93-94	Dalane, Jan Inge, MK	System Reliability in Design and Maintenance of Fixed Offshore Structures. (Dr.Ing. Thesis)
MTA-93-95	Steen, Sverre, MH	Cobblestone Effect on SES. (Dr.Ing. Thesis)
MTA-93-96	Karunakaran, Daniel, MK	Nonlinear Dynamic Response and Reliability Analysis of Drag-dominated Offshore Platforms. (Dr.Ing. Thesis)
MTA-93-97	Hagen, Arnulf, MP	The Framework of a Design Process Language. (Dr.Ing. Thesis)
MTA-93-98	Nordrik, Rune, MM	Investigation of Spark Ignition and Autoignition in Methane and Air Using Computational Fluid Dynamics and Chemical Reaction Kinetics. A Numerical Study of Ignition Processes in Internal Combustion Engines. (Dr.Ing. Thesis)
MTA-94-99	Passano, Elizabeth, MK	Efficient Analysis of Nonlinear Slender Marine Structures. (Dr.Ing. Thesis)
MTA-94-100	Kvålsvold, Jan, MH	Hydroelastic Modelling of Wetdeck Slamming on Multihull Vessels. (Dr.Ing. Thesis)
MTA-94-102	Bech, Sidsel M., MK	Experimental and Numerical Determination of Stiffness and Strength of GRP/PVC Sandwich Structures. (Dr.Ing. Thesis)
MTA-95-103	Paulsen, Hallvard, MM	A Study of Transient Jet and Spray using a Schlieren Method and Digital Image Processing. (Dr.Ing. Thesis)
MTA-95-104	Hovde, Geir Olav, MK	Fatigue and Overload Reliability of Offshore Structural Systems, Considering the Effect of Inspection and Repair. (Dr.Ing. Thesis)
MTA-95-105	Wang, Xiaozhi, MK	Reliability Analysis of Production Ships with Emphasis on Load Combination and Ultimate Strength. (Dr.Ing. Thesis)
MTA-95-106	Ulstein, Tore, MH	Nonlinear Effects of a Flexible Stern Seal Bag on Cobblestone Oscillations of an SES. (Dr.Ing. Thesis)
MTA-95-107	Solaas, Frøydis, MH	Analytical and Numerical Studies of Sloshing in Tanks. (Dr.Ing. Thesis)
MTA-95-108	Hellan, Øyvind, MK	Nonlinear Pushover and Cyclic Analyses in Ultimate Limit State Design and Reassessment of Tubular Steel Offshore Structures. (Dr.Ing. Thesis)
MTA-95-109	Hermundstad, Ole A., MK	Theoretical and Experimental Hydroelastic Analysis of High Speed Vessels. (Dr.Ing. Thesis)
MTA-96-110	Bratland, Anne K., MH	Wave-Current Interaction Effects on Large-Volume Bodies in Water of Finite Depth. (Dr.Ing. Thesis)
MTA-96-111	Herfjord, Kjell, MH	A Study of Two-dimensional Separated Flow by a Combination of the Finite Element Method and

		Navier-Stokes Equations. (Dr.Ing. Thesis)
MTA-96-112	Æsøy, Vilmar, MM	Hot Surface Assisted Compression Ignition in a Direct Injection Natural Gas Engine. (Dr.Ing. Thesis)
MTA-96-113	Eknes, Monika L., MK	Escalation Scenarios Initiated by Gas Explosions on Offshore Installations. (Dr.Ing. Thesis)
MTA-96-114	Erikstad, Stein O., MP	A Decision Support Model for Preliminary Ship Design. (Dr.Ing. Thesis)
MTA-96-115	Pedersen, Egil, MH	A Nautical Study of Towed Marine Seismic Streamer Cable Configurations. (Dr.Ing. Thesis)
MTA-97-116	Moksnes, Paul O., MM	Modelling Two-Phase Thermo-Fluid Systems Using Bond Graphs. (Dr.Ing. Thesis)
MTA-97-117	Halse, Karl H., MK	On Vortex Shedding and Prediction of Vortex-Induced Vibrations of Circular Cylinders. (Dr.Ing. Thesis)
MTA-97-118	Igland, Ragnar T., MK	Reliability Analysis of Pipelines during Laying, considering Ultimate Strength under Combined Loads. (Dr.Ing. Thesis)
MTA-97-119	Pedersen, Hans-P., MP	Levendefiskteknologi for fiskefartøy. (Dr.Ing. Thesis)
MTA-98-120	Vikestad, Kyrre, MK	Multi-Frequency Response of a Cylinder Subjected to Vortex Shedding and Support Motions. (Dr.Ing. Thesis)
MTA-98-121	Azadi, Mohammad R. E., MK	Analysis of Static and Dynamic Pile-Soil-Jacket Behaviour. (Dr.Ing. Thesis)
MTA-98-122	Ulltang, Terje, MP	A Communication Model for Product Information. (Dr.Ing. Thesis)
MTA-98-123	Torbergsen, Erik, MM	Impeller/Diffuser Interaction Forces in Centrifugal Pumps. (Dr.Ing. Thesis)
MTA-98-124	Hansen, Edmond, MH	A Discrete Element Model to Study Marginal Ice Zone Dynamics and the Behaviour of Vessels Moored in Broken Ice. (Dr.Ing. Thesis)
MTA-98-125	Videiro, Paulo M., MK	Reliability Based Design of Marine Structures. (Dr.Ing. Thesis)
MTA-99-126	Mainçon, Philippe, MK	Fatigue Reliability of Long Welds Application to Titanium Risers. (Dr.Ing. Thesis)
MTA-99-127	Haugen, Elin M., MH	Hydroelastic Analysis of Slamming on Stiffened Plates with Application to Catamaran Wetdecks. (Dr.Ing. Thesis)
MTA-99-128	Langhelle, Nina K., MK	Experimental Validation and Calibration of Nonlinear Finite Element Models for Use in Design of Aluminium Structures Exposed to Fire. (Dr.Ing. Thesis)
MTA-99-	Berstad, Are J., MK	Calculation of Fatigue Damage in Ship Structures.

129		(Dr.Ing. Thesis)
MTA-99-130	Andersen, Trond M., MM	Short Term Maintenance Planning. (Dr.Ing. Thesis)
MTA-99-131	Tveiten, Bård Wathne, MK	Fatigue Assessment of Welded Aluminium Ship Details. (Dr.Ing. Thesis)
MTA-99-132	Søreide, Fredrik, MP	Applications of underwater technology in deep water archaeology. Principles and practice. (Dr.Ing. Thesis)
MTA-99-133	Tønnessen, Rune, MH	A Finite Element Method Applied to Unsteady Viscous Flow Around 2D Blunt Bodies With Sharp Corners. (Dr.Ing. Thesis)
MTA-99-134	Elvekrok, Dag R., MP	Engineering Integration in Field Development Projects in the Norwegian Oil and Gas Industry. The Supplier Management of Norne. (Dr.Ing. Thesis)
MTA-99-135	Fagerholt, Kjetil, MP	Optimeringsbaserte Metoder for Ruteplanlegging innen skipsfart. (Dr.Ing. Thesis)
MTA-99-136	Bysveen, Marie, MM	Visualization in Two Directions on a Dynamic Combustion Rig for Studies of Fuel Quality. (Dr.Ing. Thesis)
MTA-2000-137	Storteig, Eskild, MM	Dynamic characteristics and leakage performance of liquid annular seals in centrifugal pumps. (Dr.Ing. Thesis)
MTA-2000-138	Sagli, Gro, MK	Model uncertainty and simplified estimates of long term extremes of hull girder loads in ships. (Dr.Ing. Thesis)
MTA-2000-139	Tronstad, Harald, MK	Nonlinear analysis and design of cable net structures like fishing gear based on the finite element method. (Dr.Ing. Thesis)
MTA-2000-140	Kroneberg, André, MP	Innovation in shipping by using scenarios. (Dr.Ing. Thesis)
MTA-2000-141	Haslum, Herbjørn Alf, MH	Simplified methods applied to nonlinear motion of spar platforms. (Dr.Ing. Thesis)
MTA-2001-142	Samdal, Ole Johan, MM	Modelling of Degradation Mechanisms and Stressor Interaction on Static Mechanical Equipment Residual Lifetime. (Dr.Ing. Thesis)
MTA-2001-143	Baarholm, Rolf Jarle, MH	Theoretical and experimental studies of wave impact underneath decks of offshore platforms. (Dr.Ing. Thesis)
MTA-2001-144	Wang, Lihua, MK	Probabilistic Analysis of Nonlinear Wave-induced Loads on Ships. (Dr.Ing. Thesis)
MTA-2001-145	Kristensen, Odd H. Holt, MK	Ultimate Capacity of Aluminium Plates under Multiple Loads, Considering HAZ Properties. (Dr.Ing. Thesis)
MTA-2001-146	Greco, Marilena, MH	A Two-Dimensional Study of Green-Water

		Loading. (Dr.Ing. Thesis)
MTA-2001-147	Heggelund, Svein E., MK	Calculation of Global Design Loads and Load Effects in Large High Speed Catamarans. (Dr.Ing. Thesis)
MTA-2001-148	Babalola, Olusegun T., MK	Fatigue Strength of Titanium Risers – Defect Sensitivity. (Dr.Ing. Thesis)
MTA-2001-149	Mohammed, Abuu K., MK	Nonlinear Shell Finite Elements for Ultimate Strength and Collapse Analysis of Ship Structures. (Dr.Ing. Thesis)
MTA-2002-150	Holmedal, Lars E., MH	Wave-current interactions in the vicinity of the sea bed. (Dr.Ing. Thesis)
MTA-2002-151	Rognebakke, Olav F., MH	Sloshing in rectangular tanks and interaction with ship motions. (Dr.Ing. Thesis)
MTA-2002-152	Lader, Pål Furset, MH	Geometry and Kinematics of Breaking Waves. (Dr.Ing. Thesis)
MTA-2002-153	Yang, Qinzheng, MH	Wash and wave resistance of ships in finite water depth. (Dr.Ing. Thesis)
MTA-2002-154	Melhus, Øyvin, MM	Utilization of VOC in Diesel Engines. Ignition and combustion of VOC released by crude oil tankers. (Dr.Ing. Thesis)
MTA-2002-155	Ronæss, Marit, MH	Wave Induced Motions of Two Ships Advancing on Parallel Course. (Dr.Ing. Thesis)
MTA-2002-156	Økland, Ole D., MK	Numerical and experimental investigation of whipping in twin hull vessels exposed to severe wet deck slamming. (Dr.Ing. Thesis)
MTA-2002-157	Ge, Chunhua, MK	Global Hydroelastic Response of Catamarans due to Wet Deck Slamming. (Dr.Ing. Thesis)
MTA-2002-158	Byklum, Eirik, MK	Nonlinear Shell Finite Elements for Ultimate Strength and Collapse Analysis of Ship Structures. (Dr.Ing. Thesis)
IMT-2003-1	Chen, Haibo, MK	Probabilistic Evaluation of FPSO-Tanker Collision in Tandem Offloading Operation. (Dr.Ing. Thesis)
IMT-2003-2	Skaugset, Kjetil Bjørn, MK	On the Suppression of Vortex Induced Vibrations of Circular Cylinders by Radial Water Jets. (Dr.Ing. Thesis)
IMT-2003-3	Chezhian, Muthu	Three-Dimensional Analysis of Slamming. (Dr.Ing. Thesis)
IMT-2003-4	Buhaug, Øyvind	Deposit Formation on Cylinder Liner Surfaces in Medium Speed Engines. (Dr.Ing. Thesis)
IMT-2003-5	Tregde, Vidar	Aspects of Ship Design: Optimization of Aft Hull with Inverse Geometry Design. (Dr.Ing. Thesis)
IMT-	Wist, Hanne Therese	Statistical Properties of Successive Ocean Wave

2003-6		Parameters. (Dr.Ing. Thesis)
IMT-2004-7	Ransau, Samuel	Numerical Methods for Flows with Evolving Interfaces. (Dr.Ing. Thesis)
IMT-2004-8	Soma, Torkel	Blue-Chip or Sub-Standard. A data interrogation approach of identity safety characteristics of shipping organization. (Dr.Ing. Thesis)
IMT-2004-9	Ersdal, Svein	An experimental study of hydrodynamic forces on cylinders and cables in near axial flow. (Dr.Ing. Thesis)
IMT-2005-10	Brodtkorb, Per Andreas	The Probability of Occurrence of Dangerous Wave Situations at Sea. (Dr.Ing. Thesis)
IMT-2005-11	Yttervik, Rune	Ocean current variability in relation to offshore engineering. (Dr.Ing. Thesis)
IMT-2005-12	Fredheim, Arne	Current Forces on Net-Structures. (Dr.Ing. Thesis)
IMT-2005-13	Heggernes, Kjetil	Flow around marine structures. (Dr.Ing. Thesis
IMT-2005-14	Fouques, Sebastien	Lagrangian Modelling of Ocean Surface Waves and Synthetic Aperture Radar Wave Measurements. (Dr.Ing. Thesis)
IMT-2006-15	Holm, Håvard	Numerical calculation of viscous free surface flow around marine structures. (Dr.Ing. Thesis)
IMT-2006-16	Bjørheim, Lars G.	Failure Assessment of Long Through Thickness Fatigue Cracks in Ship Hulls. (Dr.Ing. Thesis)
IMT-2006-17	Hansson, Lisbeth	Safety Management for Prevention of Occupational Accidents. (Dr.Ing. Thesis)
IMT-2006-18	Zhu, Xinying	Application of the CIP Method to Strongly Nonlinear Wave-Body Interaction Problems. (Dr.Ing. Thesis)
IMT-2006-19	Reite, Karl Johan	Modelling and Control of Trawl Systems. (Dr.Ing. Thesis)
IMT-2006-20	Smogeli, Øyvind Notland	Control of Marine Propellers. From Normal to Extreme Conditions. (Dr.Ing. Thesis)
IMT-2007-21	Storhaug, Gaute	Experimental Investigation of Wave Induced Vibrations and Their Effect on the Fatigue Loading of Ships. (Dr.Ing. Thesis)
IMT-2007-22	Sun, Hui	A Boundary Element Method Applied to Strongly Nonlinear Wave-Body Interaction Problems. (PhD Thesis, CeSOS)
IMT-2007-23	Rustad, Anne Marthine	Modelling and Control of Top Tensioned Risers. (PhD Thesis, CeSOS)
IMT-2007-24	Johansen, Vegar	Modelling flexible slender system for real-time simulations and control applications
IMT-2007-25	Wroldsen, Anders Sunde	Modelling and control of tensegrity structures.

		(PhD Thesis, CeSOS)
IMT-2007-26	Aronsen, Kristoffer Høye	An experimental investigation of in-line and combined inline and cross flow vortex induced vibrations. (Dr. avhandling, IMT)
IMT-2007-27	Gao, Zhen	Stochastic Response Analysis of Mooring Systems with Emphasis on Frequency-domain Analysis of Fatigue due to Wide-band Response Processes (PhD Thesis, CeSOS)
IMT-2007-28	Thorstensen, Tom Anders	Lifetime Profit Modelling of Ageing Systems Utilizing Information about Technical Condition. (Dr.ing. thesis, IMT)
IMT-2008-29	Berntsen, Per Ivar B.	Structural Reliability Based Position Mooring. (PhD-Thesis, IMT)
IMT-2008-30	Ye, Naiquan	Fatigue Assessment of Aluminium Welded Box-stiffener Joints in Ships (Dr.ing. thesis, IMT)
IMT-2008-31	Radan, Damir	Integrated Control of Marine Electrical Power Systems. (PhD-Thesis, IMT)
IMT-2008-32	Thomassen, Paul	Methods for Dynamic Response Analysis and Fatigue Life Estimation of Floating Fish Cages. (Dr.ing. thesis, IMT)
IMT-2008-33	Pákozdi, Csaba	A Smoothed Particle Hydrodynamics Study of Two-dimensional Nonlinear Sloshing in Rectangular Tanks. (Dr.ing.thesis, IMT/ CeSOS)
IMT-2007-34	Grytøyr, Guttorm	A Higher-Order Boundary Element Method and Applications to Marine Hydrodynamics. (Dr.ing.thesis, IMT)
IMT-2008-35	Drummen, Ingo	Experimental and Numerical Investigation of Nonlinear Wave-Induced Load Effects in Containerships considering Hydroelasticity. (PhD thesis, CeSOS)
IMT-2008-36	Skejic, Renato	Maneuvering and Seakeeping of a Singel Ship and of Two Ships in Interaction. (PhD-Thesis, CeSOS)
IMT-2008-37	Harlem, Alf	An Age-Based Replacement Model for Repairable Systems with Attention to High-Speed Marine Diesel Engines. (PhD-Thesis, IMT)
IMT-2008-38	Alsos, Hagbart S.	Ship Grounding. Analysis of Ductile Fracture, Bottom Damage and Hull Girder Response. (PhD-thesis, IMT)
IMT-2008-39	Graczyk, Mateusz	Experimental Investigation of Sloshing Loading and Load Effects in Membrane LNG Tanks Subjected to Random Excitation. (PhD-thesis, CeSOS)
IMT-2008-40	Taghipour, Reza	Efficient Prediction of Dynamic Response for Flexible amd Multi-body Marine Structures. (PhD-thesis, CeSOS)
IMT-2008-41	Ruth, Eivind	Propulsion control and thrust allocation on marine

		vessels. (PhD thesis, CeSOS)
IMT-2008-42	Nystad, Bent Helge	Technical Condition Indexes and Remaining Useful Life of Aggregated Systems. PhD thesis, IMT
IMT-2008-43	Soni, Prashant Kumar	Hydrodynamic Coefficients for Vortex Induced Vibrations of Flexible Beams, PhD thesis, CeSOS
IMT-2009-43	Amlashi, Hadi K.K.	Ultimate Strength and Reliability-based Design of Ship Hulls with Emphasis on Combined Global and Local Loads. PhD Thesis, IMT
IMT-2009-44	Pedersen, Tom Arne	Bond Graph Modelling of Marine Power Systems. PhD Thesis, IMT
IMT-2009-45	Kristiansen, Trygve	Two-Dimensional Numerical and Experimental Studies of Piston-Mode Resonance. PhD-Thesis, CeSOS
IMT-2009-46	Ong, Muk Chen	Applications of a Standard High Reynolds Number Model and a Stochastic Scour Prediction Model for Marine Structures. PhD-thesis, IMT
IMT-2009-47	Hong, Lin	Simplified Analysis and Design of Ships subjected to Collision and Grounding. PhD-thesis, IMT
IMT-2009-48	Koushan, Kamran	Vortex Induced Vibrations of Free Span Pipelines, PhD thesis, IMT
IMT-2009-49	Korsvik, Jarl Eirik	Heuristic Methods for Ship Routing and Scheduling. PhD-thesis, IMT
IMT-2009-50	Lee, Jihoon	Experimental Investigation and Numerical in Analyzing the Ocean Current Displacement of Longlines. Ph.d.-Thesis, IMT.
IMT-2009-51	Vestbøstad, Tone Gran	A Numerical Study of Wave-in-Deck Impact usin a Two-Dimensional Constrained Interpolation Profile Method, Ph.d.thesis, CeSOS.
IMT-2009-52	Bruun, Kristine	Bond Graph Modelling of Fuel Cells for Marine Power Plants. Ph.d.-thesis, IMT
IMT 2009-53	Holstad, Anders	Numerical Investigation of Turbulence in a Sekwed Three-Dimensional Channel Flow, Ph.d.-thesis, IMT.
IMT 2009-54	Ayala-Uraga, Efren	Reliability-Based Assessment of Deteriorating Ship-shaped Offshore Structures, Ph.d.-thesis, IMT
IMT 2009-55	Kong, Xiangjun	A Numerical Study of a Damaged Ship in Beam Sea Waves. Ph.d.-thesis, IMT/CeSOS.
IMT 2010-56	Kristiansen, David	Wave Induced Effects on Floaters of Aquaculture Plants, Ph.d.-thesis, CeSOS.
IMT 2010-57	Ludvigsen, Martin	An ROV-Toolbox for Optical and Acoustic Scientific Seabed Investigation. Ph.d.-thesis IMT.

IMT 2010-58	Hals, Jørgen	Modelling and Phase Control of Wave-Energy Converters. Ph.d.thesis, CeSOS.
IMT 2010- 59	Shu, Zhi	Uncertainty Assessment of Wave Loads and Ultimate Strength of Tankers and Bulk Carriers in a Reliability Framework. Ph.d. Thesis, IMT/ CeSOS
IMT 2010-60	Shao, Yanlin	Numerical Potential-Flow Studies on Weakly-Nonlinear Wave-Body Interactions with/without Small Forward Speed, Ph.d.thesis,CeSOS.
IMT 2010-61	Califano, Andrea	Dynamic Loads on Marine Propellers due to Intermittent Ventilation. Ph.d.thesis, IMT.
IMT 2010-62	El Khoury, George	Numerical Simulations of Massively Separated Turbulent Flows, Ph.d.-thesis, IMT
IMT 2010-63	Seim, Knut Sponheim	Mixing Process in Dense Overflows with Emphasis on the Faroe Bank Channel Overflow. Ph.d.thesis, IMT
IMT 2010-64	Jia, Huirong	Structural Analysis of Intect and Damaged Ships in a Collission Risk Analysis Perspective. Ph.d.thesis CeSoS.
IMT 2010-65	Jiao, Linlin	Wave-Induced Effects on a Pontoon-type Very Large Floating Structures (VLFS). Ph.D.-thesis, CeSOS.
IMT 2010-66	Abrahamsen, Bjørn Christian	Sloshing Induced Tank Roof with Entrapped Air Pocket. Ph.d.thesis, CeSOS.
IMT 2011-67	Karimirad, Madjid	Stochastic Dynamic Response Analysis of Spar-Type Wind Turbines with Catenary or Taut Mooring Systems. Ph.d.-thesis, CeSOS.
IMT - 2011-68	Erlend Meland	Condition Monitoring of Safety Critical Valves. Ph.d.-thesis, IMT.
IMT – 2011-69	Yang, Limin	Stochastic Dynamic System Analysis of Wave Energy Converter with Hydraulic Power Take-Off, with Particular Reference to Wear Damage Analysis, Ph.d. Thesis, CeSOS.
IMT – 2011-70	Visscher, Jan	Application of Particla Image Velocimetry on Turbulent Marine Flows, Ph.d.Thesis, IMT.
IMT – 2011-71	Su, Biao	Numerical Predictions of Global and Local Ice Loads on Ships. Ph.d.Thesis, CeSOS.
IMT – 2011-72	Liu, Zhenhui	Analytical and Numerical Analysis of Iceberg Collision with Ship Structures. Ph.d.Thesis, IMT.
IMT – 2011-73	Aarsæther, Karl Gunnar	Modeling and Analysis of Ship Traffic by Observation and Numerical Simulation. Ph.d.Thesis, IMT.
Imt – 2011-74	Wu, Jie	Hydrodynamic Force Identification from Stochastic Vortex Induced Vibration Experiments with Slender Beams. Ph.d.Thesis, IMT.

Imt – 2011-75	Amini, Hamid	Azimuth Propulsors in Off-design Conditions. Ph.d.Thesis, IMT.
IMT – 2011-76	Nguyen, Tan-Hoi	Toward a System of Real-Time Prediction and Monitoring of Bottom Damage Conditions During Ship Grounding. Ph.d.thesis, IMT.
IMT- 2011-77	Tavakoli, Mohammad T.	Assessment of Oil Spill in Ship Collision and Grounding, Ph.d.thesis, IMT.
IMT- 2011-78	Guo, Bingjie	Numerical and Experimental Investigation of Added Resistance in Waves. Ph.d.Thesis, IMT.
IMT- 2011-79	Chen, Qiaofeng	Ultimate Strength of Aluminium Panels, considering HAZ Effects, IMT
IMT- 2012-80	Kota, Ravikiran S.	Wave Loads on Decks of Offshore Structures in Random Seas, CeSOS.
IMT- 2012-81	Sten, Ronny	Dynamic Simulation of Deep Water Drilling Risers with Heave Compensating System, IMT.
IMT- 2012-82	Berle, Øyvind	Risk and resilience in global maritime supply chains, IMT.
IMT- 2012-83	Fang, Shaoji	Fault Tolerant Position Mooring Control Based on Structural Reliability, CeSOS.
IMT- 2012-84	You, Jikun	Numerical studies on wave forces and moored ship motions in intermediate and shallow water, CeSOS.
IMT- 2012-85	Xiang ,Xu	Maneuvering of two interacting ships in waves, CeSOS
IMT- 2012-86	Dong, Wenbin	Time-domain fatigue response and reliability analysis of offshore wind turbines with emphasis on welded tubular joints and gear components, CeSOS
IMT- 2012-87	Zhu, Suji	Investigation of Wave-Induced Nonlinear Load Effects in Open Ships considering Hull Girder Vibrations in Bending and Torsion, CeSOS
IMT- 2012-88	Zhou, Li	Numerical and Experimental Investigation of Station-keeping in Level Ice, CeSOS
IMT- 2012-90	Ushakov, Sergey	Particulate matter emission characteristics from diesel enignes operating on conventional and alternative marine fuels, IMT
IMT- 2013-1	Yin, Decao	Experimental and Numerical Analysis of Combined In-line and Cross-flow Vortex Induced Vibrations, CeSOS
IMT- 2013-2	Kurniawan, Adi	Modelling and geometry optimisation of wave energy converters, CeSOS

IMT-2013-3	Al Ryati, Nabil	Technical condition indexes doe auxiliary marine diesel engines, IMT
IMT-2013-4	Firoozkoohi, Reza	Experimental, numerical and analytical investigation of the effect of screens on sloshing, CeSOS
IMT-2013-5	Ommani, Babak	Potential-Flow Predictions of a Semi-Displacement Vessel Including Applications to Calm Water Broaching, CeSOS
IMT-2013-6	Xing, Yihan	Modelling and analysis of the gearbox in a floating spar-type wind turbine, CeSOS
IMT-7-2013	Balland, Océane	Optimization models for reducing air emissions from ships, IMT
IMT-8-2013	Yang, Dan	Transitional wake flow behind an inclined flat plate-----Computation and analysis, IMT
IMT-9-2013	Abdillah, Suyuthi	Prediction of Extreme Loads and Fatigue Damage for a Ship Hull due to Ice Action, IMT
IMT-10-2013	Ramìrez, Pedro Agustìn Pèrez	Ageing management and life extension of technical systems- Concepts and methods applied to oil and gas facilities, IMT
IMT-11-2013	Chuang, Zhenju	Experimental and Numerical Investigation of Speed Loss due to Seakeeping and Maneuvering. IMT
IMT-12-2013	Etemaddar, Mahmoud	Load and Response Analysis of Wind Turbines under Atmospheric Icing and Controller System Faults with Emphasis on Spar Type Floating Wind Turbines, IMT
IMT-13-2013	Lindstad, Haakon	Strategies and measures for reducing maritime CO2 emissons, IMT
IMT-14-2013	Haris, Sabril	Damage interaction analysis of ship collisions, IMT
IMT-15-2013	Shainee, Mohamed	Conceptual Design, Numerical and Experimental Investigation of a SPM Cage Concept for Offshore Mariculture, IMT
IMT-16-2013	Gansel, Lars	Flow past porous cylinders and effects of biofouling and fish behavior on the flow in and around Atlantic salmon net cages, IMT
IMT-17-2013	Gaspar, Henrique	Handling Aspects of Complexity in Conceptual Ship Design, IMT
IMT-18-2013	Thys, Maxime	Theoretical and Experimental Investigation of a Free Running Fishing Vessel at Small Frequency of Encounter, CeSOS
IMT-19-2013	Aglen, Ida	VIV in Free Spanning Pipelines, CeSOS
IMT-1-2014	Song, An	Theoretical and experimental studies of wave diffraction and radiation loads on a horizontally submerged perforated plate, CeSOS

IMT-2-2014	Rogne, Øyvind Ygre	Numerical and Experimental Investigation of a Hinged 5-body Wave Energy Converter, CeSOS
IMT-3-2014	Dai, Lijuan	Safe and efficient operation and maintenance of offshore wind farms ,IMT
IMT-4-2014	Bachynski, Erin Elizabeth	Design and Dynamic Analysis of Tension Leg Platform Wind Turbines, CeSOS
IMT-5-2014	Wang, Jingbo	Water Entry of Freefall Wedged – Wedge motions and Cavity Dynamics, CeSOS
IMT-6-2014	Kim, Ekaterina	Experimental and numerical studies related to the coupled behavior of ice mass and steel structures during accidental collisions, IMT
IMT-7-2014	Tan, Xiang	Numerical investigation of ship's continuous- mode icebreaking in leverl ice, CeSOS
IMT-8-2014	Muliawan, Made Jaya	Design and Analysis of Combined Floating Wave and Wind Power Facilities, with Emphasis on Extreme Load Effects of the Mooring System, CeSOS
IMT-9-2014	Jiang, Zhiyu	Long-term response analysis of wind turbines with an emphasis on fault and shutdown conditions, IMT
IMT-10-2014	Dukan, Fredrik	ROV Motion Control Systems, IMT
IMT-11-2014	Grimsmo, Nils I.	Dynamic simulations of hydraulic cylinder for heave compensation of deep water drilling risers, IMT
IMT-12-2014	Kvittem, Marit I.	Modelling and response analysis for fatigue design of a semisubmersible wind turbine, CeSOS
IMT-13-2014	Akhtar, Juned	The Effects of Human Fatigue on Risk at Sea, IMT
IMT-14-2014	Syahroni, Nur	Fatigue Assessment of Welded Joints Taking into Account Effects of Residual Stress, IMT
IMT-1-2015	Bøckmann, Eirik	Wave Propulsion of ships, IMT
IMT-2-2015	Wang, Kai	Modelling and dynamic analysis of a semi-submersible floating vertical axis wind turbine, CeSOS
IMT-3-2015	Fredriksen, Arnt Gunvald	A numerical and experimental study of a two-dimensional body with moonpool in waves and current